Diss. ETH No. 24107

Optimal Design of Highly Efficient, Compact and Silent Medium Frequency Transformers for Future Solid State Transformers

A dissertation submitted to attain the degree of
DOCTOR OF SCIENCES of ETH ZURICH
(Dr. sc. ETH Zurich)

presented by
PENG SHUAI
M.Sc. RWTH Aachen University
born on 29. August 1984
citizen of Chengdu, P.R. China

accepted on the recommendation of
Prof. Dr. Jürgen Biela, examiner
Prof. Dr. Torbjörn Thiringer, co-examiner

2017

Acknowledgements

First of all, I would like to express my sincere thanks to Prof. Dr. Jürgen Biela for providing me the opportunity to carry out my PhD study at the Laboratory for High Power Electronic Systems (HPE) at ETH Zurich. His guidance and numerous inspiring discussions throughout my research work are highly appreciated. Also, I want to extend my sincere gratitude to Prof. Dr. Torbjörn Thiringer for his interest in my work and for being part of the examination committee. His advices and contributions resulting from evaluating my dissertation are highly valuable.

Special thanks goes to Dr. Johannes Hengstler and Mario Weder from the Institute for Mechanical Systems (IMES), ETH Zurich, Dr. Kurt Heutschi and Mr. Patrik Strebel from the Signal and Information Processing Laboratory (ISI), ETH Zurich, for providing the equipments and helping me to perform the vibration and acoustic measurement in their labs. I am really grateful to their technical instructions and suggestions during the experimental work.

Also, I would like to thank Mr. Junchao Sun and Mr. Olivier de Loriol from Vacuumschmelze GmbH for providing sample cores and useful informations about magnetic materials. This research work was initiated by the ECPE (European Center for Power Electronics), I gratefully acknowledge their financial support.

Additionally, I would like to thank our secretary Jacqueline Perez and our technician Emir Arnautović for their strong support on administrative tasks and hardware prototyping. Furthermore, I want to thank my students Songzi Qiu, Anup Anurag and Francesca Meyer for their contributions on my research work through their semester/mater thesis projects.

Many thanks to my colleagues and friends at HPE, namely, Sebastian Blume, Johannes Burkard, Christoph Carstensen, Daniel Christen, Simon Fuchs, Dominic Gerber, André Hillers, Tõnis Hõbejõgi, Michael Jaritz, Felix

Jauch, Andreas Jehle, David Leuenberger, Dimosthenis Peftitsis, Tobias Rogg, Hasan Inanç Sari, Milos Stojadinovic, Georgios Tsolaridis and Jonas Wyss, for their help with technical and non-technical advices as well as for providing a lively and enjoyable work and leisure environment.

Finally, I would like to thank my parents and other family members, this thesis would not have been possible without their endless support throughout these years. Last but not least, I want to express my deepest thanks to my wife Huilin for her long-term understanding, support and encouragement.

Zürich, May 2017 *Peng Shuai*

Abstract

Nowadays, renewable energy sources and storage systems have been increasingly integrated into the electric power grid. Due to the inherently fluctuating and geographically distributed characteristics, a dynamic power flow control and a highly flexible power delivery are demanded for the integration of these new energy systems. Conventional power transformers adapt the voltage among the generation, transmission and distribution levels and provide the galvanic isolation between different power grids. These transformers operating at the line frequency of 50/60 Hz are bulky and heavy. As intrinsically passive devices, they cannot actively control the power flow. On the contrary, solid state transformers (SSTs) consisting of power electronic converters and medium frequency transformers (MFTs) not only provide fundamental functionalities of conventional transformers but also regulate the power flow. Therefore, the SST is considered to be a promising technology for the future smart grid and is gaining more and more attentions. Furthermore, due to the operation at a much higher frequency, the size and weight of transformers in SST systems can be significantly reduced. Consequently, SSTs are very attractive for applications where the size/weight of the system is crucial.

As key components of SSTs, MFTs play an important role for the system. The reduced size of MFTs poses new design challenges due to the isolation requirement and thermal management in a limited space. Furthermore, the operating frequency of a SST is usually in the kHz range due to unacceptable switching losses of semiconductor devices at a higher frequency. Consequently, the acoustic noise emission from the MFT cannot be avoided and could become a critical issue since the frequency of the noise is in a more sensitive range of human ears.

This dissertation deals with the design and optimization of the MFT

towards an efficient, compact and silent solution. The dissertation begins with a brief overview of SST systems focusing on structures and applications. Then design challenges of MFTs are addressed and previously constructed MFT prototypes presented in literatures are reviewed. For the MFT design, an optimization model is developed with major efforts devoted to the thermal modeling and the isolation design. For the dual-active-bridge converter, a combined optimization model aimed at minimizing the total loss including the loss of semiconductor devices and the loss of the MFT is further developed based on the MFT optimization model. By using this model, the design of a 2400 V/400 V, 25 kW converter is performed. The resulting optimal design of a 4 kHz MFT with standard nanocrystalline cores and forced air-cooling achieves a power density of approximately 8 kW/L. According to the calculation result, the total efficiency of the designed DC-DC converter is above 98% and the power density is 3.63 kW/L.

Based on an intensive literature review, sources of the acoustic noise in transformers are identified focusing on electromagnetic origins. Mechanisms of the Maxwell force and the magnetostriction causing the vibration of tape wound cores typically being used for MFTs are investigated. Furthermore, vibration and acoustic modeling methods for transformers are reviewed and core materials suitable for MFTs are compared. Based on the investigation, a finite element method (FEM) based model to simulate the core vibration is developed where the material model of the laminated core is derived focusing on the amorphous and the nanocrystalline alloys. The model is used for some case studies to compare the electromagnetic forces and various factors influencing core vibrations. Moreover, vibration and acoustic noise measurements are performed on magnetic cores made by different materials and with various geometric shapes. Furthermore, the vibration and the acoustic noise of windings are also measured and compared with the core.

Finally, Pareto fronts regarding the power density and the efficiency of MFTs considering various core materials and core geometric shapes are compared. A prototype transformer based on nanocrystalline uncut cores is built. Acoustic measurements are performed on this MFT while operating it with a single-active-bridge converter and a series resonant converter. Results show that a low acoustic noise emission is achieved with a measured sound pressure level of less than 70 dBA (including the background noise of more than 60 dBA). The core noise is effectively reduced while the remaining noise is mainly caused by the winding.

Kurzfassung

Heutzutage werden immer mehr verteilte Energiequellen und Energiespeichersysteme ins elektrische Netz integriert. Diese Systeme weisen oft eine stark schwankende Energienachfrage- und Bedarfscharakteristik sowie geographische Verteilung auf, sodass eine dynamische und flexible Leistungsflusskontrolle notwendig wird. Die Stellung der verschiedenen Spannungspegel von Erzeugungs-, Übertragungs- und Verteilnetz, sowie die galvanische Trennung zwischen den verschiedenen Netzen, wird klassischerweise mit Leistungstransformatoren realisiert. Diese werden üblicherweise bei Netzfrequenz (50 Hz/60 Hz) betrieben und weisen oft ein hohes Bauvolumen und Gewicht auf. Ausserdem ist keine aktive Steuerung des Leistungsflusses möglich. Um den Anforderungen der hohen Regeldynamik des Netzes gerecht zu werden, wurde das Konzept des Solid State Transformators (SST) eingeführt. Ein SST ist ein leistungselektronisches System bestehend aus leistungselektronischen Konvertern und Mittel-Frequenz Transformatoren (MFT). SSTs ermöglichen nicht nur die herkömmlichen Funktionalitäten des Leistungstransformators sondern auch eine aktive und dynamische Steuerung des Leistungsflusses. Durch die erhöhte Betriebsfrequenz des MFTs können sowohl das Bauvolumen als auch das Gewicht reduziert werden. Diese Vorteile machen das SST Konzept für Anwendungen, welche eine hohe Regeldynamik des Leistungsflusses erfordern oder bei welchen die Größe/das Gewicht systemkritisch sind, zu einer attraktiven Lösung.

Eine Schlüsselkomponente des SSTs ist der MFT. Die Anforderungen an das thermische Design und die Isolationsfestigkeit bei reduzierten Platzverhältnissen stellen eine grosse Herausforderung dar. Der MFT wird üblicherweise im tiefen kHz Bereich betrieben um überhöhte Schaltverluste in den Halbleiterbauelementen zu vermeiden. Folglich kann die akustische Geräuschemission im Hörbereich nicht vermieden werden, welche im kriti-

schen Fall zur Beeinträchtigung des menschlichen Hörvermögens führen kann.

Der Fokus dieser Dissertation liegt auf der Modellierung und der Optimierung eines MFTs, mit dem Ziel eines effizienten, kompakten und geräuscharmen Designs. Zu Beginn wird ein Überblick über die Anwendung und die Struktur von SST-Systemen gegeben. Basierend auf den neusten Entwicklungen in diesem Gebiet, werden anschliessend die Herausforderungen an den MFT identifiziert. Um das optimale Design des MFTs zu erreichen, sind exakte und detaillierte Modelle notwendig. Innerhalb dieser Dissertation werden bestehende Modelle weiterentwickelt mit dem Fokus auf der Isolationsfestigkeit und dem thermischen Verhalten des MFTs. Darauf wird ein kombiniertes Optimierungsmodell für den Dual-Active-Bridge (DAB) Konverter zur Minimierung der Gesamtverluste einschließlich der Verluste von Halbleiterbauelementen und der Verluste von MFT aufgebaut. Basierend auf den Optimierungsergebnissen wird das Design eines DAB-Konverters (2400 V/400 V, 25 kW) vorgestellt. Der realisierte Prototyp des optimierten MFTs mit nanokristallinen Kernen und forcierter Luftkühlung, der bei einer Frequenz von 4 kHz betrieben wird, erreicht eine Leistungsdichte von 8 kW/L. Laut der Berechnung könnte das gesamte System eine Effizienz von mehr als 98% bei einer Gesamtleistungsdichte von 3.63 kW/L erreichen.

Im zweiten Teil dieser Dissertation werden die Geräuschemissionen des MFTs untersucht. Als verursachende Mechanismen wurden die Maxwell-Kraft und die Magnetostriktion identifiziert. Diese werden am Beispiel von Schnittbandkernen, welche typischerweise bei MFTs angewendet werden, detailliert untersucht. Zusätzlich werden die Schwingungs- und Akustikmodellierungsverfahren für Transformatoren diskutiert und geeignete Kernmaterialien evaluiert. Um die analytischen Resultate zu validieren und weitere Einflüsse zu untersuchen, werden verschiedene Kerndesigns in einer Finite-Elemente-Methode(FEM)-Simulation aufgebaut und bezüglich der auftretenden Vibrationen evaluiert. Darüber hinaus werden selektierte Kernmaterialien und Kerngeometrien bezüglich ihrer Geräuschemissionen und Vibrationen für verschiedene Betriebsbedingungen vermessen. Zusätzlich wird der Vibrations- und Geräuschpegel der Windung gemessen und mit denjenigen der Kerne verglichen.

Schließlich werden die MFT Designs basierend auf verschiedenen Kernmaterialien und Kerngeometrieformen bezüglich ihrer Effizienz und Leistungsdichte in einer Pareto-Front Analyse verglichen. Abschließend wird

ein MFT-Prototyp mit nanokristallinen ungeschnittenen Kernen in einen Single-Active-Bridge Konverter respektive in einen Serienresonanzkonverter integriert und akustisch vermessen. Die Ergebnisse zeigen, dass ein geräuscharmes Transformator-Design mit einem gemessenen Schalldruckpegel von weniger als 70 dBA (einschließlich des Hintergrundgeräusches von mehr als 60 dBA) erreicht wird. Das Kerngeräusch wird effektiv reduziert, während das verbleibende Geräusch hauptsächlich durch die Windung verursacht wird.

Abbreviations

1D	...	One-dimensional
2D	...	Two-dimensional
3D	...	Three-dimensional
AC	...	Alternating current
ADC	...	Analog to digital converter
CCP	...	Constant current power
CHB	...	Cascaded H-bridge
CSPI	...	Cooling system performance index
DABC	...	Dual-active-bridge converter
DC	...	Direct current
DoF	...	Degree of freedom
DSRC	...	Dual-series-resonant converter
EEA	...	Equivalent easy axis
EMU	...	Electric multiple unit
EV	...	Electric vehicle
FB	...	Full-bridge
FC	...	Flying capacitor
FEM	...	Finite element method
FFT	...	Fast Fourier transform
GA	...	Genetic algorithm
HB	...	Half-bridge
HFT	...	High frequency transformer
HV	...	High voltage
HVAC	...	High voltage alternating current
HVDC	...	High voltage direct current
IGSE	...	Improved generalized Steinmetz equation
IUT	...	Intelligent universal transformer
LFT	...	Line frequency transformer

LV	...	Low voltage
LVAC	...	Low voltage alternating current
MFT	...	Medium frequency transformer
MMC	...	Modular multilevel converter
MV	...	Medium voltage
MVAC	...	Medium voltage alternating current
MVDC	...	Medium voltage direct current
NPC	...	Neutral point clamped
PC	...	Personal computer
PET	...	Power electronic transformer
RMS	...	Root mean square
SABC	...	Single-active-bridge converter
SER	...	Smart energy router
SiC	...	Silicon carbide
SIL	...	Sound intensity level
SPL	...	Sound pressure level
SRC	...	Series resonant converter
SST	...	Solid state transformer
STATCOM	...	Static synchronous compensator
SWL	...	Sound power level
VHDL	...	VHSIC hardware description language
ZCS	...	Zero-current switching
ZVS	...	Zero-voltage switching

Contents

1 Introduction

Transformers are static devices that transfer electrical energy between electric circuits based on the electromagnetic induction without the alteration of the frequency [1]. Transformers basically consist of magnetic cores, primary and secondary windings. As an electromagnetic energy conversion device, the electrical energy fed into the primary winding is first converted to a magnetic energy and then converted back to an electrical energy in the secondary winding. Since there is no electrical connection between the primary and the secondary windings, galvanic isolation of the circuits on both sides of the transformer is achieved. By adapting the turns ratio of the winding, the voltage on the secondary side can be adjusted to be higher, lower or equal to the voltage on the primary side according to the demand.

1.1 Distribution transformer

In conventional electric power systems, the electrical energy received from high voltage (HV) transmission lines are stepped down to the medium voltage (MV) level by power transformers. Between MV grids (3.6 kV up to 27.5 kV) and low voltage (LV) grids (100 V to 690 V) for domestic/industry applications, the isolation and the voltage level adaption are accomplished by distribution transformers [2].

Traditionally, magnetic cores of distribution transformers are constructed by low-cost iron-based materials such as the silicon steel (Si-Fe). The high insulation level between the primary and the secondary winding is usually provided by additional isolation materials, e.g. oil or resin. Due to the oper-

ation at the line frequency (50/60 Hz), a relative large cross-sectional area of magnetic cores are required. Therefore, line frequency transformers (LFT) are usually bulky and heavy.

Although LFTs have some advantages such as high efficiency, high reliability and relative low cost, as being completely passive devices, they do not feature any protection functionality or controllability for the power flow. The disturbance on one side of the transformer may also be represented on the other side, such as a voltage sag on the input side and harmonics in the load current.

To minimize power losses in transmission lines, distribution transformers are usually placed in the immediate vicinity of the load/user. Consequently, these transformers are located in or close to residential areas in many cases.

1.2 Solid state transformer

In future, more and more renewable energy sources and energy storage systems will be integrated into the electric power system. Due to the dependency on unpredictable weather conditions, renewable energy sources such as solar and wind power are inherently fluctuating. Furthermore, the renewable energy is not only generated in large-scale power plants such as offshore wind farms but also available as distributed sources, e.g. small photovoltaic converters for households. The integration of these highly dynamic and geographically distributed energy sources into the electric power system poses new challenges to the system stabilization and the power flow control. Consequently, besides the basic functions of transformers, energy conversion interfaces interconnecting the MV and the LV grids need to provide additional features such as LV DC-link, power factor correction, reactive power compensation, active filtering and smart protection [3].

Due to the limit of traditional LFTs, they cannot fulfill the requirement for the future electric power system as mentioned above. More advanced power conversion concepts are demanded to realize these additional functionalities. A feasible solution for such power conversion interfaces is the solid state transformer (SST), which is a concept to achieve the voltage isolation based on a medium frequency link. As shown in Fig. 1.1, a SST basically consists of power electronic converters and a medium frequency

transformer (MFT), where the low frequency electrical energy from the MV grid is adapted to the medium frequency range by a power electronic converter and transferred through the MFT. The electrical energy is further adapted back to the low frequency range and feed to the LV grid.

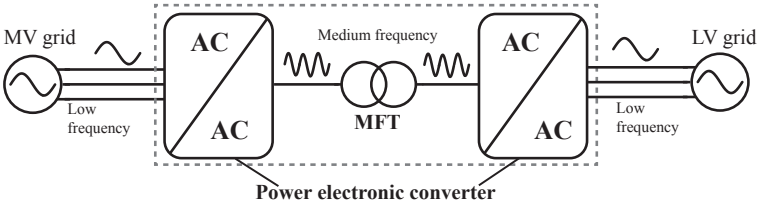

Figure 1.1: Basic concept of the solid state transformer.

Although the basic concept of the SST has already been introduced as the electronic transformer in 1970 [4] and further developed from 1980s to 1990s [5–7], it has not been widely adopted for distribution power systems, mainly due to the limited availability of high voltage, high power switching devices as well as reliability and economic issues [8]. With continuous technology advancements such as magnetic materials and semiconductor technologies, the SST is drawing more and more attentions since the 21st century and is becoming eligible for MV high power applications [9]. New terminologies for the SST such as the power electronic transformer (PET)[10], the intelligent universal transformer (IUT) [11], the smart energy router (SER) [12] are also presented in various literatures.

SST structure

To implement the SST as shown in Fig. 1.1, AC-AC conversion stages on both sides of the MFT can be configured as a single-stage converter without an intermediate DC-link, i.e. a matrix converter [13]. Alternatively, it can be configured as a two-stage converter with an intermediate DC-link, i.e. a rectifier and an inverter. With different configurations of the AC-AC conversion stage, structures of the SST can be generally categorized as:

- Structure A: single-stage converter on both sides.
- Structure B: two-stage converter with DC-link on the MV side, single-stage converter on the LV side.

- Structure C: single-stage converter on the MV side, two-stage converter with DC-link on the LV side.
- Structure D: two-stage converter on both sides, with MV and LV DC-links.

These four structures are schematically shown in Fig. 1.2. The matrix converter can be implemented as direct or indirect types. Depending on AC-AC converter topologies, structures A,B,C can be further divided into different groups. As a result, structures of SSTs can be classified into 9 groups as been introduced in [14].

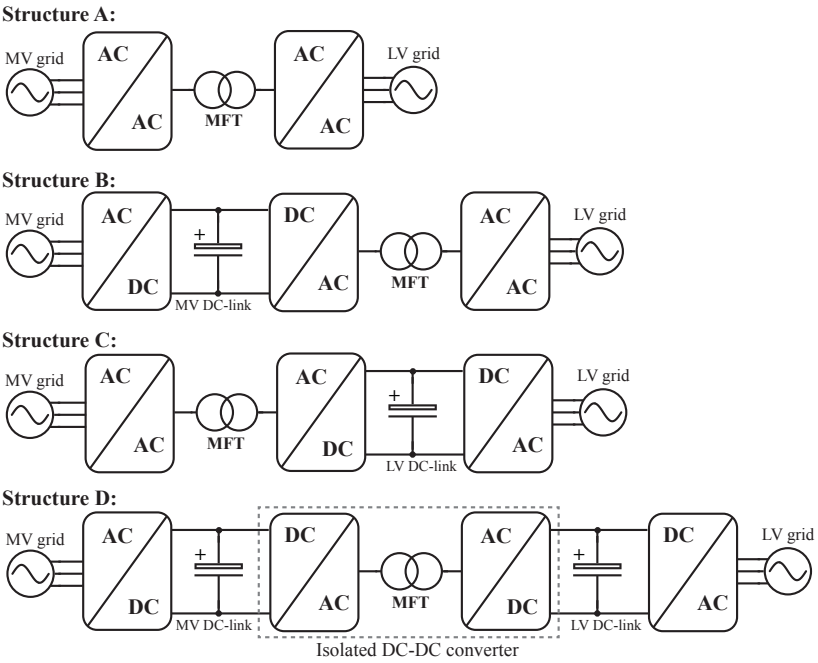

Figure 1.2: Classification of SST structures.

Among these structures, the type D is the most widely considered one [11, 15–24], where the SST can be separated into three converters:

- AC-DC rectifier

- Isolated DC-DC converter with MFT
- DC-AC inverter

Although this structure is more complex compared to other variants, the available DC-link on both sides can bring more attractive features and enable additional functionalities. Due to the separated structure, more converter topologies can be used and it is possible to achieve an optimal design for each stage in terms of the efficiency and the power density. The desired functionalities can be realized, such as the reactive power and voltage sag compensation, the fault and disturbance isolation. The LV DC-link is also essential for the integration of renewable energy sources and energy storage systems. In substations, the LV DC-link can be used to feed control equipments and to supply a DC micro grid [25]. Furthermore, by choosing suitable converter topologies, a bidirectional power transfer can be implemented.

On the MV side, the AC-DC converter needs to handle a high voltage. Therefore, multilevel converters are commonly employed due to the possibility of using switching devices with a lower voltage rating. Furthermore, multilevel converters also feature a lower common-mode voltage, reduced harmonics of input current, smaller input/output filters and possible fault tolerant operations [26]. The available multilevel topologies to implement this stage including the neutral point clamped (NPC) converter [17], the flying capacitor (FC) converter, the cascaded H-bridge (CHB) converter [20, 21] and the modular multilevel converter (MMC) [12]. On the LV side, the DC-AC converter can be implemented as conventional single-phase or three-phase bridge converters.

As key building blocks of the SST, isolated DC-DC converters with MFTs realize the galvanic isolation and the voltage level adaption, which are considered to be core circuits for the next-generation MV power conversion system [27]. For this stage, a dual-active-bridge converter(DABC) [28, 29] as shown in Fig. 1.3 (a) is widely employed, e.g. [17, 20, 24]. Major advantages of the DABC include small number of components, possible soft-switching for all devices, buck-boost and bidirectional operation. For applications where only an unidirectional power transfer is necessary, one of the active bridges can be replaced by a passive bridge, i.e. the DC-DC converter can be implemented as a single-active-bridge converter (SABC).

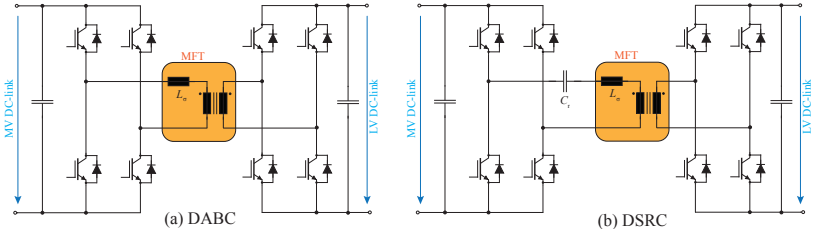

Figure 1.3: Topologies of the DABC and the DSRC for isolated DC-DC converters in SSTs.

Another topology that often been used is the dual-series-resonant converter (DSRC) as shown in Fig. 1.3 (b), which requires an additional capacitor bank to be connected to the transformer, e.g. in [10, 30, 31]. The leakage inductance of the MFT is normally utilized to form the resonant tank with the capacitor bank. Due to the inherent soft-switching property of resonant converters, the switching loss of the DSRC is usually lower than the DABC. Since a nearly sinusoidal current is flowing in the DSRC, current harmonics are much less than in the case of the DABC, where the current waveform usually has a triangular or a trapezoidal shape. The main drawback of the DSRC compared with the DABC is that the range of the output voltage control is limited and is strongly dependent on the load, which is not desirable for some applications. Furthermore, the additional capacitor bank requires more space and may add extra cost. Similar as the DABC, one of the active bridges of the DSRC could be replaced by a passive bridge. Also, both the DABC and the DSRC can be configured as three-phase topologies, e.g. in [32].

For high voltage, high power applications, a modular design is usually more feasible due to the limited voltage and power rating of semiconductor devices and the maximal size of magnetic components. On the MV side, SST modules can be connected in series to handle the high voltage while a parallel connection of the modules can be implemented on the LV side to handle the high current.

DC-DC converters in SSTs are usually operated in the kHz range and therefore the size and weight of the transformer can be significantly reduced compared with a LFT. Consequently, SSTs are especially attractive for applications where the space is limited, e.g. in offshore wind farms and traction

systems of locomotives.

Application of the SST in smart grid

As mentioned before, one of major applications of the SST is aimed for the future electric power distribution system, i.e. the smart grid. The concept of such a system is based on the efficient and flexible distribution of the electrical energy. The detailed information about the energy consumption, generation and storage of the entire utility grid is monitored and accordingly the energy flow in the grid can be flexibly coordinated. Distributed renewable energy sources, storage systems and loads can be easily tied to the grid based on the plug-and-play principle. Such applications of SSTs have been comprehensively demonstrated e.g. in the UNIFLEX project [33] and the FREEDM system [34].

In Fig. 1.4, an example configuration of the SST interfacing a MV grid and a LV grid for the future electric power distribution system is shown. Functionally, SSTs substitute classical LFTs to realize the galvanic isolation, voltage adaption and supply the conventional LVAC grid [2, 11, 20]. Additionally, SSTs provide the disturbance isolation and fault protection between the MV and the LV grids. On the one hand, the change of MV grid parameters (voltage, frequency) does not disturb the LV grid. The LV DC-link voltage can be well regulated and loads on the LV side are unaffected by disturbances of the utility grid [35]. On the other hand, nonlinear characteristics of the load, harmonic-distorted load currents and fluctuating behaviors of distributed energy sources have no influence on the MV grid. The input of SSTs features a clean sinusoidal current and unit power factor. The stability of the utility grid is enhanced since SSTs appear to be resistive loads and the LV grid is decoupled from the MV grid [36]. Under fault conditions such as the load over voltage or short-circuit of individual components, a protection strategy can be implemented to prevent damages of other components in the system [37]. Furthermore, SSTs also provide a reactive power compensation and can be utilized for the transient-fault-ride-through which is typically done by a STATCOM [38].

With the available LV DC-link, distributed renewable energy sources can be connected through individual power conversion stages according to the voltage level and the port type, e.g. PV arrays connected by DC-DC converters and wind power generators connected by AC-DC converters.

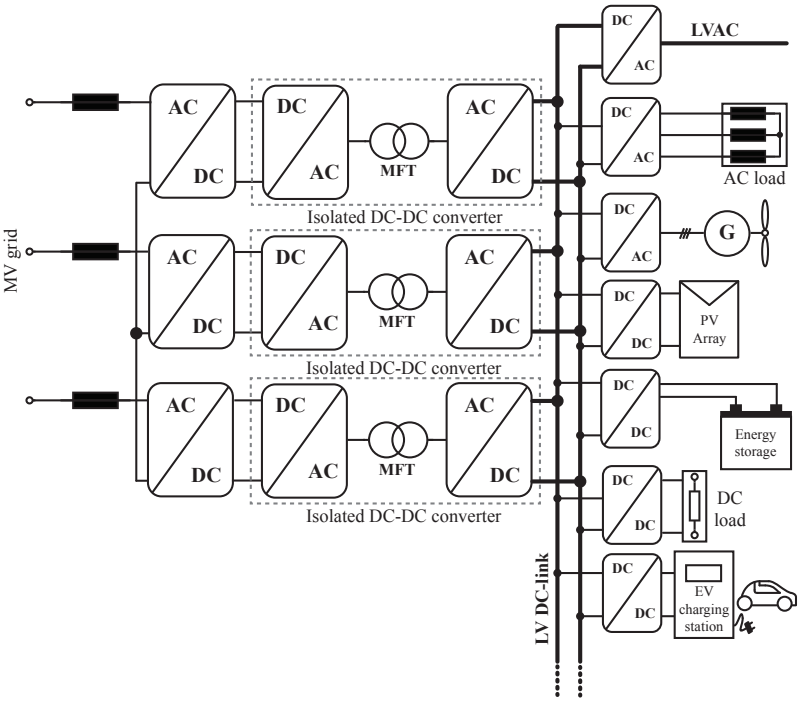

Figure 1.4: Example configuration of a three-phase SST system for the smart grid application.

Energy storage systems such as a battery bank can be connected to the LV DC-link through a bidirectional DC-DC converter. Depending on the voltage level, the LV DC-link could also be utilized to supply fast charging stations for the electric vehicles (EV) [39], data centers [40] or other DC loads, either directly or through DC-DC converters for the voltage adaption. Furthermore, AC loads such as motors, household appliances can be connected to the LVAC port or through individual inverters to the LV DC-link.

Application of the SST in traction system

The conventional power supply for the traction chain in the railway electrification system is based on the LFT connected to the single-phase AC

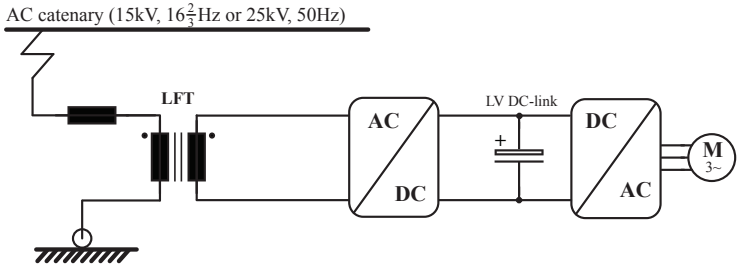

(a) Traction converter system based on LFT

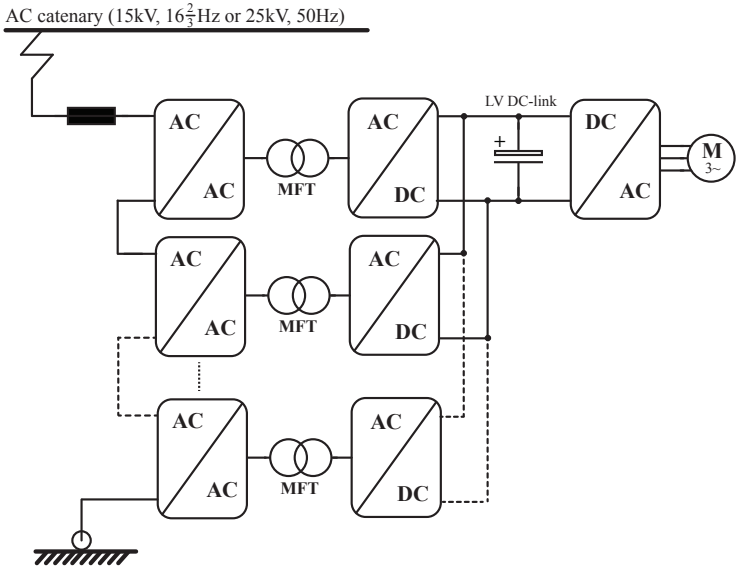

(b) Traction converter system based on SST

Figure 1.5: Traction converter system: (a) classical solution based on LFT, (b) new solution based on SST.

catenary line, e.g. 15 kV, $16\frac{2}{3}$ Hz or 25 kV, 50 Hz in Europe [41].

As shown in Fig. 1.5 (a), the high voltage of the AC catenary line is stepped down through a LFT. A rectifier is connected to the LV side of the LFT and provides a DC-link. Traction motors are fed by three-phase inverters connected to the provided DC-link. At such a low operating frequency, transforms are

bulky and heavy. In case of the electric multiple unit (EMU), the propulsion system is distributed throughout the train. LFTs take significant space and their weight also decrease the performance of the propulsion system. Due to the limited space on board and in order to reduce the weight, traction transformers are usually designed for a restricted size. Furthermore, these transformers are heavily loaded during the operation. As a result, the typical efficiency of traction transformers is about 90% to 92% [42], which is significantly lower than the efficiency (typically around 99%) of distribution transformers in utility grid.

By reducing the size/weight of transformers, more space for passengers/cargoes are gained and the performance of the propulsion system can be improved. In recent years, the demand of low-floor solutions and the size/weight reduction has been driving the application of SSTs in the traction converter system and several prototypes have been developed [30, 43–50]. As a milestone, the world's first power electronic transformer based traction converter system has been installed on a locomotive for regular service in the 15 kV/16.7 Hz railway grid in 2012. The implemented SST system has 9 cascaded modules with a total nominal power of 1.2 MW [10, 51, 52].

As shown in Fig. 1.5 (b), the SST based traction converter system is commonly designed as a modular structure with cascaded modules on the MV side to handle the high voltage and these modules are paralleled to provide the LV DC-link. Each module contains a MFT operated at the medium frequency. The size/weight of such a MFT is significantly smaller compared with the traditional LFT.

With the new structure, the volume and weight of the system can be reduced by approximately 30% and 50% respectively, compared with the conventional solution [44]. The achievable power density of the converter system based on the SST (from AC to DC) is in the range of 0.5 to 0.75 kW/kg, which is significantly higher than the power density of the conventional LFT and rectifier system (0.2 to 0.35 kW/kg). Furthermore, the total efficiency of the SST system (from AC to DC) can reach above 95%, which is also higher than the efficiency of the conventional system (typically 88% to 90%) [51]. Due to these benefits, the SST is considered to be a promising technology for the future traction application.

Application of the SST for offshore wind farm

Offshore wind farms can be located far from the coast in the ocean where the wind speed is larger and more constant. As a result, the power generation can be higher and more stable compared with an onshore wind farm [53]. However, the size and weight of the power conversion system for offshore wind farms is more crucial due to the higher installation cost. Since the available space for the arrangement of wind turbines is huge, offshore wind farms are normally large-scaled with a power generation in the range of multi-hundred MW up to multi-GW. Due to the long distance to the onshore utility grid and the high power level, HVDC transmission is more favorable than the HVAC transmission [54].

For the collection system of the wind farm, the conventional configuration is based on the parallel AC connection as shown in Fig. 1.6 (a). Back-to-back converter systems and line frequency step-up transformers are employed to connect wind turbines to a common MVAC collection port. At the offshore substation, the MVAC power is further converted to the HVDC power by a step-up transformer and an AC-DC converter. The DC power is transmitted through HVDC cables to the onshore substation and then converted back to the AC power by a DC-AC converter and the voltage is stepped down by a transformer to the utility grid level.

One of the drawbacks of the AC collection system is the bulky and heavy LFTs installed offshore since the cost of the system increases with the weight of components. Furthermore, the utilization of power electronics is not optimized and the required output filter to achieve the sinusoidal voltage also results in additional losses and costs [55].

To avoid these drawbacks, one of the alternative solutions is the parallel DC collection system as shown in Fig. 1.6 (b), which is based on the concept of the SST. For such a configuration, the AC voltage from the wind turbine generator is rectified to a DC voltage and stepped up to be connected to the MVDC collection grid. The AC-DC conversion stage can be implemented as a rectifier and an isolated DC-DC converter with an intermediate DC-link, where the isolation is provided by a MFT. Alternatively, a single stage AC-AC converter without DC-link can be used as the conversion stage between the generator and the MFT, similar as the SST structure C shown in Fig. 1.2. The voltage level is further stepped up by a centralized DC-DC converter at the offshore substation and connected to the HVDC transmission

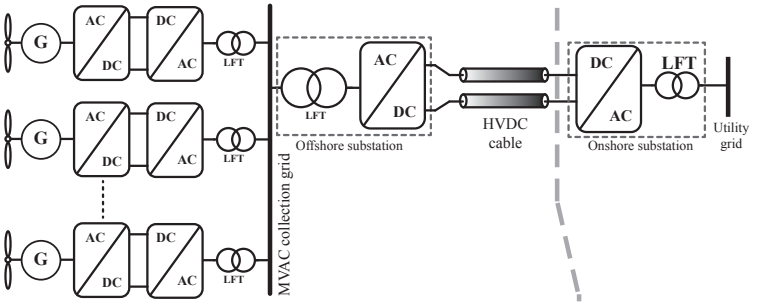

(a) Parallel AC collection system and HVDC transmission

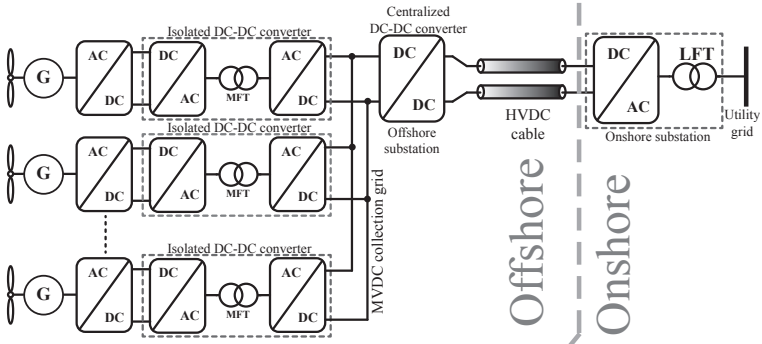

(b) Parallel DC collection system and HVDC transmission

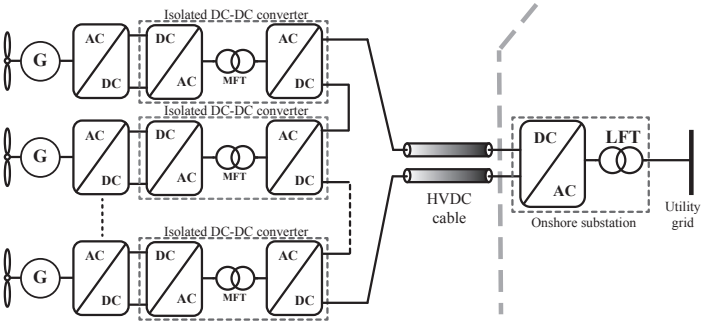

(c) Series DC connection and HVDC transmission

Figure 1.6: Wind power generation and transmission system based on (a) parallel AC collection grid, (b) parallel DC collection grid, (C) series DC connection grid.

line. The structure of the onshore receiving end is similar as the previous configuration.

Due to a significantly higher operating frequency, the size/weight of transformers installed offshore are much smaller compared with LFTs [56], which is apparently advantageous for cost reduction. The utilization of power electronics can be easily optimized to reduce losses and achieve higher system efficiency [55]. Furthermore, additional functionalities such as the reactive power compensation and the fault isolation can also be implemented [38]. The main challenge of this configuration is the high isolation requirement for wind turbine generators and converters [54]. In recent years, the offshore wind farm based on the parallel DC collection system has been widely investigated, e.g. [53, 56–61]. However, a practical implementation of this concept is not carried out yet.

A more practical configuration is the series connection of the wind turbines as shown in Fig. 1.6 (c), where the output terminals of isolated DC-DC converters are cascaded and connected directly to HVDC cables [55, 62–64]. With this configuration, DC-AC converters in each turbine (in case of the parallel AC collection system) and in the offshore substation can be omitted, which leads to a significant cost saving. Furthermore, the system efficiency is increased due to a smaller number of power converters [54]. If a wind turbine needs to be shut down, e.g. for maintenance, a bypass switch can be used to disconnect it from the DC network. However, if more wind turbines need to be shut down at the same time, the total DC voltage may fall below the threshold for transmission. With the reduced size and weight, MFT based converters can be placed inside the nacelle of the wind turbine and reduce the complexity and cost of installation [64].

1.3 Medium frequency transformer

For the SST based MV power conversion system, MFTs are the key components, which are essential for fulfilling the voltage adaption and isolation requirements and have a decisive impact on the power density and efficiency of the system. The low frequency power transformers and high frequency transformers (HFT) used in power electronic circuits have been deeply investigated and widely employed in practice applications for many years. Methodologies and practical experiences for the design and optimization of these transformers can be found in numerous literatures. However, the

research work for MFTs is still in its early stage. Existing design methodologies and experiences used for LFTs and HFTs are only partly applicable for MFTs due to distinct differences of operating conditions and requirements.

Design challenges of the MFT

As mentioned, SSTs are generally aimed for medium voltage high power applications. Compared with 50/60 Hz power transformers, the operating frequency of MFTs is significantly higher, which leads to a drastic volume and weight reduction. On the one hand, the high power density of MFTs is advantageous for applications where the space and weight are restricted. On the other hand, the high voltage, high power operating conditions of the transformer with a reduced volume also set new design challenges:

- To achieve high power density and high efficiency, advanced magnetic materials with high saturation level, low loss and superior thermal conductivity are essential.
- The thermal management becomes more crucial due to the higher power density, excellent thermal conducting materials and advanced cooling concepts need to be considered.
- High isolation level requires electric field conform design and good insulation materials due to

  – high voltage operation and cascaded structure, where one module usually needs to withstand the full system voltage.

  – an oil-insulation is normally not considered for compact designs.

  – non-sinusoidal operating waveforms lead to a higher dielectric stress due to the fast changing of the voltage.

  – dielectric losses are more significant at high frequencies.
- More attentions need to be paid to the structure of the core and the winding arrangement since their influences on losses, the isolation and the thermal management are more significant.
- The operation of DC-DC converters is highly dependent on the leak-

age inductance of the transformer. An accurate design of parasitics of the transformer is crucial to achieve the desired operating conditions especially for a resonant type converter, e.g. the DSRC.

- The acoustic noise emission of the transformer becomes more critical since the operating frequency is shifted to a more sensitive range of human ears and the non-sinusoidal excitation condition also results in more harmonics of the acoustic noise.

These new challenges have drawn attentions from both academic and industrial research institutes in the last two decades. Several research projects have been dedicated to the design of the isolated DC-DC converter including the optimization and characterization of the MFT. These research works are aimed for various applications including the aforementioned ones and some prototypes are built for experimental validation.

Previously constructed MFT prototypes

In Table 1.1, some of the previously constructed MFTs and there design information which can be found in literatures are listed. The information not provided by authors is indicated as 'N/A' in the table. The rated power of these MFTs varies from 10 kW to several hundred kW, where low power prototypes are mostly down-scaled from full power systems due to the limitation of laboratory test. Since a modular design is usually considered for the SST, the power rating of the MFT in each module is much lower than the power rating of the whole system. For example, the 1.2 MVA SST system in [50, 52] consists of 9 modules where the MFT in each module is rated at 150 kVA (one redundancy is considered).

The operating frequencies of listed transformers are selected from a few 100 Hz to a few tens of kHz. However, high frequency prototypes operated at above 20 kHz are mainly considered in the early stage which are not aimed for medium voltage, high power applications, e.g. [65, 67, 70]. Due to the limited switching speed of high voltage silicon IGBTs, the operating frequency of the SST is generally selected at below 10 kHz. In recent years, the development of high voltage silicon carbide (SiC) devices has drawn the attention for SST applications. The utilization of these fast switching devices with high blocking voltage gives the possibility to increase the operating frequency in order to further reduce the size of the MFT and other

Table 1.1: Main specifications of MFTs reported in literatures

Source/ Type	P_n kVA	Freq. kHz	U_{iso} kV	Core mat.*	Cooling method	Tran. Power density†	Eff.⋆ %	Struct./ Wind.+
GE:1992[65] Dry	50	50	N/A	Ferr.	Air	12(wt)	$99.4^{a,c}$	Coaxial/ Cable
GE:2008[66] Dry	150	10	N/A	Amor.	Air	N/A	N/A	Core/ Ro. Litz
UWM:1995[67] Dry	120	20.4	N/A	Ferr.	Water	59.5(vol)	$99.6^{a,c}$	Coaxial/ Cable
ABB:2002[43] Dry	350	10	15	Nano.	Water	>7(wt)‡	N/A	Coaxial/ Cable
ABB:2007[47] Oil	75	0.4	15	Si-Fe	Oil	N/A	$>95^{b,c}$	So. Cu
ABB:2011[50, 52] Oil	150	1.75	15	Nano.	Oil	N/A	$\approx 96^{b,c}$	Ro. Litz
KTH:2009[68] Oil	170	4	30	Amor.	Water Oil	3.45(wt)	$99^{a,c}$	Shell/ Ro. Litz Foil
TUD:2005[69, 70] Dry	50	25	N/A	Nano.	Water	≈50(vol)	$>97^{b,c}$	Shell/ Foil
Bomb:2007[30] Dry	500	8	15	Nano.	Water	27.8(wt)	N/A	Shell/ Hol. Al
FAU:2011[71] Oil	450	5.6	25	Nano.	Water Oil	N/A	N/A	Core/ Hol. Al
NCSU:2010[72]◇ Dry	10	3	15	Amor.	Air	N/A	$96.76^{a,c}$ $97.3^{a,c}$ $97.16^{a,c}$	Core/ Ro. Litz
NCSU:2012[73] Dry	30	20	9.5	Nano.	Air	N/A	$99.5^{a,d}$	Coaxial/ Ro. Litz So. Cu
EPFL:2010[8] Dry	25	2	8	Amor.	Air	2.5(vol)	$99.13^{a,d}$	Shell/ Rec. Litz
IK4:2012[74]◇ Dry	400	<1	18	Si-Fe	Air	3.41(vol)	$99.36^{a,d}$	Shell
		>5		Nano.	Fan	14.88(vol)	$99.76^{a,d}$	Core
ETH:2013[14, 23]◇ Dry	166	20	N/A	Nano.	Water	32.7(vol)	$99.5^{a,c}$	Shell/ Rec. Litz
				Ferr.	Fan	8.21(vol)	$99.4^{a,c}$	
ETH:2015[75]◇ Dry	25	25	N/A	Ferr.	Air	8.2(vol)	N/A	Matrix/ Litz
		50				13.3(vol)		
		83				15.9(vol)		
Chalm:2016[76]◇ Dry	50	5	6	Nano.	Air	15.1(vol)	$99.66^{a,c}$	Shell/ Rec. Litz
				Ferr.	Air	11.5(vol)	$99.58^{a,c}$	
STS:2014[77] Oil/Dry∇	450	8	>30	N/A	Oil Air	9(wt)	$99.7^{a,c}$	Shell/ Litz

N/A: Information not available.

* Core material: Amor.=Amorphous, Nano.=Nanocrystalline, Ferr.=Ferrite

† Transformer power density: vol=Volume power density in [kW/L], wt=Weight power density in [kW/kg].

⋆ Efficiency: ^{a} Transformer only, ^{b} Converter system, ^{c} Measured at rated power, ^{d} Calculated

+ Structure/Winding type: Ro. Litz=Round Litz, Rec. Litz=Rectangular Litz, So. Cu=Solid Copper, Hol. Al=Hollow Aluminum tube

‡ The exact value is not given, the weight is less than 50 kg.

◇ More than one prototypes are built.

∇ Only the winding is immersed in oil.

components in the system such as filters, e.g. [73, 75].

Regarding the transformer core, four kinds of magnetic materials are generally considered: Si-Fe, Fe-based amorphous alloy, nanocrystalline alloy and ferrite. It can be seen that Si-Fe cores are only used at a frequency below 1 kHz due to its high loss, e.g. [47, 74]. Ferrite cores are generally used at above 20 kHz due to the low saturation level. In the frequency range from 1 kHz up to 20 kHz, commonly used core materials are Fe-based amorphous and nanocrystalline alloys due to their low loss and relatively high saturation flux density. More details about core materials for MFTs are discussed in chapter 4.

The structures of these constructed MFTs can be classified into four types:

- Coaxial type
- Shell type
- Core type
- Matrix type

The coaxial type transformer is based on the coaxial cable, in which the inner and outer conductors are used as two windings as shown in Fig. 1.7 (a). Ring cores are normally used for this type of transformer since a better fitting of windings in the core window can be realized. By using this structure, the leakage inductance can be easily calculated and a very small value can be achieved. The field distribution inside the coaxial cable is more homogeneous which is good from insulation point of view. A copper tube is generally used as the outer winding which could be separated into several segments to obtain more turns [67]. Also, Litz-wires can be used as the inner winding as shown in Fig. 1.7 (a), which is implemented in [65, 73]. The main drawback of this structure is that the flexibility of selecting the number of turns for both windings is limited due to the difficulty of construction [9]. Therefore, this structure is not widely considered for the MFT.

Except for the coaxial type, the other three types are all solenoidal structures, which is more favorable for design, construction and the cost is also lower [9]. Especially the shell type and the core type structure as shown in Fig. 1.7 (b) and (c), which have been adopted for most of MFT prototypes

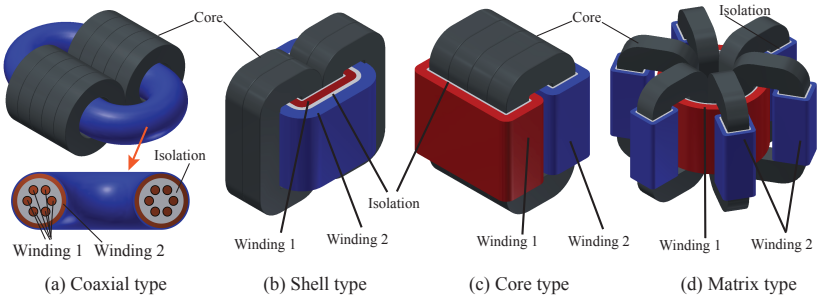

(a) Coaxial type (b) Shell type (c) Core type (d) Matrix type

Figure 1.7: Structures of transformers for medium frequency applications.

listed in the table. The shell type structure are commonly used for large power transformers, which can be constructed by E-shaped cores or by a combination of two rectangular-shaped cores. Windings are normally wound concentrically around the central leg of the core where one winding is surrounded by another. The analytical calculation of the leakage inductance for the concentric winding is convenient and a low inductance value can be achieved for the transformer. Alternatively, the winding can be arranged as split winding, with a separated structure as in the case of the MFT reported in [74].

Core type transformers are normally constructed by rectangular-shaped cores with windings arranged separately on two core legs as shown in Fig. 1.7 (c). This structure is the most convenient one for manufacturing among these mentioned structures and a more compact design can be achieved compared with shell type transformers [9]. It also provides a better isolation between the two windings since they are well separated. However, the analytical calculation of the leakage inductance becomes sophisticated due to the unknown distribution of the magnetic field outside of the winding. It is also more difficult to obtain a low leakage inductance value compared with the shell type structure. Alternatively, both windings can be arranged concentrically around one of the core legs and the leakage inductance calculation in this case is the same as for the shell type transformer with concentric winding.

For both the shell and the core type transformer, several cores can be easily stacked to achieve the required cross-sectional area. The winding is usually constructed with copper foil or Litz-wire which are typical for high

frequency applications. To achieve a higher copper fill factor in the core window, the rectangular Litz-wire can be used instead of the round Litz-wire, e.g. in [14, 74]. To further reduce the leakage inductance, the LV winding can be split up and interleaved with the HV winding [58]. However, this requires additional isolation space and the size of the winding is increased. Furthermore, the complexity of construction is also higher. Therefore, the interleaved winding is normally not considered for MFTs. It is worth to mention that for MFT prototypes reported in [30, 71], windings are constructed by rectangular aluminum tubes, where the deionized water flows through the tube for direct cooling of the winding.

The matrix type structure is generally considered for transformers with high turns ratio (e.g. >10:1), where several magnetic cores are inter-wired with series/parallel conductors. Compared with other structures, less turns of the HV winding are required which could reduce the construction effort. Furthermore, the split core arrangement enables the magnetic paralleling of semiconductor devices so that a better current distribution among devices can be obtained [78]. Due to the cascaded structure of the SST, the required turns ratio for each isolated DC-DC converter is normally less than 5:1. Moreover, it is shown that this type of structure has no benefit in terms of efficiency and power density compared with other structures [78]. Therefore, MFTs built with this structure is not found in literature. In [78], a matrix type MFT design with a turns ratio of 12:1 is analyzed and compared with other structures. Three transformers with a turns ratio of 10:1 built with rectangular-shaped cores arranged circularly similar as the matrix type structure are reported in [75]. The LV winding is not split up to each core, instead, it is wound concentrically outside the HV winding. The purpose of using this structure is to keep the same number of turns for the three designs considered to be operated at different frequencies. Although these prototypes are indicated as matrix type in Table 1.1, the difference should be noticed.

As one of the critical issues for MFTs, the isolation design is essential. It can be seen that the isolation voltage level for the built transformers are generally more than 10 kV. For example, the MFT usually needs to withstand the full line voltage of 15 kV or 25 kV for traction application [43, 71]. Both oil-immersed and dry-type designs are employed as shown in Table 1.1. In case of the dry-type transformer, the oil tank is eliminated which could save the space and reduce the cost. Materials with a high dielectric strength are normally used as isolation layers and for mechanical parts such as the

bobbin. Furthermore, casting the transformer by the epoxy resin can be considered to achieve a higher isolation level. The oil-immersed transformer is more favorable for a high isolation requirement and the oil can also be used as cooling medium, e.g. [52]. With careful designs, a high isolation level for MFTs is achievable while keeping a relative small size. This is validated by experimental measurements, e.g. in [30, 43, 73].

For the thermal management, the natural convection (indicated as 'Air' in Table 1.1) is favorable since no additional component for the active cooling is required, such as fans or pumps. However, to achieve a more efficient cooling and a more compact design, active cooled heat sinks by fans or water are usually mounted, e.g. [14]. More advanced cooling concepts such as the direct cooling of windings by deionized water [30, 71] are also used in order to have a more efficient cooling.

It can be seen that with advanced core materials and careful designs, the efficiency of MFTs can reach over 99.5%, especially when nanocrystalline cores are used. The power density of MFTs is highly dependent on the isolation requirement. Generally, a high isolation voltage level requires larger distances to insert the insulation material and the power density of the transformer becomes smaller. In order to reach the equivalent power density with a higher isolation requirement, solid insulation materials with a high dielectric strength or oil can be used as the insulation medium instead of air. In [77], a MFT with oil-immersed windings is built with a power density of 9 kW/kg and the achieved isolation voltage is over 30 kV.

1.4 Motivation of the work

To reduce the size of the transformer, it is desirable to operate the DC-DC converter at a higher frequency. However, without using expensive SiC devices, the operating frequency are normally selected in the range of a few 100 Hz to a few kHz for high power applications as shown in the previously built SST systems. The limitation of further increasing the frequency is mainly to retain the required system efficiency and to reduce the effort for the thermal management [52]. With the increase of the frequency, the switching loss of semiconductor devices and the core loss of magnetic components are significantly higher. As a result, the system efficiency decreases dramatically and larger heat sinks or more advanced cooling systems are necessary to dissipate the heat generated by these additional losses. On the

other hand, the volume of the transformer cannot be effectively reduced by increasing the frequency above a certain level due to the isolation requirement and the thermal limit [79]. For these reasons, it is more beneficial to keep the operating frequency in the kHz range for high power applications with the state-of-the-art technology. However, due to the operation in the audible frequency range, the acoustic noise emission of the transformer cannot be avoided, which is an undesirable issue especially for applications close to residential areas. The measurement of an amorphous core based MFT excited to the flux density of 0.45 T shows that the generated acoustic noise can be over 100 dB [8]. This implicates a noise level of over 100 times higher than the sound level of a normal conversation (60 dB).

The acoustic noise emission of magnetic devices has been constantly investigated in the past few decades. The research work focusing on electrical machines are rather extensive, e.g. [80–82]. In case of transformers, the studies are mainly focusing on Si-Fe based power transformers operated at the line frequency, e.g. [83–85]. So far, in the medium frequency range, the acoustic noise issue for magnetic components has been mainly investigated for inductors [86–91].

For the MFT, the research work regarding the acoustic noise is rarely to be found. As one of the major problem for MFTs to be solved, it demands more detailed investigations. Although sources of acoustic noise in LFTs are well identified and related measures to reduce the noise are also widely investigated, a reevaluation for MFTs is still demanded for the following reasons:

- Commonly used core materials for MFTs are amorphous and nanocrystalline alloys, whose properties differ from the Si-Fe used for LFTs.
- MFTs are operated under the excitation of a non-sinusoidal voltage and current in a much higher frequency range (typical waveforms of LFTs and MFTs are shown in Fig. 1.8).
- MFTs usually employ Litz-wires or copper foils, the mechanical property and construction of the winding is different compared with the winding of LFTs normally built with solid conductors.
- The mechanical construction of the magnetic core and transformer body also has significant differences between the MFT and the LFT.

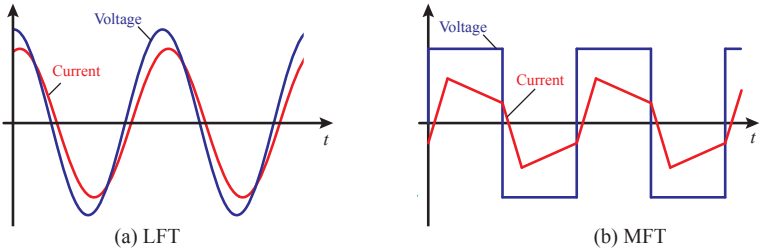

Figure 1.8: Typical voltage and current waveforms of the LFT and the MFT.

Therefore, origins of acoustic noise in MFTs need to be identified focusing on the magnetic core and the winding. Accordingly, measures to reduce the acoustic noise emission for MFTs need to be found, which can be taken into account for the future MFT design.

As major performance indexes of transformers, a high efficiency and a high power density are always demanded. Measures taken to reduce the acoustic noise may also have impact on the performance of the transformer. Therefore, the evaluation of these influences are necessary in oder to find the best compromise among these factors. On the other hand, the isolation and the thermal management are critical issues for the MFT design which demand further investigations. To accomplish these tasks, a design and optimization methodology with improved models needs to be established. The ultimate object is to achieve a compact, efficient and silent design for the MFT.

1.5 Contributions of the dissertation

Main contributions of this dissertation are summarized below:

A) Origins of acoustic noise in MFTs and vibration/acoustic modeling

- In this dissertation, sources of acoustic noise associated with MFTs are identified based on a literature survey for conventional large-scale power transformers. The most relevant electromagnetic origins of acoustic noise for MFTs are identified to be the Maxwell force, the magnetostriction and the Lorentz force.

- Focusing on tape wound cores with a laminated structure, mechanisms of the Maxwell force and the magnetostriction inducing the vibration of the magnetic core are analyzed with emphasis on the influence of air gaps/cut of the core.

- Methods for the vibration and acoustic noise modeling of MFTs using the finite element method (FEM) are investigated. A material model for tape wound cores based on the elementary mixture rules for fiber-reinforced laminae is proposed, where the material parameters for amorphous and nanocrystalline alloys based tape wound cores are derived. In addition, a simplified FEM model for the analysis of the core vibration is implemented. By using the FEM model, the impact of various effects on the core vibration induced by the electromagnetic forces and the magnetostriction is evaluated.

B) Vibration/acoustic noise measurements of magnetic cores/windings

- Vibration and acoustic measurements are performed on various magnetic cores. Vibration measurements are performed by using a laser scanning vibrometer and acoustic noise measurements are performed in an anechoic chamber. The investigated cores are made of various materials suitable for MFTs, including the ferrite, the Fe-based amorphous alloy, the Co-based amorphous alloy and the nanocrystalline material. Based on the measurement result, the most suitable core material and geometric shape for the MFT design is identified.

- Vibration and acoustic measurements are also performed for windings made of Litz-wires. The acoustic noise induced by the winding vibration and by the core vibration is compared.

C) Optimization of the DABC including the MFT

- Based on an intensive literature study, an optimization model of the MFT is developed with significant extensions on the isolation design and the thermal modeling. An analytical calculation of the maximal electric field strength based on the charge simulation method is included in the optimization process. In addition, a detailed thermal model for windings based on the round Litz-wire is implemented and an iterative calculation is employed to calculate temperatures.

- A combined optimization model of a DABC to minimize the total loss including semiconductor losses and transformer losses is developed, where operation parameters of the DABC and design parameters of the MFT are included as free parameters in the optimization.
- A case study of a down-scaled DABC design for the SST application is performed where the operating frequency is determined based on the investigation of the limitation for reducing the transformer volume by increasing the operating frequency. By using the combined optimization model, an optimal design of the DABC including the MFT is determined.

D) Design considerations for MFTs

- Material properties of core materials with potential for MFTs are compared with respect to the loss, the saturation level and the magnetostriction, which are relevant to the efficiency, the power density and the acoustic noise emission of the transformer. The design of MFTs considering several core materials and geometric shapes are investigated resulting in efficiency-power density Pareto fronts of MFTs for various core materials and core shapes. Based on vibration and acoustic noise measurements and optimization results, suitable core materials and geometric shapes for an efficient, compact and silent MFT design are identified.
- A prototype transformer based on nanocrystalline rectangular uncut cores has been built. Acoustic measurements are performed on the transformer when operating it with a SABC and a series resonant converter (SRC). Measurement results show that the measured acoustic noises of the transformer in both cases are similar. The prototype transformer achieves a relatively low acoustic noise emission, where the contribution of the core vibration is effectively reduced and the remaining acoustic noise is mainly caused by the winding vibration.

1.6 Outline of the dissertation

In this introductory chapter, basic concepts of SSTs and their potential applications are introduced. For the key component of SSTs, design challenges

of the MFT are addressed and previously constructed MFT prototypes are reviewed. As one of the major problems for MFTs, the acoustic noise issue is pointed out, which has rarely been investigated. Based on these backgrounds, motivations and objects of this dissertation are stated. Finally, major contributions of this work are briefly summarized.

Chapter 2 deals with the design and optimization of isolated DC-DC converters considering a case study of a 2400 V to 400 V, 25 kW DABC. Firstly, the topology selection and modulation methods of the DABC are discussed. Then an optimization model of the MFT is presented, where calculation procedures are introduced. The emphasis is put on the thermal management and the isolation design. An improved thermal model including the modeling of the Litz-wire and an iterative temperature calculation is presented. Furthermore, the calculation of the maximal electric field strength based on a 2D analytical method is introduced, which is included in the optimization model. The developed model is used to investigate the influence of the isolation requirement on the MFT design regarding the frequency and volume dependency. Based on the result, the operating frequency of the converter is determined. Finally, a combined optimization model to minimize the total loss of the DABC based on the developed MFT optimization model is presented. By using this model, the optimal design of the DABC for the studied case is determined.

In chapter 3, basic concepts of acoustic noise emission are introduced, including the quantification, the measurement and the evaluation of sound. Then sources of acoustic noise associated with transformers are reviewed focusing on electromagnetic origins. As the most relevant aspect for the MFT, the mechanism of noise generation in case of a tape wound core is analyzed. Furthermore, fundamentals of the vibration and acoustic modeling of transformers are introduced including modeling procedures, mathematical descriptions of models and coupling methods. The elastic model of laminated structures based on an analytical approximation is introduced in detail, which is relevant to tape wound cores.

Based on the model introduced in chapter 3, the vibration modeling of magnetic cores by using the FEM is discussed in chapter 4. At first, magnetic materials for the MFT application are reviewed and relevant properties of these materials are compared. Focusing on the amorphous and the nanocrystalline alloys, magnetic and elastic parameters are derived based on the manufacturers' information, literatures and an analytical approxima-

tion. According to the derived data, the model is described and simulation results are presented focusing on the comparison of core materials and geometric shapes.

In chapter 5, vibration and acoustic measurements performed on magnetic cores and windings are discussed. The chapter begins with an introduction of vibration and acoustic measurements regarding sensors and measurement environments. Then the experimental setup and sample cores used for measurements in this work are introduced. In the last part, measurement results are presented, which also focus on the influence of the core material and the geometric shape.

In chapter 6, the transformer optimization model presented in chapter 2 is further used to investigate Pareto fonts of MFTs based on magnetic cores with different materials and geometric shapes. The adaption of the model in order to match different core shapes is presented and design results are discussed. As a final evaluation, a MFT prototype based on a nanocrystalline uncut core is built. Acoustic measurements are performed on this prototype and results are presented.

Finally, in chapter 7, the work carried out and conclusions are summarized. Based on the achievement, an outlook for the future work is given.

1.7 List of publications

Different parts of this thesis, including text, tables and figures have already been published in international scientific journals and conference proceedings. Related publications generated in course of this PhD dissertation are listed below:

- P. Shuai and J. Biela, "Design and optimization of medium frequency, medium voltage transformers", in *Proc. of the 15th European Conference on Power Electronics and Applications (EPE)*, Lille, France, Sept. 2013.
- P. Shuai and J. Biela, "Investigation of acoustic noise sources in medium frequency, medium voltage transformers", in *Proc. of the 16th European Conference on Power Electronics and Applications (EPE)*, Lappeenranta, Finland, Aug. 2014.

- P. Shuai and J. Biela, "Impact of core shape and material on the acoustic noise emission of medium frequency, medium voltage transformers", in *Proc. of the 17th European Conference on Power Electronics and Applications (EPE)*, Geneva, Switzerland, Sept. 2015.
- P. Shuai and J. Biela, "Influence of Material Properties and Geometric Shape of Magnetic Cores on Acoustic Noise Emission of Medium-Frequency Transformers", *IEEE Transactions on Power Electronics*, Volume: 32, Issue: 10, Page(s):7916-7931, Oct. 2017.

Further publications:

- P. Shuai and J. Biela, "Acoustic Noise Emission of Magnetics", *ECPE Workshop: Innovations in Passive Components for Power Electronics Applications*, Berlin, Germany, Oct. 2014.
- J. Biela, M. Jaritz, D. Leuenberger, P. Shuai and A. Hillers, "Design, Modelling and Optimisation of Magnetic Components for Power Electronic Converters", *European PhD School - Power Electronics, Electrical Machines, Energy Control and Power Systems*, Gaeta, Italy, May 2017.

2 Isolated DC-DC Converter Design and Optimization

In solid state transformers, isolated DC-DC converters are key building blocks which convert the power flow between the medium voltage and the low voltage level and provide the galvanic isolation through the integrated transformers operated in the kHz range.

As a case study, a three-phase SST system interfacing the 7.2 kV MV grid and the 400 V LV grid as shown in Fig. 2.1 is considered. The DC-link voltage on the MV side is 12 kV and on the LV side is 400 V as considered in [14]. This chapter focuses on the DC-DC converter and transformer design.

2.1 Isolated DC-DC converter

To achieve a high voltage of the MV DC-link in SSTs, DC-DC converters usually consist of several modules connected in series. On the LV side, these modules are connected in parallel to be able to conduct the high current.

2.1.1 Topology of DC-DC converter

As mentioned, to enable a bidirectional power transfer, the DABC or the DSRC is commonly employed for the DC-DC power conversion stage. Since an additional resonant capacitor is required in the DSRC, the DABC is selected in this work for its simplicity. Normally, converters on both sides of the transformer can be chosen among the half bridge (HB), the full bridge (HB) and the NPC topologies as shown in Fig. 2.2.

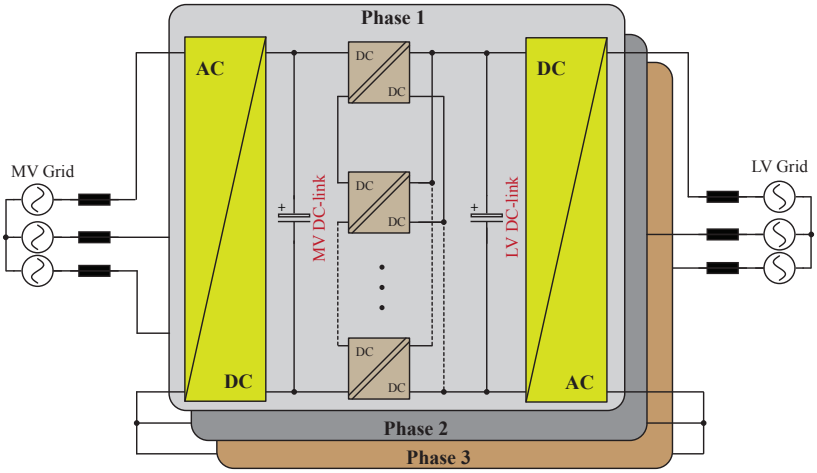

Figure 2.1: Example configuration of a three-phase SST system.

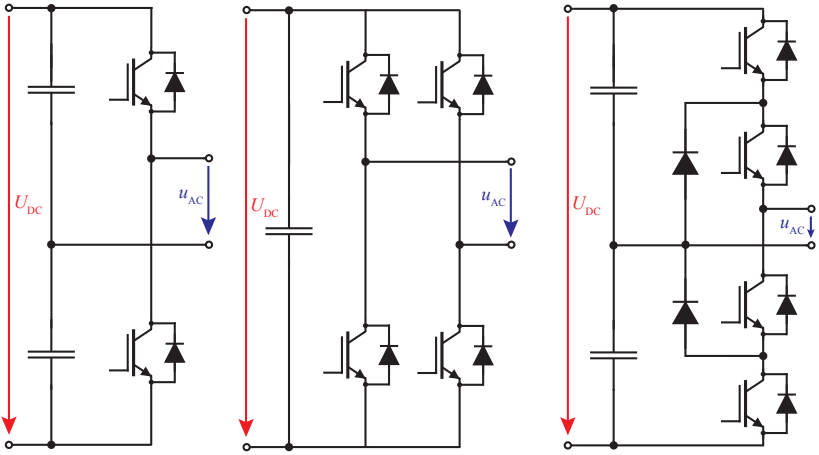

Figure 2.2: Considered active bridge topologies for both sides of the DABC.

The HB topology is simple with only 2 switches and each switch needs to withstand the full DC-link voltage U_{DC}. The AC output voltage u_{AC} has a rectangular waveform with an amplitude of $U_{DC}/2$ during each half of

the switching cycle. The FB and the NPC topologies need 4 switches and the output voltage can be clamped at 0. Therefore, the duty ratio of u_{AC} can be adjusted between 0 and 0.5. This gives more possibilities for the modulation of the DABC, which is helpful to realize the soft switching. The blocking voltage of a single switch in the FB topology is also U_{DC} but the amplitude of u_{AC} is doubled compared with the HB topology. For the NPC topology, the amplitude of u_{AC} is the same as in the HB topology, but the blocking voltage of a single switch is only half of the DC-link voltage. This enables the utilization of IGBTs with lower voltage level which features lower on-state voltage drop and higher switching speed. The comparison of the three mentioned topologies are summarized in Table 2.1.

Table 2.1: Comparison of three active bridge topologies for the DABC

Topology	Blocking voltage of a single switch	Amplitude of u_{AC}	Duty ratio of u_{AC}
HB	U_{DC}	$U_{DC}/2$	50%
FB	U_{DC}	U_{DC}	0~50%
NPC	$U_{DC}/2$	$U_{DC}/2$	0~50%

With the state-of-the-art technology of semiconductor devices, the blocking voltage of SiC IGBTs up to 15 kV has already been considered for SST application [92]. But the high cost and commercial availability are still barriers for a wide application of high voltage SiC devices. Therefore, silicon based high voltage IGBTs are considered to be the switching device in this work. Commercially, the blocking voltage of a IGBT module can reach up to 6.5 kV. However, due to the low switching speed, the switching loss of high voltage IGBTs (3.3 kV and above) is quite significant when operated in the kHz range. Therefore, IGBTs with a blocking voltage up to 1.7 kV are considered to be used on the MV side of the DABC.

If the HB or the FB topology is used, the maximal blocking voltage of a single DC-DC converter module is only 1.7 kV. Therefore, at least 8 cascaded DC-DC converter modules are required to withstand the DC-link voltage on the MV side. On the other hand, if the NPC topology is employed, twice of the blocking voltage can be achieved for a single module. Accordingly, only 4 DC-DC converter modules are necessary for the given DC-link voltage. This results in the same total number of IGBTs as using 8 HF converters, but the total number of IGBTs on the LV side is reduced by 50% since the

number of converter modules is smaller. Another benefit of using the NPC topology is the possibility to adjust the duty ratio of u_{AC} as mentioned before. For these reasons, the NPC topology is selected for the MV side bridge converter. However, 2 additional clamping diodes are needed in each converter module. Since the resulting blocking voltage (1.5 kV) for a single switch is close to the voltage rating of the IGBT in case of using 4 modules, one additional module is necessary for safety reason. This structure results in a DC-link voltage of 2.4 kV for each DABC module on the MV side.

On the LV side, the voltage is not critical. The FB topology is selected due to the desired flexibility of adjusting the duty ratio of the AC voltage and the full utilization of the DC-link voltage. Furthermore, the two clamping diodes can be saved compared with using the NPC topology. The resulting topology of the DC-DC converter module is shown in Fig. 2.3, where the AC output ports of the two bridge converters are interconnected by a MFT.

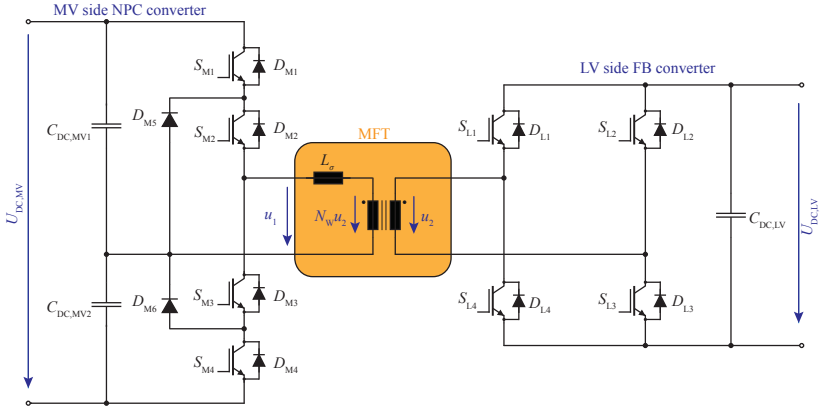

Figure 2.3: Selected topology for the DC-DC converter module.

2.1.2 Specifications of DC-DC converter

According to previous defined DC-link voltages, specifications of the DABC module with a down-scaled power are given in Table 2.2. For safety reason, the isolation voltage is defined as two times of the full MV DC-link voltage. The switching frequency of the DABC is considered to be fixed and the determination of the frequency is discussed later. With the defined voltage

and a fixed switching frequency, the maximal transferable power of the DABC is only dependent on the leakage inductance and the turns ratio of the MFT. Therefore, the leakage inductance and turns ratio of the MFT is determined in a later step considering the modulation of the DABC.

Table 2.2: Specifications of the DABC

MV DC-link Voltage	$U_{\mathrm{DC,MV}}$	2400 V
LV DC-link Voltage	$U_{\mathrm{DC,LV}}$	400 V
Nominal power	P_{n}	25 kW
Isolation voltage level	U_{iso}	24 kV

In order to calculate the loss of the converter, semiconductor devices need to be selected. To achieve a high power density, discrete devices are considered instead of power modules. Therefore, several devices may need to be paralleled to conduct the current. Selected semiconductor devices for the DABC are listed in Table 2.3, which are considered for the loss calculation.

Table 2.3: Selected semiconductor devices for the DABC

Device	Type	Part number	Package	Numbers of devices in parallel
MV side switch	IGBT	IHW30N160R2	TO-247	2
MV side clamping diode	SiC Diode	C3D25170H	TO-247	1
LV side switch	IGBT	IKW40N65F5	TO-247	4

2.2 Modulation of the DABC

By simplifying bridge converters on both sides as AC voltage sources with a rectangular waveform, the DABC can be represented by an equivalent circuit as shown in Fig. 2.4. The following assumptions are applied:

1. All losses are neglected.

2. The transformer is considered to be ideal and the magnetizing inductance and the parasitic capacitance are neglected.

3. All quantities are referred to the MV side.

4. DC-link voltages ($U_{\mathrm{DC,MV}}$ and $U_{\mathrm{DC,LV}}$) are considered to be constant.

5. All switching devices and diodes are assumed to be ideal.

The leakage inductance L_σ is referred to the MV side and $i_{L\sigma}$ is the current flowing through the MV winding of the MFT. The AC voltage u_1 of the MV bridge converter is applied on the MV winding of the MFT and u_2 is the AC voltage on the LV winding. The turns ratio N_{W} is defined as N_1/N_2 with N_1 and N_2 being the number of turns on the MV side and on the LV side respectively.

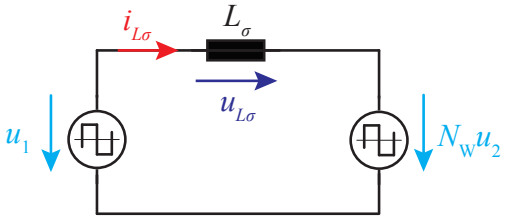

Figure 2.4: Equivalent circuit of the DABC.

According to the selected topology as shown in Fig. 2.3, the amplitudes of u_1 and u_2 are given as

$$U_1 = \frac{U_{\mathrm{DC,MV}}}{2} \tag{2.1}$$

and

$$U_2 = U_{\mathrm{DC,LV}} \tag{2.2}$$

For convenience, a voltage ratio factor M is defined as

$$M = \frac{N_{\mathrm{W}}U_2}{U_1} = \frac{N_W \cdot U_{\mathrm{DC,LV}}}{U_{\mathrm{DC,MV}}/2} \tag{2.3}$$

To regulate the power flow in the considered DABC, three modulation parameters can be adjusted[i]:

[i] The switching frequency, the leakage inductance and the turns ratio of the transformer are considered to be constant.

- ϕ – phase shift angle between the voltage on the MV side and the voltage on the LV side
- τ_1 – interval when a non-zero voltage is applied on the MV winding of the MFT
- τ_2 – interval when a non-zero voltage is applied on the LV winding of the MFT

Since there is no DC component in the voltage and current in a transformer, the waveforms are symmetrical in one switching cycle. Therefore, ϕ can vary from $-\pi$ to π, while τ_1 and τ_2 take values between 0 and π. In this dissertation, the phase shift angle is defined as the angle of the LV side voltage u_2 referred to the MV side voltage u_1. The positive value of ϕ represents that u_2 lags behind u_1 and vice versa.

2.2.1 Phase shift modulation

The simplest modulation method for the DABC is to operate the NPC and the FB converter as a HB converter. On the MV side, the switches S_{M1}, S_{M2} and accordingly S_{M3}, S_{M4} are turned on together for half of the switching period respectively. On the LV side, the group S_{L1}, S_{L3} and the group S_{L2}, S_{L4} are switched separately with a phase shift angle ϕ. In this case, duty ratios of voltages on both sides are fixed at 50%, i.e. $\tau_1 = \tau_2 = \pi$. The only possibility to adjust the power flow is to regulate the phase shift angle. In Fig. 2.5, example waveforms of this modulation method with the power flow from the MV side to the LV side ($0 < \phi < \pi$) is shown. According to the half-cycle symmetry, following relations can be applied to the voltage/current:

$$\begin{aligned} u_1(t + T_\mathrm{s}/2) &= -u_1(t), \\ u_2(t + T_\mathrm{s}/2) &= -u_2(t), \\ i_{L\sigma}(t + T_\mathrm{s}/2) &= -i_{L\sigma}(t). \end{aligned} \tag{2.4}$$

As shown in the figure, each switching cycle can be divided into 4 time intervals ($T_\mathrm{I} \sim T_\mathrm{IV}$). Due to the symmetry, only the first half switching cycle is analyzed. The current flowing through the MV winding of the transformer

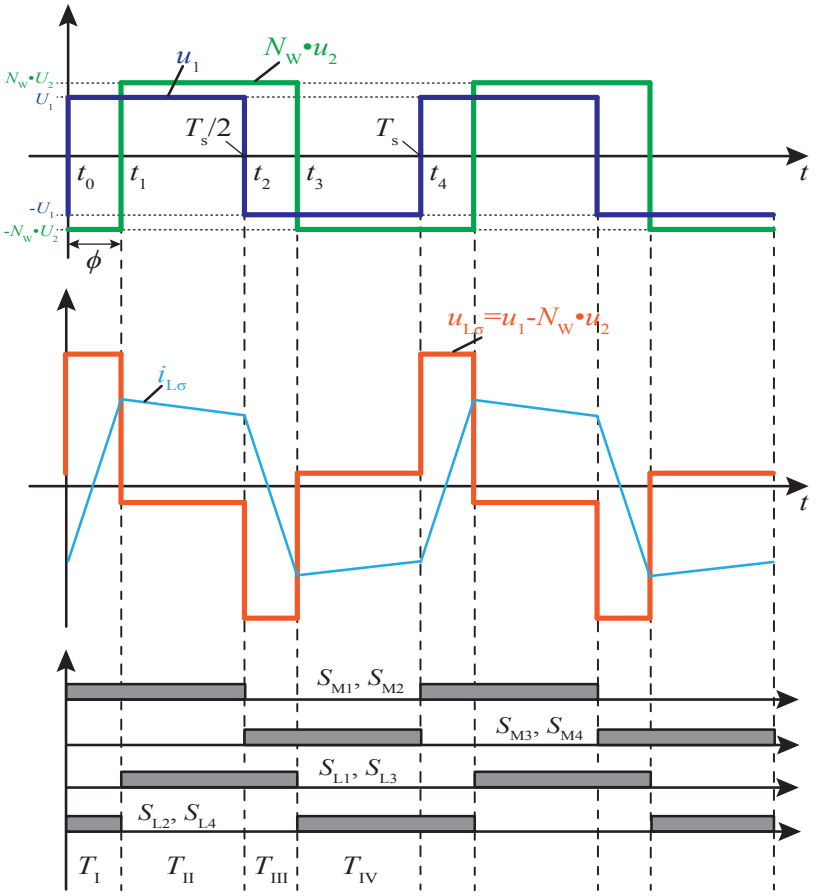

Figure 2.5: Example waveforms of the voltage and the current for the DABC operated with the phase shift modulation ($0 < \phi < \pi$).

in this half cycle is expressed as

$$\begin{aligned} i_{L\sigma}(t) &= i_{L\sigma}(t_0) + \frac{(U_1 + N_W U_2)}{L_\sigma}(t - t_0) \qquad 0 \le t \le t_1 \\ i_{L\sigma}(t) &= i_{L\sigma}(t_1) + \frac{(U_1 - N_W U_2)}{L_\sigma}(t - t_1) \qquad t_1 \le t \le T_s/2 \end{aligned} \tag{2.5}$$

According to (2.4), the current at the beginning of a switching cycle t_0 can

be solved as

$$i_{L\sigma}(t=t_0) = \frac{\pi(N_W U_2 - U_1) - 2\phi N_W U_2}{4\pi f_s L_\sigma} \tag{2.6}$$

The transfered power can be calculated by the integration of voltage and current waveforms over the whole switching cycle which gives

$$P = \frac{N_W \cdot U_1 \cdot U_2 \cdot \phi \cdot (\pi - |\phi|)}{2\pi^2 f_s L_\sigma} \tag{2.7}$$

The maximal transferable power P_{max} from the MV side to the LV side is achieved at the phase shift angle of $\phi = \pi/2$, which results in

$$P_{max} = \frac{N_W \cdot U_1 \cdot U_2}{8 f_s L_\sigma} \tag{2.8}$$

For the power flow from the LV side to the MV side ($-\pi < \phi < 0$), the analysis is similar, with the maximal transferable power at $\phi = -\pi/2$. The waveforms shown in Fig. 2.5 are in the case of $N_W U_2 > U_1$, i.e. $M > 1$. If $M < 1$, then the current $i_{L\sigma}$ increases further during the second time interval T_{II}.

At t_0, S_{M1} and S_{M2} are turned on. If $i_{L\sigma} < 0$ as the case shown in Fig. 2.5, the current is flowing through the anti-parallel diodes D_{M1}, D_{M2}. Therefore, the ZVS turn-on is achieved for switches S_{M1} and S_{M2}. On the LV side, the current flows through the anti-parallel diode at turn-on of each switch. Therefore, there is generally no turn-on loss for all switches [93]. However, the turn-off of all switches on both sides are hard-switching. On the other hand, in some cases, the current $i_{L\sigma}$ may change its polarity from positive to negative during the second interval T_{II}. In this case, $i_{L\sigma}(t=t_0) > 0$, the ZVS turn-on for MV side switches are lost. If N_W and L_σ are constant, the phase shift angle at the boundary between these two conditions is

$$\phi = \frac{\pi}{2}\left(1 - \frac{U_1}{N_W U_2}\right) \tag{2.9}$$

The phase shift modulation is easy to implement since there is only one control variable. It is also possible to use the HB topology on both sides of the DABC. The disadvantage of this modulation method is the limited soft-switching possibility and a relatively high RMS current [94].

2.2.2 Triangular/trapezoidal current modulation

To reduce losses, more advanced modulation methods are demanded, which require all three modulation parameters (ϕ, τ_1, τ_2) to be adjustable.

More details about these modulation methods can be found in [94].

In this work, the focus is put on the MFT design. The main reason for choosing the NPC topology on the MV side is to enable the use of IGBTs with a lower voltage rating. Therefore, the NPC converter is treated as a HB converter with two series connected switches. In this case, the NPC-FB DABC is operated in the same way as the HB-FB DABC, where only two modulation parameters are adjustable, i.e. ϕ and τ_2. Another modulation parameter τ_1 is fixed as π representing the constant 50% duty ratio of the voltage on the MV side. In fact, since L_σ and N_W are not defined yet, there are 4 variables in total which need to be considered for the converter design. A desired power transfer for defined DC voltages and the switching frequency can be realized through a suitable combination of these variables.

In general, modulation conditions of the considered converter can be categorized into 4 modes depending on ϕ and τ_2. In Fig. 2.6, example waveforms of voltages on both sides of the transformer in different modulation modes are shown. The difference among these operation modes is the overlapping intervals of the voltage u_1 and u_2. The MV side voltage u_1 is a square wave and is taken as the reference. The angle ϕ is considered as the phase shift between positive rising edges (or negative rising edges) of the voltages u_1 and u_2, where $\phi \in (-\pi, \pi)$. For $\phi \in [0, \pi)$, u_1 is leading as shown in the case of mode 1 and 2. A negative value of ϕ indicates that the LV side voltage u_2 is leading as shown in the case of mode 3 and 4. The duty ratio of the voltage u_2 also varies in $[0, \pi]$. Due to the half-cycle symmetry, the relations given in (2.4) are also valid. It can be seen that in each half switching cycle, waveforms can be separated into three time intervals. In Table 2.4, these operation modes and the voltage $u_{L\sigma}$ across the leakage inductance L_σ during each intervals are summarized.

Similar as for the phase shift modulation, the current $i_{L\sigma}$ of the transformer within each time interval can be calculated for each mode as following:

$$\textbf{Mode 1: } i_{L\sigma}(t) = \begin{cases} i_{L\sigma}(t_0) + \dfrac{U_1}{L_\sigma}(t - t_0) & 0 \le t \le t_1 \quad (2.10) \\ i_{L\sigma}(t_1) + \dfrac{(U_1 - N_\mathrm{W} U_2)}{L_\sigma}(t - t_1) & t_1 \le t \le t_2 \quad (2.11) \\ i_{L\sigma}(t_2) + \dfrac{U_1}{L_\sigma}(t - t_2) & t_2 \le t \le T_\mathrm{s}/2 \quad (2.12) \end{cases}$$

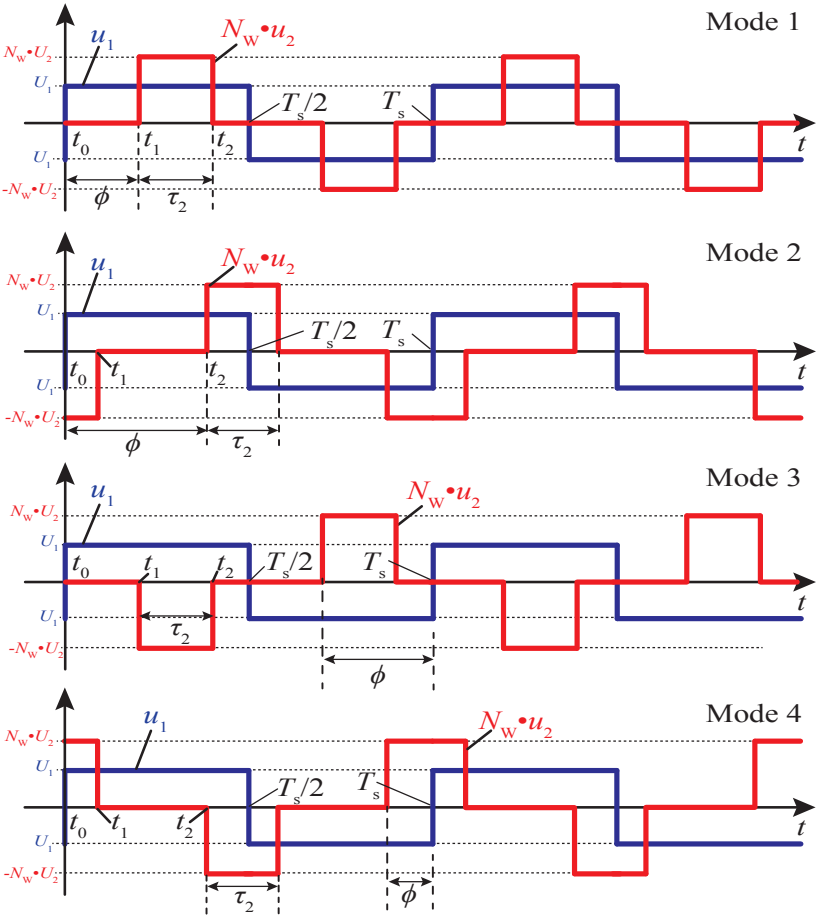

Figure 2.6: Example voltage waveforms of the DABC operated in different modes.

$$\textbf{Mode 2: } i_{L\sigma}(t) = \begin{cases} i_{L\sigma}(t_0) + \dfrac{(U_1 + N_W U_2)}{L_\sigma}(t - t_0) & 0 \le t \le t_1 \quad (2.13) \\ i_{L\sigma}(t_1) + \dfrac{U_1}{L_\sigma}(t - t_1) & t_1 \le t \le t_2 \quad (2.14) \\ i_{L\sigma}(t_2) + \dfrac{(U_1 - N_W U_2)}{L_\sigma}(t - t_2) & t_2 \le t \le T_s/2 \quad (2.15) \end{cases}$$

$$\textbf{Mode 3: } i_{L\sigma}(t) = \begin{cases} i_{L\sigma}(t_0) + \dfrac{U_1}{L_\sigma}(t-t_0) & 0 \le t \le t_1 \quad (2.16) \\ i_{L\sigma}(t_1) + \dfrac{(U_1 + N_W U_2)}{L_\sigma}(t-t_1) & t_1 \le t \le t_2 \quad (2.17) \\ i_{L\sigma}(t_2) + \dfrac{U_1}{L_\sigma}(t-t_2) & t_2 \le t \le T_s/2 \quad (2.18) \end{cases}$$

$$\textbf{Mode 4: } i_{L\sigma}(t) = \begin{cases} i_{L\sigma}(t_0) + \dfrac{(U_1 - N_W U_2)}{L_\sigma}(t-t_0) & 0 \le t \le t_1 \quad (2.19) \\ i_{L\sigma}(t_1) + \dfrac{U_1}{L_\sigma}(t-t_1) & t_1 \le t \le t_2 \quad (2.20) \\ i_{L\sigma}(t_2) + \dfrac{(U_1 + N_W U_2)}{L_\sigma}(t-t_2) & t_2 \le t \le T_s/2 \quad (2.21) \end{cases}$$

Table 2.4: Operation modes of the DABC depending on the phase shift angle ϕ and the active interval τ_2 of the voltage on the LV side

		Mode 1	Mode 2	Mode 3	Mode 4
ϕ		$0 \le \phi < \pi$	$0 \le \phi < \pi$	$-\pi < \phi \le 0$	$-\pi < \phi \le 0$
τ_2		$\tau_2 + \lvert\phi\rvert \le \pi$	$\tau_2 + \lvert\phi\rvert > \pi$	$\tau_2 + \lvert\phi\rvert \le \pi$	$\tau_2 + \lvert\phi\rvert > \pi$
$u_{L\sigma}$	$T_I : t_0 \sim t_1$	U_1	$U_1 + N_W U_2$	U_1	$U_1 - N_W U_2$
	$T_{II} : t_1 \sim t_2$	$U_1 - N_W U_2$	U_1	$U_1 + N_W U_2$	U_1
	$T_{III} : t_2 \sim T_s/2$	U_1	$U_1 - N_W U_2$	U_1	$U_1 + N_W U_2$

Accordingly, the current at t_0 can be solved by using the half-cycle symmetry and the transfered power can be calculated. Analytical expressions of $i_{L\sigma}$ and the power for each mode are listed below by introducing the voltage ratio factor M as defined in (2.3):

Mode 1:

$$i_{L\sigma}(t_0) = \frac{U_1}{4\pi f_s L_\sigma}(M\tau_2 - \pi) \quad (2.22)$$

$$P = \frac{M U_1^2}{4\pi^2 f_s L_\sigma}\left[\tau_2(\tau_2 + 2\phi - \pi)\right] \quad (2.23)$$

Mode 2:

$$i_{L\sigma}(t_0) = \frac{U_1}{4\pi f_s L_\sigma}\left[-M\tau_2 - 2M\phi + (2M-1)\pi\right] \quad (2.24)$$

$$P = \frac{MU_1^2}{4\pi^2 f_s L_\sigma}\left[\pi(2\phi+\tau_2-\pi)-(\phi+\tau_2-\pi)^2-\phi^2\right] \tag{2.25}$$

Mode 3:

$$i_{L\sigma}(t_0) = \frac{U_1}{4\pi f_s L_\sigma}(-M\tau_2-\pi) \tag{2.26}$$

$$P = \frac{MU_1^2}{4\pi^2 f_s L_\sigma}\left[\tau_2(2\phi-\tau_2-\pi)\right] \tag{2.27}$$

Mode 4:

$$i_{L\sigma}(t_0) = \frac{U_1}{4\pi f_s L_\sigma}\left(M\tau_2-2M\phi-\pi\right) \tag{2.28}$$

$$P = \frac{MU_1^2}{4\pi^2 f_s L_\sigma}\left[\tau_2^2-(2\phi+\pi)\tau_2+2\phi^2)\right] \tag{2.29}$$

For each operation mode listed above, a bidirectional power transfer is possible to be realized with a suitable combination of ϕ and τ_2 according to (2.23), (2.25), (2.27) and (2.29). For the same amount of transferred power, there could be several possibilities of modulations in different modes which result in different waveforms.

In Fig. 2.7, example waveforms and gate signals of the DABC in operation mode 2 is illustrated where the case of $N_W U_2 > U_1$ ($M > 1$) is shown. It is also possible to operate the DABC in the same mode (as well as in other modes) when $N_W U_2 \leq U_1$ ($M \leq 1$). During each time interval, the voltage on L_σ is constant and $i_{L\sigma}$ changes linearly with the possibility of reversing its polarity. At instances t_0, t_1, t_2 in each half switching cycle, switching actions take place. The values of the current $i_{L\sigma}$ at these instances are relevant to the switching loss. After calculating $i_{L\sigma}$ at t_0 by using (2.22), (2.24), (2.26) and (2.28), the current values at t_1, t_2 can be calculated according to e.g. (2.12) for mode 1.

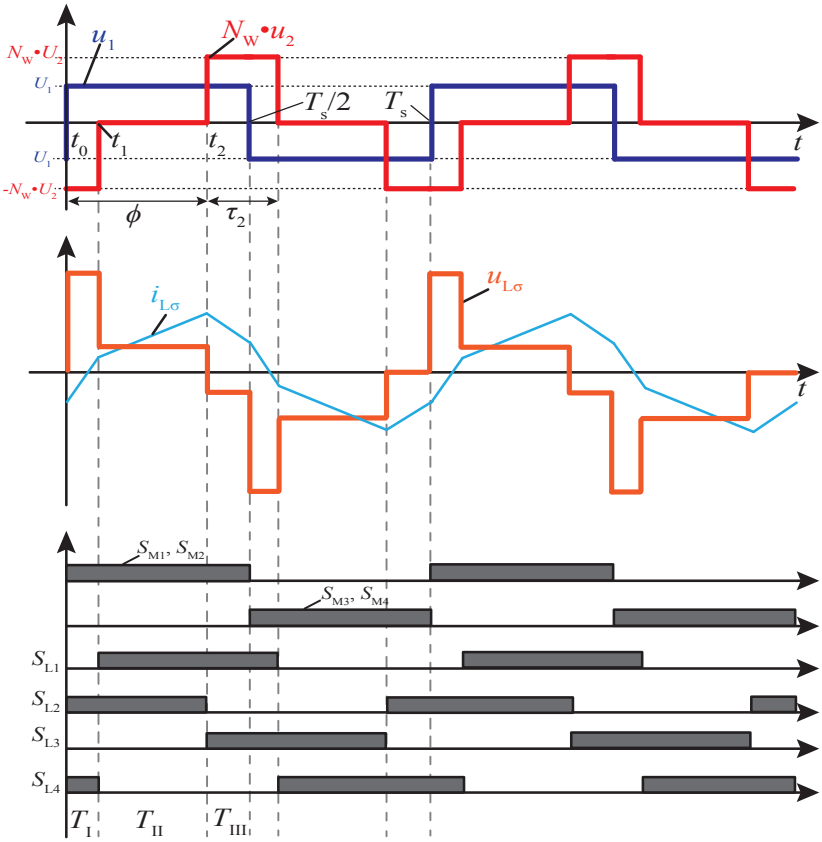

Figure 2.7: Example waveforms and gate signals for the DABC in operation mode 2.

To achieve an effective power transfer, the voltage $u_{L\sigma}$ and the current $i_{L\sigma}$ waveforms with the same polarity are desired to be overlapped in a large time interval approaching $T_s/2$. To reduce losses, it is desired to turn-on the switch under ZVS condition and turn-off the switch at or close to zero-current. Usually, switches on the MV side are more critical due to the lower switching speed compared with switches on the LV side. Also, a low RMS current is desired to reduce conduction losses, not only for switches but also for the transformer.

2.3 Optimization of the MFT

The medium frequency transformer is the key component of the DC-DC converter, which provides the galvanic isolation and realizes the voltage level matching. Generally, the transformer is desired to be compact and efficient. The goal of the transformer optimization in this work is to find design parameters which results in a transformer with the highest efficiency for a given total volume (boxed volume) and fulfills all constraints. To achieve this object, an optimization model for transformers is developed. In this section, design requirements and optimization procedures are explained in detail with emphasis on the thermal modeling and the isolation design.

2.3.1 Procedures of the transformer optimization

In Fig. 2.8, the optimization procedure for the MFT is illustrated. In the pre-design phase, operation conditions of the DABC are defined, i.e. P_{n}, $U_{\mathrm{DC,MV}}$, $U_{\mathrm{DC,LV}}$ and f_s. Additionally, the required turns ratio and the leakage inductance of the transformer also need to be defined. Since the current $i_{L\sigma}$ in the transformer is non-sinusoidal, its harmonics are required for the winding loss calculation, which can be derived by the Fourier transform from the current waveform according to defined operation conditions. To find the optimal design of the MFT for the same power density, the total boxed volume Vol_{tot} of the transformer is also given.

Moreover, materials for the magnetic core, the winding conductor and isolation layers as well as the structure of the transformer (core shape, winding arrangement, etc.) are also selected during the pre-design phase. The required material parameters are related to the loss calculation, thermal modeling and isolation design, such as the Steinmetz parameter, thermal conductivity and dielectric strength. According to the required isolation voltage U_{iso} and the dielectric strength of the selected isolation material, the maximal allowed electric field strength E_{max} can be defined. The Pareto front regarding the efficiency and the power density for a given set of materials and structure can be found through optimizations with different given volumes. If the cost should also be included in the optimization, relevant coefficients can be added in the pre-design phase.

As mentioned before, for MFTs operated at a few kHz, the amorphous or nanocrystalline alloys are normally chosen as the core material. The

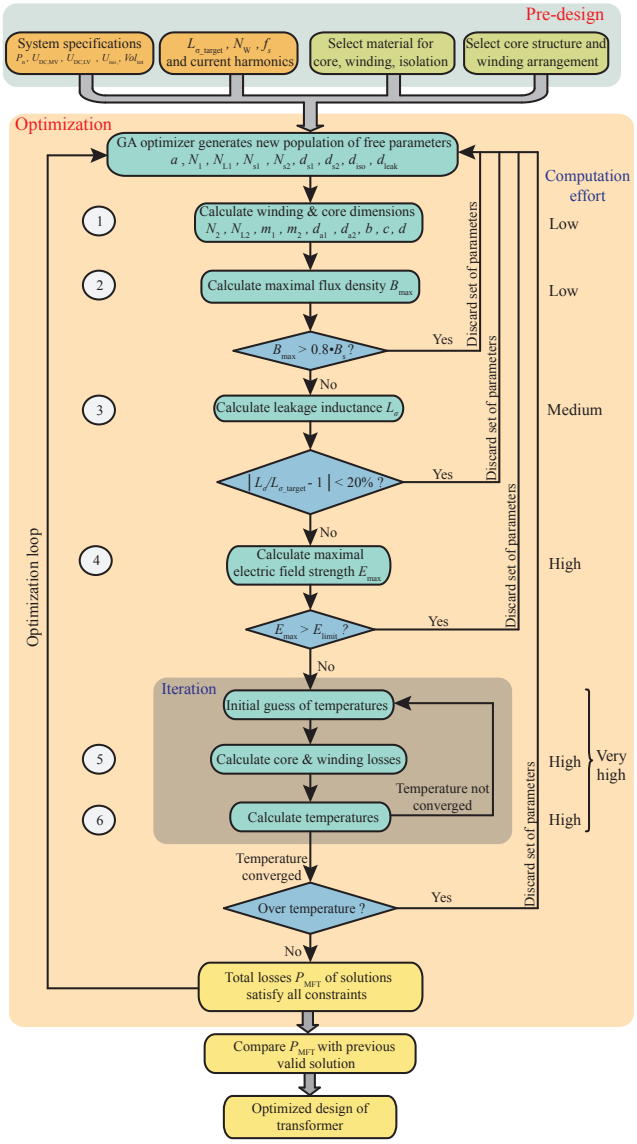

Figure 2.8: Flow chart of the MFT design and optimization procedure.

commonly used round Litz-wire is considered for the winding construction. To achieve a high power density and the required isolation voltage level, casting the winding by the epoxy resin and using heat sinks with forced air-cooling for the transformer core are considered. The leakage inductance of the MFT is an important parameter for the operation of the DABC. Therefore, the shell type structure with the concentric winding as shown in Fig. 2.9 is selected for the design to constrain the leakage flux. In this case, two sets of commonly used rectangular cores are combined to form a set of EE core. The LV winding is located inside of the MV winding since this leads to a smaller length of the LV winding which carries a higher current. All parameters shown in Fig. 2.9 are listed and explained in Table 2.5. Obviously, some of these parameters must be integers.

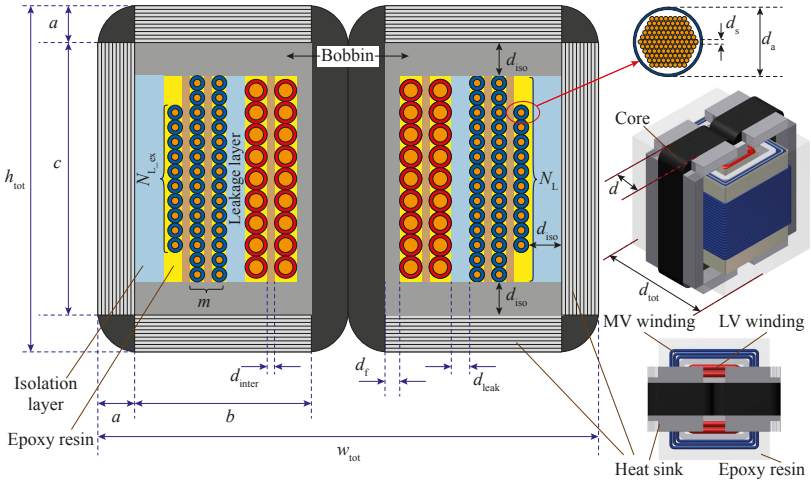

Figure 2.9: Structure and geometry parameters of the MFT.

Besides the defined parameters, there are still 9 free parameters related to the core geometry and the winding construction of the transformer. Theoretically, even if only 10 possible values are available for each parameter, there are 10^9 possible combinations of the 9 parameters. Assume that the average calculation time of one cycle during the optimization is 0.1 s, it would take more than thousand days to calculate all 10^9 possible combinations, which is impractical. In practice, possible values for the free parameters are far more than 10. Consequently, the calculation time to cover all possible combinations is not affordable. Therefore, the generic algorithm (GA) is

Table 2.5: Design parameters of the MFT

Parameter symbol	Origin	Description
a	free	Width of core leg
b	calculated	Width of core window
c	calculated	Height of core window
d	calculated	Depth of core
h_{tot}	calculated	Total height of transformer/core
w_{tot}	calculated	Total width of transformer
d_{tot}	calculated	Total thickness of transformer
d_{f}	pre-defined	Thickness of bobbin (isolation distance between winding and core central leg)
d_{iso}	free	Isolation distance between winding and core
d_{leak}	free	Thickness of leakage layer
d_{inter}	pre-defined	Isolation distance between winding layers
N_1	free	Number of turns of the MV winding
N_2	calculated	Number of turns of the LV winding
N_{L1}	free	Number of turns of a complete layer (MV winding)
N_{L2}	calculated	Number of turns of a complete layer (LV winding)
m_1, m_2	calculated	Number of complete layers (MV and LV windings)
$N_{\text{L1\_ex}}$, $N_{\text{L2\_ex}}$	calculated	Number of turns of the incomplete layer if available (MV and LV windings)
N_{s1}, N_{s2}	free	Number of strands of the Litz-wire (MV and LV windings)
d_{s1}, d_{s2}	free	Strand diameter of the Litz-wire (MV and LV windings)
d_{a1}, d_{a2}	calculated	Outer diameter of the Litz-wire (MV and LV windings)

selected as the optimizer which is available in MATLAB. The GA optimizer finds better solutions based on solutions which have already been found, and the problem evolves towards the optimal solution. Also, a valid initial solution is not necessary to be provided in case of using the GA. This is advantageous since a valid initial guess is rather difficult for such a compli-

cated problem. Another advantage of using the GA is that free parameters can be set to take only integer values. This is helpful to limit the number of possible values: on the one hand, some of free parameters have to be integer, e.g. N_1, N_2, then non-integer values are automatically excluded. On the other hand, to further reduce the number of possible values, non-integer free parameters can be scaled to a desired precision, then the unnecessary values with a higher precision can be excluded. For example, for the geometry parameter a in the range of 1 mm to 50 mm with a resolution of 0.1 mm, a scale factor of 10 is applied and a is scaled as an integer from 10 to 500 with 491 possible values in total. At the end of the optimization, a is divided by 10 to obtain the actual value.

Before the calculation starts, the optimizer assigns a population containing a number of individuals within the defined range of parameters, where an individual means a complete set of the 9 free parameters. The optimization process consists of 6 steps. The order of computation tasks are arranged according to their computational efforts as indicated on the right side in Fig. 2.8. If constraint is not satisfied at a certain step, the calculation restarts immediately with a new set of parameters. This prevents executing high effort calculations arranged in later steps and thus saves calculation time.Calculation steps are described below where the unit of all the geometric dimensions is meter.

Step 1: Winding and core dimensions

In the first step, the complete geometry of the core and the construction of windings are determined based on pre-defined and generated free parameters.

Since the strand diameter d_s can not be an arbitrary value, a lookup table with a list of diameters for standard AWG wires is implemented. According to the generated free parameter as an index, d_s can be selected from the table. With the known number of strands N_s, the outer diameter of the Litz-wire can be approximately calculated according to the empirical equation [95] as

$$d_a = 135 \times 10^{-6} \cdot \left(\frac{N_s}{3}\right)^{0.45} \cdot \left(\frac{d_s}{40 \times 10^{-6}}\right)^{0.85} \tag{2.30}$$

The number of turns for the MV winding N_1 and the turns ratio are known

and the number of turns N_2 for the LV winding is then determined as

$$N_2 = \text{round}\left(\frac{N_1}{N_W}\right) \tag{2.31}$$

Notice that N_2 has to be rounded as an integer.

To determine the window size of the core, the isolation distance between the core and the winding d_{iso} needs to be taken into account. Since the MV winding has a higher electric potential, it is more critical for the isolation compared with the LV winding. The height of the MV winding is determined according to the known number of turns per layer N_{L1} and the calculated outer diameter:

$$H_{w1} = N_{L1} \cdot d_{a1} \tag{2.32}$$

Then the number of turns per layer N_{L2} for the LV winding is determined by the quotient of H_{w1}/d_{a2}. With the known total number of turns, the arrangement of both MV and LV windings can be completely defined, i.e. values of m_1, m_2, N_{L1_ex}, N_{L2_ex} are determined. If there is an additional incomplete layer, these extra turns are arranged in the middle of the winding in vertical direction as shown in Fig. 2.9.

With the known winding dimension, the size of the core window can be determined. In the horizontal direction, the total width of the winding is

$$D_w = \begin{cases} m \cdot d_a + (m-1) \cdot d_{leak} & N_{L\_ex} = 0 \quad (2.33) \\ (m+1) \cdot d_a + m \cdot d_{leak} & N_{L\_ex} > 0 \quad (2.34) \end{cases}$$

The equation is valid for both the MV and the LV winding and results in the width D_{w1}, D_{w2} of the corresponding winding. Then the width of the core window is determined by the sum of the winding width, the isolation distance and the thickness of the leakage layer:

$$b = d_f + D_{w1} + d_{leak} + D_{w2} + d_{iso} \tag{2.35}$$

The height of the core window is given as

$$c = H_{w1} + 2d_{iso} \tag{2.36}$$

It can be seen in the 3D design shown in Fig. 2.9 that the arrangement of the heat sink does not increase the total boxed volume of the transformer. With

the known core leg width a, the total width w_{tot} and total height h_{tot} of the transformer can be determined as

$$w_{\text{tot}} = 4a + 2b \tag{2.37}$$

and

$$h_{\text{tot}} = 2a + c \tag{2.38}$$

Since the total boxed volume is pre-defined, then the total thickness d_{tot} is

$$d_{\text{tot}} = \frac{Vol_{\text{tot}}}{w_{\text{tot}} \cdot h_{\text{tot}}} \tag{2.39}$$

Finally, the thickness of the core can be determined as

$$d = d_{\text{tot}} - 2b \tag{2.40}$$

So far, all geometry parameters of the core and the construction of windings are completely defined.

Step 2: Maximal flux density

As shown in the previous section, the excitation voltage of the transformer has a rectangular waveform. The peak flux density calculated from the MV side is

$$B_{\text{max}} = \frac{U_1 D_{\text{M}}}{4 f_s A_{\text{c,eff}} N_1} \tag{2.41}$$

where D_{M} is the duty ratio of the voltage on the MV side, which is equal to 1 since $\tau_1 = \pi$. It should be noticed that $U_1 = U_{\text{DC,MV}}/2$, as already discussed. The effective core cross-sectional area $A_{\text{c,eff}}$ is calculated as

$$A_{\text{c,eff}} = A_{\text{c}} \cdot l_{\text{F}} = 2a \cdot d \cdot l_{\text{F}} \tag{2.42}$$

with l_{F} the lamination factor of the core. For amorphous and nanocrystalline cores, the minimal value of l_{F} given by the data sheet is 0.82~0.84. Then B_{max} is compared with the saturation flux density B_{s} where a margin of $20\% \cdot B_{\text{s}}$ is considered.

Step 3: Leakage inductance

In this step, the leakage inductance is calculated by analytical formulas based on the well known 1D approximation method. The magnetic filed distribution in the core window is approximated by a trapezoidal function in the horizontal direction as shown in Fig. 2.10. To calculate the leakage inductance, the stored magnetic energy W_{m} needs to be determined, which includes the energy stored in each winding layer, inter winding layers and the leakage layer. Since the Litz-wire is considered, the porosity factor needs to be taken into account. The round Litz-wire is converted to a square shaped conductor with the same copper area. The procedure of the leakage inductance calculation is explained in detail in [8].

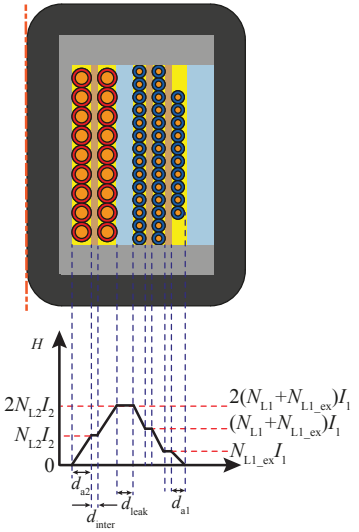

Figure 2.10: 1D magnetic field distribution in the transformer core window with multi-layer windings.

To achieve a higher accuracy, the circular length of each winding layer and the gap between layers are calculated separately instead of using a common mean length. Accordingly, the contribution of each individual layer to the total leakage inductance is calculated separately according to its individual length. In Fig. 2.11, the cross-sectional view of the transformer is sketched to illustrate the length calculation, where the circular length in the

middle of each layer is accounted. For example, the length of the first layer of the LV winding is calculated as

$$l = 2 \cdot [(2a + 2d_{\mathrm{f}} + d_{\mathrm{a2}}) + (d + 2d_{\mathrm{f}} + d_{\mathrm{a2}})] \tag{2.43}$$

For the next layer, the increment of the length based on the length of its inner layer is

$$\Delta l = 2 \cdot (4d_{\mathrm{a2}} + 4d_{\mathrm{inter}}) \tag{2.44}$$

The length of other outer layers can be further calculated in a similar way. Finally, the calculated leakage inductance is compared with the target value. Normally, the two values cannot perfectly match with each other. Therefore, an 1% deviation to the target value is set as the constraints, i.e.

$$|L_\sigma - L_{\sigma,\mathrm{target}}| / L_{\sigma,\mathrm{target}} < 1\% \tag{2.45}$$

This 1% deviation is so small that its influence on the electrical model of the converter can be neglected.

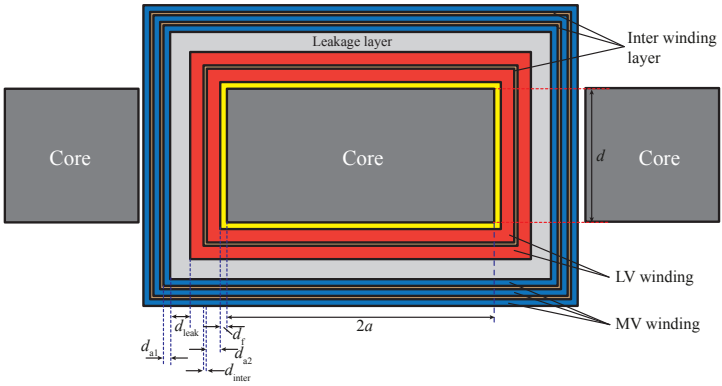

Figure 2.11: Cross-sectional view of the transformer winding and core.

Step 4: Maximal electric field strength

This step is to check if the maximal electric field strength E_{max} exceeds the allowable value. The electric field distribution is calculated by the charge simulation method and details are discussed later in this chapter.

Step 5: Loss calculation

Due to the non-sinusoidal excitation voltage, the improved generalized Steinmetz equation (IGSE) is used for the core loss calculation [8]. The well known Steinmetz equation for the specific core loss calculation is

$$p_{\mathrm{Fe}} = k f_s^{\alpha} B^{\beta} \tag{2.46}$$

where the Steinmetz parameters k, α, β can be derived from the data sheet. By using the IGSE, the specific core loss is calculated as

$$p_{\mathrm{Fe}} = 2^{\alpha+\beta} k_i f_s^{\alpha} B_{\mathrm{max}}^{\beta} D_{\mathrm{M}}^{1-\alpha} \tag{2.47}$$

where the improved Steinmetz parameter k_i is calculated as

$$k_i = \frac{k}{(2\pi)^{\alpha-1} \int_0^{2\pi} |cos(\theta)|^{\alpha} 2^{\beta-\alpha} \mathrm{d}\theta} \tag{2.48}$$

To save the calculation time, k_i can be pre-evaluated and directly defined before the optimization process. Again, for the rectangular voltage on the MV side, $D_{\mathrm{M}} = 1$. Therefore, (2.47) is further simplified to

$$p_{\mathrm{Fe}} = 2^{\alpha+\beta} k_i f_s^{\alpha} B_{\mathrm{max}}^{\beta} \tag{2.49}$$

Notice that B_{max} should also be calculated on the MV side. The obtained specific core loss is the volume loss density and the core volume is required to calculate the total core loss. The mean magnetic length of the core is calculated as

$$l_{\mathrm{Fe}} = 2(b+c) + 2\pi a \tag{2.50}$$

And the total core volume is

$$V_{\mathrm{Fe}} = l_{\mathrm{Fe}} \cdot A_{\mathrm{c}} \tag{2.51}$$

where A_{c} is the core cross-sectional area given in (2.42). Notice that A_{c} is the total cross-sectional area of two cores in case of the considered shell type structure. To have a larger safety margin for the thermal design, the actual core volume is used for the loss calculation instead of using the effective volume of the magnetic material. This leads to an overestimated core loss of about 16~18%.

The core loss is considered to be independent on the temperature and it is calculated outside the iteration loop. However, the temperature dependency of the copper resistivity is taken into account for calculating the winding loss. Further calculation to solve the thermal model also involves temperature dependent variables. Therefore, iterative calculation is necessary for the last two steps and they have the highest computational effort.

Before the winding loss calculation, an initial temperature is assumed for the copper. The temperature dependency of the copper resistivity is described as

$$\rho_{\mathrm{Cu}} = \rho_{\mathrm{Cu},20} \cdot [1 + \alpha_{\mathrm{T}}(T_{\mathrm{Cu}} - 20)] \tag{2.52}$$

where $\rho_{\mathrm{Cu},20} = 1.68 \times 10^{-8}\ \Omega\mathrm{m}$ is the copper resistivity at 20 °C and the temperature coefficient $\alpha_{\mathrm{T}} = 0.0039\ \mathrm{K}^{-1}$.

Due to the operation in the kHz range, the loss caused by high frequency effects are significant, i.e. the skin effect and the proximity effect. Since Litz-wire is considered, the loss due to the proximity effect is further divided into two parts induced by the internal and the external magnetic field. The loss calculation is based on the Bessel-Kelvin function originally introduced in [96].

As mentioned, the current in the transformer winding is non-sinusoidal. Therefore, harmonics derived by the Fourier transformation are used for calculation. The loss due to each harmonic are calculated separately and summed up to obtain the total loss. Major steps of the calculation method is briefly introduced below, which is applied separately for both the MV and the LV winding.

The DC resistance of a single strand of the Litz-wire per unit length is calculated as

$$r_{\mathrm{s,DC}} = \frac{4\rho_{\mathrm{Cu}}}{\pi d_{\mathrm{s}}^2} \tag{2.53}$$

Then the total DC resistance of a Litz-bundle consists of N_{s} strands with a total length of L_{W} is

$$R_{\mathrm{DC}} = r_{\mathrm{s,DC}} \frac{L_{\mathrm{W}}}{N_{\mathrm{s}}} = \frac{4\rho_{\mathrm{Cu}}}{\pi d_{\mathrm{s}}^2 N_{\mathrm{s}}} L_{\mathrm{W}} \tag{2.54}$$

where L_{W} has been calculated in the previous step. For the n-th current

harmonic, the skin depth δ_n is given as

$$\delta_n = \sqrt{\frac{\rho_{\mathrm{Cu}}}{n\pi f_s \mu_0}} \tag{2.55}$$

Accordingly, the penetration ratio of the n-th harmonic is

$$\Delta_n = \frac{d_{\mathrm{s}}}{\delta_n} \tag{2.56}$$

Define the factor $\xi_n = \Delta_n/\sqrt{2}$, then the skin effect factor $Fr_{\mathrm{skin},n}$ for the n-th harmonic can be expressed by the Bessel function as

$$Fr_{\mathrm{skin},n} = \frac{\xi_n}{4\sqrt{2}} \left[\frac{K_{\mathrm{Be0},n}(K'_{\mathrm{Be1},n} - K_{\mathrm{Be1},n}) - K'_{\mathrm{Be0},n}(K_{\mathrm{Be1},n} + K'_{\mathrm{Be1},n})}{(K_{\mathrm{Be1},n})^2 + (K'_{\mathrm{Be1},n})^2} \right] \tag{2.57}$$

where $K_{\mathrm{Be0},n}$, $K'_{\mathrm{Be0},n}$ are respectively the real and imaginary parts of the 0th order Kelvin function (Bessel functions of the first kind) for the n-th harmonic, with

$$J_0(\xi_n e^{\mathrm{j}\frac{3}{4}\pi}) = K_{\mathrm{Be0,r}} + \mathrm{j}K_{\mathrm{Be0,i}} \tag{2.58}$$

And $K_{\mathrm{Be1},n}$, $K'_{\mathrm{Be1},n}$ are the terms of the 1st order Kelvin function. Then the loss due to the skin effect of the n-th harmonic is calculated as

$$P_{\mathrm{skin},n} = R_{\mathrm{DC}} \cdot Fr_{\mathrm{skin},n} \cdot \hat{I}_n^2 \tag{2.59}$$

where $\hat{I}_n$ is the peak value of the n-th current harmonic. Similarly, the proximity effect factor $Fr_{\mathrm{prox},n}$ for the n-th harmonic is

$$Fr_{\mathrm{prox},n} = -\frac{\xi_n \pi^2 d_{\mathrm{s}}^2}{2\sqrt{2}} \left[\frac{K_{\mathrm{Be2},n}(K_{\mathrm{Be1},n} + K'_{\mathrm{Be1},n}) + K'_{\mathrm{Be2},n}(K'_{\mathrm{Be1},n} - K_{\mathrm{Be1},n})}{(K_{\mathrm{Be0},n})^2 + (K'_{\mathrm{Be0},n})^2} \right] \tag{2.60}$$

where $K_{\mathrm{Be2},n}$, $K'_{\mathrm{Be2},n}$ are the terms of the 2nd order Kelvin function. The loss due to the internal proximity effect of the n-th harmonic in the Litz-bundle is calculated as

$$P_{\mathrm{prox\_in},n} = \frac{R_{\mathrm{DC}} \cdot N_{\mathrm{s}}^2 \cdot Fr_{\mathrm{prox},n} \cdot \hat{I}_n^2}{2\pi^2 d_{\mathrm{a}}^2} \tag{2.61}$$

The external proximity effect is caused by the magnetic field induced by other Litz-wires. For a winding with m complete layers of wires, the averaged magnetic field strength due to the n-th current harmonic is calculated as

$$H_{\text{avg},n} = \sum_{k=1}^{m} \frac{(2k-1)N_{\text{L}}\hat{I}_n}{2H_{\text{w}}} \tag{2.62}$$

The total loss of the external proximity effect due to the magnetic field induced by the n-th current harmonic is then

$$P_{\text{prox\_ex},n} = r_{\text{s,DC}} \cdot l_{\text{w}} \cdot N_{\text{s}} \cdot N_{\text{L}} \cdot Fr_{\text{prox},n} \cdot H_{\text{avg},n}^2 \tag{2.63}$$

where l_{w} is the length per turn. If an incomplete layer also exists, the loss of these extra turns due to the external proximity effect is calculated similarly as (2.63) and added to $P_{\text{prox\_ex},n}$. The total loss of the winding generated by the n-th current harmonic is then the sum of the three parts, i.e.

$$P_{\text{Cu},n} = P_{\text{skin},n} + P_{\text{prox\_in},n} + P_{\text{prox\_ex},n} \tag{2.64}$$

Finally, the total winding loss is given by the summation of losses due to all considered current harmonics:

$$P_{\text{Cu}} = \sum_{n=1}^{n_{\text{tot}}} P_{\text{Cu},n} \tag{2.65}$$

where the considered total number of harmonics n_{tot} can be set to a demanded quantity.

The calculation above is performed for both the MV and the LV winding iteratively until the copper temperature is converged. The final value at the converged temperature is taken as the winding loss.

Step 6: Temperature calculation

The final step is to solve the thermal model and check if temperatures are within the constraint. Before the iteration, all non temperature-dependent thermal resistances need to be calculated according to geometry parameters and material properties. Then initial values of temperatures are assumed for each unknown temperature node of the thermal model. The calculated core loss and winding loss as discussed in previous steps are applied as thermal sources together with thermal resistances to the thermal model to

calculate node temperatures. The model is solved iteratively as the winding loss and some temperature dependent thermal resistances are calculated repetitively until temperatures of all nodes converge. The converged values are compared with the temperature limit at the end of the calculation. Details of the thermal model is introduced later in this chapter.

If all constraints described above are fulfilled, the calculated total loss is compared with the lowest value so far and the better solution is saved. The process described above is repeated for a number of times which can be defined by the user. At the end of the optimization, the valid solution with the lowest total loss is obtained. In some cases, a valid solution may not be found or only a local optimal solution is found. Therefore, the best solutions obtained so far can be used as initial values of the free parameters for further optimization if necessary.

2.3.2 Maximal electric field strength

For the isolation design, it is important to determine the electric field distribution in the core window area. For Litz-wires, there exists air between Litz-strands. To obtain a homogeneous electric field distribution inside the Litz-wire, the Litz-bundle can be coated with electrical semi-conductive materials before wrapped by the outer insulation layer. In this way, the Litz-wire can be considered as a round conductor for electric field calculation. Since the electrical conductivity of the semi-conductive layer is relative low, the influence on the magnetic field distribution and losses due to the skin and the proximity effect can be neglected. According to the data from the Litz-wire manufacturer [97], the outer insulation layer is made of two polyester bands with a total thickness of 6 µm.

The calculation of the electric field strength is based on a 2D model under following assumptions:

1. The core is connected to the negative DC-link terminal of the LV side converter, which means that they have the equal electric potential.

2. The winding voltage is equally distributed across the turns.

3. The first turn of the LV winding has the potential of U_2/N_2 and the last one has U_2.

4. The first turn of the MV winding has the potential of $U_{iso} + U_1/N_1$ and the last one has $U_{iso} + U_1$.

The calculation is based on the charge simulation method [98] and the basic principle is shown in Fig. 2.12. For a round conductor with a radius of r, several simulation charges are located inside the conductor and equally distributed around the center of the conductor (ref. Fig. 2.12 (a), where 4 simulation charges are shown). The distance d from the simulation charges to the center of the conductor is in the range of $(0, r)$. Accordingly, a contour point is located on the surface of the conductor for each simulation charge. The conductor is located in the core window, i.e. the rectangular box on the right top corner shown in Fig. 2.12 (b). For each simulation charge, there are 3 image charges which are located at positions mirrored with the frame of the core window. For the original box, 8 mirrored boxes are also given as shown in Fig. 2.12 (c). Accordingly, the image charges are also introduced in each box. As a result, there are 36 conductors and 144 charges in total.

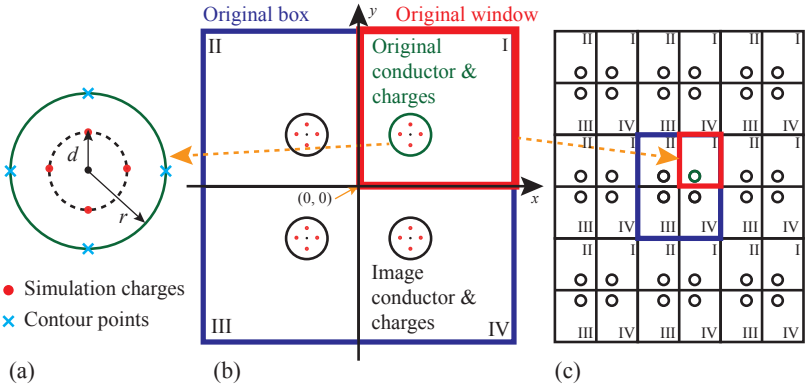

Figure 2.12: Basic principle of the 2D analytical calculation of electric field by using the charge simulation method: (a) Original conductor: 4 simulation charges equally distributed around the conductor center. (b) Original box: original conductor with 4 charges. (c) Nine boxes, each box contains 4 windows.

In general, considering a transformer with $N = N_1 + N_2$ windings, each winding has N_q simulation charges. If the total number of boxes is N_{box}, the total number of charges (including simulation charges and their image

charges) is

$$N_{\text{q,tot}} = 4N \cdot N_{\text{q}} \cdot N_{\text{box}} \tag{2.66}$$

The point at the left bottom corner of the original core window is selected as the origin of the coordinate system. Accordingly, the coordinates of all simulation charges, their image charges and contour points can be determined.

There are $N_{\text{contour}} = N \cdot N_{\text{q}}$ contour points in total. The electric potential of each contour point is equal to the potential of the corresponding conductor, which is already known. Therefore, potentials of all contour points form a $N_{\text{contour}} \times 1$ vector $\mathbf{\Phi_c}$. According to the charge simulation method, the electric potential of each contour point can be expressed in a matrix form by the superposition of the effects of all simulation charges and image charges as

$$\mathbf{\Phi_c} = \mathbf{P} \cdot \mathbf{Q} \tag{2.67}$$

where $\mathbf{Q}$ is the charge quantities of each simulation charge, which is also a $N_{\text{contour}} \times 1$ vector. The potential coefficient matrix $\mathbf{P}$ has a dimension of $N_{\text{contour}} \times N_{\text{contour}}$.

To calculate the electric field strength at an arbitrary point, the charge quantity of each simulation charge needs to be known which can be solved from (2.67), i.e.

$$\mathbf{Q} = \mathbf{P}^{-1} \cdot \mathbf{\Phi_c} \tag{2.68}$$

The element p_{ij} at the i-th line and j-th column of the matrix $\mathbf{P}$ represents the potential coefficient of the i-th contour point taking effects of unit charges at positions of the j-th simulation charge and its image charges in all boxes into account. p_{ij} is calculated as

$$\begin{aligned} p_{ij} &= \frac{1}{2\pi\varepsilon} \sum_{k=1}^{N_{\text{box}}} \left(\ln\frac{1}{D_{i,j,k,\text{I}}} - \ln\frac{1}{D_{i,j,k,\text{II}}} + \ln\frac{1}{D_{i,j,k,\text{III}}} - \ln\frac{1}{D_{i,j,k,\text{IV}}} \right) \\ &= \frac{1}{2\pi\varepsilon} \sum_{k=1}^{N_{\text{box}}} \ln\frac{D_{i,j,k,\text{II}} \cdot D_{i,j,k,\text{IV}}}{D_{i,j,k,\text{I}} \cdot D_{i,j,k,\text{III}}} \end{aligned} \tag{2.69}$$

where ε is the dielectric constant of the isolation medium. The variable $D_{i,j,k,m}$ (m={I,II,II,IV}) represents the distance between the i-th contour point at the position with coordinates of (x_i, y_i) and the j-th simulation

charge in the m-th quadrant of the k-th box with coordinates of $(x_{j,k,m}, y_{j,k,m})$, i.e.

$$D_{i,j,k,\mathrm{m}} = \sqrt{(x_i - x_{j,k,m})^2 + (y_i - y_{j,k,m})^2} \tag{2.70}$$

Since image charges in the II and IV quadrants are negative, the terms $\ln(1/D_{i,j,k,\mathrm{II}})$ and $\ln(1/D_{i,j,k,\mathrm{IV}})$ in (2.69) have a negative sign.

With the known potential coefficient matrix $\mathbf{P}$, charge quantities $\mathbf{Q}$ can be calculated by (2.68) and charge quantities of all image charges are obtained.

At a point with coordinates of (x, y) inside the core window, the electric field strength $E(x, y)$ is calculated as

$$E(x, y) = \sqrt{E_x^2 + E_y^2} \tag{2.71}$$

where E_x, E_y are two components of the electric field strength in the x and y-direction respectively. To determine E_x, E_y, effects of all $N_{\mathrm{q,tot}}$ charges at the point (x, y) are summed up according to the superposition principle as

$$E_x = \sum_{n=1}^{N_{\mathrm{q,tot}}} \frac{Q_{\mathrm{n}}}{2\pi\varepsilon} \left[\frac{x - x_{\mathrm{n}}}{(x - x_{\mathrm{n}})^2 + (y - y_{\mathrm{n}})^2} \right] \tag{2.72}$$

and

$$E_y = \sum_{n=1}^{N_{\mathrm{q,tot}}} \frac{Q_{\mathrm{n}}}{2\pi\varepsilon} \left[\frac{y - y_{\mathrm{n}}}{(x - x_{\mathrm{n}})^2 + (y - y_{\mathrm{n}})^2} \right] \tag{2.73}$$

In Fig. 2.13, the 2D electric field distribution in the transformer core window obtain by analytical calculation and the FEM simulation are compared. Here the analytical result is obtained by using 100×4 simulation charges ($N_{\mathrm{q}} = 4$ and $N_{\mathrm{box}} = 25$) for each conductor. The electric field distribution plot is obtained by evaluating $500 \times 1495 = 7.475 \times 10^5$ points which are equally distributed in the core window area. As can be seen, field distributions calculated by both methods match quite well. To obtain more accurate results, one can use more simulation charges and image charges (increase N_{q} and/or N_{box}). To obtain more detailed field distribution plot, one can increase the density of points for calculation, i.e., more points in the same core window area can be calculated. However, by increasing the number of charges and calculation points, more computation time is required.

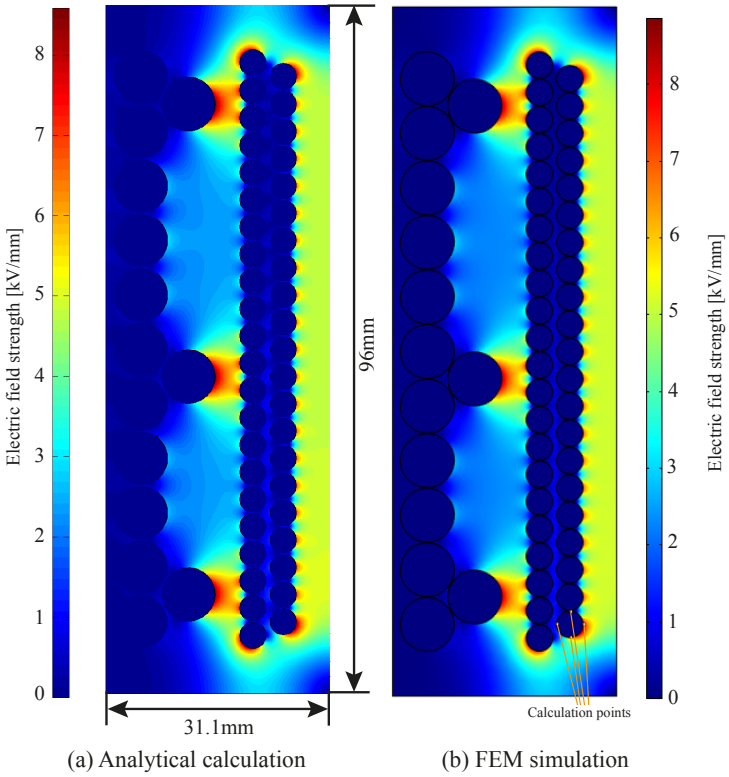

Figure 2.13: Comparison of the analytical calculation and the FEM simulation for the electric field distribution in the core window area.

During the optimization process, the calculation time is critical due to the large quantity of data to be processed. Since only the maximal electric field strength $E_{\max}$ is of interest, the number of calculation points can be reduced to save the calculation time. Due to a higher electric potential, the large electric field strength normally appears at the surface of the MV winding at locations nearest to the core and the LV winding, which can be seen in Fig. 2.13. For the same example, the calculation time and results of $E_{\max}$ obtained by the FEM simulation and the analytical method are listed in Table 2.6. It can be seen that to calculate the field distribution with nearly one million points by using the analytical method, the time consuming is quite significant, which is impractical to be included in the optimization

procedure.

Table 2.6: Comparison of different methods for E_{max} calculation

Methods	FEM	Analytic (7.475×10^5 points)	Analytic (228 points)
Calculation time [s]	5	385	0.5
E_{max} [kV/mm]	8.854	8.587	8.568

In this example, there are 57 conductors in total. If 4 points, which are equally distributed on the contour of conductors, are selected for calculation (see Fig. 2.13 (b)), the total number of points to be calculated is only $57 \times 4 = 228$. In this case, the calculation time is roughly 0.5 s, which is significantly reduced compared with the calculation time for the complete field distribution with 7.475×10^5 points. On the other hand, the obtained E_{max} with this simplified method is still very close to the results obtained by FEM simulation with a difference of approximately 3%. Therefore, this simplified approach can be integrated into the optimization process.

As the first estimation and to accelerate the calculation process, only contour points of windings are evaluated during the optimization. To improve the accuracy of E_{max}, more points can be taken into account. For the practical implementation, 16 equally distributed points on the contour of each winding are selected for electric field calculation. For each conductor, 16 simulation charges and 9 mirroring boxes are used as shown in Fig. 2.12. For safety reason, E_{max} is limited to 8.75 kV/mm, which is 25% of the dielectric strength of the considered epoxy resin [99].

2.3.3 Thermal model of the MFT

The thermal model for the shell type transformer with concentric winding arrangement as shown in Fig. 2.9 is illustrated in Fig. 2.14. To simplify the model, following assumptions are made:

1. The core loss is assumed to be equally distributed in the core.
2. The winding loss is equally distributed in the MV and the LV winding respectively.

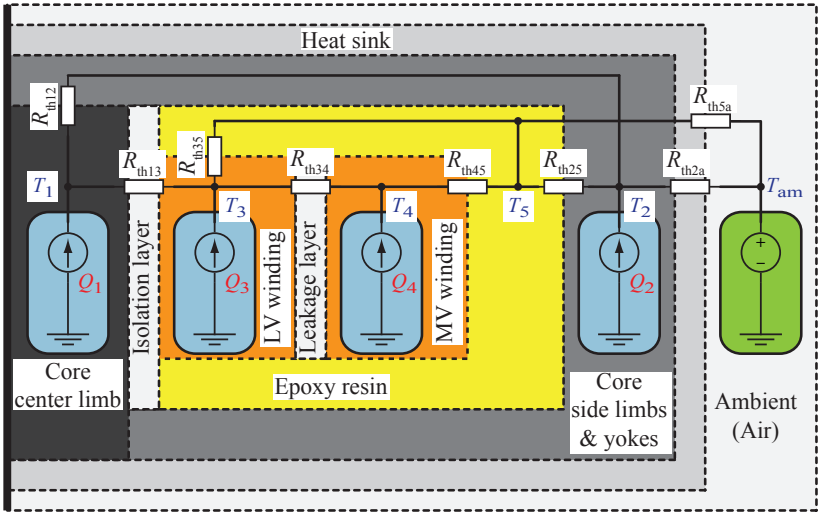

Figure 2.14: Thermal model of the shell type transformer with the concentric winding arrangement.

Description of thermal model

The core is divided into two parts: the central limb with the temperature T_1 and the side limbs and yokes with the temperature T_2. The LV winding and the MV winding are assumed to have the temperature T_3 and T_4 respectively. Both windings are completely surrounded by the epoxy resin with the temperature T_5. There are four thermal sources, i.e. two parts of core losses Q_1, Q_2, copper losses of the LV winding Q_3 and the MV winding Q_4. Thermal resistances shown in the graph are explained as below:

- R_{th12} – between the core center limb and the side limb, yokes
- R_{th13} – between the core center limb and the MV winding through the bobbin layer
- R_{th25} – between the core side limbs, yokes and the epoxy resin
- R_{th2a} – between the core side limbs, yokes and the ambient through heat sinks

- R_{th34} – between the MV winding and the LV winding
- R_{th35} – between the MV winding and the epoxy resin
- R_{th45} – between the LV winding and the epoxy resin
- R_{th5a} – between the epoxy resin and the ambient.

The thermal model can be described in matrix form as

$$\mathbf{A} \cdot \mathbf{T} + \mathbf{B} \cdot \mathbf{U} = 0 \tag{2.74}$$

where

$$\mathbf{A} = \begin{bmatrix} A_{11} & A_{12} & A_{13} & A_{14} & A_{15} \\ A_{21} & A_{22} & A_{23} & A_{24} & A_{25} \\ A_{31} & A_{32} & A_{33} & A_{34} & A_{35} \\ A_{41} & A_{42} & A_{43} & A_{44} & A_{45} \\ A_{51} & A_{52} & A_{53} & A_{54} & A_{55} \end{bmatrix} \tag{2.75}$$

The elements of **A** are given as

$$\begin{aligned}
A_{11} &= -\left(\frac{1}{R_{\text{th12}}} + \frac{1}{R_{\text{th13}}}\right) \\
A_{22} &= -\left(\frac{1}{R_{\text{th12}}} + \frac{1}{R_{\text{th25}}} + \frac{1}{R_{\text{th2a}}}\right) \\
A_{33} &= -\left(\frac{1}{R_{\text{th13}}} + \frac{1}{R_{\text{th34}}} + \frac{1}{R_{\text{th35}}}\right) \\
A_{44} &= -\left(\frac{1}{R_{\text{th34}}} + \frac{1}{R_{\text{th45}}}\right) \\
A_{55} &= -\left(\frac{1}{R_{\text{th25}}} + \frac{1}{R_{\text{th35}}} + \frac{1}{R_{\text{th45}}} + \frac{1}{R_{\text{th5a}}}\right) \\
A_{12} &= A_{21} = \frac{1}{R_{\text{th12}}}, \quad A_{13} = A_{31} = \frac{1}{R_{\text{th13}}} \\
A_{25} &= A_{52} = \frac{1}{R_{\text{th25}}}, \quad A_{34} = A_{43} = \frac{1}{R_{\text{th34}}} \\
A_{35} &= A_{53} = \frac{1}{R_{\text{th35}}}, \quad A_{45} = A_{54} = \frac{1}{R_{\text{th45}}}
\end{aligned}$$

The rest of elements are all equal to 0. The matrix

$$\mathbf{B} = \begin{bmatrix} 1 & 0 & 0 & 0 & 0 & 0 \\ 0 & 1 & 0 & 0 & 0 & \frac{1}{R_{\text{th2a}}} \\ 0 & 0 & 1 & 0 & 0 & 0 \\ 0 & 0 & 0 & 1 & 0 & 0 \\ 0 & 0 & 0 & 0 & 1 & \frac{1}{R_{\text{th5a}}} \end{bmatrix} \tag{2.76}$$

And $\mathbf{T} = [T_1, T_2, T_3, T_4, T_5]^{\mathbf{T}}$ is the vector of all temperature nodes to be determined, $\mathbf{U} = [Q_1, Q_2, Q_3, Q_4, 0, T_{\text{am}}]^{\mathbf{T}}$ with T_{am} the ambient temperature defined as 40 °C.

An initial temperature is assumed for each node before solving the thermal model in order to calculate temperature dependent quantities, i.e. the copper loss and some of the thermal resistances. Then, (2.74) is solved to obtain new nodes temperatures. If new temperatures do not converge with assumed values, then newly calculated values are assigned as initial values for nodes and temperature dependent quantities are re-calculated. In this way, (2.74) is solved iteratively until the convergence of all node temperatures is achieved.

Heat transfer

The heat transfer process can be divided into three types: conduction, convection and radiation [100]. Inside the transformer, the heat transfer is through the thermal conduction. On the surface of the transformer, the heat dissipation to the ambient air is through the convection and the radiation.

By conduction heat transfer through a path with the length of l in a homogeneous material with a thermal conductivity of λ and an unique cross-sectional area of A_c, the corresponding thermal resistance is calculated as

$$R_{\text{th,cond}} = \frac{l}{\lambda A_c} \tag{2.77}$$

By free convective heat transfer, the thermal resistance is calculated as

$$R_{\text{th,conv}} = \frac{L_{\text{Ch}}}{\lambda_{\text{air}} \cdot N_{\text{u}} \cdot A_{\text{Sur}}} \tag{2.78}$$

where λ_{air} is the thermal conductivity of air evaluated at the average temperature $T_{\text{avg}} = (T_{\text{Sur}} + T_{\text{amK}})/2$, with T_{Sur} the temperature of the solid surface

in [K]. $T_{\mathrm{amK}} = T_{\mathrm{am}} + 273.15$ [K] is the temperature of the air in [K] and A_{Sur} is the surface area. Therefore, λ_{air} is calculated as

$$\lambda_{\mathrm{air}} = 0.0243 + 7.14 \times 10^{-5} \cdot (T_{\mathrm{avg}} - 273.15) \tag{2.79}$$

The characteristic length L_{Ch} for a rectangular surface with dimensions of $h \times w$ is given as

$$L_{\mathrm{Ch}} = \begin{cases} h & \text{vertical surface with height of } h \quad (2.80) \\ \dfrac{2hw}{h+w} & \text{horizontal surface} \quad (2.81) \end{cases}$$

The Nusselt number N_{u} needs to be evaluated according to the type of the surface as[ii] [101]

$$N_{\mathrm{u}} = \begin{cases} \left[0.825 + 0.387\left(R_{\mathrm{a}} \cdot f_1(P_{\mathrm{r}})\right)^{\frac{1}{6}}\right]^2 & \text{(ver.)} \quad (2.82) \\ 0.766\left[R_{\mathrm{a}} \cdot f_2(P_{\mathrm{r}})\right]^{\frac{1}{5}} & \text{(hor. up., } R_{\mathrm{a}} f_2(P_{\mathrm{r}}) \le 7 \times 10^4) \quad (2.83) \\ 0.15\left[R_{\mathrm{a}} \cdot f_2(P_{\mathrm{r}})\right]^{\frac{1}{3}} & \text{(hor. up., } R_{\mathrm{a}} f_2(P_{\mathrm{r}}) > 7 \times 10^4) \quad (2.84) \\ 0.6\left[R_{\mathrm{a}} \cdot f_1(P_{\mathrm{r}})\right]^{\frac{1}{5}} & \text{(hor. down., } 10^3 < R_{\mathrm{a}} f_1(P_{\mathrm{r}}) < 10^{10}) \quad (2.85) \end{cases}$$

where functions $f_1(P_{\mathrm{r}})$ and $f_2(P_{\mathrm{r}})$ are dependent on the Prandtl number P_{r} and are defined as

$$f_1(P_{\mathrm{r}}) = \left[1 + \left(\frac{0.492}{P_{\mathrm{r}}}\right)^{\frac{9}{16}}\right]^{-\frac{16}{9}} \tag{2.86}$$

$$f_2(P_{\mathrm{r}}) = \left[1 + \left(\frac{0.322}{P_{\mathrm{r}}}\right)^{\frac{11}{20}}\right]^{-\frac{20}{11}} \tag{2.87}$$

The Rayleigh number R_{a} is the product of P_{r} and the Grashof number G_{r}, i.e.

$$R_{\mathrm{a}} = P_{\mathrm{r}} \cdot G_{\mathrm{r}} \tag{2.88}$$

where G_{r} is found in (2.92). The Prandtl number is also evaluated at T_{avg} as

$$P_{\mathrm{r}} = \frac{c_{\mathrm{p}}(T) \cdot \nu}{\lambda_{\mathrm{air}}} \qquad (T = T_{\mathrm{avg}}) \tag{2.89}$$

[ii] ver.=vertical, hor.=horizontal, up.=upwards, down.=downwards.

where the specific thermal capacity of air c_p (in [J/(kg·K)]) at a constant pressure and the temperature T_{avg} is

$$c_p = 1002.5 + 275 \times 10^{-6} \cdot (T_{avg} - 200)^2 \tag{2.90}$$

And the dynamic viscosity ν (in [kg/(m·s)]) of air is

$$\nu = \frac{1.458 \times 10^{-6} \cdot T_{avg}^{1.5}}{T_{avg} + 110.4} \tag{2.91}$$

The Grashof number G_r is evaluated as

$$G_r = G_{r\_co} \cdot (T_{Sur} - T_{amK}) \cdot L_{Ch}^3 \tag{2.92}$$

where the temperature dependent coefficient G_{r_co} at T_{avg} is

$$G_{r\_co} = \frac{\rho^2 \cdot g}{T_{avg} \cdot \nu^2} \tag{2.93}$$

with $\rho = 1.293 \cdot 273.15 / T_{avg}$ [kg/m^3] as the air density at T_{avg} and g=9.8 m/s^2 is the gravitational acceleration.

The thermal resistance in case of the thermal radiation is independent on the orientation of the solid surface, which is calculated as

$$R_{th,rad} = \frac{T_{Sur} - T_{amK}}{\epsilon_i \, \sigma \, A_{Sur} (T_{Sur}^4 - T_{amK}^4)} \tag{2.94}$$

where $\sigma = 5.67 \times 10^{-8}$ [W/(m^2·K^4)] is the Stefan-Boltzmann constant and ϵ_i is the emissivity factor.

2.3.4 Calculation of thermal resistances

The major effort of the thermal modeling is devoted to calculate thermal resistances, especially for the winding. For the thermal conduction, thermal resistances are independent on the temperature. However, for the heat convection and the radiation, thermal resistances are dependent on the temperature difference between the solid surface and the ambient air. For the considered transformer structure, the heat dissipation to the ambient is through heat sinks mounted on the core, surfaces of core directly exposed to ambient and surfaces of the epoxy resin surrounding the winding. Therefore,

only R_{th2a} and R_{th5a} are temperature dependent and need to be calculated iteratively. Other thermal resistances are evaluated only once before the iterative calculation. According to the structure, the composition of each thermal resistance shown in Fig. 2.14 are explained as below.

$R_{\text{th,12}}$ — The core loss in the central leg is assumed to be concentrated in the geometric center. The heat transfer from this point to the upper and lower yokes of the core is in vertical direction. The thermal resistance of the central leg in vertical direction is calculated by using (2.77) as

$$R_{\text{th,Cleg,Ver}} = \frac{c}{\lambda_{\text{core}} A_{\text{c}}} \tag{2.95}$$

Therefore, $R_{\text{th,12}}$ is equivalent to two parallel-connected thermal resistances with value of $R_{\text{th,Cleg,Ver}}/2$, which results in

$$R_{\text{th,12}} = R_{\text{th,Cleg,Ver}}/4 \tag{2.96}$$

where λ_{core} is the thermal conductivity of the core[iii].

$R_{\text{th,13}}$ — The source of winding losses Q_3 and Q_4 are also considered to be concentrated in the middle of the winding. The heat transfer from node 1 to node 3 is in the horizontal direction through the core central leg, the bobbin, and half of the LV winding. Therefore, $R_{\text{th,13}}$ is a series connection of three thermal resistances:

$$R_{\text{th,13}} = R_{\text{th,Cleg,Hor}} + R_{\text{th,Bobbin,Hor}} + R_{\text{th,WLV,Hor}}/2 \tag{2.97}$$

where the thermal resistance of the core central leg $R_{\text{th,Cleg,Hor}}$ and the bobbin $R_{\text{th,Bobbin,Hor}}$ in horizontal direction are calculated by (2.77) with applications of corresponding dimensions and thermal conductivities. Notice that the heat transfer are considered in four directions in the horizontal plane, which means there are four parallel connected thermal resistances. The calculation of the winding thermal resistance $R_{\text{th,WLV,Hor}}$ will be explained later.

$R_{\text{th,34}}$ — This is the thermal resistance between node 3 and node 4, which consists of three series connected parts in the horizontal direction: half of the LV winding, the leakage layer and half of the MV winding, i.e.

$$R_{\text{th,34}} = R_{\text{th,WMV,Hor}}/2 + R_{\text{th,Leak,Hor}} + R_{\text{th,WLV,Hor}}/2 \tag{2.98}$$

[iii] This is the worst case estimation. In fact, $R_{\text{th,12}}$ is calculated as $R_{\text{th,Cleg,Ver}}/8$.

$R_{\text{th,35}}$ — In vertical directions, the heat Q_3 also transfers through winding layers to the epoxy resin surrounding the winding. Therefore, $R_{\text{th,35}}$ is a parallel connection of two thermal resistances equal to $R_{\text{th,WLV,Ver}}/2$, with $R_{\text{th,WLV,Ver}}$ the thermal resistance of the LV winding in vertical direction and results in

$$R_{\text{th,35}} = R_{\text{th,WLV,Ver}}/4 \tag{2.99}$$

$R_{\text{th,45}}$ — The heat transfer from the MV winding to the epoxy resin is in both horizontal and vertical directions. In vertical directions, the thermal resistance is calculated similarly as (2.99) for the MV winding. In horizontal directions, the thermal resistance is half of the total value. The parallel connection of thermal resistances in two directions leads to

$$R_{\text{th,45}} = (R_{\text{th,WMV,Ver}}/4) \parallel (R_{\text{th,WMV,Hor}}/2) \tag{2.100}$$

$R_{\text{th,25}}$ — This thermal resistance accounts for the epoxy resin between the winding and the core surface in the core window. Therefore, $R_{\text{th,25}}$ is calculated by using (2.77) with $l = d_{\text{iso}}$ and A_{c} replaced by the surface area inside of the core window with contact to the epoxy resin.

$R_{\text{th,2a}}$ — This thermal resistance represents the interface from the core surface to the ambient. As shown in Fig. 2.9, part of the core surface is covered by heat sinks. The thermal resistance for these areas is equal to the thermal resistance of the heat sink $R_{\text{th,heatsink}}$, which is estimated by the volume of the heat sink according to its Cooling System Performance Index (CSPI) as introduced in [102]. The volume of the heat sink is calculated according to dimensions of the core as

$$V_{\text{heatsink}} = 4abc + 8ab^2; \tag{2.101}$$

The CSPI is defined as $5\,\text{W}/(\text{K}\cdot\text{L})$, which is relatively conservative considering the forced-air cooling. The thermal resistance of the heat sink is then

$$R_{\text{th,heatsink}} = \frac{1}{\text{CSPI}\cdot V_{\text{heatsink}}} \tag{2.102}$$

For surface areas not covered by heat sinks, the thermal resistance for free convection $R_{\text{th,Core,conv}}$ is calculated according to (2.78) and the thermal resistance for radiation $R_{\text{th,Core,rad}}$ according to (2.94). Notice that

$R_{\text{th,Core,conv}}$ needs to be evaluated separately for each surface depending on the orientation. The final value of $R_{\text{th,Core,conv}}$ is obtained as the parallel connected thermal resistances of all surfaces by convection. On the contrary, $R_{\text{th,Core,rad}}$ can be calculated directly for all surfaces. The final value of $R_{\text{th,2a}}$ is then

$$R_{\text{th,2a}} = R_{\text{th,Core,conv}} \parallel R_{\text{th,Core,rad}} \parallel R_{\text{th,heatsink}} \tag{2.103}$$

Arc surfaces on corners of the core are not taken into account.

$R_{\text{th,5a}}$ — On the front and the rear surface, the heat transfers from the surface of the epoxy resin to the ambient. Similar as $R_{\text{th,2a}}$, $R_{\text{th,5a}}$ can be calculated in the same way as in (2.103) without considering the thermal resistance of the heat sink.

As mentioned before, $R_{\text{th,2a}}$ and $R_{\text{th,5a}}$ need to be calculated iteratively. However, some quantities such as the surface area are not temperature dependent. These quantities are also evaluated before the iterative process to save calculation time.

Thermal resistance of the multi-layer winding

To calculate the thermal resistance of the multi-layer winding consists of Litz-wires with N_{s} strands, a winding with m layers is considered, where each layer consists of N_{L} turns. There are $m \times N_{\text{L}}$ thermal resistances in total. The heat transfer from one turn to its adjacent turn is simultaneously via two paths: in the tangential direction along the conductor and in the radial direction through the isolation layer. In the vertical direction, the heat transfers from one turn to the next one is through the conductor with the length of a single turn l_{w}. Therefore, the tangential thermal resistance in the vertical direction is given as

$$R_{\text{th\_ver,tan}} = \frac{l_{\text{w}}}{\lambda_{\text{Cu}} A_{\text{Cu}}} \tag{2.104}$$

where λ_{Cu} is the thermal conductivity of copper and A_{Cu} is the cross-sectional area of the conductor. On the contrary, the heat transfers through the conductor of a whole layer with the total length of $l_{\text{w}} \cdot N_{\text{L}}$ to reach the next turn in the horizontal direction. The tangential thermal resistance for the horizontal direction is then given as

$$R_{\text{th\_hor,tan}} = \frac{l_{\text{w}} \cdot N_{\text{L}}}{\lambda_{\text{Cu}} A_{\text{Cu}}} \tag{2.105}$$

The analytical calculation of the the radial thermal resistance is based on the electric and thermal analogy as heat flux lines and electric field lines between two round conductors are similar [95]. To explain the calculation method, the cross-sectional area of 2×2 conductors composed of Litz-wires is shown in Fig. 2.15 (a). A single Litz-bundle is modeled by 4 equal thermal resistances, two in the horizontal direction and another two in the vertical direction. Each resistance is represented as $R_{\text{th,Bundle}}/2$, which is half of the thermal resistance of the Litz-bundle. The radial thermal resistance between two Litz-bundles are represented by $R_{\text{th\_hor,rad}}$ in the horizontal direction and $R_{\text{th\_ver,rad}}$ in the vertical direction. The difference of the thermal resistance between the two directions is that there is an additional isolation layer with a thickness of d_{inter} between two winding layers in the horizontal direction (see Fig. 2.15 (a)).

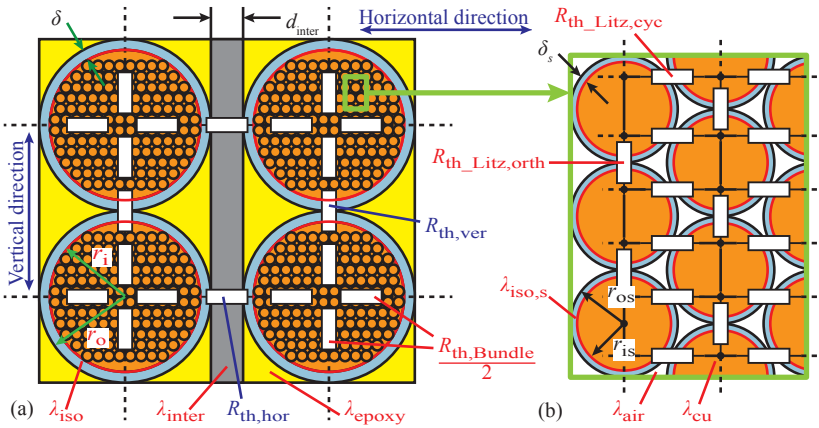

Figure 2.15: Thermal model of 2×2 conductors with Litz-wires: (a) thermal model of Litz-wires, (b) thermal model of a single Litz-bundle.

By replacing the dielectric constant ε with the thermal conductivity λ in equations used to calculate the winding capacitance given in [103], the radial thermal resistance $R_{\text{th\_hor,rad}}$ in the horizontal direction can be calculated as

$$R_{\text{th\_hor,rad}} = \left[\frac{2\lambda_{\text{epoxy}} l_{\text{w}}}{\alpha} \left(V + \frac{1}{8\lambda_{\text{iso}}/\lambda_{\text{epoxy}}} \left(\frac{2\delta}{r_{\text{o}}} \right)^2 \frac{Z}{\alpha} \right) \right]^{-1} \tag{2.106}$$

where

$$\alpha = 1 - \frac{\delta}{r_o \lambda_{iso}/\lambda_{epoxy}}, \qquad \beta = \frac{1}{\alpha}\left(1 + \frac{d_{inter}}{2 r_o \lambda_{inter}/\lambda_{epoxy}}\right) \tag{2.107}$$

$$V = \arctan\left(\sqrt{\frac{\beta+1}{\beta-1}}\right)\frac{\beta}{\sqrt{\beta^2-1}} - \frac{\pi}{4} \tag{2.108}$$

$$Z = \frac{\beta(\beta^2-2)}{(\beta^2-1)^{3/2}}\arctan\left(\sqrt{\frac{\beta+1}{\beta-1}}\right) - \frac{\beta}{2(\beta^2-1)} - \frac{\pi}{4} \tag{2.109}$$

λ_{epoxy}, λ_{iso}, λ_{inter} are thermal conductivities of the epoxy resin, the isolation layer of the Litz-bundle and the isolation material between winding layers, respectively. The outer and inner radius of the Litz-wire is r_o and r_i respectively and $\delta = r_o - r_i$ is the thickness of the outer insulation layer. Similarly, the radial thermal resistance $R_{th\_ver,rad}$ in the vertical direction can be calculated by (2.106) given that $d_{inter} = 0$.

So far, only the calculation of thermal resistances between Litz-bundles is discussed. To calculate $R_{th,Bundle}$, all Litz-strands in the bundle need to be considered. In Fig. 2.15 (b), part of the Litz-bundle is shown in detail. There are two type of thermal resistances between Litz-strands: the orthogonal thermal resistance $R_{th\_Litz,orth}$ and the orthocyclic thermal resistance $R_{th\_Litz,cyc}$. For a single Litz-strand, the thermal resistance is calculated as below:

$$R_{th\_strand,cyc} = \left[4\lambda_{air} l_w \left(M_{s1} + M_{s2}\frac{\delta_s}{r_{os}^2 \lambda_{iso,s}/\lambda_{air}}\left(r_{os} - \frac{d_{iso,s}}{2}\right)\right)\right]^{-1} \tag{2.110}$$

and

$$R_{th\_strand,orth} = \left[\frac{2\lambda_{air} l_w}{\alpha_s}\left(V_s + \frac{1}{8\lambda_{iso}/\lambda_{air}}\left(\frac{2\delta_s}{r_{os}}\right)^2 \frac{Z_s}{\alpha_s}\right)\right]^{-1} \tag{2.111}$$

with

$$M_{s1} = \int_0^{\frac{\pi}{6}} \frac{\cos^2\theta - \cos\theta\left(\sqrt{\cos^2\theta - 0.75}\right) - 0.5}{\left[\cos\theta - A_s\left(\sqrt{\cos^2\theta - 0.75} + 0.5\right)\right]^2} \mathrm{d}\theta \tag{2.112}$$

$$M_{s2} = \int_0^{\frac{\pi}{6}} \frac{\sin^2\theta + \cos\theta\left(\sqrt{\cos^2\theta - 0.75}\right)}{\left[\cos\theta - A_s\left(\sqrt{\cos^2\theta - 0.75} + 0.5\right)\right]^2} \mathrm{d}\theta \tag{2.113}$$

$$\alpha_s = 1 - \frac{\delta_s}{r_{os}\lambda_{iso,s}/\lambda_{air}}, \qquad \beta_s = 1/\alpha_s \tag{2.114}$$

$$V_s = \arctan\left(\sqrt{\frac{\beta_s + 1}{\beta_s - 1}}\right)\frac{\beta_s}{\sqrt{\beta_s^2 - 1}} - \frac{\pi}{4} \tag{2.115}$$

$$Z_s = \frac{\beta_s(\beta_s^2 - 2)}{(\beta_s^2 - 1)^{3/2}}\arctan\left(\sqrt{\frac{\beta_s + 1}{\beta_s - 1}}\right) - \frac{\beta_s}{2(\beta_s^2 - 1)} - \frac{\pi}{4} \tag{2.116}$$

where r_{os}, r_{is} are the outer and inner radius of the Litz-strand. $\delta_s = r_{os} - r_{is}$ is the thickness of the strand insulation layer with the thermal conductivity of $\lambda_{iso,s}$. Inside the Litz-bundle, the free space between Litz-strands is filled by air with the thermal conductivity of λ_{air}, which is temperature dependent according to (2.79). The air temperature inside the Litz-bundle is close to the winding temperature, which means λ_{air} can be evaluated at the winding temperature. However, this requires an iterative calculation as shown before. To simplify the calculation, λ_{air} is evaluated at T_{am}, which results in a smaller value due to a lower temperature. This is suitable for a conservative estimation since a smaller thermal conductivity leads to a larger thermal resistance.

To determine the total thermal resistance of the Litz-bundle, the round Litz-bundle is approximated as a square bundle with the same number of strands, i.e. a bundle of $\sqrt{N_s} \times \sqrt{N_s}$ strands. Then the equivalent thermal resistance of the Litz-bundle can be calculated as

$$R_{th,Bundle} = R_{th\_strand,cyc}\left(1 - \frac{1}{\sqrt{N_s}}\right) + \frac{R_{th\_strand,orth}}{\sqrt{N_s}} \tag{2.117}$$

The derivation of these equations by the thermal-electrical analogy and more details can be found in [104].

Now the total thermal resistance for the $m \times N_L$ multi-layer winding can be determined based on the calculated elementary thermal resistances. To simplify the analysis, it is assumed that the heat transfer in the horizontal and the vertical direction is independent.

In the horizontal direction, there are m thermal resistances connected in series as a string, and N_L such strings are connected in parallel. Therefore, the total thermal resistance of the winding is

$$R_{th,hor} = \frac{m}{N_L}\left[R_{th\_hor,tan} \parallel \left(R_{th\_hor,rad} + R_{th,Bundle}\right)\right] \tag{2.118}$$

In the vertical direction, there are N_L thermal resistances connected in series as a string, and m such strings are connected in parallel. The total thermal resistance is then

$$R_{th,ver} = \frac{N_L}{m}\left[R_{th\_ver,tan} \parallel \left(R_{th\_ver,rad} + R_{th,Bundle}\right)\right] \tag{2.119}$$

If there is an incomplete layer, it is assumed to be a full layer to simplify the calculation. Since the thermal conductivity of the conductor is much higher than that of the isolation material, the thermal resistance of the conductor in the radial direction can be neglected. Related thermal conductivities of the materials utilized for the winding thermal resistance calculation are given in Table 2.7.

Table 2.7: Thermal conductivities related to the thermal model of multi-layer windings consisting of Litz-wire

Element	Material	Thermal conductivity W/(m·K)
Medium inside the Litz-wire	Air	0.0272 (@40 °C)[101]
Medium between winding layers	Epoxy resin (Araldite CY221 & Aradur HY2966)	0.15 [99]
Bobbin, leakage layer, isolation layer between windings	Star-Therm W (PA66)	10 [105]
Additional isolation layer of Litz-wire	Polyester foil (Mylar)	0.155 [106]
Isolation layer of Litz-strand	Modified Polyurethane(PU)	0.245 [107]
Conductor	Copper	401[101]

2.4 Transformer volume versus frequency

For power electronic converters, the motivation of increasing the switching frequency is often to reduce the size of the system and therefore increase the power density. For inductors and transformers, it is generally known that their volume can be reduced by increasing the operating frequency. The limit for the size reduction is usually the thermal issue. If the size of magnetic components reaches the limit, further increase of the operating frequency becomes pointless considering the increasing switching loss of semiconductor devices.

For the MFT, the required isolation voltage sets a limit for the isolation distance, which may have additional impact on the volume of the transformer. In order to determine the operating frequency of the DABC, the dependency of the transformer volume on the operating frequency is investigated by using the optimization model shown in Fig. 2.8. The object of this study is to find valid designs with a minimal boxed volume at various operating frequency.

The nanocrystalline alloy VITROPERM 500F is selected as the core material for this study. The turns ratio is set to be 3:1 according to the transformer voltage ratio between the MV side and the LV side (1200 V:400 V). The optimization is performed for 5 operating frequencies: 1 kHz, 2 kHz, 4 kHz, 8 kHz and 16 kHz. To keep the same current waveform at different operating frequencies, the leakage inductance needs to be scaled according to the frequency to keep the same impedance value. The target value of L_σ is set to be 50 µH at 16 kHz and values for other frequencies are accordingly adapted, e.g. 100 µH@8 kHz and so on.

In order to calculate the maximal flux density and losses of the transformer, voltage and current waveforms need to be defined. For simplicity, the DABC is assumed to be operated at the boundary between mode 1 and mode 2, i.e., the falling edge of the voltage u_2 as shown in Fig. 2.6 is exactly at $T_s/2$. Therefore, the equation given below is valid:

$$\phi + \tau_2 = \pi \tag{2.120}$$

With this additional equation, there is only one independent operation parameter (ϕ or τ_2) to determine waveforms of the DABC. The power equations (2.23) and (2.25) for both operation modes become equivalent and are

simplified as

$$P = \frac{MU_1^2}{4\pi^2 f_s L_\sigma}\phi\tau_2 \tag{2.121}$$

With the given frequency, the transformer turns ratio and the leakage inductance, ϕ and τ_2 can be calculated by solving (2.121) and (2.120). The resulting voltage and current waveforms considering a transferred power of P=25 kW are shown in Fig. 2.16, where $\phi \approx 0.03\pi$.

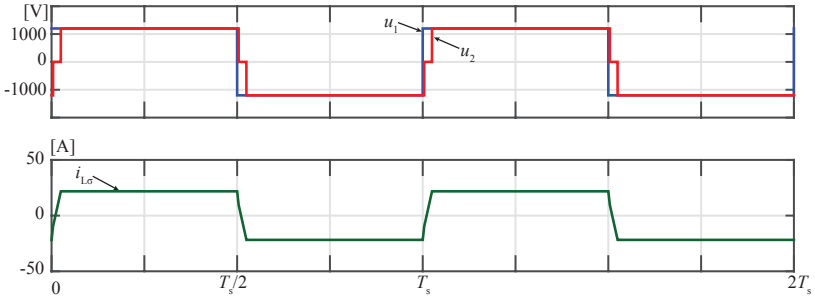

Figure 2.16: Voltage and current waveforms of the transformer considered for the optimization to evaluate the frequency dependency of the volume.

The waveforms shown above are identical for each considered frequency and are used for the optimization. For each pre-defined boxed volume, the optimizer searches the optimal design regarding the total transformer loss at the given operating frequency. The boxed volume is gradually reduced until no valid design can be found. In Fig. 2.17, the volume breakdown of the optimal transformer designs with the minimal boxed volume at each operating frequency are shown. It can be seen that the transformer volume reduction by increasing the frequency are not significant above 4 kHz. Due to the required isolation distance and necessary surface area for heat dissipation, the core volume is almost the same at 8 kHz and at 16 kHz. Also, the ratio of volume due to isolation distance to the total volume of the transformer increases with the frequency. The benefit of reducing the size by increasing the operating frequency is limited by the isolation requirement and the thermal stress above 10 kHz.

Furthermore, the switching loss of the DABC increases significantly with the frequency, especially for the MV side switch. With the same current

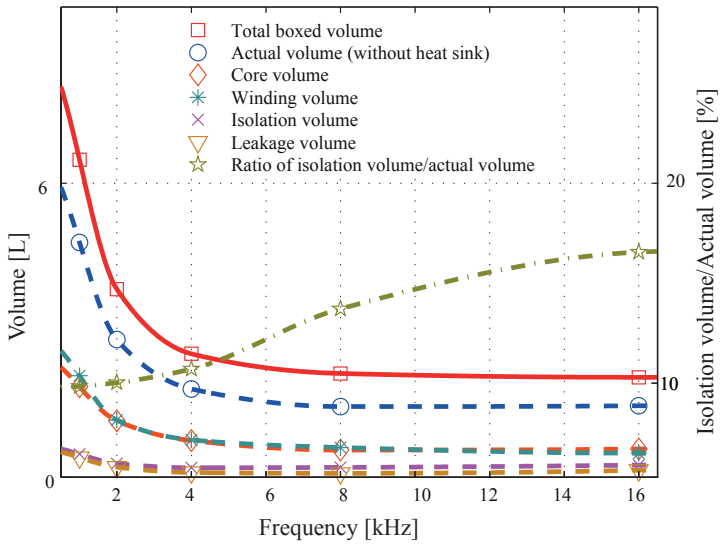

Figure 2.17: Volume reduction for optimal MFT designs with the VITROPERM 500F by increasing the operating frequency from 1 kHz to 16 kHz.

waveform shown in Fig. 2.16, the calculated total loss of semiconductor devices is 361 W at 4 kHz and it increase to 779 W at 16 kHz. Therefore, the operating frequency of the DABC is selected to be 4 kHz.

2.5 Combined efficiency optimization of DABC

For the optimal design of the DABC, the total loss including the loss in the converter and in the MFT needs to be minimized. To find the optimal operation condition of the DABC for a given transfered power in terms of the efficiency, the goal is to find the optimal combination of 4 free parameters, i.e. L_σ, N_W, ϕ and τ_2, where first two parameters are related to the MFT design. Therefore, a combined model of the converter and the transformer is developed based on an extension of the previously presented optimization model for the MFT. Since the major loss of the converter is in semiconductor devices, only the losses in IGBTs and diodes are accounted for the converter. Other losses such as those in the DC-link capacitors are neglected. In Fig. 2.18, the flow chart of the combined optimization pro-

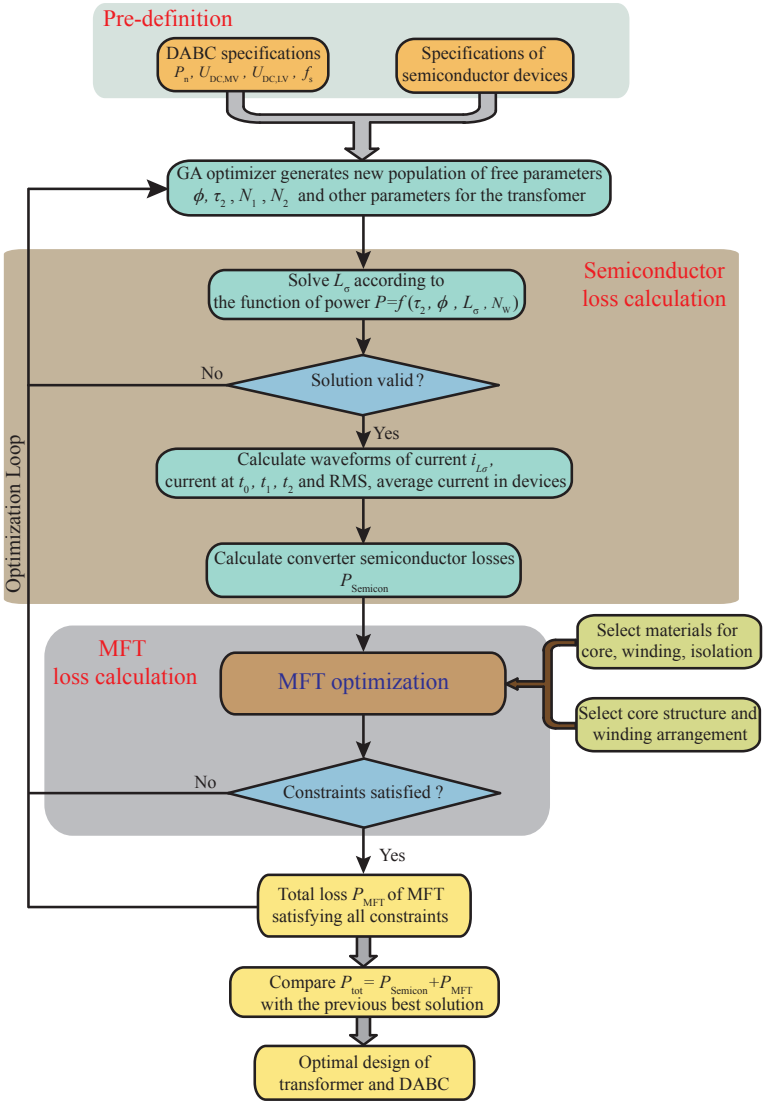

Figure 2.18: Flow chart of the DABC loss optimization considering the semiconductor loss and the transformer loss.

cedure for reducing the sum of the converter semiconductor loss and the transformer loss is shown.

Before starting the optimization process, specifications of the DABC are defined, e.g. DC-link voltages, the transfered power and functions to calculate the semiconductor loss. Also, semiconductor devices are selected and required parameters for loss calculation need to be defined according to the data sheet.

As mentioned, there are 4 parameters related to the operation of the DABC if the modulation method given in Table 2.4 is considered. In this case, there are only 3 independent parameters since the other one can be solved according to (2.23), (2.25), (2.27) and (2.29). With constant DC-link voltages, the parameter M is only dependent on N_W as given in (2.3). The transformer turns ratio N_W is separated into two integer parameters N_1 and N_2, which represent the number of turns of the MV and the LV winding respectively. If τ_2 or ϕ are to be calculated, a second-order equation needs to be solved in case of operation mode 2 and mode 4. On the other hand, to calculate L_σ, only a first-order equation needs to be solved in case of all operation modes. Therefore, τ_2 and ϕ are selected to be free parameters.

Same as for the optimization model of the MFT, the GA is used. In this case, there are 12 free parameters in total. In this section, only the part for converter loss calculation is briefly discussed. For the MFT, the calculation procedure is the same as presented in previous sections.

1. In the first step, the operation mode can be determined according to the generated values of ϕ and τ_2. Then the inductance L_σ can be calculated from the power equation according to the operation mode. If $L_\sigma \leq 0$, then the solution is invalid. The optimization is then interrupted and returns to the start with new generated values for the next round of calculation.

2. If $L_\sigma > 0$, the solution is valid. Accordingly, the waveform of $i_{L\sigma}$ can be determined and current values at instances of t_0, t_1, t_2 as well as the RMS value are calculated according to equations given in previous sections. Based on the waveform of $i_{L\sigma}$, current waveforms in each individual switch and diode can be determined and RMS, average values of current are calculated. The obtained leakage inductance L_σ is used later as the target value for the transformer optimization.

3. In the final step of the converter calculation part, conduction and switching losses for each semiconductor device are calculated and summed up as the total loss P_{Semicon}.

In the next step, the optimization proceeds further to the transformer part. Similarly, if any constraint for the transformer is not satisfied, then the optimizer will re-start with a new set of the free parameters. If all constraints are satisfied, a valid solution is found and the total loss of the transformer P_{MFT} is added to P_{Semicon} to get the total loss P_{tot}.

2.6 Example design of the DABC

As a case study, the design of the DABC with previously given specifications is performed. For the operation point at the nominal power of 25 kW transferred from the MV side to the LV side, the combined optimization algorithm shown in Fig. 2.18 is used to find the optimal solution. During the optimization, constraints for the RMS current and the peak current need to be added according to the rating of selected semiconductor devices.

For the design of the MFT, commercially available standard cores are considered. According to the selected operating frequency resulting from the previous study, the rectangular core from VACUUMSCHMELZE with part number of T60102-L2157-W159[iv] made by the nanocrystalline material VITROPERM 500F [108] is chosen. An even number of pieces of the core is required due to the considered shell type structure of the MFT. Furthermore, the same Litz-wire is considered to be used for both the MV and the LV winding, with the LV winding constructed by 4 wires in parallel arranged as a 2×2 bundle.

2.6.1 Optimization model adaption

With the consideration mentioned above, the combined optimization algorithm as shown in Fig. 2.18 is slightly adapted. Since core dimensions are known, the core leg width a can be removed from the list of free parameters. With the considered construction of windings, the diameter of Litz-strands $d_{\text{s1}} = d_{\text{s2}}$, and the number of strands of the LV winding is $N_{\text{s2}} = 4N_{\text{s1}}$. There-

[iv] The dimensions of this core is given in Table 5.1.

fore, d_{s2} and N_{s2} also can be removed from free parameters and the total number of free parameters is reduced from 12 to 9.

In the previously introduced optimization algorithm for the MFT, the size of the core window is determined based on the winding dimension and the isolation distance. In case of using a standard core, dimensions of the core window are fixed. With the known outer diameter of the Litz-wire, N_{L1} is determined as

$$N_{L1} = \frac{b - 2d_{iso}}{d_{a1}} \tag{2.122}$$

where the result needs to be rounded as an integer. Then the arrangement of the MV winding can be determined, which is similar for the LV winding. The total required width of the core window is calculated according to (2.35). An additional constraint is added that the calculated core window width is smaller or equal to the actual dimension b. The rest of the optimization procedure is the same as shown in Fig. 2.8.

2.6.2 Design results

If only two pieces of the selected core are used, a valid solution cannot be found. Therefore, four pieces of the core are considered for the design. By using the optimization algorithm, optimal operation parameters of the DABC and design parameters of the MFT are obtained. The detail of the design are discussed below.

Converter operation parameters and losses

The optimal operation parameters of the DABC are found to be:

- L_σ=115 µH
- $N_W = N_1 : N_2 = 43 : 14$
- $\phi = 0.029\pi$
- $\tau_2 = 0.975\pi$

According to the conditions given in Table 2.4, the DABC is operated in

mode 2 but close to the boundary between mode 1 and mode 2. In Table 2.8, calculated losses of the DABC under this optimal operation condition are listed. Accordingly, the loss breakdown is shown in Fig. 2.19. It can be seen that the MFT contributes less than half of the total loss of the DABC. Regarding the loss in semiconductor devices, the major part is the conduction loss, especially on the LV side due to the high current.

Table 2.8: Losses of the DABC under the optimal operation condition at the nominal power of 25 kW

Part		Loss [W]
Semiconductor devices	MV side conduction loss	71.4
	MV side switching loss	48.6
	LV side conduction loss	158.3
	LV side switching loss	11.1
	Total (Semiconductor)	289.4
MFT	Core	54.9
	MV winding	39.8
	LV winding	21.5
	Total (MFT)	116.2
DABC Total		405.6
DABC efficiency		98.4%

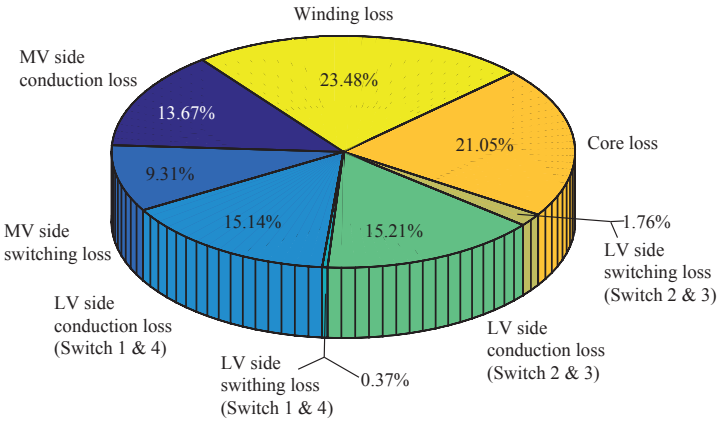

Figure 2.19: Loss breakdown of the DABC at the nominal power of 25 kW.

In Fig. 2.20, the voltage/current of the transformer and the current of switching devices are shown. Accordingly, RMS and average currents for each component are listed in Table 2.9, where parallel connected devices are considered as a single device. Since the NPC converter on the MV side is modulated as a HB converter, the cascaded IGBTs are conducting the same current. Therefore, the two IGBTs are considered as a single device. Furthermore, clamping diodes are not considered for the loss calculation.

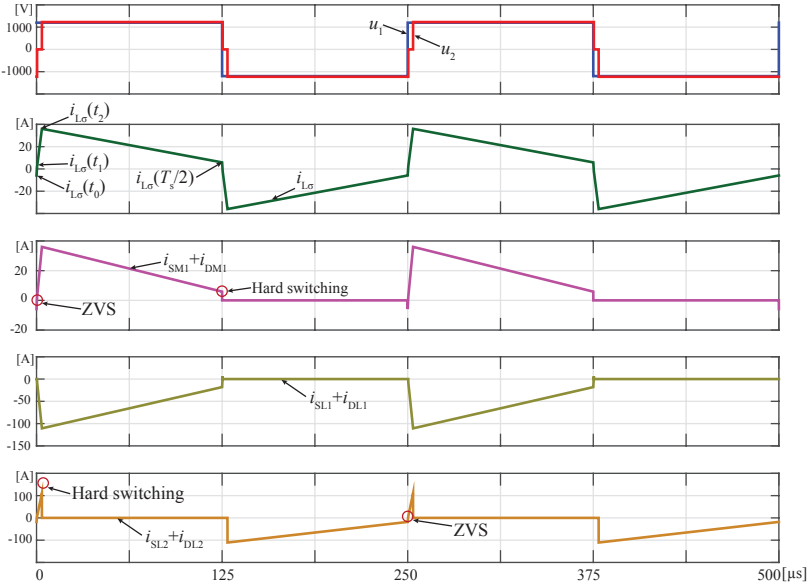

Figure 2.20: Operation waveforms of the DABC at the nominal power of 25 kW transferred from the MV side to the LV side.

It can be seen that, the current $i_{L\sigma}$ is trapezoidal and close to a triangular shape similar as shown in Fig. 2.7. The first time interval T_{I} ($t_0 \sim t_1$) is very short, which is approximately $(\phi+\tau_2-\pi)\cdot T_{\mathrm{s}}/2$=375 ns. During T_{I}, the current rises from a negative value to a positive value. Therefore, IGBTs on the MV side are turned on under the ZVS condition. To ensure the ZVS condition for S_{M1} and S_{M2}, the current $i_{L\sigma}(t_0)$ needs to be negative so that the switch is turned on when the anti-parallel diode is conducting. During the time interval T_{II} ($t_1 \sim t_2$), $i_{L\sigma}$ rises continuously until reaching the peak current at t_1. In the last time interval T_{III} of the first half switching cycle, $i_{L\sigma}$

decreases slowly to $i_{L\sigma}(T_s/2) = -i_{L\sigma}(t_0)$, which is positive but close to zero. The MV side IGBTs are turned off at $-i_{L\sigma}(t_0)$ and therefore it is beneficial for reducing the turn-off loss if $i_{L\sigma}(T_s/2)$ is close to zero. To force the current to decrease during T_{III}, the condition $M > 1$ needs to be fulfilled. For the given DC-link voltages, the only possibility is to set $N_W > 3$, which is obtained from the optimization results.

On the LV side, switches S_{L1} and S_{L4} do not conduct a current. The current is flowing through the anti-parallel diode. Therefore, there are only conduction losses and reverse recovery losses in diodes D_{L1} and D_{L4}. Switches S_{L2} and S_{L3} are turned on under the ZVS condition, but turned off at the peak current, which is equal to $N_W \cdot i_{L\sigma}(t_1)$. This is supposed to result in high switching losses. However, due to the parallel connection of 4 IGBTs on the LV side, both the switching loss and the conduction loss can be reduced.

The current $i_{L\sigma}$ at the three switching instances during the first half switching cycle are:

- $i_{L\sigma}(t_0)$=−5.87 A
- $i_{L\sigma}(t_1)$=2.18 A
- $i_{L\sigma}(t_2)$=36 A

As can be seen, under the operation conditions obtained by the optimization, the ZVS turn-on and turn-off at a near-zero current for switches on

Table 2.9: RMS and average currents of semiconductor components in the DABC under the operation conditions shown in Fig. 2.20

Component	RMS current [A]	Average current [A]
MFT MV winding	22.6	0
MV side IGBT	16	10.4
MV side Diode	0.11	0.003
LV side IGBT 1&4	0	0
LV side Diode 1&4	49.1	32
LV side IGBT 2&3	7.5	0.76
LV side Diode 2&3	48.6	31.3

the MV side is achieved. On the other hand, the RMS current is relative low which is advantageous to reduce the conduction loss both in semiconductor devices and in transformer windings.

Transformer

For the MFT, the number of turns N_W and the leakage inductance L_σ of the optimal design are already given. The MV winding consists of a 620×0.1 mm round Litz-wire with an outer diameter of 3.8 mm. The LV winding consists of 4 parallel wires with the same specifications. Other major parameters of the MFT are listed in Table 2.10.

Table 2.10: Parameters of the MFT obtained by the combined optimization

Parameter	Value
d_{iso}	4.6 mm
d_{leak}	3.3 mm
B_{max}	0.937 T (limit: 0.96 T)
E_{max}	8.57 kV/mm (limit: 8.75 kV/mm)
Maximal temperature	98.5 °C (limit: 120 °C)
Efficiency	99.54%
Volume	3.13 L
Power density	8 kW/L

As shown that the peak flux density [v] and the electric field strength are very close to the limit while the maximal temperature is far below the limit. Since the core cross-sectional area, the voltage and the frequency are fixed, the peak flux density is only determined by the number of turns, which is also related to the total winding length. On the one hand, the flux density is desired to be low to reduce the core loss. On the other hand, the winding length is desired to be small to reduce the copper loss. Since the loss of the VITROPERM 500F is relatively low and the heat dissipation from the core is more effective than from the winding, it is preferred to have less number of turns to reduced the winding length while exciting the core close to the limit of the flux density. In this way, the loss of the winding is partly shifted

[v] Here the peak flux density is calculated according to the effective core cross-sectional area given in the data sheet, which actually results in a lamination factor of approximately 0.67, compared with the measured core cross-sectional area.

to the core as given by the optimization result. On the other hand, to reduce the length of the MV winding, it is also preferred to reduce the thickness of the leakage layer d_{leak} . However, the allowed maximal electric field strength limits the reduction of d_{leak} as E_{max} is close to the limit.

In Fig. 2.21, CAD drawing of the MFT is shown with indicated total dimensions, which results in a boxed volume of 3.13 L and a power density of 8 kW/L. It should be pointed out that since the object of the combined optimization is to reduce the total loss of the DABC, the obtained design may not be optimal for the transformer itself considering the same condition.

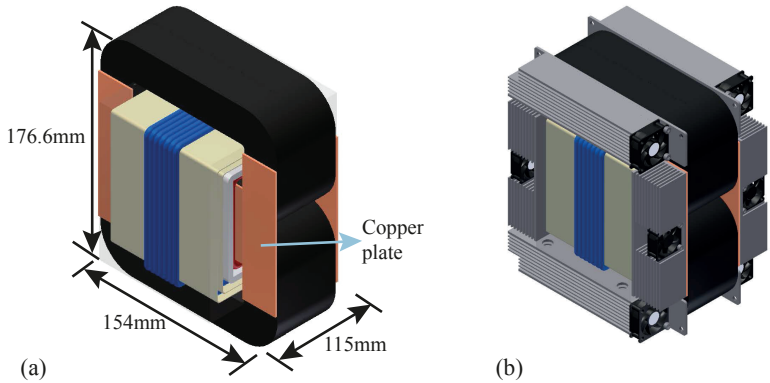

Figure 2.21: CAD drawings of the optimal MFT design: (a) without heat sink, (b) with heat sink and fans.

DABC design

In Fig. 2.22, the CAD design of the DABC module is shown. Converters on both sides are designed to match the dimension of the transformer. As can be seen that the total height and thickness of the converter are only slightly increased compared with the transformer. The converter also use the forced air-cooling with three 40 mm×40 mm×28 mm fans on each side. DC-link capacitors on both sides have the same dimensions, with four pieces on each side. On the LV side, four 600 V, 75 µF capacitors (part number: C4AEHBW5750A3NJ) are connected in parallel resulting in a total capacitance of 300 µF. On the MV side, two 1300 V, 27 µF capacitors (part number: B32778G1276K) are connected in parallel and cascaded with an-

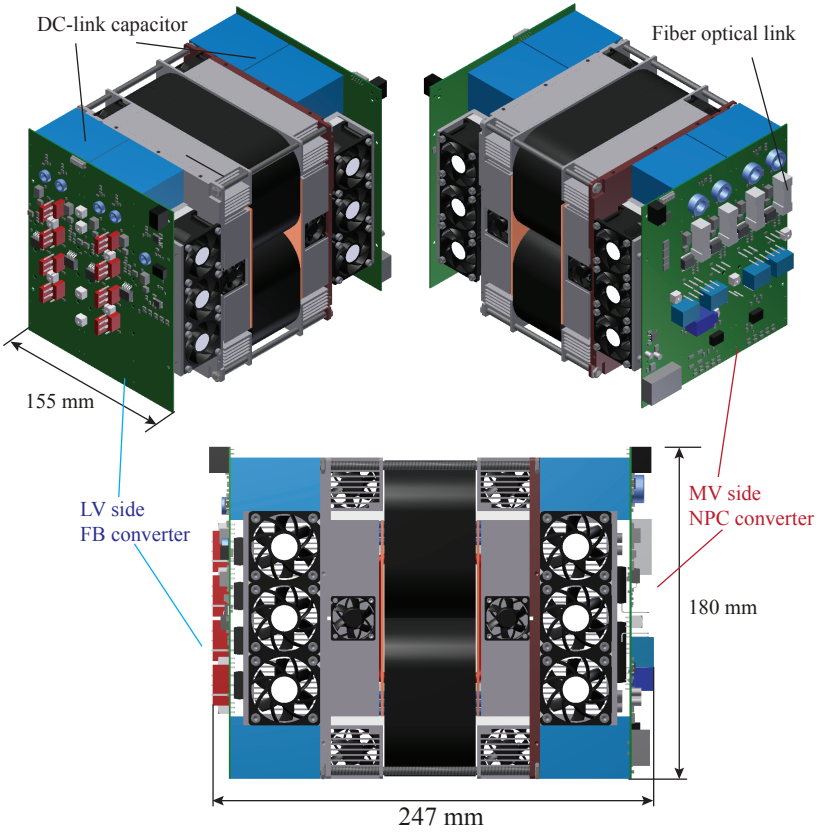

Figure 2.22: CAD drawings of the DABC.

other two parallel connected pieces, then the total capacitance is still 27 µF. Gate signals on the LV side are isolated by normal opto-couplers while the fiber optics link (Avago HFBR-3810Z) is utilized to provide the isolation for gate drivers on the MV side.

The final dimension of the DABC is 247 mm×155 mm×180 mm=6.89 dm^3, which results in a power density of 3.63 kW/dm^3. The transformer occupies roughly half of the total volume and each converter composes around 1/4 of the total volume. The volume of the transformer can be reduced by using customized cores and more advanced cooling concepts such as the water

cooling. Also, the size of the heat sink of the converter can be reduced by using a more efficient cooling system.

2.7 Summary and conclusions

In this chapter, a design case for the isolated DC-DC converter of a three-phase SST system is performed. For the considered application, the design of a 24 kV/400 V DABC with the nominal power down-scaled to 25 kW is studied. The selection of the topologies for the active bridges on both sides of the MFT is discussed with considerations of the modulation flexibility. For given specifications, the NPC topology is selected for the MV side in order to use semiconductor devices with lower voltage rating and reduce losses. The FB topology is selected for the LV side to enable more modulation possibilities. For the selected topology, possible modulation methods by considering the NPC converter as a HB converter are discussed.

Focusing on the transformer, an optimization model using the GA is developed and implemented in MATLAB, for which the procedures and models are described in detail. The emphasis is put on the electric field strength calculation and the thermal modeling. An analytical approach based on the 2D charge simulation method is implemented to evaluate the maximal electric field strength. By carefully selecting the positions where the electric field strength are calculated and limiting the number of calculation points, this approach can be integrated into the optimization process and a high accuracy can be achieved which is verified by the FEM simulation. For the thermal model, the iterative calculation of temperatures is implemented to achieve a higher accuracy. Furthermore, the thermal model for the Litz-wire based on the thermal-electrical analogy is implemented to obtain more accurate thermal resistances of the winding. Due to the complexity of models, the calculation procedure is essential for saving the computation time. Therefore, calculation steps are arranged according to their computational effort. The step with a lower effort is arranged in an earlier stage. If any constraint is not met, the calculation process can be restarted without proceeding to later steps with higher computational efforts. In this way, the total computation time can be significantly reduced.

The developed MFT optimization model is used to investigate the frequency dependency of the transformer volume in order to determine the operating frequency of the converter. The study is performed by searching

the lowest achievable volume of the MFT with same specifications at various operating frequencies. Results show that above a few kHz, the volume reduction of the transformer by increasing the operating frequency is not significant. The required isolation voltage leads to a certain isolation distance and restricts the volume reduction. The benefit of increasing the operating frequency is lost on the one hand due to the almost constant transformer volume and on the other hand due to the significantly increased switching loss. Therefore, the operating frequency for the considered DABC design is selected to be 4 kHz.

In order to minimize the total loss of the DABC, a combined optimization model based on the MFT optimization model is further developed. The model includes modulation parameters and the MFT design parameters and is aimed to find optimal design parameters of the MFT and operation parameters of the DABC at a given power level and boxed volume of the transformer, which result in the lowest total loss of the transformer and semiconductor devices.

Finally, the combined optimization model is employed to find the optimal operation and design parameters of the DABC and the MFT for the studied case. A standard nanocrystalline core and the same round Litz-wire for both the MV and the LV winding are considered for the design. Results show that the semiconductor loss is dominant, which is more than 2 times higher than the transformer loss. With the optimal operation parameters, the MV side switches are turned on under the ZVS condition and turned off at a near-zero current. Therefore, the switching loss which is critical on the MV side due to the slow switching speed of devices can be significantly reduced. The dominant part of the loss in semiconductor devices is the conduction loss especially on the LV side due to the high conducting current. For the designed DABC, an efficiency of over 98% at the nominal power can be achieved according to the calculation. The final design of the DABC with the forced air-cooling can reach a power density of 3.63 kW/L, where the MFT achieves a power density of 8 kW/L and occupies around half of the total volume of the converter.

3 Acoustic Noise in Transformers: Origins and Modeling

As shown in chapter 2, the operating frequency of the MFT is selected as 4 kHz, which is in the audible range. Consequently, acoustic noise emission from the MFT becomes inevitable. In order to reduce the acoustic noise, it is necessary to investigate its origins.

Acoustic noise is sound waves perceived by human ears, which are induced by vibrations of certain objects. The origin of vibration is normally mechanical forces acting on the object and cause a periodic deformation or movement of the mechanical body. Major parts of transformers are magnetic cores and windings. Additionally, the construction also includes mechanical parts for mounting, isolation and cooling. The electrical excitation generates electromagnetic fields in and around the core and windings which induce electromagnetic forces. The magnetization of the core also causes deformation due to the magnetostriction effect. The origin of acoustic noise associated with transformers are the magnetostriction and the electromagnetic forces as they lead to vibrations of the core and windings. Through mechanical connections, vibrations of the whole transformer body are induced and transferred to the surface of the structure. In this way, particles in the surrounding air are forced to vibrate and generate acoustic waves. In case of oil-immersed transformers, the transmission path of the vibration also includes oil and mechanical attachments between the transformer body as well as the oil tank. Additionally, auxiliary equipments such as fans and oil pumps also generate acoustic noise. In this work, the investigation only focuses on electromagnetic origins considering a dry type transformer.

3.1 Basic of acoustics

Before the discussion about the acoustic noise emission of transformers, basics of acoustics relevant to this work are briefly reviewed. Per definition, acoustics is the interdisciplinary science that deals with the study of all mechanical waves in gases, liquids, and solids including topics such as vibration, sound, ultrasound and infrasound [109]. Sound is defined as vibrations transmitted through an elastic solid, liquid or gas with frequencies in the approximate range of 20 Hz to 20 000 Hz, capable of being detected by human ears.

Sound consists of two elements:

- The particle velocity $\vec{\mathbf{v}}$ is a vector quantity associated with the cause of the acoustic event.
- The sound pressure p is a scalar quantity associated with the result.

In air, the sound propagates as acoustic waves with the wavelength given by

$$\lambda = \frac{c}{f} \tag{3.1}$$

where c is the speed of sound and f is the frequency of the wave.

3.1.1 Sound fields

Consider a sound source located in the center of a room as shown in Fig. 3.1, the space around the sound source can be divided into the following sound fields:

- Near field
- Far field
  - Free field
  - Reverberant field

The near field is the area close to the sound source with a distance less than the larger one of the two values below:

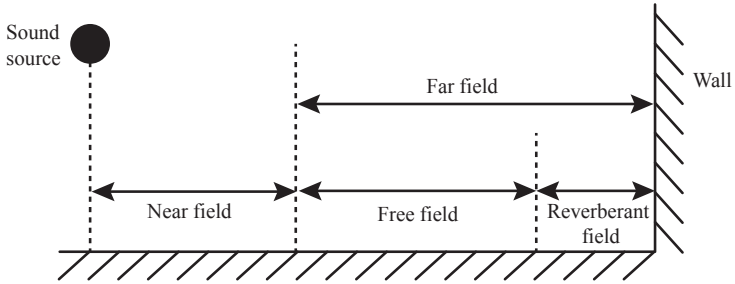

Figure 3.1: Sound fields in a room.

- The wavelength of the acoustic wave with the lowest frequency emitted from the source
- Twice of the largest dimension of the sound source

In this field, the sound pressure and the acoustic particle velocity are not in phase. The sound pressure may vary widely at different locations and there is no simple relation between the sound pressure level and the distance. Therefore, a meaningful quantification of the sound cannot be obtained in this field.

The far field is the sound field located far away from the sound source, which can be further divided into the free field and the reverberant field. The transition from the near field to the far field occurs gradually in the transition region.

In the free field, the sound behaves as in the open air without reflecting surfaces to interfere with its propagation. The amplitude of the sound pressure at any point is inversely proportional to the distance between this point and the sound source. Therefore, if the distance is doubled, the amplitude of the sound pressure and the particle velocity is halved and the sound pressure level (SPL) reduces 6 dB.

In the region close to the wall, acoustic waves reflected by the wall interact with waves directly emitted from the sound source. The reverberant wave is dominant and the field approaches the diffuse condition. The sound pressure level is more or less constant and independent on the distance to the sound source in this field.

3.1.2 Quantification of sound

Sound pressure is the incremental change from the static pressure at a given instant caused by the presence of a sound wave. The particle velocity is the velocity of a given infinitesimal part of a medium at a given instant solely due to a sound wave [110]. The sound pressure and the particle velocity are related by the specific acoustic impedance given by

$$Z_{\mathrm{s}} = \frac{p}{\vec{\mathbf{v}}} \tag{3.2}$$

In the near field, p and $\vec{\mathbf{v}}$ are not in phase, therefore Z_{s} is a complex number. In the free field, p and $\vec{\mathbf{v}}$ are in phase and Z_{s} can be expressed as

$$Z_{\mathrm{s}} = \rho c \tag{3.3}$$

where ρ is the density of air. A particle in the free field of air exposed to a sinusoidal sound pressure of 1 Pa moves back and forth with a velocity amplitude of about 2 mm/s.

In engineering, the sound pressure (in [N/m^2] or [Pa]) at a given point in the sound field is measured by the RMS value in a period T_{s} as

$$p = \sqrt{\frac{1}{T_{\mathrm{s}}} \int_0^{T_{\mathrm{s}}} \left[p(t)\right]^2 \mathrm{d}t} \tag{3.4}$$

The logarithmic scale is adopted for quantifying the variation of the sound pressure because the human hearing response varies from the threshold of hearing at 20 µPa to the threshold of pain at 200 Pa (i.e. a range of 10 millions). Then the sound pressure level is defined in decibels ([dB]) as

$$L_{\mathrm{P}} = 10 \log_{10} \frac{p^2}{p_{\mathrm{ref}}^2} = 20 \log_{10} \frac{p}{p_{\mathrm{ref}}} \tag{3.5}$$

where $p_{\mathrm{ref}} = 20\,\mu\mathrm{Pa}$ is the reference sound pressure, which is approximately the lowest RMS sound pressure at 2 kHz audible to an average person.

From energy point of view, sound can be quantified as the sound intensity $\vec{\mathbf{I}}$, which is a vector describes the rate of the sound energy flowing through a unit area (in [W/m^2]). It is determined as the product of the sound pressure and the particle velocity:

$$\vec{\mathbf{I}} = p\vec{\mathbf{v}} \tag{3.6}$$

The sound intensity in a specified direction at a given point represents the average rate at which the sound energy is transmitted through a unit area perpendicular to the specified direction at the considered point. Usually, $\vec{\mathbf{I}}$ is evaluated in the normal direction to a specified unit area through which the sound energy is flowing. Since the sound intensity is the time-averaged product of p and $\vec{\mathbf{v}}$, it is independent on time.

The sound power W describes the sound energy emitted by a sound source in a unit time. It can be evaluated by the integration of the sound intensity over an imaginary surface A surrounding the sound source, i.e.

$$W = \int_A \vec{\mathbf{I}} \cdot \vec{\mathbf{n}} \mathrm{d}A \tag{3.7}$$

where $\vec{\mathbf{n}}$ is the normal direction vector of the surface area A. Usually, it is convenient to choose a sphere or a spherical section as the surface.

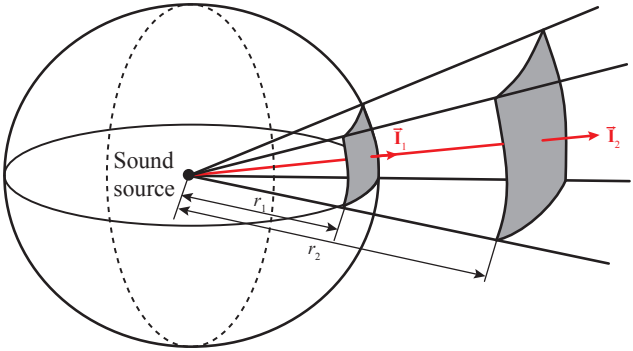

Figure 3.2: Sound intensity and sound power of a point source in free field.

As shown in Fig. 3.2, in case of a point sound source emitting spherical waves (the emission is equally in all directions) in the free field of air, the amplitude of the sound intensity evaluated in the direction normal to the spherical surface is

$$I = pv = \frac{p^2}{\rho c} \tag{3.8}$$

By selecting the spherical surface enclosing the sound source with a radius of r, the sound power is

$$W = 4\pi r^2 I \tag{3.9}$$

Since the emitted sound power from the source is constant, according to (3.9), the amplitude of the sound intensity I_1 and I_2 at the location with distance of r_1 and r_2 to the source respectively have the following relation:

$$\frac{I_1}{I_2} = \left(\frac{r_2}{r_1}\right)^2 \tag{3.10}$$

Therefore, the sound wave propagation in the free field follows the inverse square law.

Similar as the SPL, the logarithmic scale is used to define the sound intensity level (SIL), i.e.

$$L_\mathrm{I} = 10\log_{10}\frac{I}{I_\mathrm{ref}} \tag{3.11}$$

where I_ref is the reference sound intensity which is 10^{-12} W/m^2.

Accordingly, the sound power level (SWL) is defined as:

$$L_\mathrm{W} = 10\log_{10}\frac{W}{W_\mathrm{ref}} \tag{3.12}$$

where $W_\mathrm{ref} = 10^{-12}$ W is the reference sound power.

In practice, the emitted sound energy from an object, e.g. a transformer, is not identical in different directions. Therefore, the sound pressure around the object varies not only with the distance from measurement points to the object but also depends on the location of the measurement point. In this case, a SPL value measured at any single location around the object cannot give a meaningful description of the sound source. Therefor, it is necessary to introduce the mean sound pressure which is calculated by measured SPL values at a number of points on an imaginary surface enclosing the object. For instance, a hemispherical surface with a radius of 0.5 m or 1 m. Similarly, the average sound pressure can be defined (in [dB]) as

$$\bar{L}_\mathrm{P} = 20\log_{10}\frac{p_\mathrm{avg}}{p_\mathrm{ref}} \tag{3.13}$$

where p_avg is the average sound pressure on the measurement surface. According to (3.5), the mean sound pressure can be expressed in another way as

$$\bar{L}_\mathrm{P} = 10\log_{10}\left[\frac{1}{n}\left(\sum_{i=1}^{n} 10^{L_{\mathrm{P},i}/10}\right)\right] \tag{3.14}$$

where $L_{P,i}$ is the sound pressure at the i-th measurement point and n is the total number of measurement points. In order to compare the acoustic noise of different objects, the shape and the distance information of the measurement surface is required to get the mean SPL. It is therefore more convenient to compare the sound power level as defined in (3.12). The connection between the SWL and the mean sound pressure level $\bar{L}_P$ on a given measurement surface is given in [111] as

$$L_W = \bar{L}_P + 10\log_{10} A \tag{3.15}$$

where A is the total area of measurement surface (in [m^2]) and $\bar{L}_p$ is defined in (3.14). It should be pointed out that in the free field, the SWL is a unique value of a given source, regardless of the measurement surface [112].

3.1.3 Frequency analysis of sound

In practice, sound waves consisting of only a single tone, i.e. only one frequency component, are very rare. Usually, most sound signals contain different frequency components. To determine the distribution of sound level over the frequency range, the sound signal in time domain is often transformed into frequency domain, which is normally done by using the Fourier transform.

Frequency band

For further evaluation of sound, the audible frequency spectrum is divided into a number of frequency bands. The widest band used for the frequency analysis is the octave band, in which the upper frequency limit of the band is approximately twice of the lower limit. Octave bands are identified by their center frequencies, which are the mean values of the upper and the lower limit of the band [113]. In Table 3.1, the commonly used division of octave bands in audible frequency range is listed.

It can be seen that the audible frequency range is divided into 10 octave bands. The center frequency of the n-th band is twice of that of the $(n-1)$-th band. The percent fractional bandwidth of each octave band is defined as:

$$\text{BW\%} = \frac{100 \cdot (\text{Upper limit} - \text{Lower limit})}{\text{Center frequency}}\% \tag{3.16}$$

For all octave bands, this value is identical, which is approximately 70.7%.

Table 3.1: Octave bands in the audible frequency range [113]

Band number	Center frequency [Hz]	Lower limit [Hz]	Upper limit [Hz]
2	31.5	22	44
3	63	44	88
4	125	88	176
5	250	176	353
6	500	353	707
7	1000	707	1414
8	2000	1414	2825
9	4000	2825	5650
10	8000	5650	11300
11	16000	11300	22500

For a more detailed analysis, narrower bands can be used, e.g. 1/3-octave bands. In this case, each octave band is further divided into three bands. The upper limit frequency of the 1/3-octave band is $2^{1/3}$ times the lower limit and the percent fractional bandwidth is approximately 23.2%.

Frequency weighting of sound

In the audible frequency range, the sensitivity of human ears to the sound at different frequencies is not identical. In the range of 500 Hz to 8000 Hz, human ears have the most response to sound, while in lower and higher bands human ears are less sensitive to sound. To evaluate the exposure of human ears to acoustic noise more adequately, different frequency response weighting filters as shown in Fig. 3.3 have been introduced. Commonly used weighting curves are "A" and "C", which are defined in the international standard IEC 60651.

The A-weighting filter modifies the frequency response according to the equal loudness curve of 40 phons, which is more popular since it is useful for predicting the damage risk of human ears [113]. As can be seen, with the A-weighting curve, much of the low-frequency noise are filtered out. The unit of the A-weighted SPL is designated as dBA. According to the octave bands given in Table 3.1, an individual weighting factor is applied to each band as listed in Table 3.2. To give an intuitive feeling of the loudness of

sound, the SPL of some scenes in daily life are shown in Fig. 3.4.

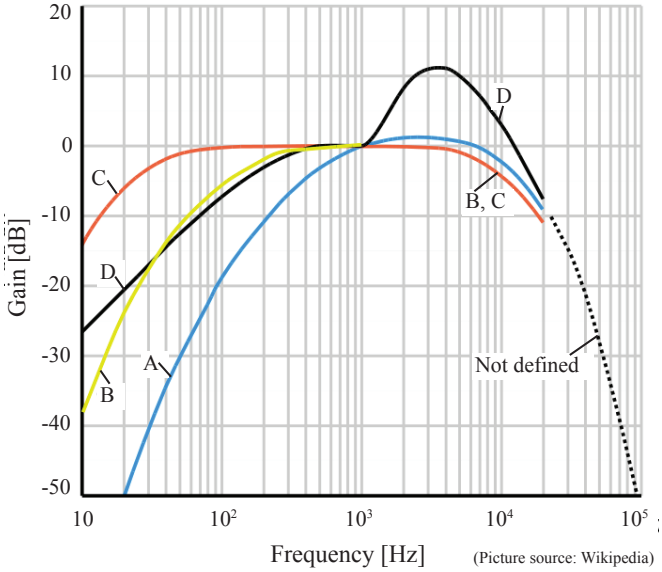

Figure 3.3: Frequency response weighting curves of sound.

Table 3.2: Frequency weighting characteristics of the A-weighting filter for octave bands [113]

Octave band center frequency [Hz]	A-weighting factor [dB]
31.5	-39.4
63	-26.2
125	-16.1
250	-8.6
500	-3.2
1000	0
2000	1.2
4000	1.0
8000	-1.1
16000	-6.6

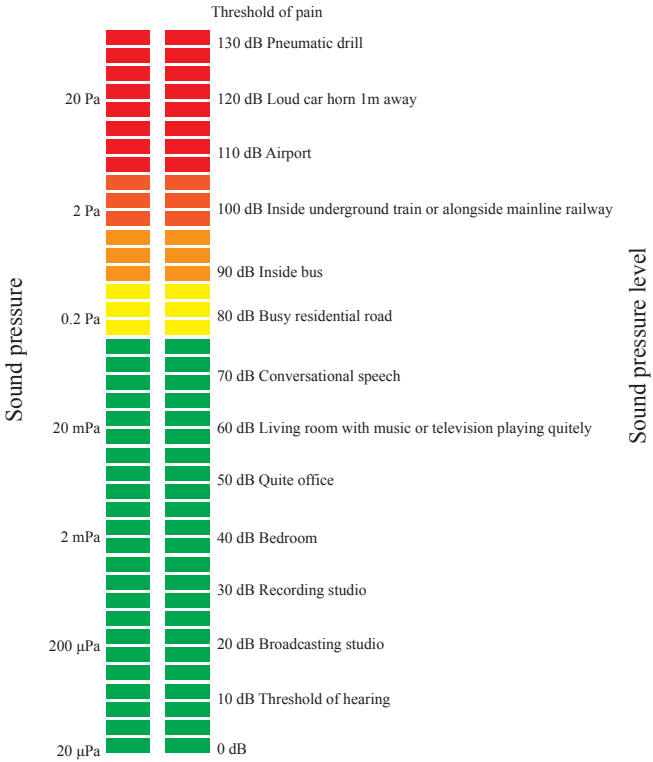

Figure 3.4: Sound pressure level in daily life scenes [114].

3.2 Origins of acoustic noise in transformers

As mentioned, there are three electromagnetic origins of the acoustic noise in transformers:

- The magnetostriction of the core
- The Maxwell force acting on the core
- The Lorentz force acting on the winding

In this section, basic theories of each effect are explained focusing on corre-

lations to the MFT.

3.2.1 Magnetostriction

The magnetostriction is a general phenomenon which occurs in almost all substances including antiferromagnet, ferrimagnet, paramagnet and even diamagnet and superconductors [115]. It represents the dimension change of a deformable substance due to the change of the magnetization. In a soft ferromagnet, the magnetostriction can be obviously observed and is therefore essential for engineering applications. However, it is generally considered to be the major cause of the core vibration in transformers [85].

The magnetostriction λ is quantified by the relative change in length of the material, which is a strain represented as

$$\lambda = \frac{\Delta l}{l} \tag{3.17}$$

where l is the length of the material and Δl is the change of the length. The value of λ at the magnetic saturation point is referred as the saturation magnetostriction and represented by λ_s, which is a property of the material. Even in strong magnetic materials, the magnetostrictive effect is small: the typical value of λ_s is in order of 10^{-5}. This value can be positive, negative or even zero in some cases, where a positive value means an elongation and a negative value represents a contraction.

Types of magnetostriction

There are two types of magnetostriction:

- The spontaneous magnetostriction due to an internal magnetic interaction
- The forced magnetostriction due to an externally applied magnetic field

Above the Curie temperature T_C, the ferromagnet is in the paramagnetic state. As shown in Fig. 3.5 (a), the magnetic moments are completely disordered due to thermal motions of the atoms. If the ferromagnet is cooled down and the temperature drops below T_C, the transition of the state from

the paramagnet to the ferromagnet occurs and the spontaneous magnetostriction is induced which leads to a dimension change of Δl.

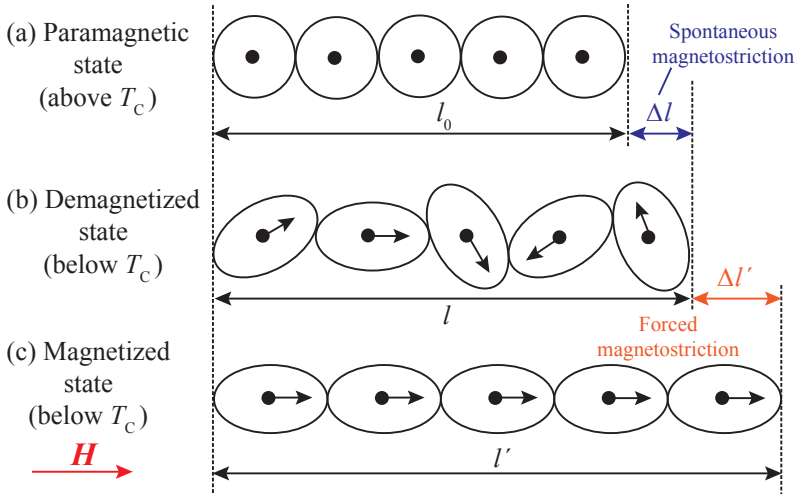

Figure 3.5: Mechanism of the magnetostriction [116].

As shown in Fig. 3.5 (b), in the ferromagnetic state, magnetic domains are formed due to the ordering of magnetic moments, but orientations of magnetic domains are random. By applying an external magnetic field, magnetic moments tend to align with the external field and the ferromagnet is magnetized. The alignment of magnetic moments to the external field as shown in Fig. 3.5 (c) leads to the rotation of the magnetic domains. As a result, a further dimension change of $\Delta l'$ is generated which increases with the strength of the external field till the magnetic saturation point of the ferromagnet.

For transformers under a normal operation condition, the core temperature is far below T_C. Therefore, only the forced magnetostriction is of interest, which involves several direct and inverse magneto-elastic effects. The most relevant effects are briefly discussed here.

Joule magnetostriction

The Joule magnetostriction is the anisotropic aspect of the forced magnetostriction, which refers to the elongation or shrink of the material due to the applied magnetic field. Below the magnetic saturation point, the magnetostrictive strain λ increases with the applied magnetic filed strength as a non-linear function. When the flux density of the ferromagnet reaches the saturation point, the magnetostriction also reaches its saturation value λ_s, which is a material parameter and remains independent of the demagnetized state. In Fig. 3.6, a typical $\lambda(B)$ curve of ferromagnet with positive magnetostriction is shown.

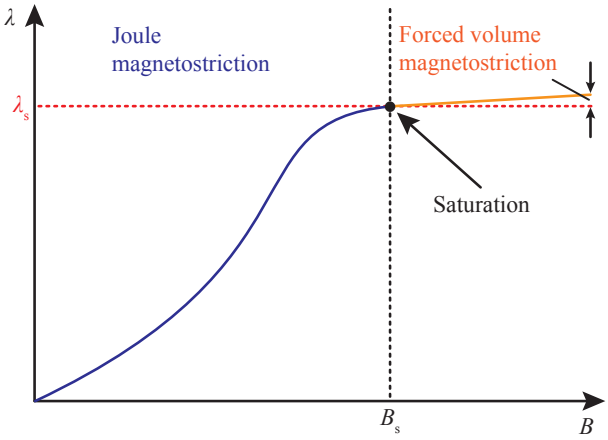

Figure 3.6: Dependency of the magnetostriction on the strength of the applied magnetic field.

For ferromagnetic materials, the magnetization $\vec{\mathbf{M}}$ is an odd function of $\vec{\mathbf{H}}$ and the magnetostriction λ is an even function of $\vec{\mathbf{H}}$. In case of a positive magnetostriction, λ could become negative at a high field strength. The $\lambda(\vec{\mathbf{H}})$ function is therefore not always monotonous and the curve shows hysteresis at a low field strength. For isotropic materials, the magnetostrictive strain in the direction of the applied magnetic field can be calculated as

$$\lambda_{\mathrm{p}} = \lambda_{\mathrm{s}} \cdot (\frac{B}{B_{\mathrm{s}}})^2 \tag{3.18}$$

With the Joule magnetostriction, the volume of the ferromagnet remains

constant. This indicates that there exists a strain λ_t in transverse directions with an opposite sign, i.e.

$$\lambda_t = -\frac{1}{2}\lambda_p \tag{3.19}$$

The Joule magnetostriction is not only field dependent but it is also related to the mechanical stress σ. There exist two major mechanisms [115] :

- The macroscopic mechanism – the anisotropy of the ferromagnet is modified due to the magneto-elastic energy and hence the demagnetized state changes as well. This may lead to a significant modification of the shape of the $\lambda(\vec{\mathbf{H}})$ curve but the magnetostriction coefficients are not affected.
- The microscopic mechanism – the existing magnetostriction coefficients are modified and new coefficients will appear due to the change of inter-atomic distances in case of a hydrostatic pressure and a symmetry lowering in case of an anisotropic stress.

Furthermore, the Joule magnetostriction is also dependent on the temperature and λ_s is usually a monotonous function of the temperature. The λ_s of iron and iron-rich Fe-Si alloys increases slowly with the temperature and decreases rapidly when the temperature approaches T_C. However, for a temperature far below T_C, the dependency is insignificant [117].

Villari effect

The inverse effect of the Joule magnetostriction, i.e. the Villari effect, describes the dependency of the magnetization curve $\vec{\mathbf{M}}(\vec{\mathbf{H}})$ on the mechanical stress σ, which is often described as the $\vec{\mathbf{B}}(\vec{\mathbf{H}},\sigma)$ function. The physical origin of this effect is that the applied mechanical stress can alter the magnetic domain structure and introduce new sources of magnetic anisotropy [118]. In Fig. 3.7, B-H curves of a ferromagnetic material under different mechanical stress are shown.

ΔE effect

Due to the magneto-elastic coupling, elastic properties of the ferromagnet may also be modified due to the magnetic interaction. According to Hook's

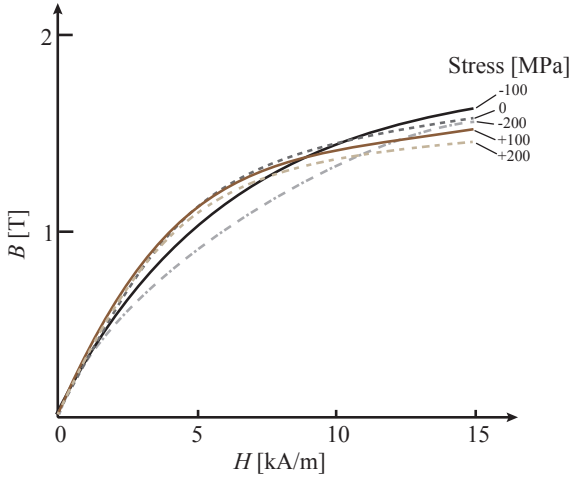

Figure 3.7: Influence of the mechanical stress on the magnetization curve of a ferromagnetic material [119].

law, the elastic strain ε_{el} of a non-magnetic material due to an externally applied mechanical stress is determined according to the elastic modulus (Young's modulus) E as

$$\varepsilon_{el} = \frac{\sigma}{E} \tag{3.20}$$

However, for a ferromagnet, the total strain ε_{tot} differs from the value calculated by (3.20). There is an additional strain ε_{ex} due to the reorientation of magnetic domains by the applied stress, i.e.

$$\varepsilon_{tot} = \varepsilon_{el} + \varepsilon_{ex} \tag{3.21}$$

As a result, the elastic modulus seems to be decreased to

$$E' = \frac{\sigma}{\varepsilon_{el} + \varepsilon_{ex}} \tag{3.22}$$

And the relative decrease compared to the original value E is

$$\frac{\Delta E}{E} = \frac{E' - E}{E} = -\frac{\varepsilon_{ex}}{\varepsilon_{el} + \varepsilon_{ex}} \tag{3.23}$$

This relative change of E is usually small, e.g. $\Delta E/E < 0.4\%$ for iron [117]. However, this value could be significant if it is measured at the resonant frequency of the vibration with a small amplitude [118]. At the magnetic saturation point, $\varepsilon_{ex} = 0$, no reorientation can occur. Therefore, the total strain is limited by the saturation magnetostriction and dependent on its sign [117]:

$$\begin{aligned} \varepsilon_{tot} &= \varepsilon_{el} + \lambda_s \qquad \text{for} \quad \lambda_s > 0 \\ \varepsilon_{tot} &= \varepsilon_{el} + \lambda_s/2 \qquad \text{for} \quad \lambda_s < 0 \end{aligned} \tag{3.24}$$

In Fig. 3.8, the schematic stress-strain curve is shown, which demonstrates the ΔE effect of a ferromagnetic material with a positive magnetostriction. As can be seen, the additional strain of the magnetic material due to the magnetostriction results in a lager total strain ε_{tot} compared to the stain of the non-magnetic material under the same stress.

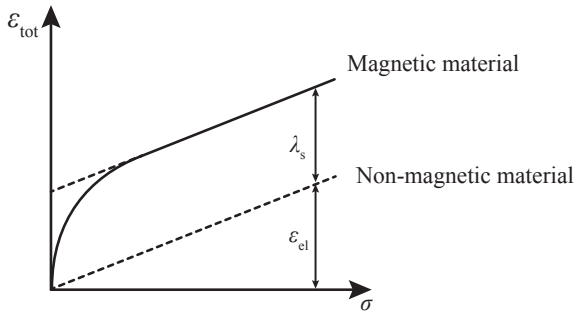

Figure 3.8: Stress-strain curve showing the ΔE effect of a ferromagnetic material with $\lambda_s > 0$ [117].

Volume magnetostriction

As mentioned before, the volume of a ferromagnet does not change with the Joule magnetostriction. In contrast, there exists the volume magnetostriction which slightly changes the volume of the material. Also, the volume magnetostriction is isotropic which differs from the Joule magnetostriction. Similar to the definition given in (3.17), the volume magnetostriction ω is defined according to the relative change of the volume as

$$\omega = \frac{\Delta V}{V} \tag{3.25}$$

The anomalous thermal expansion observed near T_C of the material is the spontaneous volume magnetostriction. With the externally applied magnetic field at the temperature far below T_C, the forced volume magnetostriction is induced, which is a combination of three effects described as [115]

$$\omega = \omega_0 + \omega_K + \omega^F \tag{3.26}$$

The forced magnetostriction is mainly induced by ω_0 and ω_K, which are due to the influence of the volume and the magnetization $\vec{\mathbf{M}}$ on the magnetic moment and the spin-orbit coupling [117]. The component ω_0 only depends on the magnitude of $\vec{\mathbf{M}}$, while ω_K is due to the crystal effect and depends on both the magnitude and the direction of $\vec{\mathbf{M}}$. As shown in Fig. 3.9, beyond the magnetic saturation point, the major contribution of the forced volume magnetostriction is from ω_0. The last component ω^F represents the contribution due to the form effect (also called dipolar magnetostriction), which is caused due to the tendency of the magnetized body to minimize its magneto-static energy [118]. Therefore, in contrary to the Joule magnetostriction, the form effect is dependent on the shape of the sample and is always positive. The magnetostriction due to the form effect is proportional to M^2 and stops at the saturation point. By further increasing the magnetic field above the saturation level, the dominant component is ω_0, which increases linearly and slightly with the field strength as already shown in Fig. 3.6.

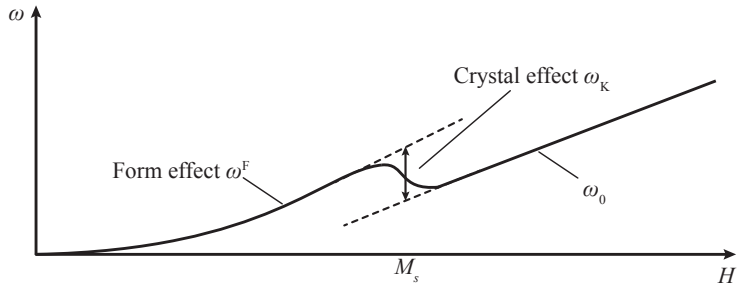

Figure 3.9: Volume magnetostriction due to the form effect ω^F, the crystal effect ω_K and ω_0 [117].

Summary of magnetostriction related to transformer core vibration

The magnetostriction in ferromagnetic materials with an applied mechanical stress is a very complex phenomenon, lots of efforts are still being put on the research of this topic. For the vibration analysis of transformer cores, the most relevant are the magneto-elastic effects within the magnetic saturation point of the ferromagnet as listed below:

- Joule magnetostriction
- Villari effect
- ΔE effect
- Forced volume magnetostriction including the form effect

3.2.2 Maxwell force

The Maxwell force is acting on boundaries (surfaces) between two magnetic media with different magnetic properties (reluctivity), such as the air gap region. The significant difference of the magnetic permeability between air and the magnetic material causes a considerable Maxwell force. In electrical machines, the Maxwell force exists in the air gap region between the stator and rotor and is considered to be the major cause of acoustic noise [80]. Air gaps also present in inductors, where a large Maxwell force is generated and pull the two core parts embracing the air gap towards each other [87].

Although the air gap is desired to be eliminated in transformers, the use of cut cores due to the construction convenience still introduces very thin air gaps (within 1 mm), where the Maxwell force also presents. Additionally, the laminated structure of magnetic cores contains gaps between layers and at joints in the same layer. It has been shown that there are various mechanisms of the Maxwell force in these gap regions [83].

Mathematically, the total Maxwell force acting on the surface of a deformable body can be calculated by the surface integration of the local force density based on the Maxwell stress tensor:

$$\vec{\mathbf{F}} = \iint (\vec{\mathbf{H}} \cdot (\vec{\mathbf{B}} \cdot \vec{\mathbf{n}}) - \frac{1}{2}(\vec{\mathbf{H}} \cdot \vec{\mathbf{B}}) \cdot \vec{\mathbf{n}}) \, \mathrm{d}S \tag{3.27}$$

where $\vec{\mathbf{F}}$ is the force, $\vec{\mathbf{H}}$ is the magnetic field strength, $\vec{\mathbf{B}}$ is the magnetic flux density and $\vec{\mathbf{n}}$ is the vector in normal direction to the surface S of the deformable body.

3.2.3 Lorentz force

The Lorentz force is acting on current-carrying conductors presented in a magnetic field. Unlike the Maxwell force, the Lorentz force is not only acting on the surface, but also on the inner part of the conductor. Therefore, it is represented as a volume force and the force density is calculated by

$$\vec{\mathbf{f}}_{\mathrm{v}} = \vec{\mathbf{J}} \times \vec{\mathbf{B}} \tag{3.28}$$

where $\vec{\mathbf{J}}$ is the current density in the conductor.

In literatures, the contribution of the Lorentz force to acoustic noise of transformers is usually considered to be less significant than other two sources. However, it is concluded in [86] that the winding is always a source of mechanical stresses, so it cannot be ignored in the mechanical analysis.

3.2.4 Mechanisms of Maxwell force and magnetostriction in laminated core

As mentioned before, transformer cores used for medium frequency applications are different with that used in the low frequency range, not only the material but also the construction. For MFT applications, magnetic cores are usually wound by very thin ribbons (typically 15 µm to 25 µm) made by amorphous or nanocrystalline alloys [120]. The thickness of the ribbon is at least 10 times smaller than silicon steel sheets used for LFTs. On the other hand, manufacturing processes of tape wound cores indicate that there exists no joints withing a single layer, i.e. no air gap in case that the core is not cut. However, due to the convenience for construction, tape wound cores are usually cut in the middle of legs.

Considering a core material with a positive magnetostriction, a part of a rectangular cut core including the air gap is shown in Fig. 3.10, where the laminated structure of thin ribbons is roughly sketched. Based on the analysis in [83], the mechanism of the magnetostriction is illustrated. In the bulk region far from the air gap, the propagation of magnetic flux lines are

parallel to ribbons. The in-plane magnetostriction causes an elongation of the ribbon along the flux line and the ribbon becomes thinner and narrower due to the volume conservation of the Joule magnetostriction. Since the core is approximately a closed loop, the elongation of ribbons leads to an outward expansion of the core. Near the air gap region, stretched ribbons on both sides of the air gap due to the in-plane magnetostriction cause a reduction of air gap length and may lead to a strike of the two parts. On the other hand, the distortion of flux lines due to the fringing field at the air gap leads to an off-plane magnetostriction which induces the local increase of the lamination height as shown in the graph.

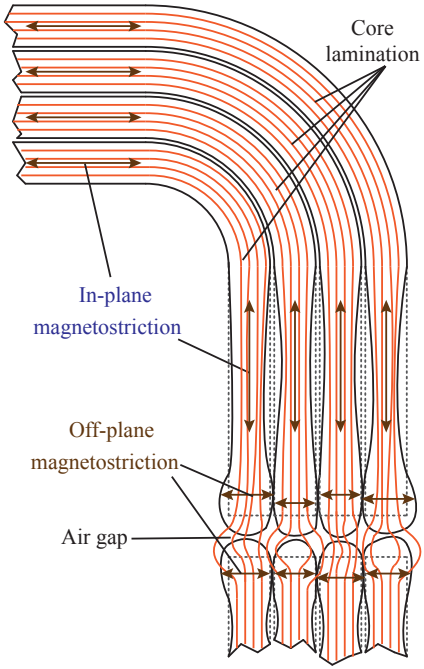

Figure 3.10: Mechanisms of the magnetostriction in tape wound cores.

Besides magnetostriction, following mechanisms of the Maxwell force as shown in Fig. 3.11 can be assumed for tape wound cores:

- Repulsive forces between lamination sheets

- In-plane attractive forces between sheet ends (air gap region)
- Off-plane attractive forces between lamination sheets near the air gap

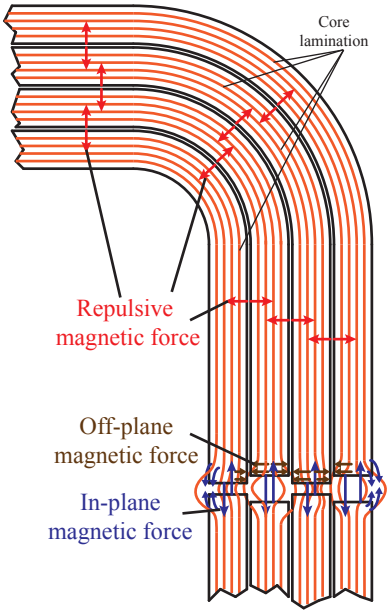

Figure 3.11: Mechanisms of the Maxwell force in tape wound cores.

In the region far from the air gap, repulsive forces between lamination sheets are considered to be negligibly small [83]. Therefore, the major effect of the Maxwell force is in the air gap region, where the in-plane attractive force pull the two core parts towards each other and the off-plane attractive force drag the sheets ends together.

Mechanisms of the Maxwell force and the magnetostriction at ribbon ends are linked and enhanced with each other, which induce excessive vibrations of the core. Therefore, the presence of thin gaps in case of a cut core is considered to have a significant contribution to the acoustic noise emission of transformers which is experimentally verified as presented in [121].

3.3 Fundamentals of vibration and acoustic modeling

The generation of forces in transformers till the perception of acoustic noise by human ears is a multi-physic process which involves electromagnetic, mechanic and acoustic interactions. Accordingly, the vibration and acoustic modeling for transformers includes multiple steps:

- A. electromagnetic field analysis
- B. electromagnetic force and magnetostriction calculation
- C. mechanical modeling
- D. acoustic modeling

In Fig. 3.12, the flow chart of the modeling process is shown and each step is briefly introduced below.

3.3.1 Electromagnetic field analysis

The first step of the modeling is to calculate the electromagnetic field distribution. In general, all electromagnetic problems can be represented by the well-known Maxwell's equations and constitutive equations. By applying appropriate boundary conditions in space and time, the problem can be completely defined. The desired magnetic quantities can then be acquired by solving Maxwell's equations under the given boundary conditions.

In case of transformers, the excitation condition is usually given as a current or a voltage applied on windings. Depending on the type of the problem to be solved, the current/voltage can be defined as an instant value (e.g. the peak value) for the static problem, as time harmonics for the quasi-static problem or as a function of time for the time-dependent problem.

Related electromagnetic properties of the material are also required, i.e. the electrical conductivity γ, the permeability μ and the permittivity ε for winding and core materials and the ambient medium. The permeability is the most important one for solving the magnetic field distribution. Depend-

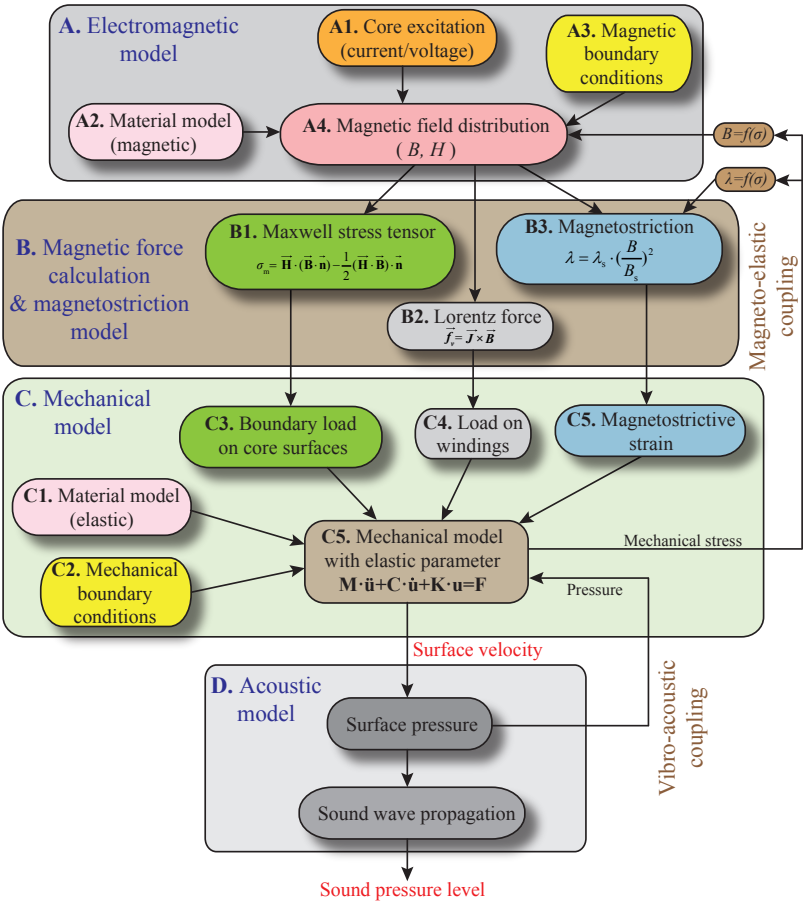

Figure 3.12: Modeling process of the acoustic noise emission of transformers.

ing on the type of the material, it can be represented as a single constant for isotropic materials or as a matrix for anisotropic materials. If the nonlinearity and saturation is considered, the B-H curve should be defined which can be further extended to include the hysteresis.

Based on the definition of excitation conditions and material properties, the electromagnetic problem can be solved by applying appropriate bound-

ary conditions, which results in the distribution of the magnetic field and local quantities of B, H are known.

3.3.2 Magnetic force and magnetostriction calculation

Based on the solved magnetic field distribution in the core, windings and free space from the previous step, the local magnetic force and magnetostriction can be calculated. For the vibration analysis, the local force distribution instead of the global force is required.

Force balance in stationary case [122]

Commonly used methods for electromagnetic force calculation are based on the Maxwell stress tensor or the virtual work principle.

Considering a solid body surrounded by air in the stationary state (no acceleration), the force balance according to Cauchy's equation of continuum mechanics is

$$\nabla \cdot \boldsymbol{T} + \vec{\mathbf{f}}_{\mathbf{ex}} = 0 \tag{3.29}$$

where $\boldsymbol{T}$ is the stress tensor, $\vec{\mathbf{f}}_{\mathbf{ex}}$ is the density of an external volume force (in $[\mathrm{N\,m^{-3}}]$) such as the gravity. The stress tensor is a second-order tensor which can be represented by a 3-by-3 matrix. In a certain case, it can be separated into a mechanical part $\boldsymbol{\sigma}_{\mathbf{M}}$ and an electromagnetic part $\boldsymbol{T}_{\mathbf{EM}}$, i.e.

$$\boldsymbol{T} = \boldsymbol{\sigma}_{\mathbf{M}} + \boldsymbol{T}_{\mathbf{EM}} \tag{3.30}$$

The density of the electromagnetic force is given by the divergence of the electromagnetic stress tensor:

$$\vec{\mathbf{f}}_{\mathbf{EM}} = \nabla \cdot \boldsymbol{T}_{\mathbf{EM}} \tag{3.31}$$

By introducing (3.30) and (3.31) into (3.29), the force balance is represented as

$$-\nabla \cdot \boldsymbol{\sigma}_{\mathbf{M}} = \vec{\mathbf{f}}_{\mathbf{EM}} + \vec{\mathbf{f}}_{\mathbf{ex}} \tag{3.32}$$

On the boundary between the solid and air, the stress tensor must be continuous, i.e.

$$(\boldsymbol{T}_{\mathbf{air}} - \boldsymbol{T}_{\mathbf{solid}}) \cdot \vec{\mathbf{n}} = 0 \tag{3.33}$$

where $\boldsymbol{T}_{\mathbf{solid}}$ and $\boldsymbol{T}_{\mathbf{air}}$ are the stress tensor in the solid and in the air respectively, $\vec{\mathbf{n}}$ is the 3-by-1 normal vector on the boundary pointing outwards the solid surface.

In practice, an external boundary force $\vec{\mathbf{g}}_{\mathbf{ex}}$ also needs to be included in the force balance equation, which is used to compensate the contribution of the stress tensor without enough information. For example, $\vec{\mathbf{g}}_{\mathbf{ex}}$ can represent the reaction force from another body to which the solid is attached. Therefore the continuum of the stress tensor given in (3.33) is modified to

$$(\boldsymbol{T}'_{\mathbf{air}} - \boldsymbol{T}_{\mathbf{solid}}) \cdot \vec{\mathbf{n}} = 0 \tag{3.34}$$

with

$$\boldsymbol{T}'_{\mathbf{air}} = \boldsymbol{T}_{\mathbf{air}} + \vec{\mathbf{g}}_{\mathbf{ex}} \tag{3.35}$$

Accordingly, the force balance equation of the solid is represented as

$$\nabla \cdot \boldsymbol{T}_{\mathbf{solid}} + \vec{\mathbf{f}}_{\mathbf{ex}} = 0 \tag{3.36}$$

and

$$(\boldsymbol{T}_{\mathbf{air}} - \boldsymbol{T}_{\mathbf{solid}}) \cdot \vec{\mathbf{n}} + \vec{\mathbf{g}}_{\mathbf{ex}} = 0 \tag{3.37}$$

To calculate the total force acting on the solid, the force density needs to be integrated over the whole volume of the body and over the whole boundary surface. According to the divergence theorem, the integration of the force density over a volume V can be converted to the integration of the stress tensor over the surrounding surface S:

$$\vec{\mathbf{F}} = \int_V \vec{\mathbf{f}} \, \mathrm{d}V = \int_V \nabla \cdot \boldsymbol{T} \, \mathrm{d}V = \oint_S \boldsymbol{T} \cdot \vec{\mathbf{n}} \, \mathrm{d}S \tag{3.38}$$

By applying this theorem, the volume integration of (3.36) gives

$$\oint_S \boldsymbol{T}_{\mathbf{solid}} \cdot \vec{\mathbf{n}} \, \mathrm{d}S + \int_V \vec{\mathbf{f}}_{\mathbf{ex}} \, \mathrm{d}V = 0 \tag{3.39}$$

On the boundary surface, the integration of (3.37) results in

$$\oint_S (\boldsymbol{T}_{\mathbf{air}} - \boldsymbol{T}_{\mathbf{solid}}) \cdot \vec{\mathbf{n}} \, \mathrm{d}S + \oint_S \vec{\mathbf{g}}_{\mathbf{ex}} \, \mathrm{d}S = 0 \tag{3.40}$$

The sum of (3.39) and (3.40) gives

$$\oint_S \boldsymbol{T}_{\mathbf{air}} \cdot \vec{\mathbf{n}}\, \mathrm{d}S + \int_V \vec{\mathbf{f}}_{\mathbf{ex}}\, \mathrm{d}V + \oint_S \vec{\mathbf{g}}_{\mathbf{ex}}\, \mathrm{d}S = \oint_S \boldsymbol{T}_{\mathbf{air}} \cdot \vec{\mathbf{n}}\, \mathrm{d}S + \vec{\mathbf{F}}_{\mathbf{ex}} = 0 \tag{3.41}$$

This indicates that the total external force $\vec{\mathbf{F}}_{\mathbf{ex}}$ is balanced with the internal force $\vec{\mathbf{F}}_{\mathbf{in}}$, which is calculated by the surface integration of the stress tensor in air over the boundary, i.e.

$$\vec{\mathbf{F}}_{\mathbf{in}} = \oint_S \boldsymbol{T}_{\mathbf{air}} \cdot \vec{\mathbf{n}}\, \mathrm{d}S \tag{3.42}$$

It should be noticed that, the gradient of the air pressure is neglected in this case, which is equivalent to $\nabla \cdot \boldsymbol{T}_{\mathbf{air}} = 0$. To calculate the force, the stress tensor $\boldsymbol{T}_{\mathbf{air}}$ needs to be evaluated.

Electromagnetic stress tensor [122]

Considering a general material which is elastic, dielectric and magnetic. Then the total stress tensor in the material is given by [i]

$$\boldsymbol{T} = \boldsymbol{\sigma}(\vec{\mathbf{E}}, \vec{\mathbf{B}}) - (\frac{1}{2}\vec{\mathbf{D}} \cdot \vec{\mathbf{E}} + \frac{1}{2}\vec{\mathbf{H}} \cdot \vec{\mathbf{B}} - \vec{\mathbf{M}} \cdot \vec{\mathbf{B}})\boldsymbol{I} + (\vec{\mathbf{D}} \otimes \vec{\mathbf{E}} + \vec{\mathbf{H}} \otimes \vec{\mathbf{B}} + \vec{\mathbf{E}} \otimes \vec{\mathbf{P}} - \vec{\mathbf{M}} \otimes \vec{\mathbf{B}}) \tag{3.43}$$

where $\boldsymbol{I}$ is the 3-by-3 identity tensor, $\vec{\mathbf{P}}$, $\vec{\mathbf{M}}$, $\vec{\mathbf{E}}$ and $\vec{\mathbf{B}}$ are 3-by-1 vectors with 3 components in the Cartesian coordinate system representing the polarization, the magnetization, the electrical field strength and the magnetic flux density respectively. Comparing (3.43) with (3.30), the term $\boldsymbol{\sigma}(\vec{\mathbf{E}}, \vec{\mathbf{B}})$ is dependent on $\vec{\mathbf{E}}$ and $\vec{\mathbf{B}}$, which is not a pure mechanical stress tensor and cannot be separated out.

For air, $\vec{\mathbf{P}} = 0$, $\vec{\mathbf{M}} = 0$, the stress tensor can be separated as (3.30) and represented as:

$$\boldsymbol{T}_{\mathbf{air}} = -p\boldsymbol{I} - (\frac{1}{2}\vec{\mathbf{D}} \cdot \vec{\mathbf{E}} + \frac{1}{2}\vec{\mathbf{H}} \cdot \vec{\mathbf{B}})\boldsymbol{I} + (\vec{\mathbf{D}} \otimes \vec{\mathbf{E}} + \vec{\mathbf{H}} \otimes \vec{\mathbf{B}}) \tag{3.44}$$

where p is the air pressure and the mechanical part of the stress tensor is $\boldsymbol{\sigma}_{\mathbf{M}} = -p\boldsymbol{I}$. With the approximation of air by vacuum, $p = 0$, the tensor is known as the Maxwell stress tensor:

$$\boldsymbol{T}_{\mathbf{air}} = -(\frac{1}{2}\vec{\mathbf{D}} \cdot \vec{\mathbf{E}} + \frac{1}{2}\vec{\mathbf{H}} \cdot \vec{\mathbf{B}})\boldsymbol{I} + (\vec{\mathbf{D}} \otimes \vec{\mathbf{E}} + \vec{\mathbf{H}} \otimes \vec{\mathbf{B}}) \tag{3.45}$$

[i] The dyadic product $\otimes$ between two vectors is defined as $\vec{\mathbf{A}} \otimes \vec{\mathbf{B}} = \vec{\mathbf{A}}\vec{\boldsymbol{B}}^{\mathrm{T}}$.

In this case, the stress tensor $\boldsymbol{T}_{\mathbf{air}}$ is purely due to the internal electromagnetic force in the solid. The surface integration of this tensor over the boundary gives the total electromagnetic force in the solid.

Force derivation [117]

In case of the magnetic force for transformer cores, which is considered to be a solid body surrounded by air, the Maxwell stress tensor is reduced to

$$\boldsymbol{T}_{\mathbf{air}} = \vec{\mathbf{H}} \otimes \vec{\mathbf{B}} - \frac{1}{2}(\vec{\mathbf{H}} \cdot \vec{\mathbf{B}})\boldsymbol{I} \tag{3.46}$$

Projecting the tensor to the normal direction of the surface results in

$$\boldsymbol{T}_{\mathbf{air}} \cdot \vec{\mathbf{n}} = (\vec{\mathbf{H}} \otimes \vec{\mathbf{B}}) \cdot \vec{\mathbf{n}} - \frac{1}{2}(\vec{\mathbf{H}} \cdot \vec{\mathbf{B}}) \cdot \vec{\mathbf{n}} \tag{3.47}$$

The integration of this term over the boundary surface gives the total Maxwell force as already shown in (3.27).

For the vibration analysis, the total force is not of interest. Instead, the local force distribution is required as the excitation source applied to the mechanical model. In a general form, the magnetic stress tensor for a nonlinear compressible material is given as:

$$\boldsymbol{T}_{\boldsymbol{m}} = \vec{\mathbf{B}}\vec{\mathbf{H}} - \boldsymbol{I}\int_0^H B \,\mathrm{d}H + \boldsymbol{I}\int_0^H \rho \frac{\partial \mu}{\partial \rho}\bigg|_T H \,\mathrm{d}H \tag{3.48}$$

where ρ is the mass density and the partial derivative $\frac{\partial \mu}{\partial \rho}$ needs to be evaluated at a constant magnetic field H and temperature T.

According to (3.31), the volume force density is given by the divergence of $\boldsymbol{T}_{\boldsymbol{m}}$ as

$$\vec{\mathbf{f}} = \nabla \cdot \boldsymbol{T}_{\boldsymbol{m}} = \nabla \cdot (\vec{\mathbf{B}}\vec{\mathbf{H}}) - \nabla \int_0^H B \,\mathrm{d}H + \nabla \int_0^H \rho \frac{\partial \mu}{\partial \rho}\bigg|_T H \,\mathrm{d}H \tag{3.49}$$

By introducing the vector identity $\nabla \cdot (\vec{\mathbf{B}}\vec{\mathbf{H}}) = \vec{\mathbf{H}}(\nabla \cdot \vec{\mathbf{B}}) + (\vec{\mathbf{B}} \cdot \nabla)\vec{\mathbf{H}}$ and considering Maxwell's equation $\nabla \cdot \vec{\mathbf{B}} = 0$ and the co-linearity assumption of $\vec{\mathbf{B}}$ and $\vec{\mathbf{H}}$, i.e. $(\vec{\mathbf{B}} \cdot \nabla)\vec{\mathbf{H}} = \vec{\mathbf{J}} \times \vec{\mathbf{B}} + B\nabla H$, the expression for the volume force density (3.49) can be simplified to

$$\vec{\mathbf{f}}_{\text{nonlinear,compressible}} = \vec{\mathbf{J}} \times \vec{\mathbf{B}} + B\nabla H - \nabla \int_0^H B \,\mathrm{d}H + \nabla \int_0^H \rho \frac{\partial \mu}{\partial \rho}\bigg|_T H \,\mathrm{d}H \tag{3.50}$$

In case of an incompressible material, the term $\partial\mu/\partial\rho = 0$, for nonlinear case, the tensor becomes:

$$\boldsymbol{T}_{\text{nonlinear,incompressible}} = \vec{\mathbf{B}}\vec{\mathbf{H}} - \mathbf{I}\int_0^H B\,\mathrm{d}H \tag{3.51}$$

Accordingly, the force density becomes:

$$\vec{\mathbf{f}}_{\text{nonlinear,incompressible}} = \vec{\mathbf{J}} \times \vec{\mathbf{B}} + B\nabla H - \nabla\int_0^H B\,\mathrm{d}H \tag{3.52}$$

In the simplest case, i.e. for a linear incompressible material, the tensor is:

$$\boldsymbol{T}_{\text{linear,incompressible}} = \vec{\mathbf{B}}\vec{\mathbf{H}} - \frac{BH}{2}\boldsymbol{I} \tag{3.53}$$

And the force density is:

$$\vec{\mathbf{f}}_{\text{linear,incompressible}} = \vec{\mathbf{J}} \times \vec{\mathbf{B}} - \frac{H^2}{2}\nabla\mu \tag{3.54}$$

The first term in (3.54) represents the Lorentz force and the second term is the reluctance force. If the material is isotropic, then $\nabla\mu = 0$. This implies that reluctance forces are concentrated on the surface of the body and inside the body there is no reluctance force.

Maxwell force calculation

Considering a magnetic core to be current free, i.e. $\vec{\mathbf{J}} = 0$, then there exists only the reluctance force. For an isotopic material, the permeability changes from μ (magnetic material) to μ_0 (air) on the surface boundary. To evaluate $\nabla\mu$, the permeability can be assumed to have a continuous change over an infinitesimal region with a thickness of d and taking the limit for $d \to 0$. This results in the force density of

$$\vec{\mathbf{f}} = \frac{1}{2}\left[\left(\frac{1}{\mu_0} - \frac{1}{\mu}\right)B_n^2 + (\mu - \mu_0)H_t^2\right]\vec{\mathbf{n}} \tag{3.55}$$

where B_n is the normal component of the flux density and H_t is the tangential component of the magnetic field strength regarding the surface. In most cases, $\mu \gg \mu_0$. Therefore, the force density given by (3.55) is positive and points outwards the surface.

Lorentz force calculation

Similar as air, a pure conductor is non-polarizable and non-magnetizable. i.e. $\vec{\mathbf{P}} = 0$, $\vec{\mathbf{M}} = 0$. The electromagnetic force can be obtained by the divergence of the tensor given in (3.45) by taking $\vec{\mathbf{D}} = \epsilon_0 \vec{\mathbf{E}}$ and $\vec{\mathbf{B}} = \mu_0 \vec{\mathbf{H}}$ into account. Then the volume force density is:

$$\vec{\mathbf{f}} = \gamma \vec{\mathbf{E}} + \vec{\mathbf{J}} \times \vec{\mathbf{B}} \tag{3.56}$$

where γ is the volume charge density.

The winding of transformers are usually constructed by copper or aluminum and can be considered as a perfect conductor, i.e. $\vec{\mathbf{E}}$ =0. Therefore, the volume density of Lorentz force in the winding is

$$\vec{\mathbf{f}}_{\text{Lorentz}} = \vec{\mathbf{J}} \times \vec{\mathbf{B}} \tag{3.57}$$

as already given in (3.28). Also, this equation can be deduced from (3.54) when $\nabla \mu = 0$ which is valid since the permeability of the winding material is homogeneous and approximately equal to μ_0.

Electromagnetic energy and virtual work principle

By definition, the electric energy is given as:

$$W_{\text{e}} = \int_V \left(\int_0^D \vec{\mathbf{E}} \cdot \mathrm{d}\vec{\mathbf{D}} \right) \mathrm{d}V = \int_V \left(\int_0^E \vec{\mathbf{D}} \cdot \mathrm{d}\vec{\mathbf{E}} \right) \mathrm{d}V \tag{3.58}$$

And the magnetic energy is:

$$W_{\text{m}} = \int_V \left(\int_0^B \vec{\mathbf{H}} \cdot \mathrm{d}\vec{\mathbf{B}} \right) \mathrm{d}V = \int_V \left(\int_0^H \vec{\mathbf{B}} \cdot \mathrm{d}\vec{\mathbf{H}} \right) \mathrm{d}V \tag{3.59}$$

For a deformable body in the stationary state, the electromagnetic force is evaluated by the variation of the electromagnetic energy due to the deformation according to the virtual work principle. The total electric force F_e and magnetic force F_m are calculated separately as

$$F_{\text{e}} = -\frac{\partial W_{\text{e}}}{\partial \vec{\mathbf{u}}} \tag{3.60}$$

and

$$F_{\text{m}} = -\frac{\partial W_{\text{m}}}{\partial \vec{\mathbf{u}}} \tag{3.61}$$

where $\ddot{\mathbf{u}}$ represents the deformation of the body.

By applying the virtual work principle in the finite element level, the local force density can be calculated. For transformers, this method can be applied to magnetic cores and conductors also in case of nonlinear and deformable materials [123].

Magnetostriction modeling

As mentioned before, the Joule magnetostriction is the most relevant magneto-elastic effects for vibrations of the transformer core. The magnetic flux density solved in the first step is used as the input to calculate the magnetostrictive strain. In the simplest case as for an isotropic material, the magnetostrictive strain λ_p along the direction of the magnetic field can be calculated as given in (3.18) and the transverse magnetostrictive strain λ_t is given by (3.19). To include the hysteresis, the single line magnetostriction curve can be extended to a butterfly curve (see Fig. 3.13), which can be described as [124]

$$\tau_\mathrm{m}\frac{\mathrm{d}\lambda_\mathrm{p}}{\mathrm{d}t}+\lambda_\mathrm{p}=\lambda_\mathrm{s}\cdot(\frac{B}{B_\mathrm{s}})^2 \tag{3.62}$$

where the time constant τ_m determines the width of the loop. With this function, the historical dependency is included by the first-order derivative of λ_p. Similarly, the magnetostrictive strain in the transverse direction is given by

$$\tau_\mathrm{m}\frac{\mathrm{d}\lambda_\mathrm{t}}{\mathrm{d}t}+\lambda_\mathrm{t}=-\frac{1}{2}\lambda_\mathrm{s}\cdot(\frac{B}{B_\mathrm{s}})^2 \tag{3.63}$$

In Fig. 3.13, a typical magnetostriction curve dependent on the flux density under a sinusoidal excitation is shown, where the negative value of the flux density represents the magnetic field in the opposite direction. With consideration of the hysteresis, the magnetostriction curve has a butterfly-shape as described by (3.62). Without considering the hysteresis, the magnetostriction curve is a single line described by (3.18).

For anisotropic materials, the saturation magnetostriction along different crystal easy axes are not identical. For example, the saturation magnetostriction of 3%-Si GO(grain-oriented) steel along the (100)-direction is λ_{100}=23.7 µm/m, while along the (111)-direction is λ_{111}=−4.1 µm/m. The

magnetostriction in the field direction and the transverse direction are then a function of λ_{100}, λ_{111} and the angle between the direction of the magnetization and the easy axes. More details regarding this issue are discussed in [124].

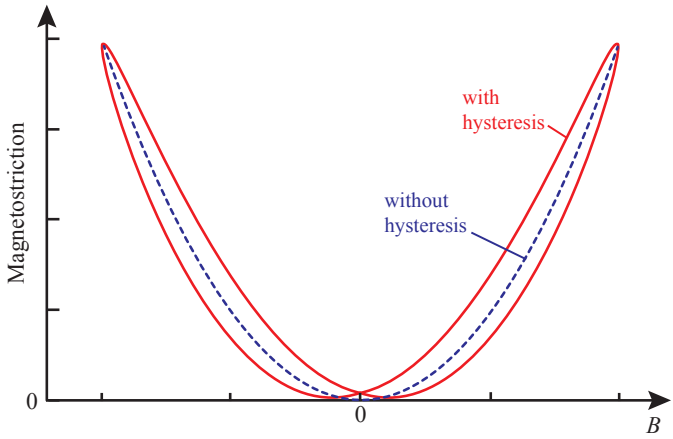

Figure 3.13: Typical magnetostriction curve with and without consideration of hysteresis.

If the influence of the mechanical stress needs to be taken into account, then a series of $\lambda(\vec{\mathbf{B}},\sigma)$ curves can be implemented in the model, which defines the dependency of the magnetostriction on the flux density under various mechanical stresses. As an example, the magnetostriction curve of the isotropic 3% Si-Fe under different tensile stresses are shown in Fig. 3.14. It can be seen that the mechanical stress has significant influences on the magnetostriction.

3.3.3 Modeling of elastic material

Before establishing the mechanical model, it is essential to set up the elastic model of the material, especially for the magnetic core. In physics, elasticity is the tendency of solid materials to return to their original shape after being deformed. Solid objects deform when forces are applied on them. If the material is elastic, the object returns to its initial shape and volume when these forces are removed. In this work, the deformation is considered to be

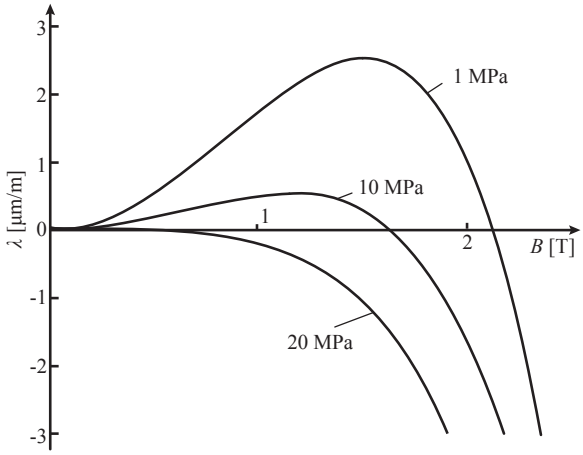

Figure 3.14: Magnetostriction of the isotropic 3% Si-Fe under different tensile stresses [117].

linear elastic.

Linear elasticity in 3D problem [125]

Hook's law For linear elastic material, the relation between the stress $\boldsymbol{\sigma}$ and the strain $\boldsymbol{\epsilon}$ is defined by the Hook's law as

$$\boldsymbol{\sigma} = \boldsymbol{C}\boldsymbol{\epsilon} \tag{3.64}$$

where $\boldsymbol{C}$ is the stiffness tensor, which is a fourth-order tensor with $3^4 = 81$ components. More specifically, (3.64) can be written with index notation as

$$\sigma_{ij} = C_{ijkl}\epsilon_{kl} \tag{3.65}$$

where $i, j, k, l = x, y, z$ denote the 3-dimensional directions in the Cartesian coordinate system.

Consider an infinitesimal cubic element as shown in Fig. 3.15, where each face of this element has 3 stress components: one normal component σ_{ij} $(i = j)$ and two shear components τ_{ij} $(i \neq j)$. Accordingly, there are also 3 strain components on each face: the normal component ϵ_{ij} $(i = j)$ and two shear components γ_{ij} $(i \neq j)$. Both stress and strain tensors can be

expressed as a matrix form with $3 \times 3 = 9$ components, i.e.

$$\boldsymbol{\sigma} = \begin{bmatrix} \sigma_{xx} & \tau_{xy} & \tau_{xz} \\ \tau_{yx} & \sigma_{yy} & \tau_{yz} \\ \tau_{zx} & \tau_{zy} & \sigma_{zz} \end{bmatrix} \quad \text{and} \quad \boldsymbol{\epsilon} = \begin{bmatrix} \epsilon_{xx} & \gamma_{xy} & \gamma_{xz} \\ \gamma_{yx} & \epsilon_{yy} & \gamma_{yz} \\ \gamma_{zx} & \gamma_{zy} & \epsilon_{zz} \end{bmatrix} \tag{3.66}$$

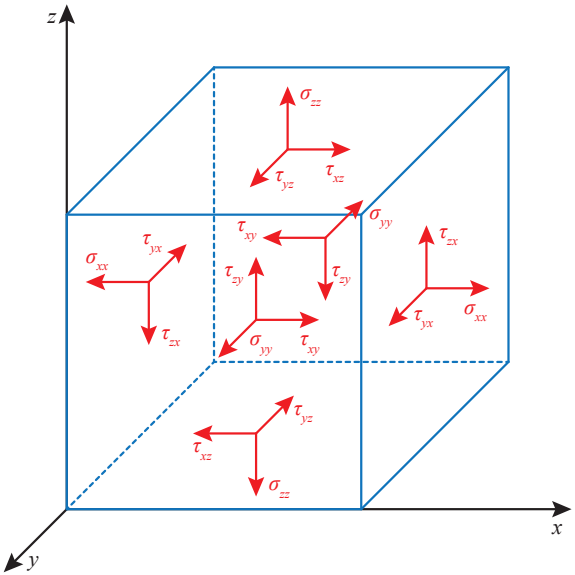

Figure 3.15: Infinitesimal cubic element and stress tensor components.

Since both stress and strain tensors are symmetric, i.e. $\tau_{ij} = \tau_{ji}$ and $\gamma_{ij} = \gamma_{ji}$, there are only 6 independent components in stress and strain tensors. Therefore, they can be represented as[ii]

$$\boldsymbol{\sigma} = \begin{bmatrix} \sigma_x & \sigma_y & \sigma_z & \tau_{xy} & \tau_{yz} & \tau_{xz} \end{bmatrix}^{\mathrm{T}} \tag{3.67}$$

and

$$\boldsymbol{\epsilon} = \begin{bmatrix} \epsilon_x & \epsilon_y & \epsilon_z & \gamma_{xy} & \gamma_{yz} & \gamma_{xz} \end{bmatrix}^{\mathrm{T}} \tag{3.68}$$

[ii] Notice that the order of the last three components in both tensors are not unique defined. In Voigt ordering, they are given as $[\sigma_x, \sigma_y, \sigma_z, \tau_{yz}, \tau_{xz}, \tau_{xy}]^{\mathrm{T}}$ and $[\epsilon_x, \epsilon_y, \epsilon_z, \gamma_{yz}, \gamma_{xz}, \gamma_{xy}]^{\mathrm{T}}$.

In linear continuum mechanics, the displacement of the infinitesimal element at each point of the body due to a deformation can be described by three components in each direction of the Cartesian coordinate system. The displacement field of each point is represented by a vector with three degrees of freedom (DoF) as

$$\mathbf{u} = \begin{bmatrix} u_x & u_y & u_z \end{bmatrix}^{\mathrm{T}} \tag{3.69}$$

Accordingly, the 6 strain components are defined as

$$\begin{cases} \epsilon_x = \dfrac{\partial u_x}{\partial x} \\ \epsilon_y = \dfrac{\partial u_y}{\partial y} \\ \epsilon_z = \dfrac{\partial u_z}{\partial z} \end{cases} \quad \text{and} \quad \begin{cases} \gamma_{xy} = \dfrac{\partial u_x}{\partial y} + \dfrac{\partial u_y}{\partial x} = 2\epsilon_{xy} \\ \gamma_{yz} = \dfrac{\partial u_y}{\partial z} + \dfrac{\partial u_z}{\partial y} = 2\epsilon_{yz} \\ \gamma_{xz} = \dfrac{\partial u_x}{\partial z} + \dfrac{\partial u_z}{\partial x} = 2\epsilon_{xz} \end{cases} \tag{3.70}$$

Notice that the three shear strain components γ_{ij} are referred to "engineering shear strains", which have the following relation with the physical strain:

$$\gamma_{ij} = \epsilon_{ij} + \epsilon_{ji} = 2\epsilon_{ij} \quad (i \neq j) \tag{3.71}$$

Anisotropic material

Physical properties of anisotropic materials are dependent on spacial directions and are generally not identical in different directions. Recall the Hook's law (3.64), the symmetry of stress and strain tensors implies the minor symmetry of the stiffness tensor:

$$C_{ijkl} = C_{jikl} = C_{ijlk} \tag{3.72}$$

This indicates that the stiffness tensor $\boldsymbol{C}$ can only have $6 \times 6 = 36$ independent components, which leads to

$$\begin{bmatrix} \sigma_x \\ \sigma_y \\ \sigma_z \\ \tau_{xy} \\ \tau_{yz} \\ \tau_{xz} \end{bmatrix} = \begin{bmatrix} C_{xxxx} & C_{xxyy} & C_{xxzz} & C_{xxxy} & C_{xxyz} & C_{xxxz} \\ C_{yyxx} & C_{yyyy} & C_{yyzz} & C_{yyxy} & C_{yyyz} & C_{yyxz} \\ C_{zzxx} & C_{zzyy} & C_{zzzz} & C_{zzxy} & C_{zzyz} & C_{zzxz} \\ C_{xyxx} & C_{xyyy} & C_{xyzz} & C_{xyxy} & C_{xyyz} & C_{xyxz} \\ C_{yzxx} & C_{yzyy} & C_{yzzz} & C_{yzxy} & C_{yzyz} & C_{yzxz} \\ C_{xzxx} & C_{xzyy} & C_{xzzz} & C_{xzxy} & C_{xzyz} & C_{xzxz} \end{bmatrix} \begin{bmatrix} \epsilon_x \\ \epsilon_y \\ \epsilon_z \\ \gamma_{xy} \\ \gamma_{yz} \\ \gamma_{xz} \end{bmatrix} \tag{3.73}$$

Moreover, the existence of the strain energy potential requires the stiffness tensor to satisfy the major symmetry condition, i.e.

$$C_{ijkl} = C_{klij} \tag{3.74}$$

This implies that the stiffness tensor has only 21 independent components, then it can be represented as

$$\boldsymbol{C} = \begin{bmatrix} C_{11} & C_{12} & C_{13} & C_{14} & C_{15} & C_{16} \\ C_{12} & C_{22} & C_{23} & C_{24} & C_{25} & C_{26} \\ C_{13} & C_{23} & C_{33} & C_{34} & C_{35} & C_{36} \\ C_{14} & C_{24} & C_{34} & C_{44} & C_{45} & C_{46} \\ C_{15} & C_{25} & C_{35} & C_{45} & C_{55} & C_{56} \\ C_{16} & C_{26} & C_{36} & C_{46} & C_{56} & C_{66} \end{bmatrix} \tag{3.75}$$

In practice, the strain is usually a phenomenon to be observed under an applied stress, it is therefore more convenient to use the inverse form of Hook's law given as

$$\boldsymbol{\epsilon} = \boldsymbol{S}\boldsymbol{\sigma} \tag{3.76}$$

where $\boldsymbol{S} = \boldsymbol{C}^{-1}$ is the compliance matrix. Accordingly, $\boldsymbol{S}$ is also symmetric and has 21 independent components, which are required to describe a completely anisotropic material. In many practical cases, there exist more symmetry in materials which could be used to simplify the stiffness and the compliance tensor. With the increasing level of isotropy, materials can be categorized as below:

- Monotropic material
- Orthotropic material
- Transversely isotropic material
- Isotropic material

Monotropic material This kind of material is symmetric with respect to only one plane, e.g. xy-plane, which means the monotropy is in the direc-

tion of the z-axis. Then the compliance matrix is simplified to

$$\boldsymbol{S} = \begin{bmatrix} S_{11} & S_{12} & S_{13} & S_{14} & 0 & 0 \\ S_{12} & S_{22} & S_{23} & S_{24} & 0 & 0 \\ S_{13} & S_{23} & S_{33} & S_{34} & 0 & 0 \\ S_{14} & S_{24} & S_{34} & S_{44} & 0 & 0 \\ 0 & 0 & 0 & 0 & S_{55} & S_{56} \\ 0 & 0 & 0 & 0 & S_{56} & S_{66} \end{bmatrix} \tag{3.77}$$

As can be seen, the number of non-zero components is reduced to 20 and only 13 components are independent.

Orthotropic material Properties of orthotropic materials are symmetric with respect to two orthogonal planes. Obviously, the symmetry is also satisfied refer to the third plane orthogonal to both planes. This leads to a further reduction of non-zero components in the compliance matrix to 12 and only 9 of them are independent. Then the compliance matrix can be written as

$$\boldsymbol{S}_{\text{orth}} = \begin{bmatrix} S_{11} & S_{12} & S_{13} & 0 & 0 & 0 \\ S_{12} & S_{22} & S_{23} & 0 & 0 & 0 \\ S_{13} & S_{23} & S_{33} & 0 & 0 & 0 \\ 0 & 0 & 0 & S_{44} & 0 & 0 \\ 0 & 0 & 0 & 0 & S_{55} & 0 \\ 0 & 0 & 0 & 0 & 0 & S_{66} \end{bmatrix} \tag{3.78}$$

By replacing these components with physical quantities, the compliance matrix for orthotropic materials is given as

$$\boldsymbol{S}_{\text{orth}} = \begin{bmatrix} \frac{1}{E_x} & -\frac{\nu_{yx}}{E_y} & -\frac{\nu_{zx}}{E_z} & 0 & 0 & 0 \\ -\frac{\nu_{xy}}{E_x} & \frac{1}{E_y} & -\frac{\nu_{zy}}{E_z} & 0 & 0 & 0 \\ -\frac{\nu_{xz}}{E_x} & -\frac{\nu_{yz}}{E_y} & \frac{1}{E_z} & 0 & 0 & 0 \\ 0 & 0 & 0 & \frac{1}{G_{xy}} & 0 & 0 \\ 0 & 0 & 0 & 0 & \frac{1}{G_{yz}} & 0 \\ 0 & 0 & 0 & 0 & 0 & \frac{1}{G_{xz}} \end{bmatrix} \tag{3.79}$$

where E_i $(i = x, y, z)$ is the Young's modulus along corresponding axis, ν_{ij} $(i \neq j;\ i, j = x, y, z)$ is the Poisson's ratio determined by the contraction $-\epsilon_j$

in the j-direction and the elongation ϵ_i in the orthogonal i-direction when a normal stress is applied in the i-direction:

$$\nu_{ij} = -\frac{\epsilon_j}{\epsilon_i} \tag{3.80}$$

And the shear stress in the ij-plane G_{ij} is defined as the ratio of the shear stress to the shear strain.

According to the symmetry of the compliance matrix, it is obvious that

$$\frac{\nu_{xy}}{E_x} = \frac{\nu_{yx}}{E_y}, \quad \frac{\nu_{xz}}{E_x} = \frac{\nu_{zx}}{E_z}, \quad \frac{\nu_{yz}}{E_y} = \frac{\nu_{zy}}{E_z} \tag{3.81}$$

Therefore, to completely describe elastic properties of orthotropic materials, 9 parameters are required: three Young's moduli E_x, E_y, E_z, three shear moduli G_{xy}, G_{yz}, G_{zx} and three Poisson's ratios ν_{xy}, ν_{yz}, ν_{xz}.

Although the stiffness tensor has the same structure as the compliance matrix, analytical expressions of its components are more complicated. For orthotropic materials, the stiffness matrix is represented as

$$\boldsymbol{C}_{\text{orth}} = \boldsymbol{S}_{\text{orth}}^{-1} = \begin{bmatrix} C_{11} & C_{12} & C_{13} & 0 & 0 & 0 \\ C_{12} & C_{22} & C_{23} & 0 & 0 & 0 \\ C_{13} & C_{23} & C_{33} & 0 & 0 & 0 \\ 0 & 0 & 0 & C_{44} & 0 & 0 \\ 0 & 0 & 0 & 0 & C_{55} & 0 \\ 0 & 0 & 0 & 0 & 0 & C_{66} \end{bmatrix} \tag{3.82}$$

with the non-zero components given as

$$\begin{aligned} &C_{11} = \frac{(1-\nu_{yz}\nu_{zy})E_x}{\Delta}, \quad C_{12} = \frac{(\nu_{xy}+\nu_{xz}\nu_{zy})E_y}{\Delta}, \\ &C_{22} = \frac{(1-\nu_{xz}\nu_{zx})E_y}{\Delta}, \quad C_{23} = \frac{(\nu_{yz}+\nu_{yx}\nu_{xz})E_z}{\Delta}, \\ &C_{33} = \frac{(1-\nu_{xy}\nu_{yx})E_z}{\Delta}, \quad C_{13} = \frac{(\nu_{xz}+\nu_{xy}\nu_{yz})E_z}{\Delta}, \\ &C_{44} = G_{xy}, \quad C_{55} = G_{yz}, \quad C_{66} = G_{xz}, \\ &\text{with} \quad \Delta = 1-\nu_{xy}\nu_{yx}-\nu_{yz}\nu_{zy}-\nu_{xz}\nu_{zx}-2\nu_{xy}\nu_{yz}\nu_{zx} \end{aligned} \tag{3.83}$$

Transversely isotropic material A transversely isotropic material has physical properties which are symmetric around one axis. In the plane normal

to this axis, the material is completely isotropic. Considering the symmetry is with respect to the z-axis (isotropy in the xy-plane), then one can conclude that the components of compliance matrix given in (3.78) fulfill the following equalities:

$$S_{11} = S_{22}, \quad S_{13} = S_{23}, \quad S_{55} = S_{66}, \quad S_{44} = 2(S_{11} - S_{12}) \tag{3.84}$$

In this case, the number of independent components in $\boldsymbol{S}$ is further reduced to five. Considering the equalities given in (3.81) and (3.84), the compliance matrix (3.79) is further simplified as

$$\boldsymbol{S}_{\text{tran}} = \begin{bmatrix} \frac{1}{E_x} & -\frac{\nu_{xy}}{E_x} & -\frac{\nu_{xz}}{E_x} & 0 & 0 & 0 \\ -\frac{\nu_{xy}}{E_x} & \frac{1}{E_x} & -\frac{\nu_{xz}}{E_x} & 0 & 0 & 0 \\ -\frac{\nu_{xz}}{E_x} & -\frac{\nu_{xz}}{E_x} & \frac{1}{E_z} & 0 & 0 & 0 \\ 0 & 0 & 0 & \frac{2(1+\nu_{xy})}{E_x} & 0 & 0 \\ 0 & 0 & 0 & 0 & \frac{1}{G_{xz}} & 0 \\ 0 & 0 & 0 & 0 & 0 & \frac{1}{G_{xz}} \end{bmatrix} \tag{3.85}$$

Therefore, only 5 elastic parameters are necessary to define the compliance matrix: two Young's moduli E_x, E_z, two Poisson's ratios ν_{xy}, ν_{xz} and one shear modulus G_{xz}.

Isotropic material The isotropic material is the simplest case, in which the material is completely symmetric with respect to all planes and axes. Physical properties are identical in all directions and there are only two independent elastic parameters: the Young's modulus E and the Poisson's ratio ν. The compliance matrix is then simplified as

$$\boldsymbol{S}_{\text{iso}} = \begin{bmatrix} \frac{1}{E} & -\frac{\nu}{E} & -\frac{\nu}{E} & 0 & 0 & 0 \\ -\frac{\nu}{E} & \frac{1}{E} & -\frac{\nu}{E} & 0 & 0 & 0 \\ -\frac{\nu}{E} & -\frac{\nu}{E} & \frac{1}{E} & 0 & 0 & 0 \\ 0 & 0 & 0 & \frac{1}{G} & 0 & 0 \\ 0 & 0 & 0 & 0 & \frac{1}{G} & 0 \\ 0 & 0 & 0 & 0 & 0 & \frac{1}{G} \end{bmatrix} \tag{3.86}$$

where the shear modulus G is given by

$$G = \frac{E}{2(1+\nu)} \tag{3.87}$$

Elastic model of laminated material

In medium frequency high power applications, tape wound cores are widely used for transformers. In order to reduce eddy current losses, these cores are composed of thousands of thin laminae (typical thickness 15 µm to 25 µm), which are made of amorphous or nanocrystalline alloys. Between magnetic layers, epoxy resin are filled to provide the electrical isolation. In Fig. 3.16, a tape wound core with the rectangular shape is shown on the left side and a part of the core is enlarged and illustrated on the right side.

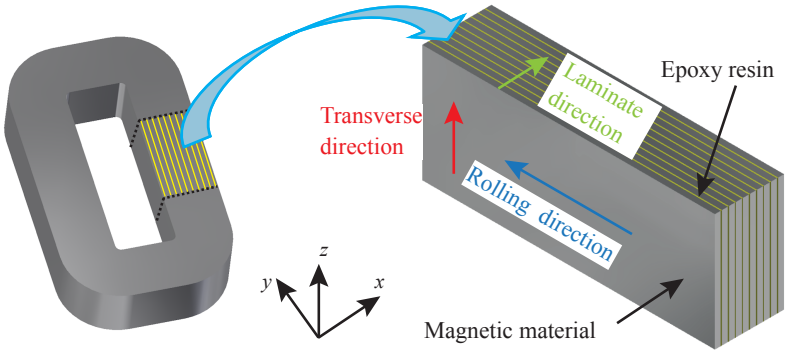

Figure 3.16: Laminated structure of the tape wound core.

If the detailed laminated structure of the tape wound core is to be modeled, e.g. by the FEM, the effort for building up the model and computation would be impractical. Instead, simplified models with certain assumptions have to be employed. Depending on the complexity, the following simplified models can be used:

- Isotropic model
- Anisotropic model
  - Orthotropic model
  - Transversely isotropic model

Isotropic model The simplest way is to ignore the laminated structure and consider the laminae as an isotropic material. In this case, only two elastic

parameters are necessary, i.e., the Young's modulus E and the Poisson's ratio ν, which can be determined either by using parameters of the magnetic material or by fitting the result obtained from numerical simulations with the result obtained by experimental measurements. However, properties of the laminated cores are related to both the magnetic material and the epoxy resin, therefore, the first approach usually leads to models with a low accuracy. On the other hand, the second approach may give an accurate model for specific samples, but the transferability of the result to other samples may be limited [82].

Anisotropic model More accurate models of laminated structure require the anisotropy of materials to be considered. As a composite of the magnetic material and the epoxy resin, the material response of a laminated core is determined by properties of both constituents. As introduced previously, the complete description of an anisotropic material requires 21 independent elastic parameters, which needs to be determined by experimental measurements. However, in engineering applications, the laminated structure can be approximated as an orthotropic or a transversely isotropic material.

Elastic parameters of the material can be determined experimentally by following methods [82]:

- Static stress/strain test – applying a force on the sample and measuring the deformation
- Ultrasonic measurements – using an ultrasonic transmitter to generate a pulse of longitudinal wave which travels through the sample and measuring the response with an ultrasonic receiver
- Frequency response measurement and fitting with the numerical model – applying a force on the sample and measuring its vibration to determine the resonant frequency and then use the modal analysis to establish a numerical model, equivalent material parameters are evaluated by the inverse problem.

Alternatively, equivalent elastic parameters can be deduced analytically according to elementary mixture rules as presented in [125] for fiber-reinforced laminae. In this case, the laminated structure can be considered as transversely isotropic, where following assumptions are made:

- The bond between the magnetic material and the epoxy resin is perfect.
- The ribbon thickness of the magnetic material and the space between lamination layers are uniform.
- Both the magnetic material and the epoxy resin are considered to be isotropic and follow laws of linear elasticity.
- There exists no void in the structure.

Assume that the magnetic material has a mass density of ρ_m, the Young's modulus and Poisson's ratio are E_m and ν_m respectively. Accordingly, same physical constants of the epoxy resin are represented by ρ_f, E_f and ν_f. The lamination factor l_F denotes the ratio between the cross-sectional area of the magnetic material A_{Fe} and the geometrical cross sectional area A_{geo}, i.e. $l_F = A_{Fe}/A_{geo}$, which is equivalent to the volume fraction of the magnetic material. According to these assumptions listed above, l_F is equivalent to the volume fraction of the magnetic material in the total volume. Then the equivalent mass density ρ_{eq} of the laminated structure is calculated as

$$\rho_{eq} = \rho_m l_F + \rho_f(1 - l_F) \tag{3.88}$$

Elastic properties in the rolling direction and the transverse direction are considered to be identical which differ from properties in the laminate direction as indicated in Fig. 3.16. Equivalent elastic parameters are deduced as following [125]:

The Young's modulus E_p in the plane parallel to lamination layers (the rolling direction and the transverse direction):

$$E_p = E_m l_F + E_f(1 - l_F) \tag{3.89}$$

The Young's modulus E_q in the direction perpendicular to lamination layers (laminate direction):

$$E_q = \frac{E_m E_f}{E_m(1 - l_F) + E_f l_F} \tag{3.90}$$

The Poisson's ratio ν_p with the stress in the rolling direction:

$$\nu_p = \nu_m l_F + \nu_f(1 - l_F) \tag{3.91}$$

The Poisson's ratio ν_q with the stress in directions perpendicular to the rolling direction (laminate direction or transverse direction):

$$\nu_q = \nu_p \frac{E_q}{E_p} \tag{3.92}$$

The shear modulus in planes perpendicular to lamination layers (laminate direction or transverse direction):

$$G_q = \frac{G_m G_f}{G_m(1-l_F) + G_f l_F} \tag{3.93}$$

where

$$G_m = \frac{E_m}{2(1+\nu_m)}, \quad G_f = \frac{E_f}{2(1+\nu_f)} \tag{3.94}$$

as given in (3.87) for isotropic materials.

2D analysis

In many engineering applications, 3D problems can be approximated by 2D problems under certain assumptions or simplifications. In linear elastic, two cases of 2D approximations are widely utilized, i.e. the plane stress and the plane strain.

Plane stress If the dimension of the analyzed material in one direction is relatively small compared with other two directions, then the stress in this direction can be neglected. This is usually the case of thin plates and the stress analysis can be performed in the 2D plane with larger dimensions. Consider the z-axis as the direction with a small dimension, the plane stress condition can be expressed as

$$\sigma_z = 0,\ \tau_{ij} = 0 \quad \text{for} \quad i = z \ \text{ or } \ j = z \tag{3.95}$$

Accordingly, the matrix form of Hook's law can be reduced to 3 equations by eliminating rows and corresponding columns with a zero stress:

$$\begin{bmatrix} \sigma_x \\ \sigma_y \\ \tau_{xy} \end{bmatrix} = \begin{bmatrix} C_{11} & C_{12} & C_{14} \\ C_{12} & C_{22} & C_{24} \\ C_{14} & C_{24} & C_{44} \end{bmatrix} \begin{bmatrix} \epsilon_x \\ \epsilon_y \\ \gamma_{xy} \end{bmatrix} \tag{3.96}$$

Note that the strain in the z-direction is not zero and an additional equation needs to be added:

$$\sigma_z = 0 = C_{13}\epsilon_x + C_{23}\epsilon_y + C_{33}\epsilon_z + C_{34}\gamma_{xy} \tag{3.97}$$

Then the out-of-plane strain can be calculated as

$$\epsilon_z = -\frac{1}{C_{33}}(C_{13}\epsilon_x + C_{23}\epsilon_y + C_{34}\gamma_{xy}) \tag{3.98}$$

Similarly, the inverse form of hook's law for plane stress conditions can be written as

$$\begin{bmatrix} \epsilon_x \\ \epsilon_y \\ \gamma_{xy} \end{bmatrix} \begin{bmatrix} S_{11} & S_{12} & S_{14} \\ S_{12} & S_{22} & S_{24} \\ S_{14} & S_{24} & S_{44} \end{bmatrix} = \begin{bmatrix} \sigma_x \\ \sigma_y \\ \tau_{xy} \end{bmatrix} \tag{3.99}$$

For orthotropic materials, $S_{14} = S_{24} = 0$. Components in the compliance matrix are exactly the same as given in (3.79), which results in

$$\boldsymbol{S}_{\text{orth,plane-stress}} = \begin{bmatrix} \frac{1}{E_x} & -\frac{\nu_{yx}}{E_y} & 0 \\ -\frac{\nu_{xy}}{E_x} & \frac{1}{E_y} & 0 \\ 0 & 0 & \frac{1}{G_{xy}} \end{bmatrix} \tag{3.100}$$

As can be seen that there are only 4 independent parameters in the compliance matrix. The stiffness tensor is then the inverse matrix of $\boldsymbol{S}$ given as

$$\boldsymbol{C}_{\text{orth,plane-stress}} = \boldsymbol{S}^{-1}_{\text{orth,plane-stress}} = \begin{bmatrix} \frac{E_x}{1-\nu_{xy}\nu_{yx}} & \frac{\nu_{yx}E_x}{1-\nu_{xy}\nu_{yx}} & 0 \\ \frac{\nu_{xy}E_y}{1-\nu_{xy}\nu_{yx}} & \frac{E_y}{1-\nu_{xy}\nu_{yx}} & 0 \\ 0 & 0 & G_{xy} \end{bmatrix} \tag{3.101}$$

Notice that components of the stiffness tensor are not the same as given in (3.83) for the 3D case. For isotropic materials, $\boldsymbol{S}$ and $\boldsymbol{C}$ are simplified as

$$\boldsymbol{S}_{\text{iso,plane-stress}} = \begin{bmatrix} \frac{1}{E} & -\frac{\nu}{E} & 0 \\ -\frac{\nu}{E} & \frac{1}{E} & 0 \\ 0 & 0 & \frac{1}{G} \end{bmatrix} \tag{3.102}$$

and

$$\boldsymbol{C}_{\text{iso,plane-stress}} = \begin{bmatrix} \frac{E}{1-\nu^2} & \frac{\nu E}{1-\nu^2} & 0 \\ \frac{\nu E}{1-\nu^2} & \frac{E}{1-\nu^2} & 0 \\ 0 & 0 & G \end{bmatrix} \tag{3.103}$$

Plane strain Plane strain is the case that the dimension of the material in one direction is relatively large in comparison with other two directions and the strain in this direction is neglected. Again, assume that the strain in the z-direction is negligible, then the plane strain condition is

$$\epsilon_z = 0,\ \gamma_{ij} = 0 \quad \text{for} \quad i = z \ \text{ or } \ j = z \tag{3.104}$$

Then Hook's law and its inverse form with the reduced matrix form is the same as given in (3.96) and (3.99) for plane stress problems. Similarly, an additional equation is added to deduce the stress in the z-direction:

$$\epsilon_z = 0 = S_{13}\sigma_x + S_{23}\sigma_y + S_{33}\sigma_z + S_{34}\tau_{xy} \tag{3.105}$$

which leads to

$$\sigma_z = -\frac{1}{S_{33}}(S_{13}\sigma_x + S_{23}\sigma_y + S_{34}\tau_{xy}) \tag{3.106}$$

For plane strain problems, components in $\boldsymbol{C}$ are the same as in the 3D case, while components in $\boldsymbol{S}$ are different and $\boldsymbol{S}$ needs to be calculated by $\boldsymbol{C}^{-1}$. Since the plane strain is not the case to be considered in this work, further discussion is omitted.

3.3.4 Structural dynamic modeling

In this step, the magnetic force and the magnetostrictive strain are used as excitation sources applied on the mechanical model.

Equation of motion

In the dynamic case, the mechanical system with multiple DoF is described by the equation of motion as

$$\mathbf{M}\cdot\ddot{\mathbf{u}} + \mathbf{C}\cdot\dot{\mathbf{u}} + \mathbf{K}\cdot\mathbf{u} = \mathbf{f} \tag{3.107}$$

where $\mathbf{M}$ is the mass matrix, $\mathbf{C}$ is the damping matrix, $\mathbf{K}$ is the stiffness matrix, $\mathbf{f}$ is the force vector and $\mathbf{u}$ is the displacement vector. The first and second order derivatives of $\mathbf{u}$ with respect to time, i.e. $\ddot{\mathbf{u}} = \frac{\partial^2\mathbf{u}}{\partial t^2}$ and $\dot{\mathbf{u}} = \frac{\partial\mathbf{u}}{\partial t}$, are the acceleration vector and the velocity vector expressed in matrix form, respectively.

The damping matrix $\mathbf{C}$ can be approximated by the Rayleigh damping model, i.e. a linear combination of the mass matrix and the stiffness matrix:

$$\mathbf{C} = \alpha_\mathrm{d}\mathbf{M} + \beta_\mathrm{d}\mathbf{K} \tag{3.108}$$

where α_d and β_d are linear damping coefficients which can be determined by an analytical approximation or, more precisely, by experimental measurements.

If all forces and displacements are at the same frequency f_s, the dynamic problem can be simplified to the time-harmonic problem. The displacement $\mathbf{u}$ and the force $\mathbf{f}$ can be expressed in the phasor form as

$$\mathbf{u} = \underline{\mathbf{u}} e^{j\omega_\mathrm{s} t} \tag{3.109}$$

$$\mathbf{f} = \underline{\mathbf{f}} e^{j\omega_\mathrm{s} t} \tag{3.110}$$

where $\omega_\mathrm{s} = 2\pi f_\mathrm{s}$ is the angular frequency. Then the problem given in (3.107) can be written as

$$\left(-\omega_\mathrm{s}^2\mathbf{M} + j\omega_\mathrm{s}\mathbf{C} + \mathbf{K}\right)\cdot\underline{\mathbf{u}} = \underline{\mathbf{f}} \tag{3.111}$$

The phasor given in (3.110) can be separated to a real and an imaginary component as

$$\mathbf{u} = \underline{\mathbf{u}}_\mathrm{r} + j\underline{\mathbf{u}}_\mathrm{i} \tag{3.112}$$

$$\mathbf{f} = \underline{\mathbf{f}}_\mathrm{r} + j\underline{\mathbf{f}}_\mathrm{i} \tag{3.113}$$

Accordingly, (3.111) can be separated as

$$\begin{cases} \left(-\omega_\mathrm{s}^2\mathbf{M} + \mathbf{K}\right)\underline{\mathbf{u}}_\mathrm{r} - \omega_\mathrm{s}\mathbf{C}\underline{\mathbf{u}}_\mathrm{i} = \underline{\mathbf{f}}_\mathrm{r} \\ \omega_\mathrm{s}\mathbf{C}\underline{\mathbf{u}}_\mathrm{r} + \left(-\omega_\mathrm{s}^2\mathbf{M} + \mathbf{K}\right)\underline{\mathbf{u}}_\mathrm{i} = \underline{\mathbf{f}}_\mathrm{i} \end{cases} \tag{3.114}$$

In case of the undamped free motion, i.e. $\mathbf{C} = 0$, $\mathbf{f} = 0$, (3.107) is simplified to

$$\mathbf{M}\cdot\ddot{\mathbf{u}} + \mathbf{K}\cdot\mathbf{u} = 0 \tag{3.115}$$

This equation can be used to find natural frequencies (eigenfrequencies) of the mechanical system. By substituting $\mathbf{u} = \underline{\mathbf{u}} e^{j\omega_\mathrm{s} t}$ into (3.115), the problem is reduced to the generalized eigenvalue problem as

$$\left(\mathbf{K} - \omega_\mathrm{s}^2\mathbf{M}\right)\underline{\mathbf{u}} = 0 \tag{3.116}$$

By solving the eigenvalue problem, natural frequencies f_i are obtained as $f_\mathrm{i} = \omega_\mathrm{i}/2\pi$ from eigenvalues $\lambda_\mathrm{i} = \omega_\mathrm{i}^2$. Accordingly, solutions of $\underline{\mathbf{u}}$ give mode shapes of the system.

In the static case, effects of mass and damping are neglected, then (3.107) is simplified to

$$\mathbf{K} \cdot \mathbf{u} = \mathbf{f} \tag{3.117}$$

This equation is used to find the nodal displacement of the system under a static load.

Deformable body in linear continuum mechanics

For a deformable body in linear continuum mechanics, the governing law is given by the Navier's equation as

$$\rho \frac{\partial^2 \mathbf{u}}{\partial t^2} = \nabla \cdot \boldsymbol{\sigma} + \mathbf{f}_\mathrm{v} \tag{3.118}$$

where ρ is the mass density of the material, $\mathbf{f}_\mathrm{v}$ is the volume force applied on the solid body.

Similar as (3.111), for the frequency domain problem, equation (3.118) is modified to

$$-\rho\omega_\mathrm{s}^2 \mathbf{u} = \nabla \cdot \boldsymbol{\sigma} + \underline{\mathbf{f}}_\mathrm{v} e^{j\omega_\mathrm{s} t} \tag{3.119}$$

In the stationary case, the acceleration $\frac{\partial^2 \mathbf{u}}{\partial t^2} = 0$, (3.118) is simplified as

$$\nabla \cdot \boldsymbol{\sigma} = -\mathbf{f}_\mathrm{v} \tag{3.120}$$

Note that the stress tensor $\boldsymbol{\sigma}$ is related to the displacement according to (3.70).

In the mechanical model, the Maxwell stress tensor is applied as a boundary load to the surface of the magnetic core and the Lorentz force is applied as a body load to the winding. The calculated local magnetostrictive stain is added to the element strain $\boldsymbol{\epsilon}$, which is also a vector derived from the elementary displacement. With these input quantities and elastic models of materials, (3.107) is solved numerically under given boundary conditions to obtain surface velocities of the structure, which are used as input quantities

for the acoustic model. The solution of the mechanical model in the static case gives the displacement **u**, which only shows the static deformation of a mechanical body and is not sufficient for further application in the acoustic model.

3.3.5 Acoustic analysis

As the last step, the acoustic analysis needs to be performed to evaluate the sound pressure. The propagation of acoustic waves in a lossless medium (no viscosity and no thermal conduction) is governed by

$$\frac{1}{\rho c^2}\frac{\partial^2 p_\mathrm{t}}{\partial t^2} + \nabla \cdot \left[-\frac{1}{\rho}(\nabla p_\mathrm{t} - q_\mathrm{d}) \right] = Q_\mathrm{m} \tag{3.121}$$

where p_t is the total pressure, which is the sum of the sound pressure p and the background pressure p_b. ρ is the density of the medium, c is the speed of sound, q_d represents the dipole source and Q_m represents the monopole source. With the absence of the two source terms and by assuming a constant density of the fluid in space, (3.121) is reduced to the standard wave equation:

$$\nabla^2 p_\mathrm{t} - \frac{1}{c^2}\frac{\partial^2 p_\mathrm{t}}{\partial t^2} = 0 \tag{3.122}$$

In the time-harmonic case, the time dependency of the pressure can be expressed as $p_\mathrm{t}(t) = p_\mathrm{t} e^{j\omega_\mathrm{s} t}$ and the wave equation (3.121) is reduced to the inhomogeneous Helmholtz equation:

$$\nabla \cdot \left[-\frac{1}{\rho}(\nabla p_\mathrm{t} - q_\mathrm{d}) \right] - \frac{\omega_\mathrm{s}^2 p_\mathrm{t}}{\rho c^2} = Q_\mathrm{m} \tag{3.123}$$

By removing the two source terms in the equation above, it can be used to solve for eigenmodes and eigenfrequencies.

In the acoustic model, the normal surface velocity or the acceleration solved in the mechanical model is applied to the boundary of the solid-fluid interface as the excitation source:

$$-\vec{\mathbf{n}} \cdot \left[-\frac{1}{\rho}(\nabla p_\mathrm{t} - q_\mathrm{d}) \right] = \vec{\mathbf{a}}_\mathrm{n} = \frac{\partial \vec{\mathbf{v}}_\mathrm{n}}{\partial t} \tag{3.124}$$

where $\vec{\mathbf{n}}$ is the outwards-pointing normal vector seen from the inside of the fluid, $\vec{\mathbf{a}}_\mathrm{n}$ and $\vec{\mathbf{v}}_\mathrm{n}$ are the normal acceleration and the surface velocity of the

solid respectively. By neglecting the source term q_d, (3.124) is simplified to

$$-\vec{\mathbf{n}} \cdot \left[-\frac{1}{\rho} (\nabla p_t) \right] = \vec{\mathbf{a}}_n = \frac{\partial \vec{\mathbf{v}}_n}{\partial t} \tag{3.125}$$

To solve the wave equation, additional conditions also need to be applied to model the acoustic boundary. To avoid the influence due to the reflection of sound waves, the matched boundary condition or the radiation boundary condition can be implemented.

After solving the wave equation (3.122) with the excitation condition (3.125) and the boundary condition, the spacial distribution of the pressure field p_t at a given time instance is known.

3.3.6 Coupling of models

As explained in previous sections, the acoustic noise emission of transformers involves three physical models. The influence of one model on another model is not unidirectional, there also exist backwards effects. Furthermore, material properties in two models may also be interdependent. As shown in Fig. 3.12, there are two couplings of fields:

- The magneto-elastic coupling
- The vibro-acoustic coupling

The electromagnetic force and the magnetostriction generated due to the electrical excitation are applied on the mechanical structure and generate the mechanical stress. Due to the stress-dependency of the magnetization and the magnetostriction, the mechanical model has a backwards influence on the electromagnetic model. Also, material properties of the magnetic core are interdependent on field quantities of the mechanical model, e.g. the permeability and the elastic modulus.

On the solid-fluid boundary, the vibration of the solid body induces the change of the pressure field of the fluid. On the other hand, the fluid pressure also adds a mechanical load on the surface of the solid body.

For a more accurate modeling, these interactions between models and the interdependency of material properties also need to be taken into ac-

count, which requires the model coupling. In general, the coupling of models can be categorized as [80]:

- Indirect coupling
  - Weak coupling
  - Strong coupling
- Direct coupling

The weak coupling is the most simple case where the effect of one model on another model is unidirectional, i.e. the backwards effect is not considered. Furthermore, the interdependency of material properties is also ignored.

By the strong coupling, the interaction between models is taken into account. This method is implemented based on an iterative calculation. For example, in the case of the magneto-elastic coupling, electromagnetic quantities are solved and applied to the mechanical model. Solved quantities of the mechanical model are used to update input quantities of the electromagnetic model. Two models are solved iteratively until reaching the convergence. On the other hand, the dependency of elastic properties of the material on the magnetic field is neglected.

In case of the direct coupling, both interactions between coupled models and the interdependency of material properties are considered. In order to achieve this, either constitutive equations for each model are coupled to variables of another model or field equations are coupled [126].

Normally, with a more complex coupling method, the accuracy of the model is higher. However, more computational effort is also needed which generally requires more calculation time.

3.4 Summary

In this chapter, basic terms of acoustics are briefly reviewed including the distribution of sound fields and the quantification of the sound.

Sources of the acoustic noise emission of transformers are investigated

with emphasis on electromagnetic origins in case of the medium frequency transformer. Based on a literature survey, major sources of the transformer acoustic noise are the magnetostriction of the core, the Maxwell force acting on the core and the Lorentz force acting on the winding. These effects cause vibrations of the transformer structure and generate acoustic noises.

The magnetostriction is a complicated phenomenon which includes several direct and inverse effects. Fundamentals of these effects are briefly introduced with focus on most relevant effects, i.e. the Joule magnetostriction and the Villari effect. The Joule magnetostriction is usually considered to be the major cause of the transformer core vibration. The Maxwell force mainly acts on the core surface and between lamination layers, which is considered to be small compared with the magnetostriction effect. The Lorentz force acts on current-conducting windings and is also considered to have a minor contribution to the acoustic noise generation of transformers.

In medium frequency applications, tape wound cores are usually utilized with a large number of laminated thin layers of magnetic materials. Mechanisms of the magnetostriction and the Maxwell force in laminated cores are analyzed. It has been shown that the Maxwell force also acts inside the core between lamination layers. However, in case that no air gap exists, the Maxwell force is relatively small. Due to the presence of air gaps in case of a cut core, there exist a large Maxwell force which pulls two separated core parts towards each other. Effects of the Maxwell force and the magnetostriction are enhanced with each other at the air gap region and may cause the strike of two core parts, which is considered to have a significant contribution to the core vibration.

Furthermore, the modeling process of acoustic noise emission of transformer is introduced, which involves three coupled models: the electromagnetic model, the mechanical model and the acoustic model. Magnetic and elastic models of core materials are also essential parts of the modeling process. For each model, the basic theory and mathematical formulas for the calculation are explained. Coupling methods of these models are also briefly introduced. Basically, a model with a higher accuracy requires more complex couplings and more computational efforts.

4 Modeling of Core Vibration

In chapter 3, the modeling of acoustic noise emission for transformers is introduced, which basically involves following steps:

- Calculation of the magnetic field distribution according to the electrical excitations
- Calculation of the electromagnetic force and magnetostriction according to the magnetic field distribution
- Calculation of the structural vibration/deformation of magnetic cores and windings induced by the magnetic force and the magnetostriction
- Calculation of the sound pressure due to the vibration of the transformer body

Due to the complexity of the physical process, analytical methods are usually only applicable for simple geometries and their accuracy is limited. For more accurate results, couplings between these physical models need to be considered, which requires more complicated models and more computational effort. For these reasons, the vibration/acoustic modeling of transformers is usually based on numerical methods, e.g. the FEM.

Since the core vibration is considered to be the major source of the acoustic noise associated with transformers, FEM simulations are performed to study the vibration of magnetic cores. The analysis is focusing on the nanocrystalline alloy and the amorphous alloy, which are commonly used

core materials for MFTs.

Due to the lack of some material parameters from literatures, they are obtained by estimation and approximation. Also, only the weak coupling method is considered on the one hand due to unknown parameters required for the strong coupling and on the other hand because of its simplicity.

4.1 Core materials for MFT applications

Besides the basic functions, i.e. the voltage level adaption and the galvanic isolation, transformers are desired to be highly efficient, compact and silent. To achieve high performances, a suitable core material is essential. Therefore, materials with low loss, high saturation level and small magnetostriction are preferred. In Table 4.1, relevant properties of several magnetic materials are listed.

Table 4.1: Properties of some magnetic materials [120]

Material	Saturation flux density [T]	Saturation magnetostriction [μm/m]	Loss @ 0.2T/20kHz [W/kg]
6.5% Si-Fe (50 μm)	1.8	0	60
Mn-Zn ferrite	0.45~0.55	-2~0	10~15
Fe-based amorphous alloy METGLAS 2605SA1	1.56	27	8~10
Co-based amorphous alloy VITROVAC 6030	0.82	<0.2	2.2
Nanocrystalline VITROPERM 500F	1.2	<0.5	1.8

Among these materials, the Si-Fe has the highest saturation level. Although the loss of this material is significantly higher, it is widely used for

low-frequency large power transformers due to the relatively low price. With the silicon weight percentage of 6.5%, the magnetostriction of the Si-Fe is nearly zero, which is advantageous to reduce the acoustic noise. In the medium frequency range, the loss of Si-Fe becomes unacceptable which prohibits its application as transformer cores. So far, Si-Fe based MFTs are only found to be operated below 1 kHz, e.g. a 400 Hz transformer is reported in [47].

The ferrite features a relatively low loss but also a low saturation level. The application of ferrite cores is typically in a much higher frequency range (>25 kHz), where the drawback of the low saturation flux density can be compensated by the increased frequency instead of increasing the cross-sectional area of cores. The magnetostriction of ferrite materials is normally negative and relatively small. Furthermore, the operation of transformers at a frequency above 20 kHz naturally eliminates the acoustic problem. However, due to limitations of semiconductor devices, switching losses of converters for medium voltage, high power applications could become inadmissible at such a high frequency without using expensive SiC devices. In a lower frequency range, the low saturation level of the ferrite is apparently unfavorable for high power density applications.

In the frequency range from 1 kHz to 25 kHz, commonly used core materials for transformers are amorphous and nanocrystalline alloys. Depending on the composition of the alloy, properties of magnetic materials are significantly different. Fe-based amorphous alloys such as the METGLAS 2605SA1 are composed of low cost raw materials, e.g. Fe, Si and B. The high content of Fe enables a high saturation flux density of the alloy which is comparable to the Si-Fe while the loss is significantly lower. However, the large magnetostriction of Fe-based alloy is obviously a drawback considering the acoustic noise emission. By adding additional contents including Co and reducing the percentage of Fe, the saturation level of amorphous alloys is lower but the loss is also significantly reduced. Depending on the Fe/Co ratio, the saturation flux density of Co-based amorphous alloys can vary from 0.4 T to 1 T. By a careful control of this ratio, a near-zero magnetostriction can be achieved, which is very attractive from the acoustic point of view[120]. Nevertheless, Co-based amorphous alloys are seldom to be found for MFT applications due to the high material cost.

Fe-based nanocrystalline alloys such as the VITROPERM 500F are composed of Fe, Si, B, Cu, Nb etc. The saturation level of this kind of materials is

relatively high and the specific loss is the lowest among the listed materials. Similarly, the Si content can be controlled at around 15-16at% (atomic percent) so that a near-zero magnetostriction can be achieved after the nanocrystallization [120]. The combination of these properties apparently shows the suitability of the nanocrystalline alloy as core materials of transformers for medium frequency, high power applications. The only drawback of this material is the relatively high cost.

4.2 Modeling procedure based on FEM

In this work, the modeling is performed by using the commercial FEM software COMSOL Multiphysics [122], where two of the physical modules are used, i.e. the Magnetic fields (mf) and the Solid mechanics (solid). In this section, procedures for establishing the model are briefly described.

The first step is to define the geometry of the model, including the magnetic core, the winding and an electromagnetic boundary. Since the modeling is focusing on the magnetic core, a simplified geometry can be used for the winding such as a hollow cylinder in the 3D case or a rectangular area in the 2D case. For the boundary of the model, a sphere (3D) or a circle (2D) enclosing the whole geometry of the core and windings can be used.

4.2.1 Material model

After establishing the geometry of the model, materials need to be assigned to each domain. The winding is defined as copper and the rest of domains, except of the core, are assigned as air. The relevant material properties of copper and air are already available in the database of the software. Material properties of the magnetic core are discussed below.

Material parameters are essential for the accuracy of the model. However, as mentioned in [80], some of the parameters of magnetic materials are usually not available. To measure these parameters, specific instruments and test samples are required, which is out of the scope of this work. Instead, parameters for the core material are derived from data sheet or by an estimation and approximation in this work. The considered material is the nanocrystalline alloy VITROPERM 500F and the Fe-based amorphous alloy METGLAS 2605SA1.

Magnetic properties

Since the epoxy resin as isolation layers in the tape wound core is not magnetizable, it can be neglected in the magnetic model. The nanocrystalline alloy has remarkably fine grain structures and the magnetic anisotropy is very low [120]. Therefore, it can be considered as an isotropic material for the magnetic model.

To account for the magnetic saturation, the B-H curve from the data sheet is used, where a series of points on the curve are extracted. B-H curves are interpolated based on these points as shown in Fig. 4.1, which are used for the simulation. The hysteresis loop for these materials is very narrow and therefore neglected. Furthermore, the dependency of the magnetization on the mechanical stress, i.e. the Villari effect, is unknown and is not considered.

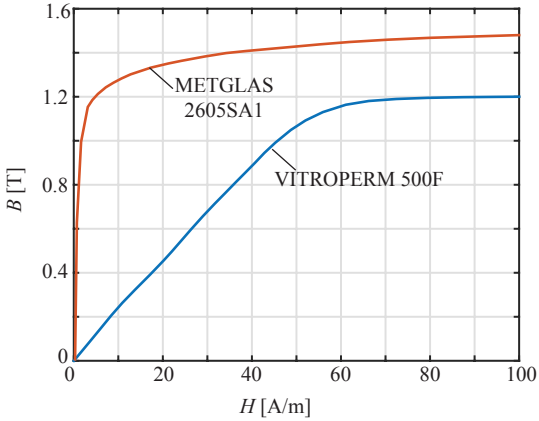

Figure 4.1: B-H curves of the VITROPERM 500F and the METGLAS 2605SA1 used for simulations.

Elastic properties

For the mechanical model, the material is considered as transversely isotropic and equivalent parameters are obtained analytically according to elementary mixture rules as introduced in the previous chapter. The used material parameters for calculations are listed in Table 4.2. For magnetic materials,

parameters are obtained from the manufacturer [108], with exception of the Poisson's ratio of the VITROPERM 500F. Since this parameter is unavailable from the manufacturer or literatures, the same value for the METGLAS 2605SA1 is used [127]. Parameters for the epoxy resin are taken as average values from [128]. Furthermore, the lamination factor is assumed to be $l_F = 0.95$.

Table 4.2: Material parameters used for the elastic model

Parameter	VITROPERM 500F	METGLAS 2605SA1	Epoxy resin
Mass density [kg/m^3]	$\rho_m = 7350$	$\rho_m = 7180$	$\rho_f = 1200$
Young's modulus [GPa]	$E_m = 150$	$E_m = 110$	$E_f = 2.5$
Poisson's ratio	$\nu_m = 0.3$	$\nu_m = 0.3$	$\nu_f = 0.33$

According to (3.88) to (3.94), equivalent parameters for the laminated structure can be calculated, which results in parameters listed below for the VITROPERM 500F:

- Equivalent mass density: ρ_{eq}=7042.5 kg/m^3
- Equivalent Young's modulus: E_p=142.63 GPa, E_q=37.98 GPa
- Equivalent Poisson's ratio: ν_p=0.3015, ν_q=0.0803
- Equivalent shear modulus: G_p=54.79 GPa, G_q=14.35 GPa

The equivalent shear modulus G_p is not an independent parameter, which is determined according to:

$$G_p = \frac{E_p}{2(1+\nu_p)} \tag{4.1}$$

To implement elastic parameters in the model, the geometry of the magnetic core is divided into several sub-domains. As an example, the division of sub-domains for a rectangular core is shown in Fig. 4.2. The global coordinate system for the model is shown on the right bottom corner, with the core window plane coincides with the x-y plane. For each sub-domain, elastic parameters are defined separately according to rolling directions of lamination layers.

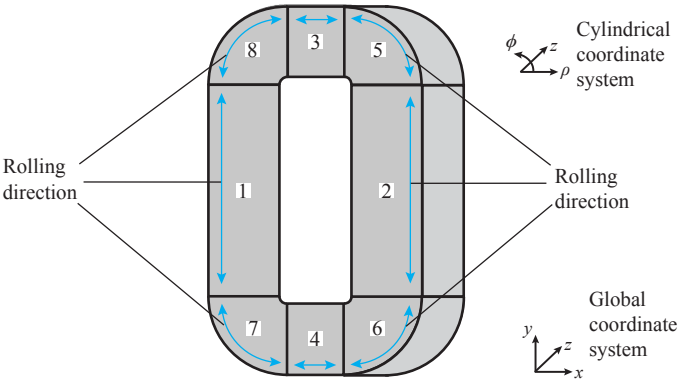

Figure 4.2: Sub-domains for the material model of magnetic core.

For sub-domains 1 and 2, the rolling direction is parallel to the y-axis and lamination layers are parallel to the y-z plane. Therefore, elastic parameters $\mathbf{E} = [E_x, E_y, E_z]^{\mathbf{T}}$, $\boldsymbol{\nu} = [\nu_{xy}, \nu_{yz}, \nu_{xz}]^{\mathbf{T}}$, $\mathbf{G} = [G_{xy}, G_{yz}, G_{xz}]^{\mathbf{T}}$ are defined as

$$\begin{cases} \mathbf{E} = [E_{\mathrm{q}}, E_{\mathrm{p}}, E_{\mathrm{p}}]^{\mathbf{T}} \\ \boldsymbol{\nu} = [\nu_{\mathrm{q}}, \nu_{\mathrm{p}}, \nu_{\mathrm{q}}]^{\mathbf{T}} \\ \mathbf{G} = [G_{\mathrm{q}}, G_{\mathrm{p}}, G_{\mathrm{q}}]^{\mathbf{T}} \end{cases} \tag{4.2}$$

For sub-domains 3 and 4, the rolling direction is parallel to the x-axis and lamination layers are parallel to the x-z plane. Similarly, elastic properties are defined as

$$\begin{cases} \mathbf{E} = [E_{\mathrm{p}}, E_{\mathrm{q}}, E_{\mathrm{p}}]^{\mathbf{T}} \\ \boldsymbol{\nu} = [\nu_{\mathrm{q}}, \nu_{\mathrm{q}}, \nu_{\mathrm{p}}]^{\mathbf{T}} \\ \mathbf{G} = [G_{\mathrm{q}}, G_{\mathrm{q}}, G_{\mathrm{p}}]^{\mathbf{T}} \end{cases} \tag{4.3}$$

For the sub-domains 5,6,7 and 8 at four corners of the core, rolling directions are parallel to the ϕ-axis of the cylindrical coordinate system as shown in Fig. 4.2. Therefore, for each of these sub-domains, a cylindrical coordinate system is established with the original point at the position corresponding to the center point of the arc in each sub-domain. Lamination layers are parallel to the ϕ-z plane of each sub-domain. Accordingly, elastic parameters

for these domains are defined as

$$\begin{cases} \mathbf{E} = [E_\rho, E_\phi, E_z]^{\mathbf{T}} = [E_\mathrm{q}, E_\mathrm{p}, E_\mathrm{p}]^{\mathbf{T}} \\ \boldsymbol{\nu} = [\nu_{\rho\phi}, \nu_{\phi z}, \nu_{\rho z}]^{\mathbf{T}} = [\nu_\mathrm{q}, \nu_\mathrm{p}, \nu_\mathrm{q}]^{\mathbf{T}} \\ \mathbf{G} = [G_{\rho\phi}, G_{\phi z}, G_{\rho z}]^{\mathbf{T}} = [G_\mathrm{q}, G_\mathrm{p}, G_\mathrm{q}]^{\mathbf{T}} \end{cases} \tag{4.4}$$

With the definition of these elastic parameters, the compliance matrix as given in (3.85) for a transversely isotropic material is completely defined.

4.2.2 Magnetic model

After the assignment of materials with defined properties, initial conditions and boundary conditions need to be defined for each physical model.

In the magnetic model, the excitation source is defined as a current flowing through the winding. According to the desired peak flux density in the core, the required current amplitude can be calculated. At the boundary of the model, the condition is set to be magnetically insulated. By solving Maxwell's equations, the magnetic field distribution within boundaries of the model can be calculated.

Accordingly, the local distribution of the Maxwell force and the Lorentz force can be calculated based on the field distribution according to the equations (3.55) and (3.57). Since the laminated structure is neglected and the magnetic properties of the core material are assumed to be isotropic, local Maxwell forces only exist on the core surface and can be treated as local mechanical stress.

4.2.3 Mechanical model

Since only the magnetic core is of interest, the mechanical modeling only needs to be performed for the core domain. The calculated surface stress due to the Maxwell force is applied as the boundary load to the magnetic core domain.

According to the solved magnetic field distribution, the local magnetostrictive strain is calculated by using (3.62) for the field direction and by using (3.63) for the transverse direction. Since the hysteresis is not considered, the differential term in both equations vanishes. Furthermore, the

stress dependency of the magnetostriction is also not taken into account.

The calculated magnetostrictive strain is applied to the strain due to the mechanical stress according to Hook's law given in (3.64). The modified equation is given as

$$\boldsymbol{\sigma} = \boldsymbol{C}[\boldsymbol{\epsilon} - \boldsymbol{\lambda}] \tag{4.5}$$

where $\boldsymbol{\lambda}$ is the magnetostrictive strain in the tensor form represented as a 3×3 matrix. The calculated stress $\boldsymbol{\sigma}$ and the force are introduce to (3.118) to solve the displacement .

4.3 Simulation results

The simulation model introduced above is implemented and used for some case studies, results are discussed below. The standard nanocrystalline rectangular core used for the MFT design presented in chapter 2 is modeled. Due to the manufacturing tolerance, the practical core shape has some deviations compared with the regular shape shown in Fig. 4.2: the core leg width (lamination height) in parts 1,2 are generally smaller than in other parts (ref. Table 5.1 and Fig. 5.3). For convenience, the core leg width is set to be identical in the model, which is 30 mm. The window size of the core is set to be 30 mm×95 mm and the thickness of the core is 27 mm. Therefore, the total height of the core is 2×30 mm+95 mm=155 mm and the total width is 2×30 mm+30 mm=90 mm.

4.3.1 Maxwell force versus Lorentz force

As mentioned before, the Lorentz force is considered to be less significant than another two electromagnetic sources of the acoustic noise for transformers. To compare the Maxwell force and the Lorentz force, 2D simulations are performed in static cases considering inductors and transformers with or without air gaps. Since the object is to calculate forces, only the magnetic model is necessary to be solved. The considered core material is the VITROPERM 500F, where the B-H curve shown in Fig. 4.1 is used. The equivalent relative permeability corresponding to the linear part of the B-H curve is approximately $\mu_\mathrm{r} = 20000$.

In Fig. 4.3, simulation results are shown, where the length of the arrows

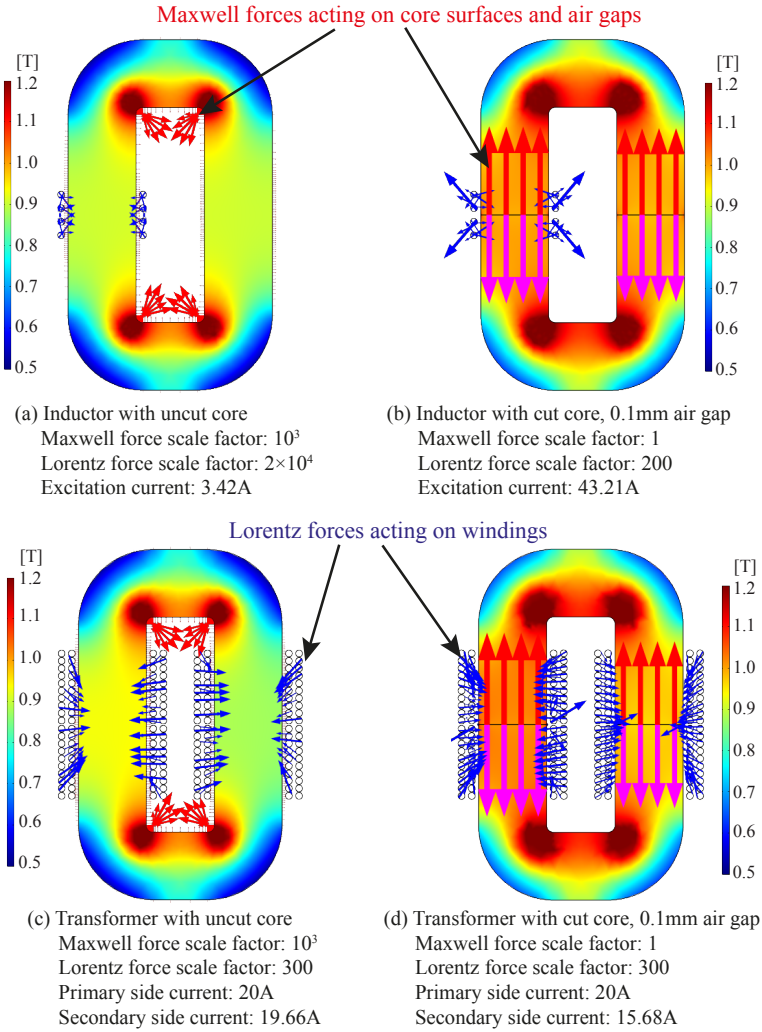

Figure 4.3: Maxwell forces and Lorentz forces distribution at the same magnetic flux density in inductors and transformers with or without air gaps.

representing the relative magnitude of forces. The inductor winding has 4 turns and the transformer winding has 40 turns (turns ratio 1:1). The

excitation currents are set so that the flux density in the middle of core limbs is approximately 1.0 T in all cases. At inner corners of the core, the flux density reaches the saturation level of 1.2 T.

In case of an uncut core, the Lorentz force is comparable to the Maxwell force, especially for the transformer. Due to a much higher current in the winding of the transformer compared to the inductor current, the Lorentz force acting on the transformer winding is significantly larger. As shown in Fig. 4.3 (c), the magnitude of the Lorentz force is even higher than the magnitude of the Maxwell force in case of the transformer with an uncut core. The Maxwell force is distributed around the core with higher amplitudes at inner corners due to the higher flux density at these locations.

In case of a cut core with a thin air gap of 0.1 mm, the inductor current is also much higher compared to the case of the inductor with an uncut core. As a result, the Lorentz force is much larger. Due to the existence of air gaps, the attractive force at the air gap region is dominant and has a significantly higher magnitude than the force at other locations of the core surface. With the same scale factor, even the force at inner corners of the core is still much smaller than the force at the air gap region. Therefore, arrows representing the Maxwell force at locations except for the air gap region cannot be seen as shown in Fig. 4.3 (b) and (d). Comparing the Lorentz force and the Maxwell force, even in case of the inductor with a cut core where the current amplitude is the highest among compared cases, the maximal magnitude of the Lorentz force is still about 100 times smaller than the Maxwell force at the air gap region.

From these simulation results, it can be concluded that the magnitude of the Lorentz force is dependent on the amplitude of the current. In case of an uncut core and a high current flowing through the winding, the Lorentz force can be larger than the Maxwell force. If an air gap exists, the attractive force at the air gap region is dominant, with a much larger magnitude than the Lorentz force.

4.3.2 Maxwell force versus magnetostriction

To compare the impact of the magnetostriction and the Maxwell force on the core vibration, static simulations are performed to calculate core deformations due to these effects, where (3.120) is solved for the mechanical

model. For simplicity, a 2D model is implemented under the assumption of the plane stress, where the stress in the z-direction as shown in Fig. 4.2 is neglected. As mentioned, the weak coupling between the electromagnetic model and mechanical model is considered. In case of uncut cores, the mechanical model is only solved for the core domain while for cut cores, only half of the core domain is solved due to the symmetry. To improve the numerical stability, the upper and the lower boundaries of the core are set to be fixed.

In Fig. 4.4, simulated deformations of cores induced by the Maxwell force and the magnetostriction are shown. The magnetic core has the same dimension and excitation conditions are kept the same as for inductors introduced in previous simulations in section 4.3.1. The magnetic field distribution can be referred to Fig. 4.3 (a) and (b) for the uncut and the cut core respectively.

It can be seen that in case of the uncut core, the Maxwell force generally cause a shrink of the core due to larger forces on the inner surface compared with forces on the outer surface. The caused deformation is very small where the maximal value is below 20 pm. The magnetostriction of the VITROPERM 500F is positive and causes an expansion of the core. In this case the maximal deformation is close to 20 nm, which is about 1000 times larger than the deformation caused by the Maxwell force.

In case of the cut core, the attractive force at the air gap region is quite significant as shown in previous simulation results. This attractive force pulls core leg towards another core half and the induced deformation is around 2 µm. Together with the attractive fore, large forces on the inner surface especially at corners also cause a shrink of the core which is more significant than in the case of the uncut core. On the other hand, the deformation of the cut core caused by the magnetostriction is slightly larger compared to the case of the uncut core where the maximal value is approximately 25 nm. The magnetostriction causes the elongation of the core where at corners (arc parts) the core is expanded. In the y-direction, the core is also prolonged towards the other core half similar as the deformation caused by the attractive Maxwell force. In practice, it can be assumed that effects of the magnetostriction and the Maxwell force are enhanced with each other at the air gap region as mentioned in chapter 3. For the cut core, the deformation caused by the Maxwell force (mainly the attractive force at air gap regions) is almost 100 times larger than the deformation caused by the

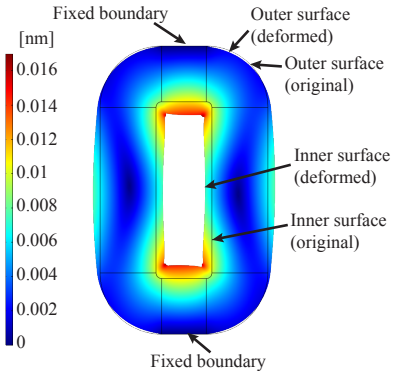

(a) Uncut core
Deformation due to Maxwell force
Scale factor: 5×10^{8}

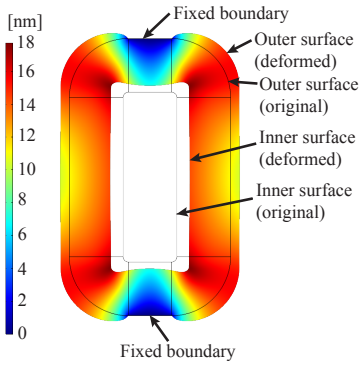

(b) Uncut core
Deformation due to magnetostriction
Scale factor: 5×10^{5}

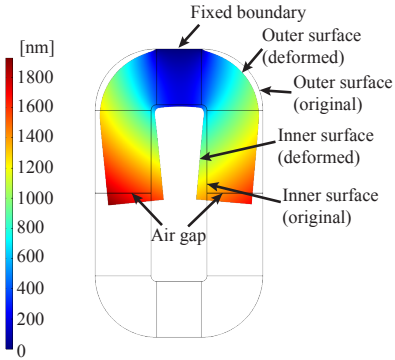

(c) Cut core
Deformation due to Maxwell force
Scale factor: 5×10^{3}

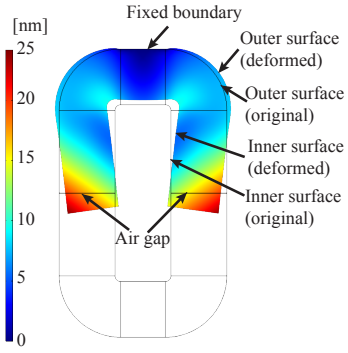

(d) Cut core
Deformation due to magnetostriction
Scale factor: 5×10^{5}

Figure 4.4: Comparison of the magnetic core deformations due to the Maxwell force and the magnetostriction.

magnetostriction. It should be noticed that the saturation magnetostriction of the considered core material is close to zero (λ_s =0.5 µm/m). If other core materials with a larger magnetostriction such as the Fe-based amorphous alloy are considered, the deformation caused by the magnetostriction in case of a cut core could be comparable to the deformation caused by the Maxwell force.

It can be concluded that in case of an uncut core, the effect of the Maxwell force is negligible compared to the effect of the magnetostriction. The deformation of the magnetic core is mainly caused by the magnetostriction even for materials with a very low saturation magnetostriction as shown in this case. On the other hand, the attractive force at the air gap region in case of a cut core can cause a much more significant deformation compared to the effect of the magnetostriction.

4.3.3 Nanocrystalline alloy versus amorphous alloy

To compare the nanocrystalline and the amorphous alloy, deformations of two rectangular uncut cores with the same dimension as used in previous simulations considering two core materials (METGLAS 2605SA1 and VITROPERM 500F) are evaluated. For the nanocrystalline core, the excitation condition is kept the same as in previous simulations, the magnetic field distribution can be refereed to Fig. 4.3 (a). For the amorphous core, the excitation current is set that the flux density in the middle of the core is around 1 T. In this case, the flux density at inner corners is about 1.5 T. The B-H curve shown in Fig. 4.1 is implemented for the magnetic model of the amorphous core.

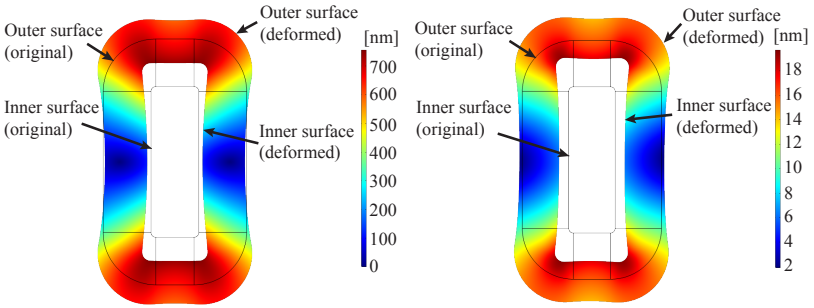

(a) METGLAS 2605SA1
Scale factor: 2×10^4

(b) VITROPERM 500F
Scale factor: 1×10^6

Figure 4.5: Deformations of magnetic cores in case of the Fe-based amorphous and the nanocrystalline alloy.

In Fig. 4.5, the simulated deformations of cores are shown, where the boundary of the core is set to be free. It has been shown in previous simulation results that in case of the uncut core, the deformation is mainly

due to the magnetostriction. Therefore, the maximal deformation of the nanocrystalline core is almost the same compared with the result shown in Fig. 4.4 (b). The maximal deformation of the core appears at inner corners where a high flux density presents. Due to the large saturation magnetostriction of the METGLAS 2605SA1, the maximal deformation of the amorphous core reaches around 750 nm while for the nanocrystalline core it is only approximately 20 nm, i.e. the difference is almost 40 times. Obviously, at the same excitation level, the vibration of the nanocrystalline core is much smaller than the Fe-based amorphous core.

4.3.4 Deformation of cores with different geometric shapes

To evaluate the deformations of magnetic cores with different geometric shapes, the simulation is performed considering the rectangular, square, oval and ring cores, where the considered core material is the VITROPERM 500F. The dimension of the rectangular core is the same as in previous simulations and for other shapes the same magnetic length of approximately 0.34 m and the same core leg width are considered. The excitation condition is kept the same, where the resulting magnetic flux density in the middle of the core legs is approximately 1 T.

In Fig. 4.6, simulated magnetic flux density distributions and deformations of different cores are shown. Under the same excitation condition, only the ring core is not saturated at any location. By comparing the flux density and the displacement distribution, it can be seen that locations with a higher flux density are subjected to a larger magnetostriction and therefore have a larger deformation. Due to the magnetostriction, these cores are all enlarged from a few nm up to around 20 nm. The deformation of the ring and the square core is symmetric due to their geometric symmetry while the oval and the rectangular core show a larger deformation alone the y-axis. Since the length of core legs along the y-axis is larger than that of along the x-axis, the magnetostrictive train is also larger along the y-axis (The change of the dimension Δl due to the magnetostriction is proportional to the length l).

For comparison, displacements of some points on the outer surface of these cores as indicated in Fig. 4.6 are evaluated and results are listed in Table 4.3. In case of the ring core, displacements of points on the outer surface are approximately equal which is around 16 nm. The maximal de-

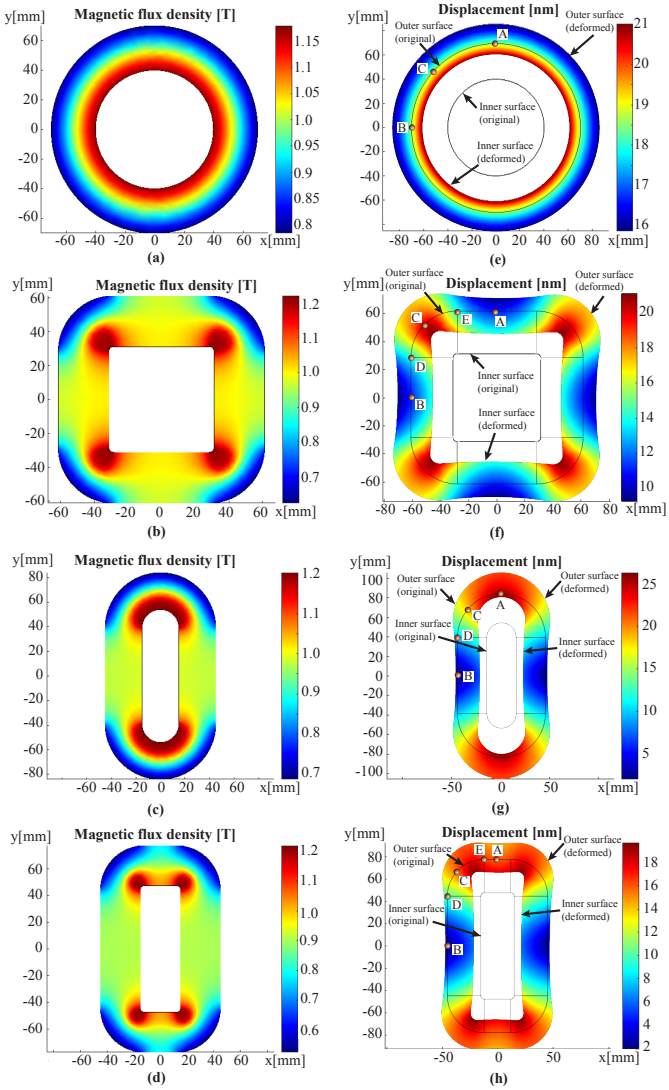

Figure 4.6: Simulated core deformations in static cases considering four different geometric shapes. (a)-(d): magnetic flux density distributions, (e)-(f): deformations (scale factor: 10^6).

Table 4.3: Displacements of points indicated in Fig. 4.6 obtained by static simulations

Disp.	Ring			Square		
[nm]	x	y	total	x	y	total
A	-0.008	15.88	15.88	0.64	9.29	9.31
B	-15.92	-0.01	15.92	-9.41	0.65	9.43
C	-11.25	11.25	15.91	-11.69	12.76	17.31
D	N/A	N/A	N/A	-11.55	8.22	14.18
E	N/A	N/A	N/A	-6.93	12.08	13.93
Disp.	Oval			Rectangular		
[nm]	x	y	total	x	y	total
A	0.01	21.78	21.78	0.59	14.3	14.31
B	-2.03	0.001	2.03	-1.91	0.32	1.94
C	-5.33	18.45	19.2	-5.08	14.85	15.69
D	-4.53	11.23	12.11	-4.4	11.06	11.9
E	N/A	N/A	N/A	-1.7	15.06	15.16

formation of the square core is at corners with a total displacement of more than 17 nm while the middle of core legs (point A and B) has the minimal displacement (below 10 nm). The oval core has the largest deformation in the middle of the arc part, which is more than 20 nm in the y-direction while the deformation of straight legs is rather small (point B). The deformation of the rectangular core is also mainly along the y-axis with the maximal deformation appearing at the corner (point C).

Generally, deformations of cores with 4 considered shapes are in a comparable range. From the acoustic point of view, the vibration on the outer surface is assumed to be more relevant to the acoustic noise emission compared with the inner surface. According to these simulation results, the deformation of the ring core on the outer surface is relative small compared to other cores. Therefore, it can be expected that the ring core has the best acoustic performance among these shapes. Furthermore, the generated acoustic noise in all directions around a ring core are expected to be the same due to the equal vibration.

The oval and the rectangular core are expected to generate more acoustic noise in the y-direction than in the x-direction due to a more significant

deformation in the y-direction. In case of the square core, the generated noise in the x and the y-direction is expected to be the same with a magnitude lies between the noise generated from the x and the y-direction of the rectangular core.

The oval core appears to have a larger deformation in the y-direction compared to the rectangular core and they have a similar deformation in the x-direction. Since the oval shape is assumed to have the advantage of the ring core with a more even distributed magnetic field and mechanical stress in arc parts, it is expected that the acoustic performance of the oval core should be between the ring core and the rectangular core. This assumption is verified by experimental measurements as introduced later in chapter 5.

4.3.5 Eigenmodes of the rectangular core

To investigate the mechanical resonance and mode shapes of the core, an eigenfrequency analysis is performed for the rectangular core based on the VITROPERM 500F. Elastic properties of the core material are defined as described before, i.e. as a transversely isotropic material. The simulation is performed in a 3D case to solve the eigenvalue problem, where the boundary condition is set to be free vibration without applying any constraint.

In Fig. 4.7 and Fig. 4.8, eigenmodes within the audible frequency range obtained from the simulation are shown. Apart from the rigid body eigenmodes, there are 24 eigenmodes found in the considered frequency range. Since material parameters used for the simulation may not be accurate, the obtained eigenfrequencies and mode shapes may have some deviations to the practical core. However, it can be seen that eigenfrequencies of magnetic cores with such a size/weight are generally in the kHz range, which is the typical range of operating frequencies for MFTs. Due to non-sinusoidal operation waveforms in transformers, the excitation current contains several higher order harmonics which are also in the audible frequency range. Therefore, it is possible that frequencies of current harmonics are close to one or more of these eigenfrequencies. In this case, more extensive core vibrations could be induced and the acoustic noise emission from the transformer can be quite significant.

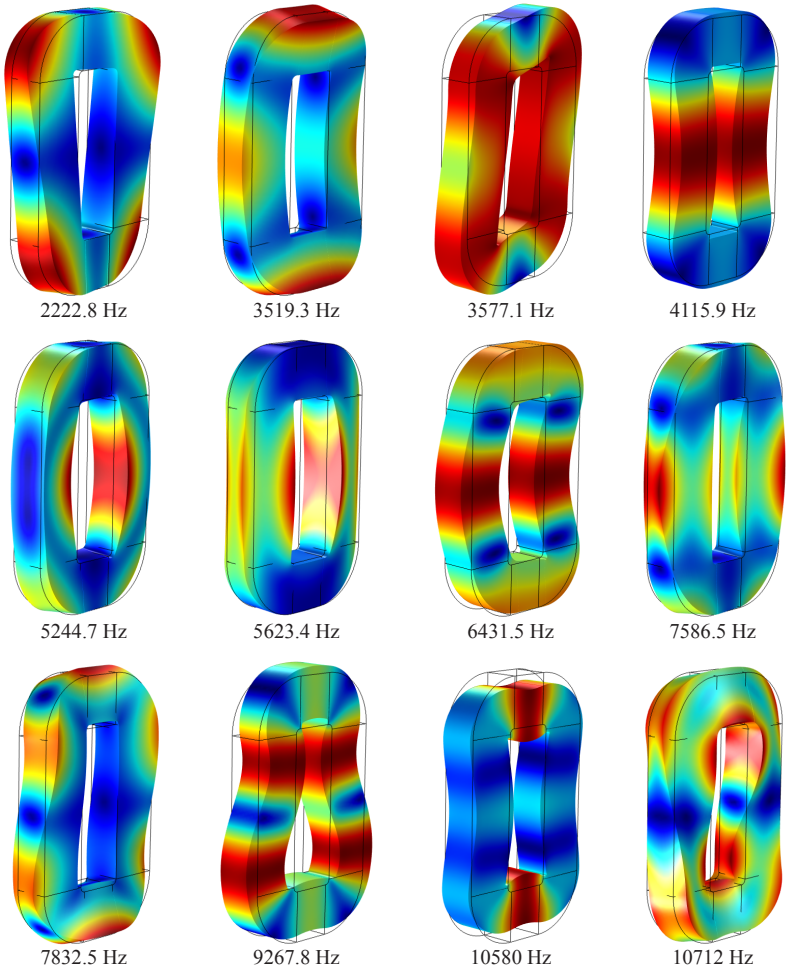

Figure 4.7: Simulated eigenmodes of the VITROPERM 500F rectangular core within the audible frequency range, part I.

4.4 Summary

In this chapter, suitable core materials for medium frequency applications are briefly reviewed and relevant material properties regarding the loss, the

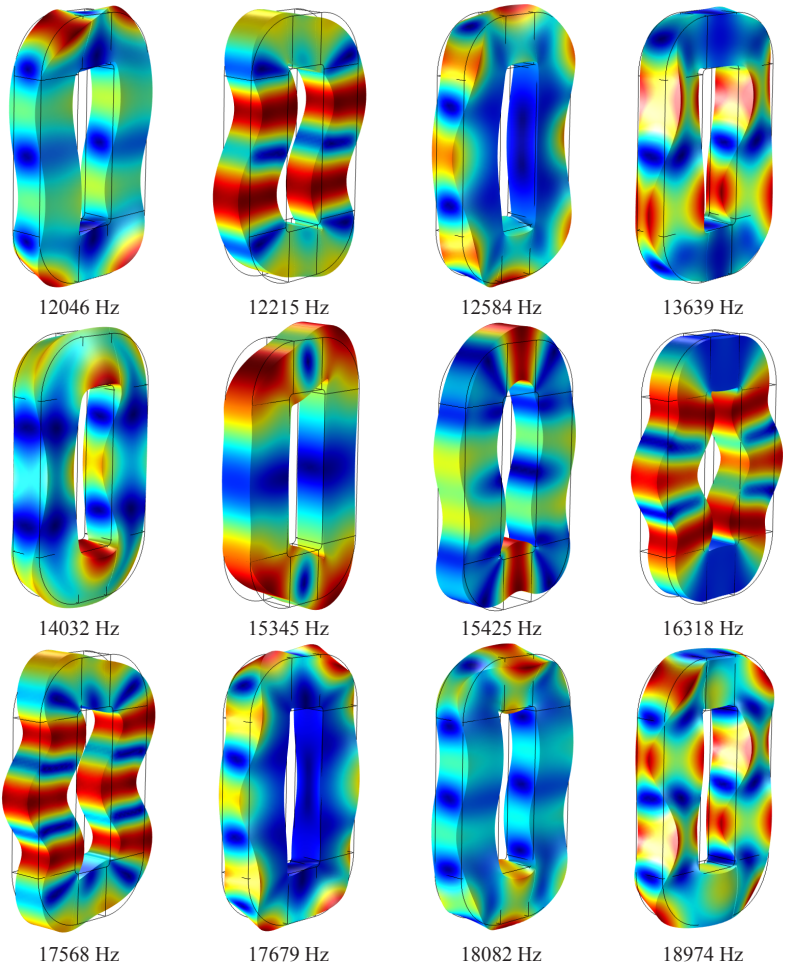

Figure 4.8: Simulated eigenmodes of the VITROPERM 500F rectangular core within the audible frequency range, part II.

saturation level and the magnetostriction are compared. It can be seen that the nanocrystalline alloy is the most suitable core material for MFTs due to its low loss, relative high saturation flux density and a near-zero magnetostriction.

Based on the FEM, a model for the analysis of core vibrations is implemented in COMSOL. The B-H curve is used to model the magnetization of the core where the hysteresis is neglected. For the mechanical model, the laminated core is modeled as a transversely isotropic material and equivalent elastic parameters are determined analytically base on elementary mixture rules for fiber-reinforced laminae. Due to the lack of information provided by the manufacturer, some parameters are taken from literatures or by approximation, which may be inaccurate. The electromagnetic and mechanical coupling is based on the weak coupling method where the influence of the mechanical model on magnetic properties of the core material is not considered. The model is used for some case studies by performing static analysis for magnetic cores based on the nanocrystalline alloy VITROPERM 500F and the Fe-based amorphous alloy METGLAS 2605SA1.

The Maxwell force and the Lorentz force are compared in case of inductors and transformers considering cut and uncut cores. The result shows that in case of using an uncut core, the Lorentz force is comparable to the Maxwell force. Especially in case of a transformer with a relatively high current in windings, where the Lorentz force can be larger than the Maxwell force. If a cut core is used, the attractive force in air gap regions is much more significant than the Lorentz force and the Maxwell force at other surface areas of the core.

The comparison of core deformations induced by the Maxwell force and by the magnetostriction shows that in case of an uncut core, the effect of the Maxwell force is negligible compared to the effect of the magnetostriction, even for a low-magnetostrictive material. On the other hand, the large force at the air gap region of a cut core can induce a significant deformation of the core leg, which is much larger than the deformation caused by the magnetostriction. Therefore, the Maxwell force in case of using a cut core is assumed to be the major cause of core vibrations if the magnetostriction of the core material is small.

Under a similar excitation condition, the Fe-based amorphous core shows much more significant deformations than the nanocrystalline core with a difference of the magnitude of about 40 times. Due to the large magnetostriction of the Fe-based amorphous core, it is expected that the generated acoustic noise is much higher than in the case of the nanocrystalline core.

Furthermore, deformations of nanocrystalline cores with different geo-

metric shapes under the same excitation condition are compared. Results show that the ring core features an even distribution of the magnetic field and it generally has the smallest deformation on the outer surface among compared cores. Therefore, it is expected that the ring core has a superior acoustic performance. The typical rectangular core shows obviously different deformations along the longer (in the y-direction) and the shorter (in the x-direction) core legs due to the dimension dependency of the magnetostrictive strain. By modifying core legs in both directions to have an equal length, i.e. the square core, the deformation is the same in the x and the y-direction. As a combination of the ring shape and the rectangular shape, the acoustic noise level of the oval core is expected to be between the ring core and the rectangular core. Further investigation of this issue by experimental measurements is introduced in the next chapter.

Finally, the eigenfrequency analysis of a standard nanocrystalline rectangular core shows that there are several eigenfrequencies in the typical operating frequency range of MFTs. Frequencies of the excitation current in transformers and its higher order harmonics may coincide with these eigenfrequencies and cause excessive core vibrations.

5 Vibration and Acoustic Noise Measurement

A transformer is basically constructed by the magnetic core, the primary and the secondary winding and other parts for isolation, cooling and mechanical mounting. To investigate the contribution to the vibration and the acoustic noise emission from individual parts of the transformer, experimental measurements are carried out. The measurement is aimed to compare contributions from the winding and the core, evaluate influences of material properties and geometric shapes on the vibration and the acoustic noise emission.

In the first part of this chapter, basic principles, instruments and environments for vibration and acoustic measurements are briefly introduced. Then the measurement setup and procedures utilized in this work are presented. Measurement results are discussed in the final part of this chapter.

5.1 Fundamentals of vibration and acoustic noise measurement

Although both the vibration and the acoustic noise are basically sound waves, their evaluation and measurement methods are totally different. In this section, commonly used methods and equipments for vibration and acoustic noise measurements are briefly introduced.

5.1.1 Basic of vibration measurement

The vibration of a surface is usually evaluated by its normal velocity or acceleration. Commonly used sensors for vibration measurements are accelerometers and laser vibrometers.

Accelerometer

An accelerometer is a small sensor that is attached on the surface of the measured object. It senses the acceleration of the attached surface, i.e. the time derivative of the surface velocity. This kind of sensor usually has a relative large bandwidth and dynamic range. However, since it has to be attached to the object, additional mounting work is necessary. Furthermore, the sensor itself may change the structure of the object and affect the measurement result.

Laser vibrometer

The laser vibrometer detects the surface velocity or the displacement at a fixed point on the surface of an object. In Fig. 5.1, the basic working principle of the laser vibrometer is shown. The laser head generates a reference laser beam with a frequency of f_0 which is split into two beams by a beam splitter. One beam is going through a Bragg cell where a known frequency shift f_b is added to the beam and then directed to the measurement surface. Due to the Doppler-effect, the movement of the object adds a frequency shift Δf_D to the beam reflected by the moving surface which is proportional to the

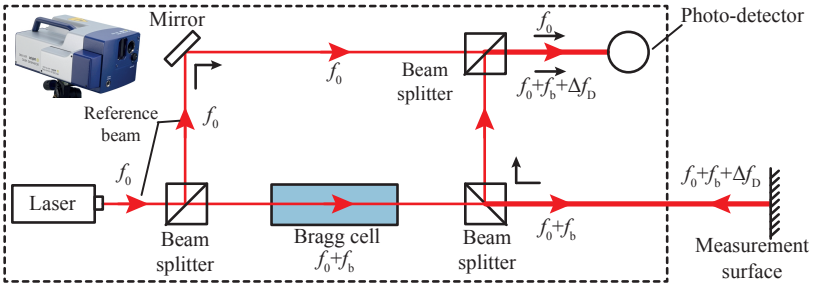

Figure 5.1: Working principle of the laser vibrometer.

velocity of the moving object, i.e.

$$\Delta f_{\mathrm{D}} = \frac{2v(t)}{\lambda}\cos\theta \tag{5.1}$$

where $v(t)$ is the surface velocity as a function of time, λ is the wavelength of the directed light wave, θ is angle between the laser beam and the velocity vector. Normally the laser beam is perpendicular to the measurement surface, therefore θ=90°.

The reflected beam with the frequency of $f_0 + f_{\mathrm{b}} + \Delta f_{\mathrm{D}}$ is collected by the vibrometer and interfered with an internal reference beam with the frequency f_0 on a photo-detector inside the vibrometer. Based on the principle of optical interference, the output of the photo-detector is converted to a standard frequency modulated signal with f_{b} as the carrier frequency and Δf_{D} as the modulation frequency. This signal can be demodulated to a voltage signal whose amplitude is proportional to the velocity. Then the voltage signal can be processed by a data acquisition system and the measured vibration velocity is obtained.

Since the laser vibrometer allows a non-contact measurement from a relatively large distance to the object (up to 100 meters), the influence of the sensor on the mechanical structure of the measured object can be avoided. Compared with the accelerometer, the vibrometer is more sensitive and has a larger frequency bandwidth and dynamic range. The drawback of the laser vibrometer is mainly the large size and high cost.

To evaluate the vibration of a whole surface, it is necessary to measure a large number of points distributed on the surface. This can be done by using a scanning vibrometer, which contains a controllable laser sensor head and an integrated video camera. The scanning vibrometer measures a series of user-defined points sequentially to provide the distribution of vibrations on the surface. With a larger number of measurement points, the spatial resolution of the surface vibration is increased. However, more measurement points also require a longer measuring time. The measuring time of a single point is proportional to the required frequency bandwidth and the frequency resolution.

To associate the data of these sequentially measured points, a periodical signal (normally a sinusoidal signal) needs to be provided as the reference to determine at which phase angle each point is measured. Based on the analysis in the frequency domain, the measured data at all points can be

used to calculate and visualize the deformation of the measured surface as an animation in relevant frequency bands.

In this work, the measured object is relatively small. To avoid the influence of the sensor on the object, a scanning vibrometer is used. Instead of transforming the Doppler frequency into a velocity-proportional voltage signal, the used scanning vibrometer is also able to count the bright-dark fringes on the detector and directly measure the displacement. The resolution of measurement results can be down to pm with digital demodulation techniques [129]. However, it is better to use the velocity demodulation in high frequency range, since the amplitude of the vibration velocity harmonic is proportional to the frequency, i.e.

$$v = 2\pi \cdot f \cdot s \tag{5.2}$$

where s is the displacement.

5.1.2 Basic of acoustic noise measurement

Measurement object

As introduced in chapter 3, the sound consists of two elements: the sound pressure and the particle velocity. Human ears can perceive the sound pressure and are not able to detect the particle velocity. The sound pressure is usually measured by a microphone which detects the pressure variation from the deflection of a thin membrane due to the difference of sound pressures inside and outside of the sensor. The functional principle of the microphone is very similar to that of human ears. The particle velocity can be measured by a microflown which is based on the thermal principle. In some cases, it is desired to measure the sound pressure gradient. This can be done by using a gradient microphone which has two acoustic entrances separated by a certain distance. The introduction here only focuses on the normal microphone, which is used for the acoustic measurement in this work. More details about other acoustic sensors can be found in specific literatures for acoustics, e.g. [130].

As already introduced, the sound is usually quantified by the SPL, the SIL and the SWL. The SPL is evaluated directly from the measured sound pressure according to (3.5). To evaluate the SIL, the sound intensity needs to be measured, which requires two acoustic sensors. According to the

definition of the sound intensity given in (3.6), both the sound pressure and the particle velocity can be measured. The sound intensity can then be calculated by integrating the product of the two measured quantities over time. The sound intensity can be used to calculate the sound power according to (3.7), which is useful for evaluating a sound source.

Sound intensity probe

In practice, sound intensity is usually measured by the sound intensity probe which consists of two phase matched microphones separated by a distance spacer. This method is based on the finite-difference approximation to the pressure gradient, which is proportional to the particle acceleration. Then the particle velocity can be obtained by the integration of the acceleration over time. This approximation is valid as long as the separation distance of the two microphones is small compared with the wavelength of the measured sound. Therefore, the upper limit of the measuring frequency of the sound intensity probe is dependent on the separation distance. Generally speaking, the higher the frequency of interest, the smaller the gap between the two microphones. The frequency range of commercially available sound intensity probes is usually up to 10 kHz [131].

In principle, the sound intensity measurement allows the evaluation of a sound source independent on the environment and other sound sources, since the steady background noise does not contribute to the sound power determined by measuring the sound intensity. In practice, this measurement method is still limited by the instrument, the background noise and conditions of the sound field [132].

Measurement microphone [133]

A microphone is a transducer that converts the sound pressure into an electrical signal by detecting the deflection or movement of a membrane due to air pressure variations. Depending on the operation principle, microphones are categorized into three types:

- Dynamic microphone
- Ribbon microphone

- Condenser microphone

For acoustic measurements, the most widely used microphone is the condenser type due to its high sensitivity, extended frequency response and transient response. The condenser microphone is based on the principle of an electrostatic transducer. In Fig. 5.2, the principle and the equivalent circuit of a condenser microphone is shown. A membrane acts as one electrode and a rigid backplate is used as another one. A DC polarization voltage U_0 (typically 200 V) provided by an external power supply creates a constant charge Q on electrodes. The charging current is flowing through a very large resistance R (>10 GΩ). The deflection of the membrane induces a variation of the distance between the two electrodes and therefore the capacitance C is changed. Since the stored electrical charge Q is constant, an AC voltage u is induced due to the change of the capacitance and added to U_0. In this way, the sound pressure is transformed into a voltage signal u which can be further processed by the data acquisition system. The relation between the sound pressure and the induced voltage is linear to an excellent approximation if the amplitude is not too high [133]. To avoid using an external power supply, a polarization voltage can be applied by placing an dielectric layer with a permanent polarization between electrodes during the manufacturing process, creating a so-called electret condenser microphone. Therefore, this type of microphone is also referred as pre-polarized microphones.

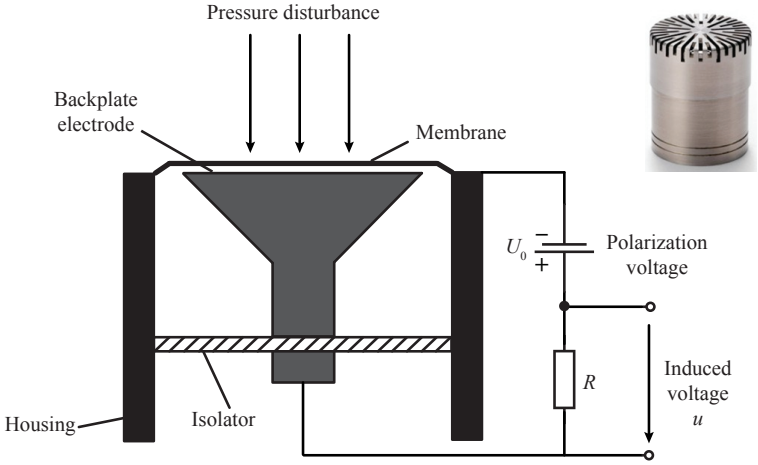

Figure 5.2: Principle and equivalent circuit of a condenser microphone.

Types of microphones according to applications in sound fields [134]

According to applications in sound fields, condenser microphones can be divided into three groups:

- Pressure-field microphone
- Free-field microphone
- Random-incidence microphone

The pressure-field microphone is designed to measure the actual sound pressure as existing on the surface of the microphone's membrane. The typical application of the pressure microphone is in an enclosure (or cavity), which is small compared with the wavelength of the measured sound. Or it can be inserted into the boundary or wall. In this case, the microphone forms part of the wall and measures the sound pressure on the wall itself.

The free-field microphone measures the sound pressure as it exists before the microphone is introduced into the sound field. This kind of microphone is designed to compensate the pressure change due to its presence in the sound field. The free-field microphone should be pointed towards the sound source, i.e. with 0° incidence.

The random-incidence microphone is deigned to respond uniformly to sound waves simultaneously coming from all directions. The application of this kind of microphone is in a diffused sound field, e.g. in an indoor environment where sound waves are reflected by walls, ceilings and other objects.

Technical specifications of measurement microphone

Besides the sound field, following specifications need to be considered by choosing the appropriate measurement microphone: sensitivity, dynamic range, frequency response, polarization type and temperature range. Typically, condenser microphones are manufactured with following outer diameters: 1", 1/2", 1/4" and 1/8".

Sensitivity: The sensitivity of a microphone is the ratio of the output voltage to the input pressure, which is usually given by a linear unit as

[mV/Pa] or expressed logarithmically in [dB] according to:

$$\text{Sensitivity[dB]} = 20\log_{10}\frac{\text{Sensitivity[mV/Pa]}}{\text{REF}} \tag{5.3}$$

where the reference value REF=1000 mV/Pa. The sensitivity is mainly determined by the microphone's size and the tension of its membrane. Typically, the sensitivity of condenser microphones is between 1 mV/Pa and 50 mV/Pa. Generally, a larger microphone with a looser membrane has a higher sensitivity and vice versa [134].

Dynamic range: This specification represents the range between the minimal and the maximal sound pressure level given in [dB], which a microphone can measure. The lower limit of the dynamic range is limited by the cartridge thermal noise (CTN), which is superimposed on the acoustically induced signal. Therefore, a signal level below the CTN can not be measured. The CTN is normally around 5 µV, therefore, the lowest measurable pressure of the microphone is related to its sensitivity as

$$p_{\text{min}} = \frac{\text{CTN}}{\text{Sensitivity[mV/Pa]}} \tag{5.4}$$

The upper limit of the dynamic range is dependent on the supplied voltage and the sensitivity of the microphone, which is defined as

$$p_{\text{max}} = \frac{\text{Voltage[mV]}}{\text{Sensitivity[mV/Pa]}} \tag{5.5}$$

where the voltage is the peak output voltage of the preamplifier. The calculated pressure level is converted to the SPL value according to (3.5). Generally, a microphone with a high sensitivity can measure a low pressure level but not a very high level [134].

Frequency response: The frequency range of a microphone gives the upper and the lower limit of the measurable frequency. The upper limit is related to the size of the microphone and the sound wavelength. At a higher frequency, the wavelength is shorter. Therefore, a smaller microphone can measure a higher frequency. The lower limit of the frequency range is determined by the static pressure equalization system [134]. The frequency response refers to the way a microphone responds to the sound pressure at different frequencies in its measurement range. At some frequencies, the measured SPL is amplified based on the actual value while at the other

frequencies the measured values are attenuated (reduced) or kept the same. The frequency response is described as a magnitude vs. frequency curve where a magnitude higher than 0 dB means at that frequency the measured sound pressure is amplified. Typically, a tolerance of +/- 2 dB is indicated in specifications of the frequency response by manufacturers. A flat response at 0 dB in the whole frequency range implies that the microphone is equally sensitive at all frequencies, which results in a more accurate representation of the original sound. However, microphones with a perfectly flat frequency response are not available in practice.

Preamplifier

Practically, the microphone needs to be connected to a preamplifier with a high input impedance in order to process the very weak voltage signal at the output of the microphone. The signal from the microphone is normally not amplified by the preamplifier but converted to a low-impedance signal so that it can drive a long cable. The preamplifier can be divided into two types: the transitional one requires an external DC voltage supply. Another type is supplied by a constant current power (CCP) which is connected by a standard coaxial cable.

A preamplifier also has its own frequency range and dynamic range. The lower limit of the frequency range is determined by the capacitance of the microphone and the higher limit is usually larger than the frequency limit of the microphone. The higher limit of the dynamic range is related to the supply voltage and the lower limit is related to the noise generated by the preamplifier itself [134]. When the microphone is mounted to a preamplifier, the self-noise of both devices are added together. The total noise floor is then determined by the combined noise.

Measurement environment

Besides the sensor, the environment is also essential for acoustic measurements. As previously discussed, the space around a sound source is separated into several sound fields. Measuring the sound pressure in the near field should be avoided due to the influence of reactive components since the sound pressure and the particle velocity are not in phase. Normally, the sound pressure is measured under the free field condition without the

influence of reflected sound waves or from other sound sources.

Measurement arrangements and chambers are configured to realize a well-defined acoustic environment. An anechoic chamber or a semi-anechoic chamber is implemented to create the free field environment, which is designed to absorb sound waves and isolate sound sources outside of the chamber. All walls, the ceiling and the floor of the anechoic chamber are mounted with wedge-like porous materials while the semi-anechoic chamber has a solid, reflecting floor for supporting heavy items.

Depending on the measured object, the dimension of the chamber must be large enough to ensure that the microphone can be placed outside the near field, i.e. to allow a required distance for measurement. Since the near field effect is also related to the sound wavelength, which is inversely proportional to the frequency, the measurement distance is determined by the lowest frequency of interest. On the other hand, a distance between the wall of the chamber and the microphone (i.e. the measurement surface) should be kept, which is at least 1/4 of the sound wavelength corresponding to the center frequency of the lowest required 1/3-octave band [132]. Accordingly, the inner dimension of the chamber should be larger than the sum of the measurement distance and the distance from the microphone to the wall.

5.2 Vibration and acoustic noise measurements

In this section, magnetic cores, major instruments and the test setup used for vibration and acoustic noise measurements are introduced.

5.2.1 Magnetic cores

Based on the design result presented in chapter 2, the standard nanocrystalline core used for the MFT design is considered to be measured. Therefore, two pieces of this core are employed and their dimension are used as the reference to select cores made by other materials. One piece of the core is cut in the middle of the leg and another one is uncut. For comparison of different materials, a Fe-based amorphous cut core with the material METGLAS 2605SA1 [127] and a ferrite cut core from KASCHKE with the material K2008 [135] are chosen. Dimensions of these cores according to the data sheet are listed in Table 5.1 with symbols of dimensions shown in

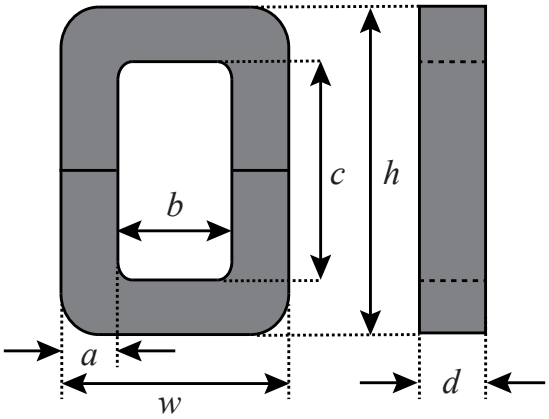

Figure 5.3: Symbols of dimensions for the rectangular core.

Table 5.1: Dimensions of magnetic cores used for measurements

Size [mm] / Core	*a*	*b*	*c*	*d*	*w*	*h*
VAC VITROPERM 500F T60102-L2157-W159	29.6	30	95	26.6	90	157.5
METGLAS 2605SA1 PS0509CA	28.6	30	95	30	87.2	152.2
KASCHKE K2008 U93/30/76	28	34.6	96	30	93	152

Fig. 5.3.

To investigate the influence of the geometric shape, an oval core and a ring core are also considered for measurements. Both cores are uncut, made by the VITROPERM 500F and have the same tape width, cross-sectional area and a similar magnetic length as the reference core. The three nanocrystalline cores and their measured dimensions are shown in Fig. 5.4. As can be seen that the width of core legs are slightly different (±1 mm) which is due to the manufacturing tolerance.

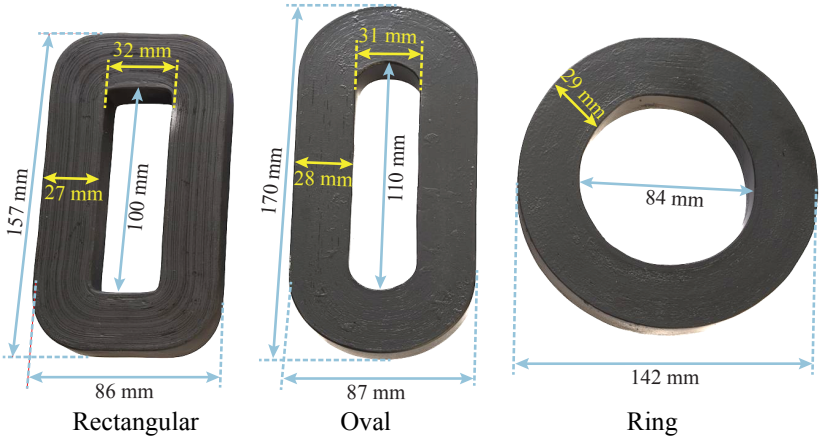

Figure 5.4: Nanocrystalline uncut cores and their measured dimensions.

5.2.2 Measurement setup

The measurement setup as shown in Fig. 5.5 has been built for both the vibration and the acoustic noise measurement. The excitation voltage/current for the core is generated by a signal generator, amplified by a power amplifier and then fed to the excitation winding of the core. A capacitor bank with a total capacitance of 5 mF is connected in series to decouple the DC component which might be introduced by the power amplifier. To control the excitation voltage to get the desired magnetic flux density in the core, a measurement winding wound by thin wires is added, on which the

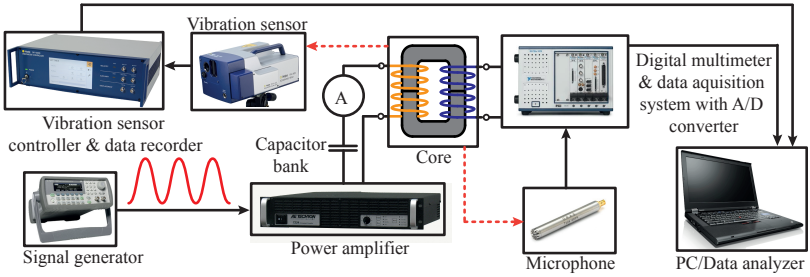

Figure 5.5: Setup for vibration and acoustic noise measurement.

voltage is measured by a digital multimeter (NI PXI-4071) and sent to a PC as feedback signal to regulate the output voltage of the signal generator by using the LabVIEW software.

The vibration of the core is measured with a laser scanning vibrometer (Polytec PSV-400) controlled by the controller (Polytec OFV-5000). The core is placed on a vibration isolated table to avoid the disturbance from the environment. The measured signal is decoded to a velocity, acquired by the data recorder and sent to the PC for further analysis.

The acoustic measurement is carried out by measuring the sound pressure in an anechoic room as shown in Fig. 5.6. The inner dimension of the room is much larger than the size of the measured core. Since the frequency of interest is from 1 kHz up to 20 kHz, the maximal wavelength of the sound determined by the lowest frequency is

$$\lambda = \frac{c}{f_s} = \frac{343\,\mathrm{m/s}}{1000\,\mathrm{Hz}} = 0.343\,\mathrm{m} \tag{5.6}$$

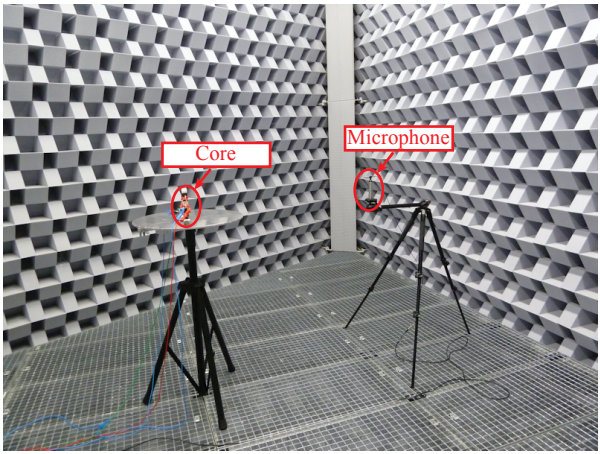

Figure 5.6: Anechoic room for the acoustic noise measurement.

The largest dimension of the measured core is roughly 17 cm, which is approximately half of the wavelength calculated by (5.6). Therefore, the measurement distance should be at least larger than the calculated wavelength. For convenience, the measurement distance is chosen to be 1 m.

On the other hand, the central frequency of the corresponding 1/3-Octave band is also 1000 Hz. Therefore, the distance from the microphone to the wall is at least 1/4 of the wavelength according to this frequency, which is approximately 0.086 m. The required distance is therefore well satisfied by the anechoic room for measurement.

A set of 1/4 inch free-field microphone with a preamplifier (G.R.A.S. 40PH) is used for measurement, which is a pre-polarized condenser microphone with a CCP type supplied preamplifier. The measured voltage signal is acquired by the dynamic signal analyzer (NI PXI-4462) and then sent to the PC.

Vibration measurements are performed on three surface areas on magnetic cores as indicated in Fig. 5.7, i.e. the front, side and top surfaces. Accordingly, the acoustic measurement are also performed separately from three directions (x, y, z-direction) normal to these surfaces. (For the ring core, only two surfaces are measured due to its symmetry). During both vibration and acoustic measurements, the sensor (vibrometer or microphone) is fixed at the same location while the core is rotated in order to measure each surface/direction. The desired peak flux density B_m is obtained by providing the calculated excitation voltage U according to

$$U = \sqrt{2}\pi f_\mathrm{s} N B_\mathrm{m} A_\mathrm{eff} \tag{5.7}$$

where f_s is the excitation frequency, N is the number of turns of the excitation winding and A_eff is the effective cross-sectional area of the core given in the data sheet.

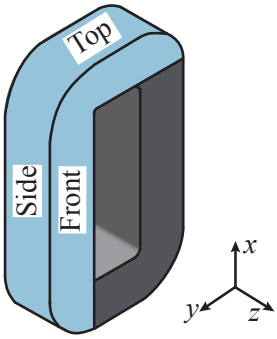

Figure 5.7: Surface areas of the core for vibration measurements.

5.3 Measurement results and discussions

By utilizing the measurement setup as described in the previous section, vibration and acoustic measurements are performed separately on different cores and windings excited with a sinusoidal voltage/current. Measurement results are analyzed and discussed below.

5.3.1 Eigenfrequencies and mode shapes of the rectangular uncut core

To investigate the eigenmode of the magnetic core, the vibration of the nanocrystalline rectangular uncut core is measured by means of a frequency sweep. The core is hanging as shown in Fig. 5.8 to enable a 'free' vibration condition. The top surface is measured by turning over the core for 90 degrees. The excitation voltage of the core applied on a 4-turn winding is a chirp signal amplified by 20 times with the power amplifier. To avoid the LC-resonance between the capacitor bank and the magnetizing inductance, the frequency sweep is started from 300 Hz and performed up to 20 kHz. Since the flux density is lower at a higher frequency with the same amplitude of the excitation voltage, the induced magnetic force is reduced with the increase of the frequency. In order to have an obvious mechanical response of the core in the whole frequency range for measurements, the frequency sweep is divided into 3 sub ranges by applying different amplitudes of excitation voltages: from 300 Hz to 5 kHz with 2 V, from 5 kHz to 10 kHz with 20 V and from 10 kHz to 20 kHz with 40 V.

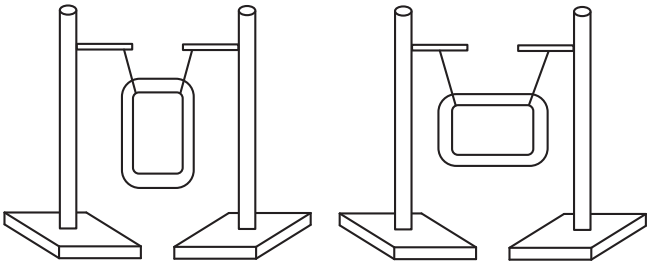

Figure 5.8: Vibration measurement setup for the eigenmode analysis.

As mentioned, the scanning vibrometer measures a set of points located on the surface of the object, where the vibration in the direction perpen-

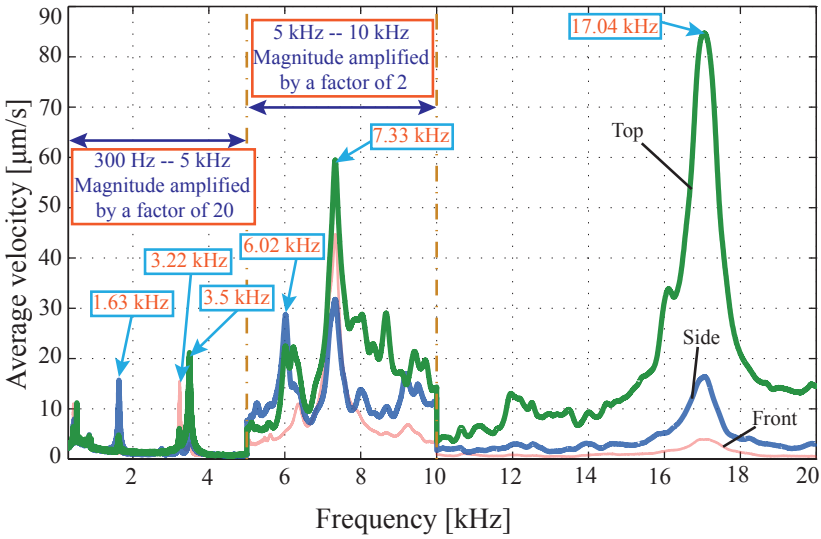

Figure 5.9: Frequency spectrum of the measured average surface velocity of the nanocrystalline rectangular uncut core by means of a frequency sweep. Eigenfrequencies are indicated with numbers.

dicular to the surface are measured. In Fig. 5.9, the frequency spectrum of the measured average velocity of each selected surface area are shown together. To have a better visibility, the magnitude of the velocity from 300 Hz to 5 kHz and from 5 kHz to 10 kHz are multiplied by a factor of 20 and 2 respectively. As can be seen from the frequency response shown in the figure, several eigenmodes of this core are within the audible frequency range. Frequencies of the excitation voltage and its harmonics may coincide with these eigenfrequencies and result in a mechanical resonance. The comparison of measured amplitudes on different surfaces evidently show that the top surface has the most significant vibration above 5 kHz, followed by the side surface while the vibration on the front surface is relative weak. This indicates that the tape wound core is more prone to vibrate in directions perpendicular to lamination layers.

Since tape wound cores are composed of magnetic material together with the epoxy resin as isolation layers between lamination layers as well as varnish outside of the core, mechanical properties of the core is anisotropic.

As introduced in [82], the laminated core can be approximated by an orthotropic structure where the in-plane (lamination layer) material property is assumed to be homogeneous while the material exhibits different properties in the direction perpendicular to the plane. In case of the measured core, vibrations measured on the side and the top surface demonstrate the out-of-plane behavior while the vibration on the front surface is related to the in-plane properties.

As illustrated in Fig. 5.10 for the first 3 dominant eigenmodes identified by measurements, similar mode shapes are observed on the side and the top surfaces which are different from mode shapes on the front surface. The first and the third mode shapes illustrate the flexure deformation of the core limbs and yokes while the second mode shape shows the torsional deformation. At higher frequencies, mode shapes are mixed with low order vibration modes and cannot be clearly distinguished.

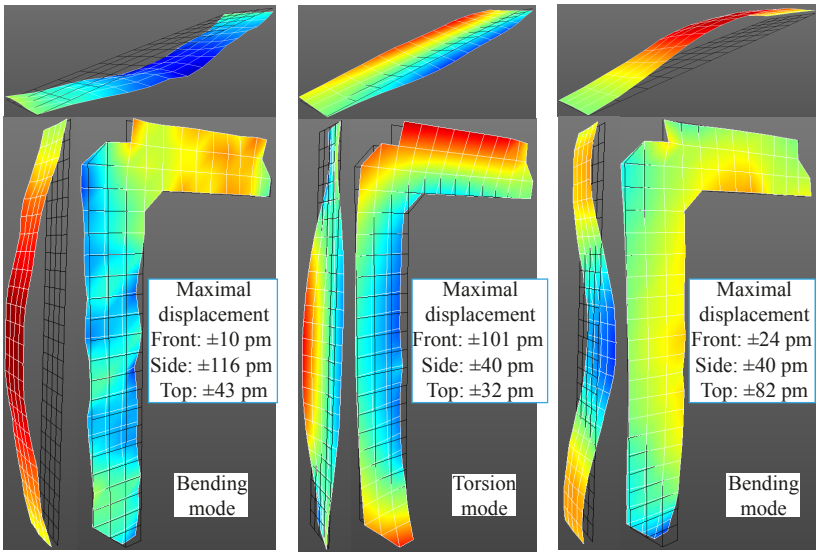

(a) Mode shape at 1.63 kHz (b) Mode shape at 3.23 kHz (c) Mode shape at 3.5 kHz

Figure 5.10: First 3 dominant eigenmodes of the nanocrystalline rectangular uncut core identified from the vibration measurement.

5.3.2 Comparison of core materials

To compare the influence of material properties, magnetic cores listed in Table 5.1 are measured. During the measurement, all cores are placed directly on the table without any additional mechanical mounting.

Vibration velocity and SPL comparison

In Fig. 5.11 and Fig. 5.12, measured average surface velocities[i] and sound pressures of these cores under the excitation of a 4 kHz sinusoidal voltage are shown. Since only harmonics in the audible frequency range are of interest, all results are calculated by RMS values of the 1st to the 5th harmonics.

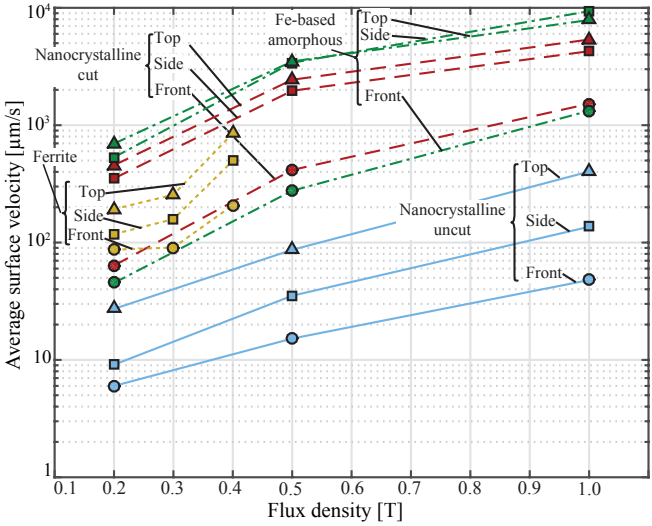

Figure 5.11: Measured average surface velocities of magnetic cores based on different materials under the excitation of a 4 kHz sinusoidal voltage (only harmonics up to 20 kHz are taken into account).

The comparison between the nanocrystalline cut and uncut cores indicates that the vibration is amplified by a factor of more than 10 while the sound pressure is 20 dB to 30 dB higher in case of the cut core when

[i]The laser vibrometer measures the velocity in the direction of the laser. For a curved surface, the measured velocity is not equal to the normal velocity of the surface.

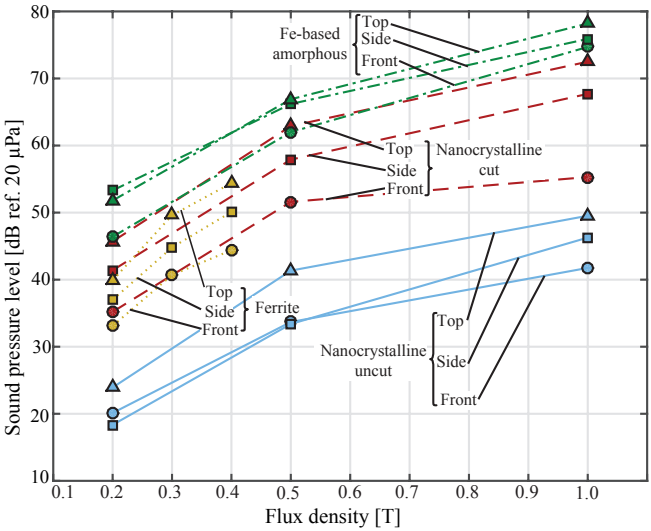

Figure 5.12: Measured sound pressure levels of magnetic cores based on different materials under the excitation of a 4 kHz sinusoidal voltage (only harmonics up to 20 kHz are taken into account).

an air gaps is present. Due to the contact of the two core parts induced by mechanisms as shown in Fig. 3.10 and Fig. 3.11, the enhancement of the vibration is quite significant especially on the top surface. Although cut cores are preferred for transformers due to the convenience of mechanical construction, they are acoustically unfavorable [121].

The comparison of cut cores made by different materials shows that the Fe-based amorphous core do have stronger vibrations and more acoustic noise emissions than cores made by other two materials due to a significantly larger magnetostriction (λ_s=27µm/m). The ferrite core is only measured at low flux density levels and it can be seen that the vibration and noise emission is less than other two cut cores. Since the magnetostriction of the Mn-Zn ferrite is small and negative, it causes a contraction of core limbs. Therefore, the magnetostrictive deformation at the air gap region is in the opposite direction to the the deformation caused by the Maxwell force. These two effects are assumed to be partly canceled with each other and cause less vibrations.

Further comparison among different surfaces/directions for each individual core generally shows the same relation of the vibration and the noise emission: top > side > front surface, which has already been shown in the frequency sweep result. The weak vibration on the front surface is mainly due to a smaller magnetostrictive strain. Since the z-direction is perpendicular to magnetic flux lines, the magnetostrictive strain is only half of the value in the field direction according to (3.19). Also, the dimension of the core in the z-direction is relatively small (i.e. the thickness d in Fig. 5.3) compared with dimensions in the x and the y-direction. According to the definition in (3.17), the magnetostrictive strain is also small. The stronger vibration on the top surface compared with the side surface is caused by a larger magnetostrictive strain since the length $b > c$ (Fig. 5.3). In case of the cut core, the strike of core pars at the air gap directly enhances the vibration in the x-direction and also causes more vibration in the y-direction. The difference of vibration intensities between the perpendicular and the parallel direction of lamination layers is more apparent.

It should be pointed out that the measured surface velocity indicate the vibration on the measured surface while the measured sound pressure in one direction is mainly emitted from the surface perpendicular to this direction, but acoustic waves generated from other surfaces also have influences on measurement results.

Distribution of vibration intensity

For a more detailed analysis, areas with relatively large magnitudes of the surface velocity on measured surfaces of each core are roughly depicted in Fig. 5.13. Here vibrations of highlighted areas are not in phase, i.e. deformations of these areas do not appear at the same time. These numbers only represent the highest amplitudes of the measured surface velocity in these areas.

On the top surface, the area with the largest vibration is located in the middle of the measured surface, which is the same for all three cores. This is related to the bending mode of the yoke as shown in Fig. 5.10. On the front surface, the intensive vibration appears at the corner as shown for nanocrystalline cores and is related to the torsion mode. On the side surface, the arc area (near the corner) are subject to a strong vibration which is related to the bending mode of the core limb. Vibrations in these areas are

amplified by the force at the air gap region in case of cut cores. These forces also directly cause strong vibrations in the nearby regions. It can be noticed that vibrations measured on the upper side and the lower side half cores are not symmetric. The reason is that the vibration of the lower side half core is influenced by the gravity of the upper side half core and also the friction with the surface of the table.

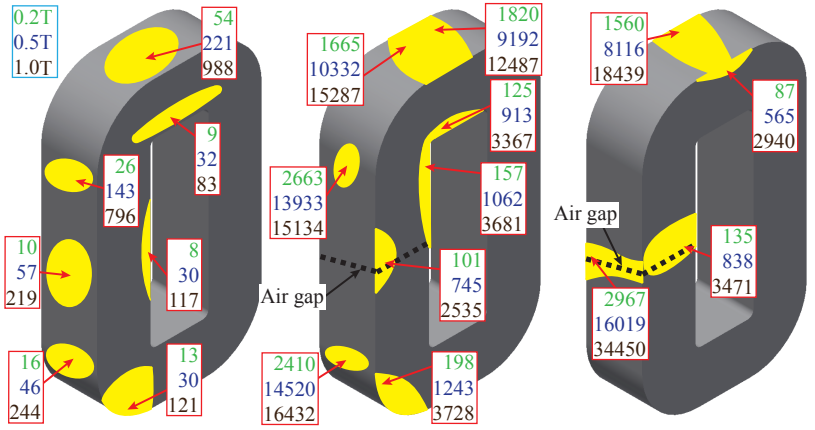

(a) Nanocrystalline uncut core (b) Nanocrystalline cut core (c) Fe-based amorphous cut core

Figure 5.13: Areas with relatively high velocities on measured surfaces of the nanocrystalline and the Fe-based amorphous cores excited by a 4 kHz sinusoidal voltage. Numbers indicate measured points with maximal surface velocities (RMS value) in [µm/m] calculated from the 1st to the 5th harmonics.

The Co-based amorphous alloy VITROVAC 6025Z has the same saturation magnetostriction compared with the VITROVAC 6030 alloy as given in Table 4.1 but a lower saturation flux density (0.58 T). Magnetic cores made by this material is not commercially available with a rectangular shape. Therefore, a pair of cut and uncut ring cores are measured for comparison. The dimension of the ring core is O.D.×I.D×H=90 mm×51 mm×25 mm.

Measurement results of these cores under the excitation to 0.4 T are listed in Table 5.2 and shown in Fig. 5.14 to compare with the ferrite core. As can be seen, the ring core also presents a larger vibration/noise emission in the direction perpendicular to lamination layers. The uncut ring core

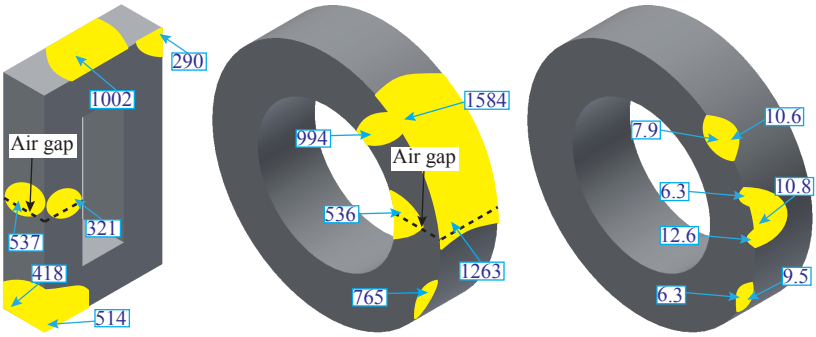

(a) Ferrite core (b) Co-based amorphous cut core (c) Co-based amorphous uncut core

Figure 5.14: Areas with relatively high velocities on measured surfaces of the ferrite and the Co-based amorphous cores excited to a flux density of 0.4 T with a 4 kHz sinusoidal voltage. Numbers indicate measured points with maximal surface velocities (RMS value) in [μm/s] calculated from the 1st to the 5th harmonics.

shows an extremely small vibration as well as a low noise emission due to the near-zero magnetostriction of this material. On the other hand, the cut core shows more vibration and noise emission compared to the ferrite core. In this case, the vibration can be assumed mainly caused by forces at air gap regions. Since the size and weight of measured ring cores is smaller compared to other cores, the upper half part of the cut core is more prone to vibrations.

Table 5.2: Comparison of vibration and sound pressure measurement results for the ferrite and the Co-based amorphous cores under the excitation of a 4 kHz sinusoidal voltage to 0.4 T

Core	Average surface velocity (μm/s)			Sound pressure (dB ref. 20 μPa)		
	Front	Side	Top	Front	Side	Top
Ferrite	192.6	255.6	851.5	44.4	50.1	54.4
VITROVAC cut	351.2	735.7	N/A	46.7	56.8	N/A
VITROVAC uncut	3.3	3.9	N/A	-16.2	2.5	N/A

Overall comparison of the A-weighted SPL

As mentioned, the sound source is usually evaluated by scaling the SPL with the A-weighting filter according to the sensitivity of human ears in the audible frequency range. As an overall comparison of these cores, A-weighted SPL averaged by measured values from the three directions are shown in Fig. 5.15. The measured background noise is approximately 30 dBA in the anechoic room.

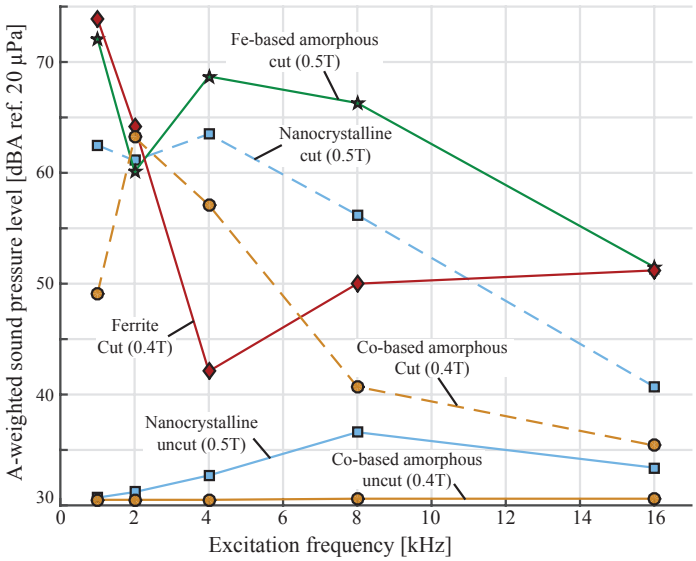

Figure 5.15: A-weighted sound pressure levels of cores made by different materials under the excitation of a sinusoidal voltage at various frequencies.

As can be seen, there is no general rule regarding the dependency of the SPL on the excitation frequency. The difference of the SPL can be quite significant when excited at different frequencies, which is strongly related to resonant frequencies of each individual core. The noise level of the two uncut cores are lower than that of cut cores at all measured excitation frequencies. Especially for the Co-based amorphous uncut core, the measured SPL is close to the noise level of the background.

5.3.3 Comparison of geometric shape

To compare the influence of the geometric shape, three nanocrystalline uncut cores are measured. During the vibration measurement, an additional setup as shown in Fig. 5.16 is used to mount the cores, where a part of the core is fixed on a metal plate with a relative large weight compared to measured cores. To reduce the mechanical influence from the setup, soft foam materials are inserted between the measured core and the metal plate for damping. During the acoustic measurement, the mechanical setup is removed to avoid its reflection of sound waves.

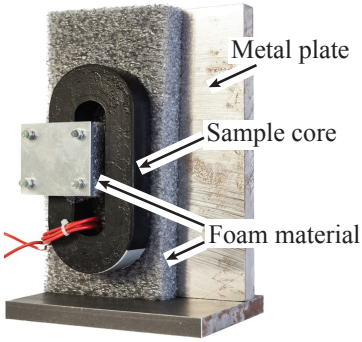

Figure 5.16: Mechanical setup used for the vibration measurement of nanocrystalline uncut cores.

Vibration velocity and SPL comparison

In Fig. 5.17, measured average surface velocities are shown. Same as the previous result, it is concluded that the vibration in the lamination direction is obviously stronger than in the parallel direction to lamination layers regardless of the geometric shape of the core. The comparison of velocities on each surface among these cores show that the vibration intensity has the following relation: rectangular core > oval core > ring core. The measured sound pressure also confirms this relation as shown in Fig. 5.18.

The comparison among different surfaces/directions for each individual core is already shown for the rectangular core, i.e. top > side > front surface for the vibration/noise emission. This relation is still valid for the oval and the ring core in terms of the vibration. However, it is not valid in

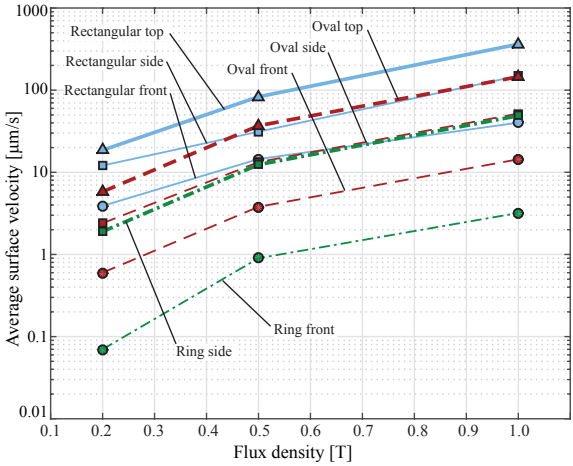

Figure 5.17: Measured surface velocities of nanocrystalline uncut cores with different shapes under the excitation of a 4 kHz sinusoidal voltage (only harmonics up to 20 kHz are taken into account).

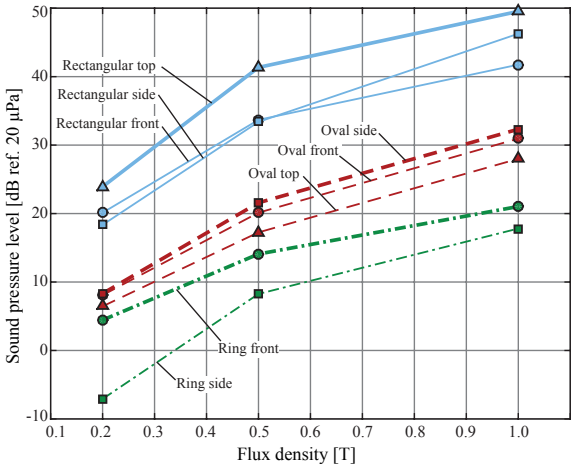

Figure 5.18: Measured sound pressures of nanocrystalline uncut cores with different shapes under the excitation of a 4 kHz sinusoidal voltage (only harmonics up to 20 kHz are taken into account).

the case of the sound pressure. For these two cores, the lowest sound pressure is measured towards the arc surface on which the highest vibration velocity is detected. This is assumed to be caused by the scattering of sound waves emitted from the curved surface which propagate towards different directions. On the contrary, emitted sound waves from a flat surface mainly propagate towards the normal direction of the surface, i.e. towards the microphone.

Harmonics of the vibration velocity

For the analysis in frequency domain, harmonics of average vibration velocities in the audible frequency range are shown in Fig. 5.19, where measurement results at 1 T are analyzed. It can be seen that the major contribution to vibrations are from the 8 kHz and the 16 kHz harmonics, which are the first and second harmonics of the magnetostriction. The first harmonic is usually dominant and has the major contribution to the acoustic noise. Accordingly, the deformation of cores due to the 8 kHz harmonic at the

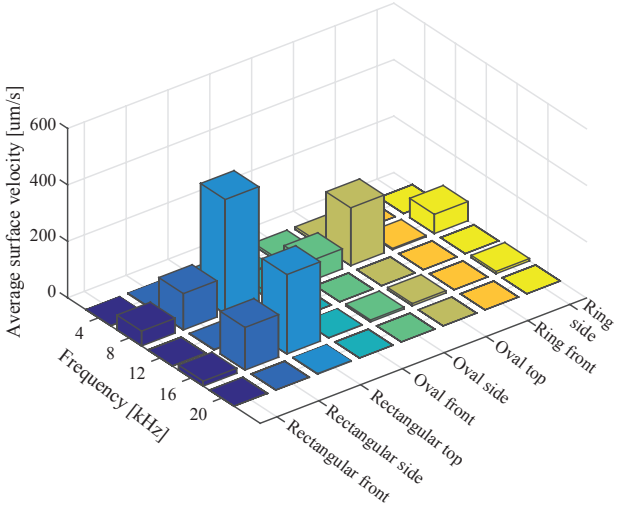

Figure 5.19: Harmonics (up to 20 kHz) of the average surface velocity of nanocrystalline uncut cores with different shapes under the excitation of a 4 kHz sinusoidal voltage to 1 T.

instance when the maximal positive displacement (towards the laser) appears are shown in Fig. 5.20. Due to the low saturation magnetostriction of the nanocrystalline material, the maximal deformation is within a very low range (< 20 nm) even at this high flux density level. These values are in the similar range compared with simulation results presented in Table 4.3.

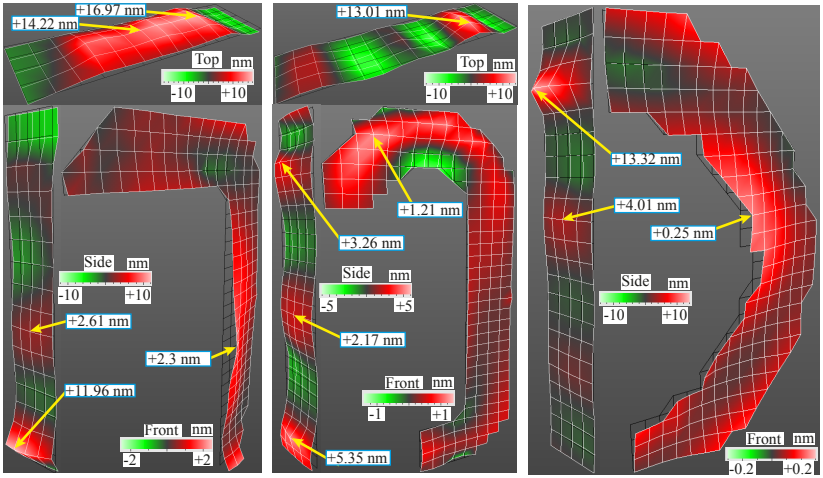

(a) Rectangular core (b) Oval core (c) Ring core

Figure 5.20: Snapshot from the vibration animation of the 8 kHz harmonic at the instance when cores show maximal outward deformations (towards the laser) under the excitation of a 4 kHz sinusoidal voltage to 1 T.

Overall comparison of the A-weighted SPL

As an overall evaluation, the A-weighted SPL of nanocrystalline uncut cores under the excitation at different frequencies to 1 T are shown in Fig. 5.21. As indicated in the graph, the ring core features the lowest acoustic noise emission at all frequencies for measurement. The SPL of the oval core is a few dB higher than the SPL of the ring core but lower than the SPL of the rectangular core. All three cores show obviously higher noise emission under the excitation at 8 kHz which might be due to the mechanical resonance.

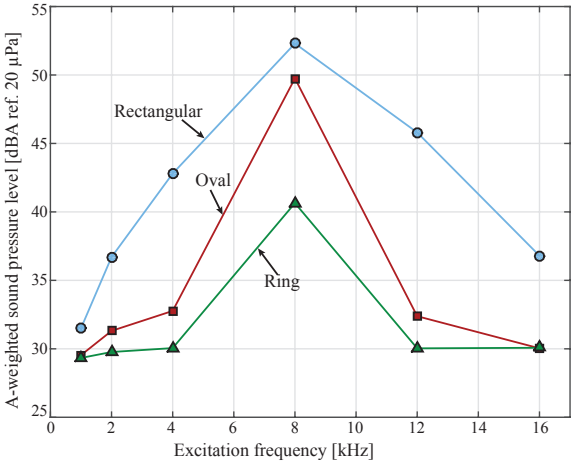

Figure 5.21: A-weighted sound pressure levels of nanocrystalline uncut cores with different shapes under the excitation of a sinusoidal voltage to 1 T at various frequencies.

5.3.4 Vibration and acoustic noise of the winding

To compare the vibration of the winding with the vibration of the core, measurements are performed on part of the front and the top surface of the nanocrystalline rectangular uncut core as well as on the surface of one turn of the 4-turn excitation winding. Measurement results of some points on the front surface shown in Fig. 5.22 (a) indicate that measured surface velocities of the winding and the core are in a comparable range. It should be pointed out that the winding and the core are mechanically coupled in this case. Therefore, the core vibration also has an influence on the winding vibration.

On the other hand, the vibration velocity on the top surface of the core shown in Fig. 5.22 (b) is much higher than the winding vibration velocity which is in the range of measured values shown in Fig. 5.22 (a). As already shown in core measurement results, the vibration on the front surface of the core is relatively weak. Therefore, the vibration of the winding is relatively small compared with the vibration of the core in case that a relatively low current (e.g. inductor built with an uncut core) is flowing through the winding.

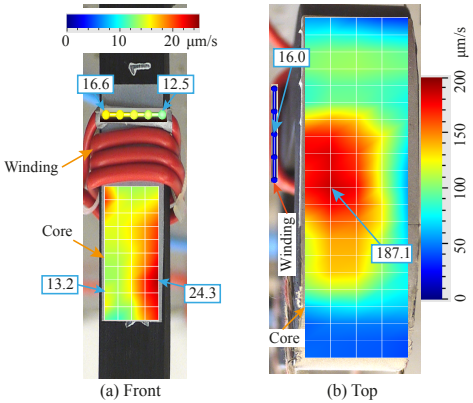

Figure 5.22: Comparison of measured vibration velocities of the winding and the nanocrystalline uncut core excited to 0.5 T at 4 kHz.

In case of a cut core excited to the same flux density level, the magnetizing current is larger, and the Lorentz force acting on the winding also increases. Furthermore, transformer windings usually conduct a high current which also results in a large Lorentz force. In Fig. 5.23 the vibration and the sound pressure measured on a winding constructed with 60 turns of Litz-wire (620×0.1 mm, 3 layers, 20 turns per layer) fed by a 20 A peak sinusoidal current are shown. It can be seen that the maximal vibration velocity can reach over 200 µm/s, which is in the range of the vibration velocity on the front surface of the nanocrystalline uncut core as shown in Fig. 5.22(b). In case that the core vibration is relatively large, e.g. the Fe-based amorphous cut core (ref. Fig. 5.13), the vibration velocity in some areas can reach over 10 mm/s, which is much higher than the measured winding vibration velocity in this case.

The measured sound pressure of the winding shown in Fig. 5.23 (b) indicates that the A-weighted SPL is 50 dBA, where the first harmonic is dominant in the frequency spectrum. In this case, the amplitude of the current is much higher compared to the excitation current during the uncut core measurement. Consequently, the noise of the winding is higher than the nanocrystalline uncut core excited to 1 T at 4 kHz as shown in Fig. 5.21. Therefore, it can be concluded that the vibration of the winding can be considered to have a minor contribution to the acoustic noise

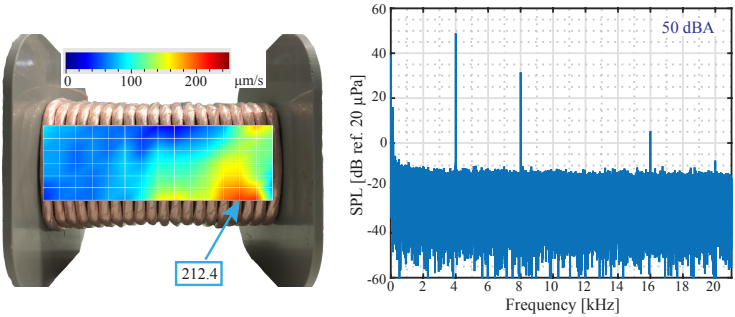

Figure 5.23: Measured vibration velocity and sound pressure spectrum of a winding constructed with round Litz-wires.

emission of transformers only if the core vibration is relatively large and the current in the winding is relatively low. This is also mentioned for large power transformers with a low induction level and improved core designs, where the load current dependent winding vibration can have a significant contribution to the transformer noise [136].

Discussion about harmonics of the vibration

From the measurement result, it can be noticed that the frequency spectrum of measured vibration velocities and sound pressures contains the fundamental component at the excitation frequency and higher order harmonics, which are present in both core and winding measurement results.

In case of a pure AC sinusoidal excitation, the winding current/voltage of transformer only contains a single harmonic at the excitation frequency. It has been discussed previously that the Maxwell force and the magnetostriction are proportional to the square of the flux density. Therefore, the vibration of the core is proportional to the square of the excitation voltage:

$$\alpha_{\text{Core}} \propto U^2 \tag{5.8}$$

Similarly, the Lorentz force is dependent on the current and the winding vibration is proportional to the square of the current:

$$\alpha_{\text{Winding}} \propto I^2 \tag{5.9}$$

The square relation between the vibration and voltage/current has been widely reported for large-scale power transformers, e.g. in [137]. Theoretically, the frequency spectrum of the core and the winding vibrations under a pure AC sinusoidal excitation only contains a single harmonic at twice of the excitation frequency. However, due to the nonlinear hysteresis between the flux density B and magnetic field strength H, the magnetostriction and electromagnetic forces contain also higher order harmonics (normally odd harmonics) [137, 138], which lead to higher order even harmonics (due to the square relation) in vibrations, e.g. 8, 16 and 32 kHz harmonics by a 4 kHz excitation. Nevertheless, odd harmonics (e.g. 4, 12 and 20 kHz) are also detected in the measured vibration signal, for both the core and the winding.

Magnetic core In case of the core vibration, odd harmonics can be caused by the DC magnetization, which leads to an asymmetrical magnetostriction within one magnetization cycle [139]. This phenomenon is well known for large power transformers, where even a small DC magnetization of the core can lead to a significant increase of the vibration [136]. Under the normal pure AC operation conditions, the excitation voltage has no DC component, the DC magnetization of transformers in power system can be caused by e.g geomagnetic induced current (GIC) and ohmic coupling effects between the HVDC and the AC transmission lines [140]. In case of the MFT operated in a DABC, DC bias current can be induced due to asymmetrical operating states of the upper and lower side switches [141].

Due to the existence of the DC magnetization, the magnetostriction during one magnetization cycle becomes asymmetrical as shown in Fig. 5.24. This phenomenon has been investigated for the electrical steel as introduced in [139], where experimental results show that the asymmetry of the magnetostriction butterfly loop increases with the superposed DC magnetic field. As a result, odd harmonics in magnetostriction are induced.

Even if there is no DC magnetization, asymmetrical magnetostriction may still exist. In [142], the frequency dependency of the magnetostriction is investigated by experimental measurements performed on the as-cast ribbon of the Fe-based amorphous alloy. It is concluded that the symmetry of the magnetostriction is reserved only if the direction of the applied magnetic field and the magnetic equivalent easy axis (EEA) of the ribbon is perpendicular or in parallel. In both cases, the symmetry (or the even condition

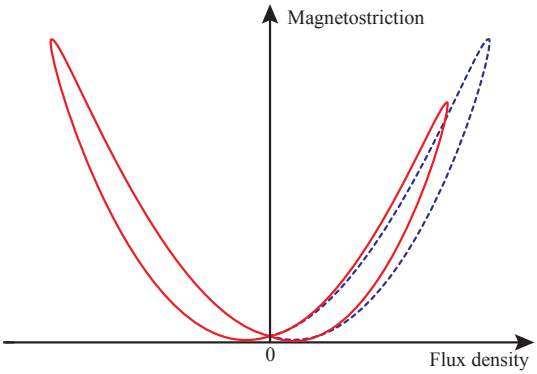

Figure 5.24: Asymmetrical magnetostriction curve.

of the magnetization variation) is fulfilled and the magnetostriction only contains even harmonics. Otherwise, the symmetry of the magnetostriction is broken which results in odd harmonics. This effect is frequency dependent: at a very low frequency, there exists the frequency doubling effect of the magnetostriction. With the increase of the frequency, the distortion of the magnetostriction becomes more significant and odd harmonics appear. For example, the frequency doubling effect is no longer given above 60 Hz according to measurement results shown in [142] for the METGLAS 2605SA1 ribbon.

Since the measured ribbon is in the as-cast state, the EEA is not in parallel to the ribbon axis but with an angle of 48°. In practice, ribbons of commercial amorphous and nanocrystalline cores are usually annealed under a strong magnetic field which leads to a field induced anisotropy. As a result, an additional uniaxial anisotropy with an easy axis along the field direction is created. According to the manufacturer's information, the METGLAS 2605SA1 ribbon is annealed in a longitudinal magnetic field (field direction parallel to the ribbon axis) [127]. This results in a Z-type hysteresis loop with a high remanence ratio ($B_r/B_s > 0.9$) as shown in Fig. 5.25. On the contrary, the VITROPERM 500F ribbon is annealed in a transverse magnetic field (field direction perpendicular to the ribbon axis) [120]. Therefore, a flat F-type hysteresis loop as shown in Fig. 5.25 with a low remanence ratio ($B_r/B_s < 0.2$) is created.

In both cases, the symmetry condition of the magnetostriction should

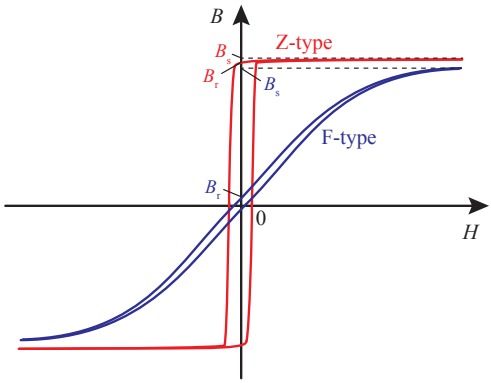

Figure 5.25: F-type and Z-type of hysteresis B-H loop.

be fulfilled. However, in practice, magnetic flux lines are not in parallel to the ribbon axis at some locations of the core. Consequently, the symmetry condition of the magnetostriction is broken at these locations and odd harmonics appear in the magnetostriction. Since a capacitor in series connection with the winding is used during the core measurement in this work, there is no DC magnetization. As mentioned, vibration measurements of the amorphous and the nanocrystalline cores are performed under the excitation in the kHz range. Therefore, it is assumed that these odd harmonics, which appear in the measured core vibration velocity spectrum, are induced due to the asymmetrical magnetostriction at high frequency.

Winding In case of the winding, a DC current (e.g. in case of the short-circuit fault) can lead to a harmonic of the Lorentz force and of the vibration at the excitation frequency [143]. Higher order odd harmonics of the winding vibration can be induced if there is also higher order even harmonics in the current. As presented in [144], if the current contains n harmonics, then the Lorentz force can be expressed as:

$$F_{\text{Lorentz}} \propto I^2 = \sum_{i=1}^{n} \hat{I}_i^2 \cdot \sin(2\pi f_i + \phi_i) \tag{5.10}$$

where f_i, $\hat{I}_i$, and ϕ_i is the frequency, amplitude and phase angle of the i-th current harmonic.

Consequently, the frequency spectrum of the Lorentz force contains the following components:

- DC component ($f_i = 0$): contributed by all current harmonics, which leads to a static deformation of the winding. This deformation does not contribute to the dynamic vibration and is not related to acoustic noise emission of the winding.
- Components at double frequency $2f_i$ of each current harmonics with the amplitude of $\hat{I}_i^2$ and the phase angle of $(2\phi_i + \pi/2)$.
- Difference components at $|f_i - f_j|$, with the amplitude of $\hat{I}_i \cdot \hat{I}_j$ and the phase angle of $(\phi_i - \phi_j + \pi/2)$ generated from two current harmonics at different frequencies f_i,f_j $(i \neq j)$.
- Sum components at $(f_i + f_j)$, with the amplitude of $\hat{I}_i \cdot \hat{I}_j$ and the phase angle of $(\phi_i + \phi_j - \pi/2)$.

It can be noticed that if the current only contains odd harmonics (no DC component, no even harmonic), then the Lorentz force only contains even harmonics due to the square relation. Furthermore, the vibration velocity is also proportional to the square of the current [137] while the sound pressure is proportional to the square of the vibration velocity and therefore proportional to the 4th power of the current [145]. As a result, both the vibration velocity and the sound pressure should not have odd harmonics if the current only contains odd harmonics.

Considering the vibration and the acoustic noise measured on the winding in this work (ref. Fig. 5.23), the odd harmonic at the excitation frequency (4 kHz) is also present. Due to the series capacitor, there is neither DC current nor even harmonics flowing through the winding. Consequently, it is assumed that this 4 kHz odd harmonic in the vibration and the sound pressure spectra is not excited by electromagnetic forces. It is also reported in [86] that the winding vibration contains the odd harmonic at the excitation frequency, and its amplitude can be even higher than the harmonic at twice of the excitation frequency (as shown in this case). This harmonic is explained to be caused by nonlinear mechanical behaviors and is related to the tightness of the winding. In fact, the cause of odd harmonics in the winding vibration signal due to a mechanical fault has been considered for diagnosis purposes, especially for detecting the winding deformation or

looseness [138, 146, 147]. In normal conditions, measured vibrations on the winding only contain even harmonics. However, if the winding is deformed, odd harmonics may appear, which is experimentally shown in [138, 147]. Nevertheless, mechanisms of odd harmonics in vibration signals due to the mechanical nonlinearity is not well explained in these publications.

5.4 Summary and conclusions

In this chapter, fundamentals of vibration and acoustic noise measurements are briefly introduced with focus on vibration and acoustic sensors and the measurement environment. In this work, a laser scanning vibrometer is used for the vibration measurement while the acoustic noise measurement is performed in an anechoic room by using an 1/4 inch free-field condenser microphone. Vibration and acoustic noise measurements are performed on magnetic cores made by various materials and with different geometric shapes as well as on windings. The excitation for measured objects is a sinusoidal voltage/current in the medium frequency range.

The vibration measurement result of a nanocrystalline rectangular uncut core by the frequency sweep shows that eigenfrequencies of the core with such a size are well in the audible frequency range. Therefore, frequencies of the excitation voltage/current and its higher order harmonics in the kHz range may coincide with eigenfrequencies of the core and results in a mechanical resonance. The comparison between the cut and the uncut core shows that the present of air gaps causes excessive magnetic forces which induce large vibrations directly near the air gap region and enhance vibrations of other core parts due to the strike of separated core parts. As a result, the cut core has a much higher acoustic noise emission compared with its uncut counterpart.

The investigation of magnetic cores is focusing on the influence of material properties and geometric shapes. Several magnetic materials with interest for medium frequency applications are compared. The ferrite core features low acoustic noise emission but its application for transformers operated at a few kHz maybe limited due to the low saturation level if a high power density is required. For the Fe-based amorphous core, the relatively strong vibration and accordingly a large acoustic noise emission due to the large magnetostriction is confirmed by measurement results. On the contrary, the Co-based amorphous alloy has a near-zero magnetostriction

which results in a much lower acoustic noise emission compared with the Fe-based amorphous alloy. Both vibration and acoustic measurements confirm that the nanocrystalline material is superior for a low noise transformer design. Moreover, this material is advantageous in terms of the power density and the efficiency compared with other core materials, which makes the nanocrystalline alloy the most suitable one for a highly efficient, compact and quiet MFT design.

Considering the individual core, vibration measurements indicate that the direction perpendicular to lamination layers of a tape wound core is subject to larger vibrations and more acoustic noise emissions compared with the direction parallel to lamination layers. In case of the rectangular core, the large curvature at corners leads to intensive vibrations on surfaces nearby which is related to the bending mode shape of the core. On the contrary, the vibration of a ring core is much weaker due to the more even-distributed magnetic field. Therefore, magnetic forces and magnetostrictive strains are also equally distributed over the entire core body. From the geometry point of view, the oval core is a combination of the rectangular shape and the ring shape. The acoustic performance of the oval core is in between, which gives a compromise for low acoustic noise and high power density.

The comparison between the core noise and the winding noise indicates that the winding has a major contribution to the acoustic noise if the core vibration is weak (e.g. in case of an uncut core with a low magnetostriction and/or a low induction level) and the current flowing through the winding is relatively small. Otherwise, the core noise is usually more significant than the winding noise.

Finally, harmonics of the vibration and the acoustic noise are analyzed. Although only the harmonic at twice of the excitation frequency should appear in the vibration and the sound if the excitation source is a pure AC sinusoidal signal, it has been shown that the harmonic at the excitation frequency and higher order harmonics are present in measurement results of the core and the winding. Both odd and even harmonics exist. Due to the absence of the DC magnetization and a sinusoidal excitation in this work, additional harmonics in the core vibration is assumed to be caused by the nonlinear hysteresis effect and the distortion of the magnetostriction. On the other hand, additional harmonics in the winding vibration is considered to be induced by the nonlinear mechanical interaction.

6 MFT design with consideration of acoustic noise

In chapter 4 and chapter 5, the impact of material properties and geometric shapes of magnetic cores on their vibration and acoustic emission has been discussed. In this chapter, the influence of these factors on the optimal design of the MFT is investigated. As a final evaluation, acoustic measurements are performed on a MFT prototype and results are presented.

6.1 Impact of core material and geometric shape on MFT design

To evaluate influences of the core material and the geometric shape on the design of MFTs, optimizations are performed separately for transformers by using the procedure shown in Fig. 2.8. Based on the optimal design parameters obtained by the combined optimization in chapter 2, specifications considered for the optimization of MFTs in this section are listed in Table 6.1.

Since the previously obtained turns ratio $N_{\mathrm{W}} \approx 3.07$ is not an integer, to get more flexibilities for choosing the number of turns, a turns ratio in the range of $3 < N_{\mathrm{W}} < 3.2$ is considered to be valid. This ensures $M > 1$ to enable the current falling stage during the time interval T_{III} as explained in chapter 2. Harmonics of the transformer current shown in Fig. 2.20 is used to calculate the winding loss. Furthermore, core dimensions and construction of the winding and Litz-wires are set to be free.

Table 6.1: Considered specifications for the MFT design to compare the influence of core materials and geometric shapes

MV side voltage U_1	1200 V
LV side voltage U_2	400 V
Power P_n	25 kW
Frequency f_s	4 kHz
Target leakage inductance $L_{\sigma,\text{target}}$	115 µH
Turns ratio N_w	$3 < N_w < 3.2$
Peak flux density B_{max}	80% of B_s
Maximal electric field strength E_{max}	8 kV/mm
Maximal fill factor of core window*	40%
Maximal allowable temperature	120 °C
Cooling system performance index	5 W/K/dm^3

* Ratio of the copper area to the core window area (without the area required for the isolation and the leakage inductance).

6.1.1 Influence of the core material

As mentioned before, a core material with a high saturation flux density and a low loss is essential for transformers to achieve high efficiency and high power density. To evaluate the influence of the core material on the MFT design, four commercially available core materials suitable for medium frequency applications are selected for comparison. In Table 6.2, relevant parameters used for calculations are listed. The Steinmetz parameters are given for (2.46) with f in [kHz], B in [T] and p_{Fe} in [W/kg].

In Fig. 6.1, specific losses at 4 kHz of these core materials depending on the flux density are shown. As indicated in the figure, the nanocrystalline material features slightly lower losses compared with the Co-based amorphous alloy which is much lower than the Fe-based amorphous material. The specific loss of the ferrite lies between the two amorphous materials.

By employing the optimization algorithm, optimal designs of the MFT with specifications given in Table 6.1 by using above mentioned core materials are derived. The transformer with the structure shown in Fig. 2.9 based on a rectangular core is considered. In Fig. 6.2, Pareto fronts of MFTs are shown, which are derived by optimizing transformers with various given boxed volumes. As shown in the graph, the power density of the MFT based

Table 6.2: Parameters of core materials for calculations

Material	B_s [T]	λ [W/(m·K)]	ρ [kg/(m^3)]	Steinmetz parameter		
				α	β	k
VITROPERM 500F	1.2	9	7350	1.8	2.3	0.66
METGLAS 2605SA1	1.56	9	7180	1.51	1.74	6.5
VITROVAC 6030F	0.82	9	7750	1.83	2.28	0.71
Ferrite PE90	0.43	5	4900	1.54	2.8	7.99

on the nanocrystalline material can reach over 10 kW/dm^3 due to its low loss and high saturation flux density. Depending on the specific core loss, the efficiency of the MFT with the same volume is lower when using a material

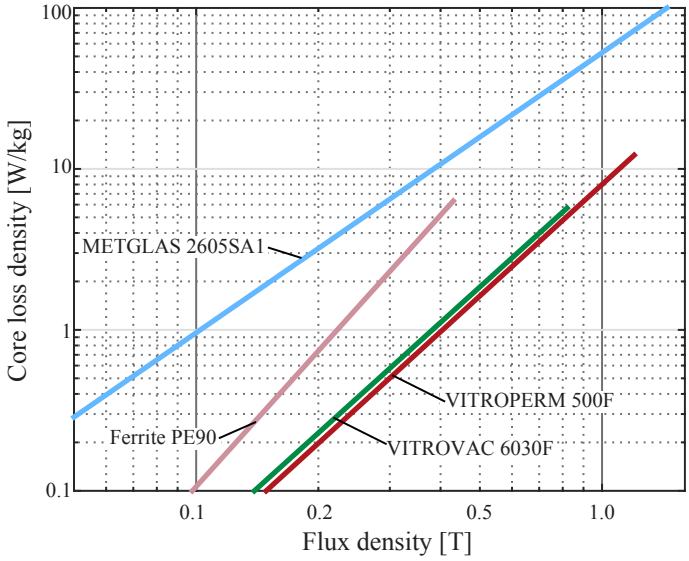

Figure 6.1: Core loss comparison of different materials depending on the flux density at 4 kHz.

with a higher loss. Compared with the MFT based on the VITROPERM 500F, the maximal achievable power density of the MFT based on the VITROVAC 6030F is lower due to the low saturation flux density (0.82 T) and further decrease of the maximal power density is observed for the MFT based on ferrite cores. Among these four core materials, the Fe-based amorphous alloy METGLAS 2605SA1 has the highest saturation flux density (1.56 T). However, the maximal achievable power density of transformers using this core material is the lowest due to the thermal limitation since this material has a relatively high loss.

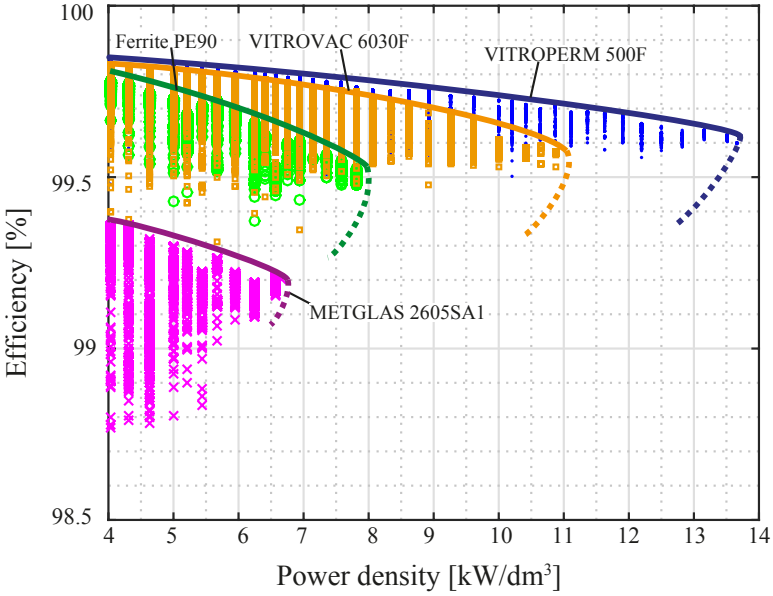

Figure 6.2: Pareto fronts of MFT designs with specifications given in Table 6.1 by using different core materials. The boxed volume of transformers is considered for the power density calculation.

Considering also the vibration and the acoustic noise measurement results presented in chapter 5, the comparison confirms that the nanocrystalline material is the most suitable one for a highly efficient, compact and silent transformer design in the medium frequency range.

6.1.2 Influence of the core shape

To compare the impact of the core geometric shape on the achievable power density of transformers, the optimization procedure is also applied on another three core shapes based on the VITROPERM 500F, i.e., the square, the oval and the ring core as simulated in chapter 4. The same structure of the transformer (shell type with concentric winding) as in the case of the rectangular core is also considered by using the square and the oval core. In case of the ring core, a more practical structure is mounting the low voltage winding directly on the core and the high voltage winding is wound outside of the low voltage winding. Calculation models used in the previous optimization procedure such as the thermal model need to be adapted to match the specific core shape.

Model adaption for the square core

The square core is basically the same as the rectangular core. The only difference is that the width and height of core window are equal, i.e. $b = c$. Therefore, after the calculation of the core window height according to (2.36), the minimal required core window width $b_{\min}$ is calculated by (2.35). An additional constraint $b_{\min} \geq c$ needs to be verified in this step. Other calculations are exactly the same as for the rectangular core.

Model adaption for the oval core

The shape and geometric parameters of the oval core is shown in Fig. 6.3. Due to the inaccuracy of the manufacturing process, the oval core used for measurement is irregular (e.g., $a \neq r_o - r_i$). For the calculation, a regular shape is considered where following equalities are valid:

$$\begin{cases} b = 2r_i & (6.1) \\ h = c + 2r_i + 2a & (6.2) \\ a = r_o - r_i & (6.3) \end{cases}$$

The number of free parameters is still 9, but b and c are selected to replace N_{L1} and d_{iso}. Therefore, after the generation of free parameters, the core dimension is defined since a, b, c are known and other dimensions can be calculated according to the equations given above.

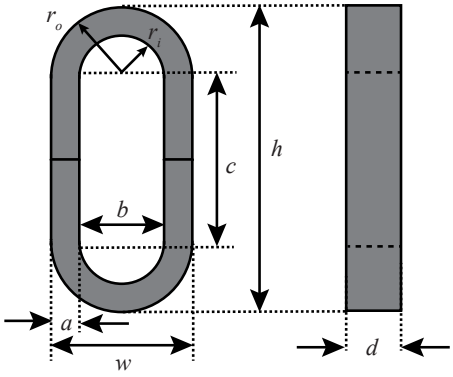

Figure 6.3: Geometric parameters of the oval core.

The arrangement of the winding is started from the inner winding (LV winding), from the inner layer to the outer layer. According to the available space for each layer, the winding is arranged to fill in the maximal available window height $h_{\max}$ as shown in Fig. 6.4. Apparently, $h_{\max}$ is different for different winding layers due to the arc part of the core. Based on the selected coordinate system, for the winding layer with center points located at $x = x_0$, the maximal available winding height is calculated as:

$$h_{\max} = c + 2y_0 = c + 2\sqrt{r_i^2 - (r_i - x_0)^2} \tag{6.4}$$

To determine the number of turns on each layer, the isolation distance at both ends needs to be subtracted from $h_{\max}$. Since the core window at the top and the bottom is arc shape, to ensure that the winding can fit the available window height, one turn is deducted from the calculated value. Therefore, for the winding with an outer diameter of d_a, the number of turns per layer N_{Lx} at the location $x = x_0$ with an available window height of $h_{\max}$ is given as

$$N_{Lx} = \left(\frac{h_{\max} - 2d_{iso}}{d_a} \right) - 1 \tag{6.5}$$

where d_{iso} is directly given as the thickness of the bobbin d_f, which also needs to be taken into account while calculating x_0, i.e., for the first layer $x_0 = d_f + d_a/2$. The result obtained by (6.5) needs to be rounded as an integer. In this way, the number of turns on each layer can be determined and all

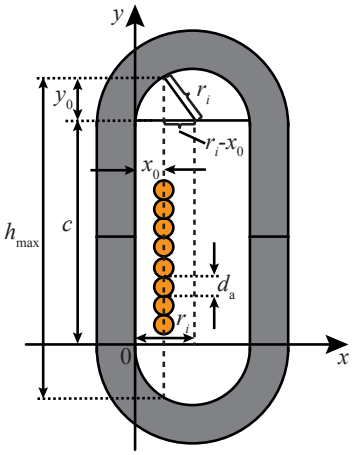

Figure 6.4: Determine the available window height $h_{\max}$ for arranging the winding layer at the location $x = x_0$ for the oval core.

winding positions are defined. The total winding width needs to be checked to ensure it does not exceed the core window width b.

Generally, for the oval core, the number of turns on each layer is different. Therefore, by calculating the winding length and the leakage inductance, each layer needs to be considered individually. Due to the arc shape, the model for calculating the electric field strength also needs to be adapted. Instead of mirroring the entire core window, a series of simulation charges is used to model the contour of the core window as shown in Fig. 6.5. For each turn, simulation charges are also placed inside of the conductor. The calculation process for $E_{\max}$ is the same as previously introduced for the rectangular core.

The thermal model also needs to be slightly adapted. As mentioned, the number of turns of each layer is different in case of the oval core. Therefore, the winding thermal resistance is calculated individually for each layer and the results are summed up to get the total thermal resistance. The part of the thermal resistance due to free convection needs to be adapted to match the arc surface. In case of the oval core, the top and bottom surfaces can be considered as half of a cylinder surface with the diameter of $(2a+b)$. The two arc surfaces are combined and considered as a complete cylinder surface

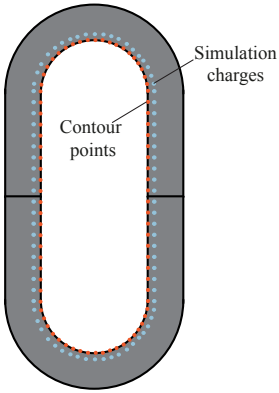

Figure 6.5: Arrangement of simulation charges and contour points for the oval core.

lying in the horizontal direction. For the outer surface of the cylinder, the characteristic length in (2.81) needs to be calculated as [101]

$$L_{\mathrm{Ch}} = \frac{\pi}{2}(2a+b) \tag{6.6}$$

The Nusselt number is calculated as

$$N_{\mathrm{u}} = \left[0.752 + 0.387\left(R_{\mathrm{a}} \cdot f_3(P_{\mathrm{r}})\right)^{\frac{1}{6}}\right]^2 \tag{6.7}$$

where the function of Prandtl number $f_3(P_{\mathrm{r}})$ is

$$f_3(P_{\mathrm{r}}) = \left[1 + \left(\frac{0.559}{P_{\mathrm{r}}}\right)^{\frac{9}{16}}\right]^{-\frac{16}{9}} \tag{6.8}$$

The area and the characteristic length of other surfaces accounted for calculating thermal resistances should also be adjusted to match the core shape. The thermal model is solved similarly as in the case of using the rectangular core.

Model adaption for the ring core

In case of using the ring core, the structure of the transformer is completely different. The number of free parameters is reduced to 7, i.e. a, N_1, N_{s1}, N_{s2},

d_{s1}, d_{s2} and d_{leak}. By giving the strand diameter and the number of strands, the outer diameter of the Litz-wire can be determined according to (2.30). To determine the core dimension, the winding arrangement inside the core window has to be defined.

As shown in Fig. 6.6, the LV winding is placed close to the core and the MV winding is located outside of the LV winding. The winding arrangement starts from the geometric center of the core with the MV winding arranged at first, from the inner layer towards the outer layer. Depending on the outer diameter d_{a1} of the Litz-wire, the first layer consists exactly 6 turns, which are placed circularly with a shift of 60°. To arrange the next layer, the perimeter of the circle through center points of the inner layer windings is calculated based on the known size of the inner layer and the inter-layer isolation distance d_{inter}. Then the maximal number of turns which can be fit into the next layer is calculated and these turns are equally distributed as a circle. The arrangement is performed further until all the turns of the MV winding are arranged. It can be seen that turns are always equally distributed as a circle for each layer. Similarly, the LV winding is arranged outside of the MV winding.

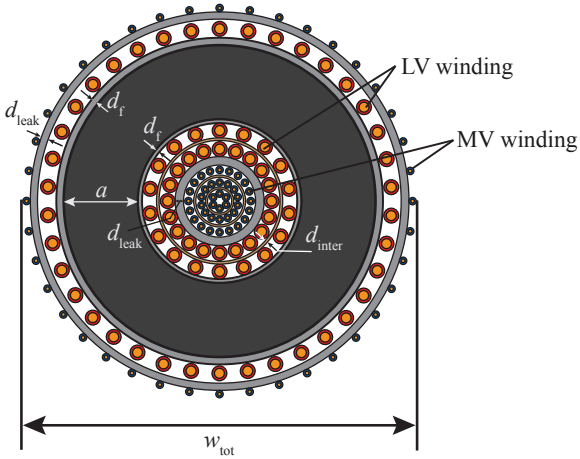

Figure 6.6: Example of the winding arrangement of the transformer by using a ring core.

After all winding turns inside the core window are arranged, the inner radius of the core can be determined. With the known core leg width a

generated by the optimizer, the outer radius of the core is also determined. Then the winding arrangement outside of the core can be performed in the similar way as introduced for the inside of the core window, first for the LV winding and then for the MV winding. Positions of the winding turns are always considered to be equally distributed around the core center. Due to a larger space, more turns can be arranged on each layer outside of the core. Therefore, the number of layers outside of the core is less than the number of layers inside of the core window.

With the given boxed volume, the total height of the transformer d_{tot} can be calculated with the known total width of the transformer w_{tot}. Then the thickness of the core d can be calculated by subtracting the winding height from d_{tot}.

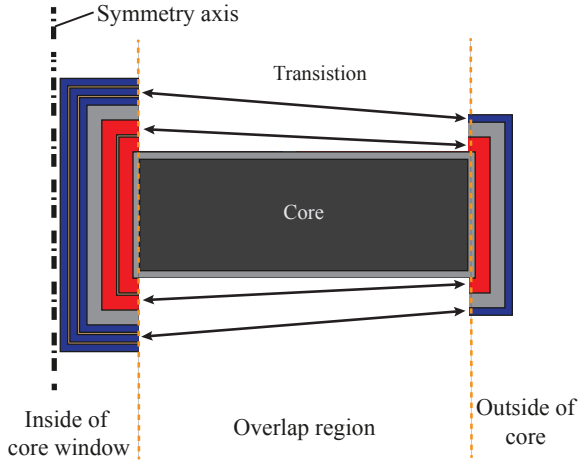

Figure 6.7: Axial symmetric cross-sectional view of the ring core transformer.

The leakage inductance is also calculated approximately by the 1D method with consideration of the axial symmetry. As shown in Fig. 6.7 for the cross-sectional view of the ring core transformer, winding structures inside and outside of the core are different. In the region where windings are overlapped with the core, the structure of the winding changes gradually to another structure. Therefore, the calculation is separated into two parts: inside of the core window and outside of the core window. For each part, the calculation is performed individually on each layer since the number of turns and the winding length of each layer is different. The perimeter of

each winding layer is then considered to be the respective layer height.

Finally, for both parts, terms of leakage fields for each winding layer and spaces between layers are summed up to obtain the total leakage inductance. For the sake of simplicity, half of the winding structure in the overlap region shown in Fig. 6.7 is assumed to be the same as the part inside of the core while another half of the winding in the overlap region is considered to be the same as the part outside of the core. Accordingly, the winding length in the overlap region can be added separately to the inner part and the outer part during the calculation of leakage inductance terms.

The calculation of $E_{\max}$ is performed in the same way as for the oval core transformer. The electric field strength both inside and outside of the core are evaluated separately and compared with the limit. Since the MV winding is completely separated from the core by the LV winding, the critical electric field lies between the MV and the LV winding.

Due to the structural limit, it is not possible to mount heat sinks on the core surface for the considered ring core transformer. The generated heat due to the core loss has to be transferred through the LV winding, the MV winding and dissipated from the surface. By considering the axial symmetry, the static thermal model of the considered ring core transformer is shown in Fig. 6.8. The core, the LV winding and the MV winding are assumed to have the same temperature respectively, i.e. T_1, T_2 and T_3. The thermal model is described in the matrix form as given in (2.74), with

$$\mathbf{A} = \begin{bmatrix} -\frac{1}{R_{\text{th12}}} & \frac{1}{R_{\text{th12}}} & 0 \\ \frac{1}{R_{\text{th12}}} & -\left(\frac{1}{R_{\text{th12}}} + \frac{1}{R_{\text{th23}}}\right) & -\frac{1}{R_{\text{th23}}} \\ 0 & \frac{1}{R_{\text{th23}}} & -\left(\frac{1}{R_{\text{th23}}} + \frac{1}{R_{\text{th3a}}}\right) \end{bmatrix} \tag{6.9}$$

$$\mathbf{B} = \begin{bmatrix} 1 & 0 & 0 & 0 \\ 0 & 1 & 0 & 0 \\ 0 & 0 & 1 & \frac{1}{R_{\text{th3a}}} \end{bmatrix} \tag{6.10}$$

and vectors $\mathbf{T} = [T_1, T_2, T_3]^{\mathbf{T}}$, $\mathbf{U} = [Q_1, Q_2, Q_3, T_{\text{am}}]^{\mathbf{T}}$.

The thermal resistance R_{th12} describes the interface between the core center and the center of the LV winding. The thermal resistance R_{th23} is between centers of the LV and the MV winding. Both thermal resistances can

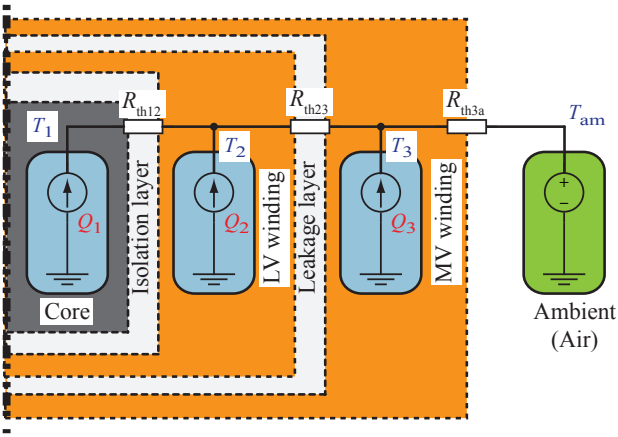

Figure 6.8: Static thermal model of the ring core transformer.

be calculated similarly as shown for the thermal model of the rectangular core based transformer. The interface for the thermal dissipation to the ambient is the surface of the MV winding. For simplicity, the winding surface is assumed to be flat and the thermal resistance is estimated as

$$R_{\mathrm{th}} = \frac{1}{\alpha_{\mathrm{S}} A_{\mathrm{sur}}} \tag{6.11}$$

where A_{sur} represents the surface area of the MV winding and α_{S} is the area dependent cooling coefficient which is given as $20\,\mathrm{W/(m^2K)}$ for a conservative estimation of a forced air-cooling [148]. The thermal resistance obtained by (6.11) is summed up with half of the thermal resistance of the MV winding to calculate R_{th3a}.

Optimization results

By using the presented optimization models, optimal designs of transformers with specifications given in Table 6.1 based on cores with the four geometric shapes are derived for various given boxed volumes. In Fig. 6.9, Pareto fronts of transformers with different core shapes are shown. It can be seen that the transformer based on the rectangular core can reach the highest power density followed by the square core, the oval core and the ring core transformer. The achievable maximal power densities of transformers

are in the range of 10 to 14 kW/dm^3 for all considered core shapes.

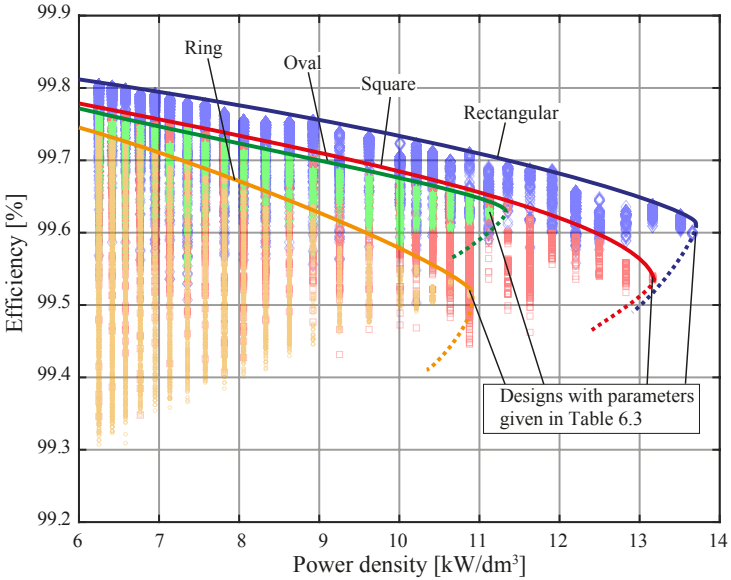

Figure 6.9: Pareto fronts of MFT designs with specifications given in Table 6.1 by using VITROPERM 500F cores with different geometric shapes. The boxed volume of transformers is considered for the power density calculation.

In Table 6.3, major parameters of the optimal design with the highest power density in case of each core shape as indicated in Fig. 6.9 are listed and 2D views of the winding arrangement are shown in Fig. 6.10. These are valid transformer designs with given specifications approaching the theoretical maximal power density in case of each core shape. As can be seen, calculated values of E_{max} and the maximal temperatures for these designs almost reach the limit.

For a given boxed volume, the highest reachable efficiency is limited by the maximal electric field strength, i.e. the isolation requirement, and the required leakage inductance. This results in additional space and leads to an increase of the core size and the winding length, which causes additional losses. On the other hand, the maximal achievable power density is limited by the allowable temperature (thermal limitation).

Table 6.3: Comparison of optimal MFT designs at the maximal power density by using cores with different shapes

Parameter \ Core	Rectangular	Square	Oval	Ring
Core cross-sectional area [mm^2]	3403.2	5029.2	2177.6	997.2
Window area [mm^2]	1703.2	1184.5	2663.9	3728.1
Magnetic length [mm]	208.2	175.4	238	291.8
Core volume [dm^3]	0.708	0.882	0.518	0.291
Boxed volume [dm^3]	1.83	1.9	2.25	2.35
Number of turns	28:9	19:6	44:14	97:32
Copper fill factor	26.13%	25.42%	28.28%	30.91%
Core loss [W]	32.32	39.98	23.35	12.83
Winding loss [W]	67.95	76.57	69.01	107.64
Efficiency	99.6%	99.54%	99.63%	99.52%
B_{max} [T]	0.96	0.957	0.955	0.945
E_{max} [kV/mm]	7.83	7.94	7.99	7.93
Maximal temperature [°C]	119	119	118	118.6
Power density [kW/L]	13.66	13.16	11.11	10.87

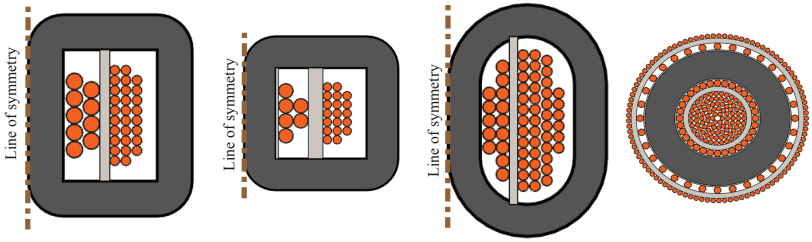

(a) Rectangular (b) Square (c) Oval (d) Ring

Figure 6.10: 2D view of optimal transformer designs with parameters given in Table 6.3 for different core shapes.

Basically, the square and the rectangular core have an equivalent shape and transformers based on both cores can achieve a very similar maximal power density. For the oval core, its arc parts are disadvantageous in

terms of the boxed volume for power density calculation compared with the rectangular core. Therefore the achievable maximal power density of the transformer based on the oval core is also smaller. In case of the ring core transformer, the heat generated in the core due to iron loss has to be transfered through windings and then dissipated to the ambient via the outer winding surface. Mounting heat sinks directly on the core surface, as in the case of transformers constructed with other cores, is not applicable. In order to dissipate the heat, a large surface area is necessary, which requires the size of the winding to be increased. Consequently, in the optimal design of the ring core transformer, core losses are relatively small while much more losses are generated in the winding. Therefore, both the power density and the efficiency of the ring core transformer are relatively low due to the limited heat dissipation capability.

6.2 Acoustic measurement of MFT

To evaluate the acoustic noise emission of the MFT, a prototype transformer is built for acoustic measurements. The transformer is operated with a SABC and a SRC. In this section, the test setup and measurement results are discussed.

6.2.1 MFT prototype

In Fig. 6.11 (a), the prototype transformer built with the shell type structure is shown. The design is based on the optimization result presented in chapter 2. The transformer consists of 4 pieces of VITROPERM 500F uncut cores. Since only one oval core is available, rectangular cores are used instead, which is the same one used for vibration and acoustic measurements as presented in chapter 5. To facilitate the construction of the winding, a plastic bobbin is printed by a 3D printer. Since the magnetic cores are uncut, the bobbin has to be produced as two halves so that they can be mounted around the core legs.

By the previous optimal design of the transformer presented in chapter 2, a single 620×0.1 mm round Litz-wire is considered to be used for the MV winding while four of the same wires are considered to be paralleled and used for the LV winding. However, due to the construction difficulty in case of using the uncut core, a single 4000×0.05 mm round Litz-wire is used for

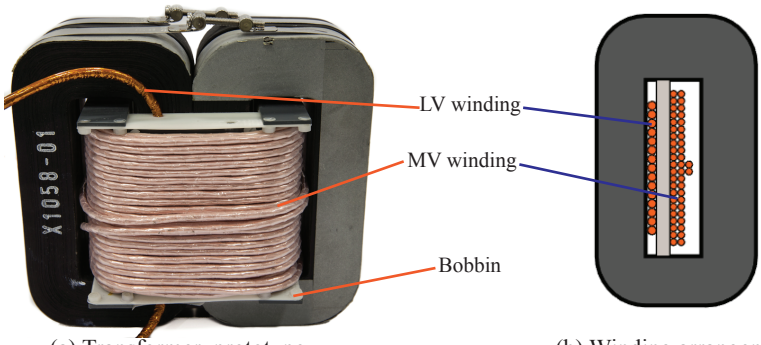

(a) Transformer prototype (b) Winding arrangement

Figure 6.11: Photo of the prototype transformer and the schematic showing the winding arrangement in the core window.

the LV winding instead of parallel wires.

Considering the adaption of the winding configuration, the transformer optimization is performed again and the obtained optimal design of the transformer is slightly different as the previous design. In Fig. 6.11 (b), the winding arrangement in the core window for the optimal transformer design in this case is shown, where the turns ratio is 46:15. The calculated total loss of the transformer is 118.2 W, which is slightly higher than the loss of the optimal MFT design using parallel wires as given in Table 2.8.

Since the leakage inductance of the transformer is essential for the operation of the converter, it is measured to check if it matches the calculated value. In Fig. 6.12, measured leakage inductances of the transformer from both the MV side and the LV side are shown. Compared with the calculated value of 114.6 µH, the measured value at 4 kHz is 121.6 µH, which has an error of approximately 6%. This error is assumed to be introduced by the calculation model and by the construction deviation to the designed winding arrangement. The calculated value refer to the LV side is 12.2 µH and the measured value on the LV winding is 13 µH.

Heat sinks change the mechanical structure of the transformer and fans add additional acoustic noise. Since the transformer is built for the acoustic measurement, heat sinks and fans are not mounted to avoid their influences on the measurement result. Furthermore, the winding of the transformer is

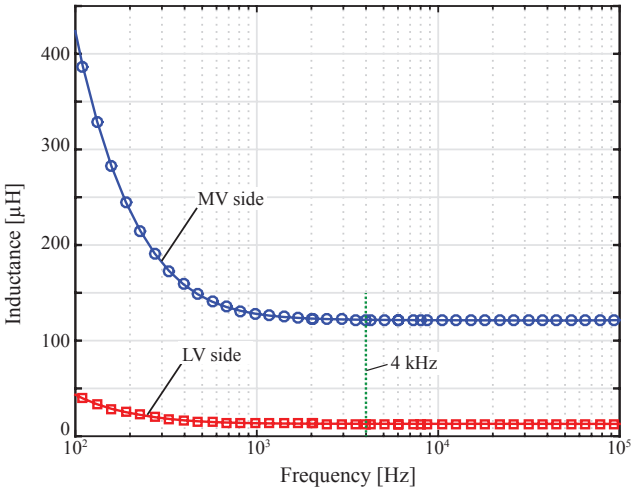

Figure 6.12: Measured leakage inductances of the prototype transformer.

not potted with the epoxy resin.

6.2.2 Test setup

In Fig. 6.13, the schematic of the test setup is shown. The FB converter on the LV side is operated as the input stage which is connected to a 400 V DC power supply. The MV winding of the transformer is connected to a diode rectifier instead of the NPC converter. In case of the SABC, the DC-link of the rectifier is connected to a load resistor, where the output voltage is regulated to be 800 V. Accordingly, the RMS voltage applied on the MV winding of the transformer is reduced to 800 V compared with the previous value of 1200 V in case of the DABC. Therefore, the number of turns of the MV winding is also reduced from 46 to 40 during the measurement.

In Fig. 6.14 the implemented prototype of the FB converter and the diode rectifier are shown. The FB converter is built in accordance with the design shown in Fig. 2.22. For the rectifier, the selected diode is STTH3010 and the output capacitor is 80 µF. A measurement circuit is also implemented to measure the output voltage. Additionally, a FPGA board is connected to the rectifier board in order to process the measured voltage signal and generate

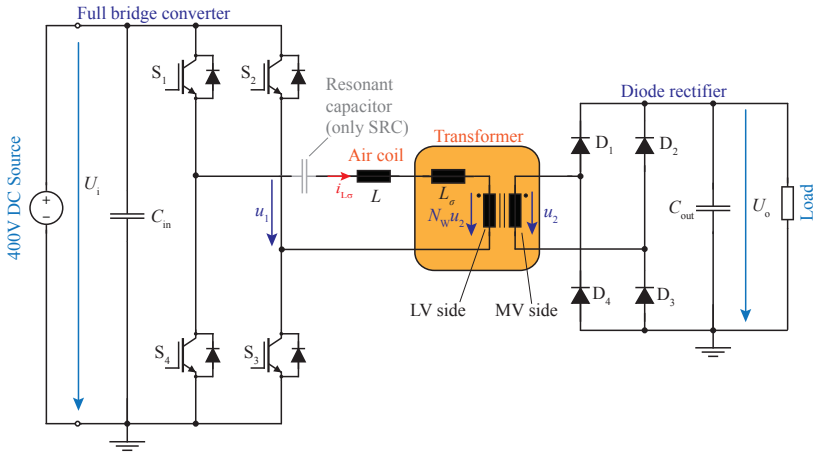

Figure 6.13: Schematic of the test setup for the MFT operated with a SABC/SRC.

gate signals for the IGBTs of the FB converter.

The operation of the SABC is based on the voltage duty ratio modulation, where the transferred power is adjusted by modifying the voltage-second

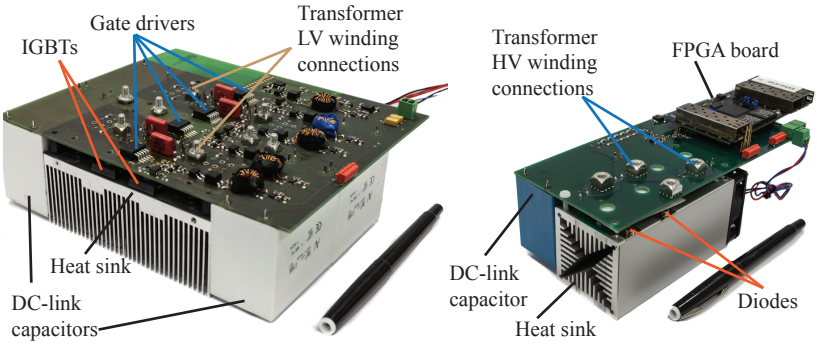

(a) FB converter (b) Diode rectifier

Figure 6.14: Implemented prototype of the FB converter and the diode rectifier.

product applied on the winding of the MFT. In Fig. 6.15, the modulation of the SABC is shown. It can be seen that the current flowing through the transformer has a triangular shape. Below the maximal transferable power, the current is discontinuous as shown in the graph. When operating at the maximal power, the current flows continuously and the voltage u_2 on the rectifier side reaches the maximal duty ratio $D = 1$, where D is defined as

$$D = \frac{\tau}{T_\mathrm{s}/2} = \frac{2\tau}{T_\mathrm{s}} \tag{6.12}$$

Then the transfered power is calculated by

$$P = \frac{U_\mathrm{i}^2 D^2 M(1-M^2)}{8 f_\mathrm{s} L_\sigma} \tag{6.13}$$

where the parameter M is defined similarly as for the DABC introduced previously, i.e.

$$M = \frac{N_\mathrm{w} U_\mathrm{o}}{U_\mathrm{i}} \tag{6.14}$$

The maximum transferred power is then

$$P_\mathrm{max} = \frac{U_\mathrm{1}^2 M(1-M^2)}{8 f_\mathrm{s} L_\sigma} \tag{6.15}$$

According to this equation, with a constant input voltage and switching frequency, the maximal power can be adapted by changing L_σ or M. As shown in Fig. 6.15, each half switching cycle is divided into 3 intervals: the current rising stage T_I, the current falling stage T_II and the zero-current stage T_III. These time intervals can be calculated as

$$\begin{cases} T_\mathrm{I} = \dfrac{1+M}{4} D T_\mathrm{s} & (6.16) \\ T_\mathrm{II} = \dfrac{1-M}{4} D T_\mathrm{s} & (6.17) \\ T_\mathrm{III} = T_\mathrm{s}/2 - T_\mathrm{I} - T_\mathrm{II} & (6.18) \end{cases}$$

To operate the SABC, the output voltage U_o is regulated based on a PI-controller. The error between the measured output voltage and the reference value is given to the PI-controller and the output value is used to

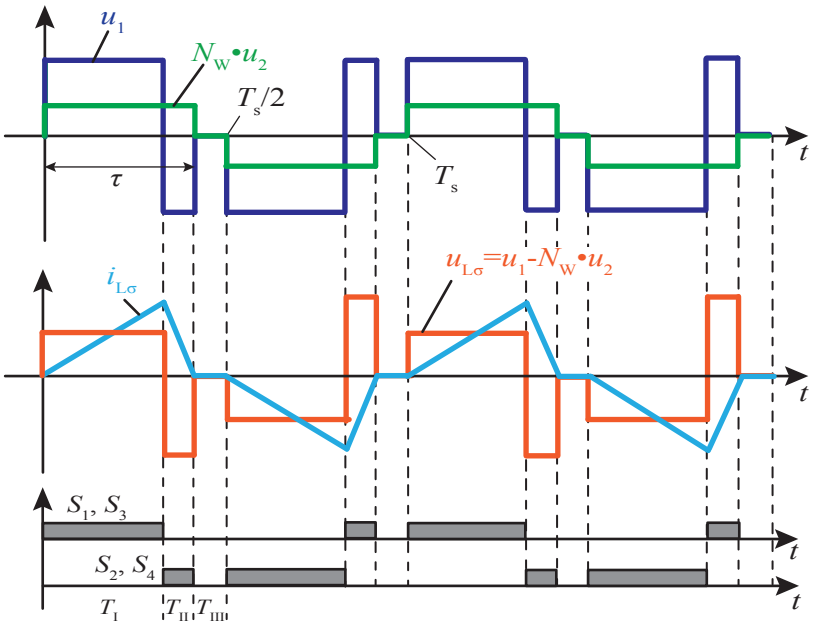

Figure 6.15: Modulation method used for operating the SABC.

calculate the rise time T_I. Then the duty ratio D can be solved from (6.16) and the fall time T_{II} can be calculated from (6.17). Based on T_I and T_{II}, gate signals for switches of the FB converter can be determined. The control algorithm is implemented in VHDL code on a FPGA board as shown in Fig. 6.14 (b). In this case, there is no current measurement, the reaction of the controller is slow. Since the the dynamic load change is not necessary for the measurement, this simple controller is adequate for this work.

Since the heat sink and fans are not mounted for the transformer, the cooling capability is significantly decreased. Therefore, the transformer needs to be operated at a reduced power level. To limit the transferred power, an additional inductor built as an air coil with the same Litz-wire used for the LV winding is connected in series on the LV side of the transformer as shown in Fig. 6.13. In this way, the maximal value of the voltage-second product can be achieved at a lower power level so that the maximal excitation of the core can be obtained with the given voltage. Due to the required interlocking time for switches, the voltage-second product is limited to approximately

98% of the theoretical maximal value.

For comparison between the SABC and the SRC, a capacitor bank with a total capacitance of 5.1 µF is also built and connected in series to the air coil. In this case, the SABC is operated as a SRC and the modulation method is the same for both cases. Accordingly, the inductance of the air coil is adapted so that by operating the SRC at the same frequency, the output power and the output voltage, as well as the voltage-second product also reaches approximately the same value as the case of the SABC.

6.2.3 Measurement results

In Fig. 6.16 (a) & (b), current and voltage waveforms of the transformer for the SABC and the SRC under the operating condition described above are shown. The SRC is operated above the resonant frequency in the continuous conduction mode. The transferred power is approximately 10 kW and in both cases the calculated peak flux density in the transformer core is approximately 0.5 T. The voltages u_1 and u_2 are measured at locations shown in Fig. 6.13. It can be seen that the peak current flowing through the LV winding is approximately 80 A for the SABC while it is around 60 A for the SRC. In Fig. 6.16 (c) & (d), the first three harmonics of the current in the transformer LV winding are shown, where the amplitudes of the first harmonic in both cases are quite similar while the amplitude of the 3rd and the 5th harmonic for the SRC are lower than for the SABC due to a more sinusoidal waveform.

With the operation condition given above, the acoustic measurement of the transformer is performed with the microphone located 1 m away from the surface of the transformer and the measurement direction is shown in Fig. 6.17. Due to the required source and load for the test setup, the measurement is not performed in the anechoic room. During the measurement, there are influences from other sound sources such as cooling fans of the converter and the DC source.

In Fig. 6.18, the measured sound pressure spectra of the transformer for both the SABC and the SRC are shown. As a reference, the background noise is also measured, where the DC source and cooling fans of the converter are also turned on during the measurement. It can be seen that the transformer generally induces additional noise harmonics above the operating

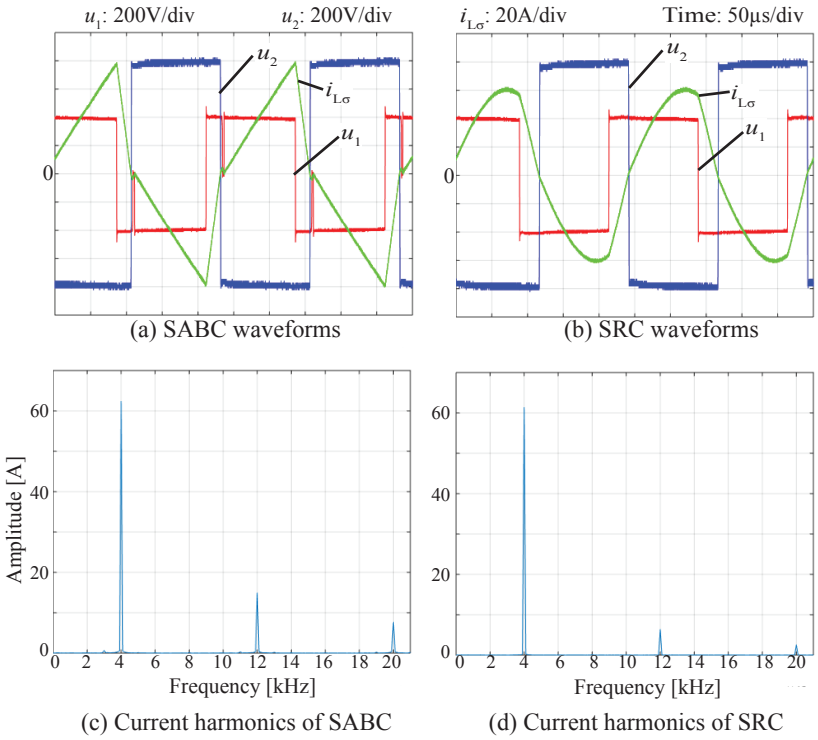

Figure 6.16: Measured waveforms of the transformer voltage/current operating at 10 kW as in the SABC and the SRC. The first 3 harmonics of the current in both cases are also shown.

frequency in the frequency spectrum. The A-weighted SPL is increased by approximately 4 to 5 dBA compared to the background noise. For the SABC and the SRC, the transformer noise is quite similar with a difference of less than 1 dBA. This can be expected by the similar excitation of the core and a similar amplitude of the fundamental component of the current (4 kHz). Although in case of the SABC, the current has higher 3rd and 5th harmonics, the induced noise due to these harmonics mainly at doubled frequencies (24 kHz and 40 kHz) are already beyond the audible range and therefore have minor contribution to the acoustic noise.

To compare the contribution of the transformer noise from the core and

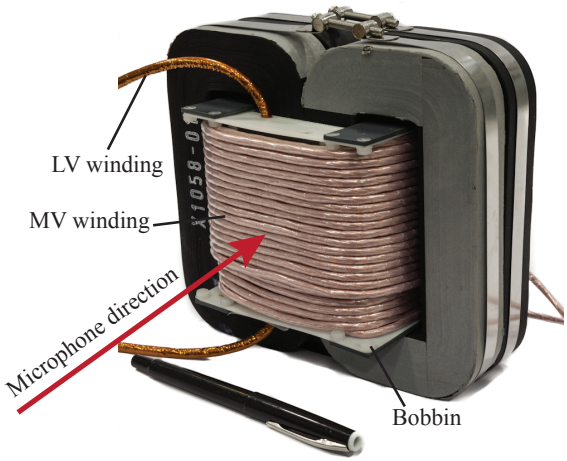

Figure 6.17: Direction of the acoustic noise measurement for the prototype transformer with the MV winding adapted to 40 turns.

the winding, the oval uncut core is measured again. During this measurement, only the AC amplifier for supplying the excitation current is turned on. In this case, the measured frequency spectra of the background noise and the core noise are shown in Fig. 6.19 (a) and (b) respectively. The core is excited by a 4 kHz sinusoidal current to the flux density level of 1.0 T (measured towards the front surface). It can be seen that even at this high induction level, the highest amplitude of the harmonic of the core noise is still lower than the amplitude of the background noise in the low frequency range.

For a further comparison, a single-layer winding with 22 turns of Litz-wires fed by a 4 kHz, 50 A peak sinusoidal current is measured and the noise spectrum is shown in Fig. 6.19 (c). This winding is built with the same Litz-wire used for the MV winding of the transformer and has the same size. By comparing the amplitude of noise harmonics, it can be seen that the winding noise has a higher amplitude than the core noise. In case of the transformer, both the LV and the MV winding contribute to the noise and the current amplitude in the MV winding is even higher than the measured current in the single-layer winding. Furthermore, the flux density in the transformer core is only half of the flux density in the measured oval core. Therefore, the transformer core is expected to have lower noise

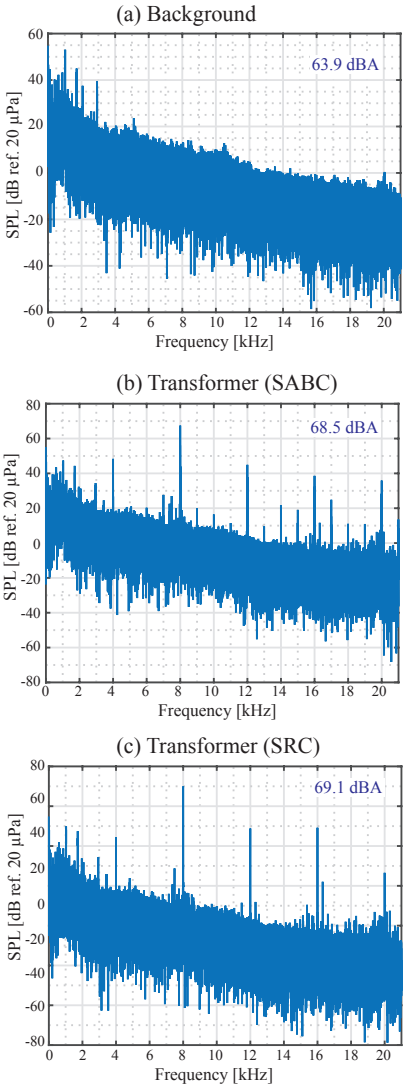

Figure 6.18: Measured SPL frequency spectra of transformers and the background noise (with the DC source and converter cooling fans turned on).

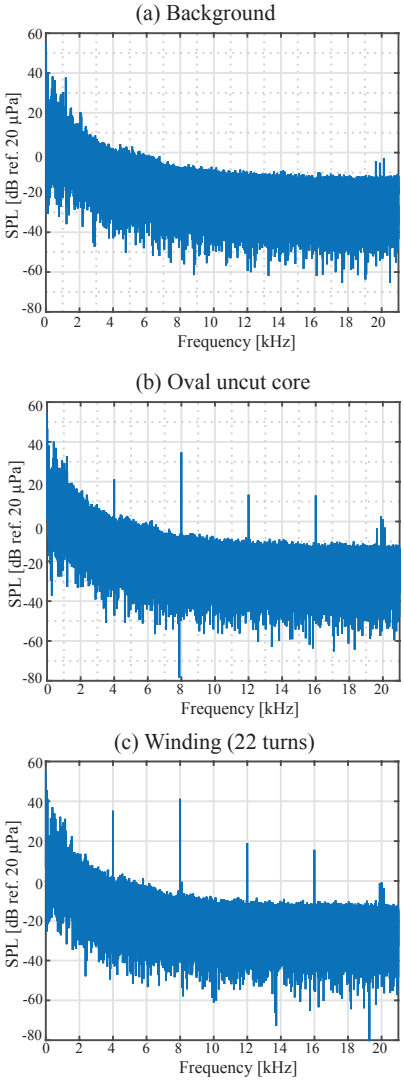

Figure 6.19: Measured SPL frequency spectra of the oval core, the single-layer winding and the background noise (with the DC source and converter cooling fans turned off).

than the measured oval core while the transformer winding is expected to generate more noise than the single-layer winding. As a result, it can be concluded that the measured transformer noise is mainly caused by the winding vibration while the core vibration only has a minor contribution due to the small magnetostriction and Maxwell force considering that the nanocrystalline uncut core is used.

6.3 Conclusions

In this chapter, optimal designs of the MFT based on magnetic cores of various materials and geometric shapes are investigated. The optimization procedure presented in chapter 2 is used. To evaluate the influence of the core material, rectangular cores based on 4 materials are considered for the MFT design with the same specifications. The optimization algorithm is applied to obtain the efficiency vs. power density Pareto front for transformers using these core materials. Among these considered materials, results show that transformers based on the nanocrystalline core can achieve the highest power density. For the same boxed volume, nanocrystalline core based transformers also reach the highest efficiency. Due to the relative high saturation flux density and low loss, the nanocrystalline alloy is the most suitable core material for MFT applications regarding the power density and the efficiency.

To evaluate the influence of the core geometric shape, nanocrystalline cores with 4 shapes are considered for the transformer design. The optimization model is adapted to match each shape and the structure of the transformer. Pareto fronts show that with a conventional rectangular core, the transformer can reach the highest power density due to the high flexibility of adapting the dimension. If the core window height and width are limited to be the same, i.e. in case of the square shape, the flexibility is lower and the achievable power density of the transformer is reduced. The oval core is disadvantageous considering the boxed volume due to the arc part, which further limits the achievable power density of the transformer. In case of the ring core, the limited thermal dissipation and cooling possibility have a negative impact on the power density of the transformer. As above, the rectangular core is the best solution regarding the power density of the transformer.

Based on measurement results presented in chapter 5 and optimization

results in this chapter, a nanocrystalline uncut core with the oval shape is a promising solution for an efficient, compact and silent MFT design.

Finally, a prototype transformer based on the nanocrystalline uncut core with the rectangular shape is built and acoustic measurements are performed on it. The transformer is operated in the case of a SABC and a SRC, where the power, voltage, frequency are kept the same. Results show that under the excitation of a rectangular voltage, higher order harmonics in the frequency spectrum of the acoustic noise are more significant than in the case of under a sinusoidal excitation. In case of the SABC, the triangular-shaped current has higher amplitudes of high order harmonics compared to the case of the SRC with a more sinusoidal-shaped current. However, the transformer noise is similar in both cases due to the same excitation voltage and similar amplitudes of the fundamental component of the current.

The measurement result shows that in case the magnetic core is uncut and has a low magnetostriction, the winding vibration induced by the Lorentz force has a more significant contribution to the acoustic noise of the transformer due to the high current amplitude, which confirms the result obtained from the core and the winding measurement. Compared with a transformer built with Fe-based amorphous cut cores reported in the literature, the transformer built in this work is proved to have a much lower acoustic noise emission. Based on these measurement results, the effort to reduce the acoustic noise emission of such a transformer should be put on the winding. It is expected that by a suitable mechanical damping or potting the winding with the epoxy resin, the winding vibration can be effectively reduced.

7 Summary and Outlook

With the advancement of semiconductor devices and magnetic materials, the solid state transformer which consists of power electronic converters and medium frequency transformers become a potential substitution of conventional low frequency transformers for medium voltage, high power applications. Besides basic functionalities of the LFT, i.e. the galvanic isolation and voltage adaption, the SST also provides other useful functionalities such as the power flow control and power quality improvement. With these advantageous features, SSTs are useful for the future smart grid, where a large number of inherently fluctuating and geographically distributed renewable energy sources and energy storage systems are integrated. Furthermore, the size/weight of the AC-AC power conversion system can be reduced and a higher efficiency can be achieved compared with LFTs. Therefore, SSTs are especially attractive for space/weight critical applications such as traction systems and offshore wind farms.

The medium frequency transformer is a key component of SSTs and the optimal design of MFTs is essential for the performance of the whole system. Due to a higher operating frequency, the size of MFTs can be significantly reduced compared with LFTs. On the one hand, the size reduction is a great advantage for achieving a higher power density. On the other hand, the high voltage isolation requirement and thermal management within a limited space propose new challenges to the transformer design. The non-sinusoidal voltage/current waveform involving fast changing slope is also more critical for the design. Special attentions need to be paid to the structural design of windings due to the unfavorable high frequency effects such as the proximity and the skin effect. Furthermore, the acoustic noise

emission becomes more crucial since the operating frequency of MFTs are usually within the most sensitive audible range.

As one of major problems to be solved for the MFT, the acoustic noise issue demands a detailed investigation since the accomplished research works are mainly focusing on LFTs. A reevaluation for the MFT is necessary due to the difference in structure, core material, winding construction and operation condition compared with LFTs. Based on the result, suitable measures to reduced the acoustic noise can be taken into account during the design phase of MFTs. Furthermore, the influence of these measures on the performance of the transformer such as the power density and efficiency also needs to be evaluated. The optimal design of MFTs is desired to be compact, efficient and silent.

7.1 Conclusions

The first major part of this dissertation deals with the optimization of the MFT. In chapter 2, a design case of the isolated DC-DC converter, i.e. a DABC with a down-scaled power for the SST application is carried out. An extensive optimization model for the MFT is developed and implemented in MATLAB. As most crucial aspects for the MFT design, major efforts have been devoted to improve the thermal model and the isolation design. A detailed model based on the thermal-electrical analogy for multi-layer of Litz-wires is established to obtain more accurate thermal resistances of the winding. An iterative calculation of temperatures is also implemented to achieve higher accuracy. In order to take the limit of the electric field strength into account during the optimization phase, an analytical approach based on the 2D charge simulation method is implemented and the accuracy of the calculation result is verified by the FEM simulation. By carefully selecting the points to be calculated, this approach is successfully integrated into the optimization process with an acceptable calculation time. Furthermore, calculation procedures for such a complex optimization model are carefully arranged according to the computational effort of each step. As a result, a reasonable total calculation time is kept.

Generally, by increasing the operating frequency, the size of magnetic components can be reduced. To investigate the validity of this principle in case of the MFT design and to determine the operating frequency for the DC-DC converter, the optimization model is used to find lowest achievable

volumes of the transformer with same specifications at various operating frequencies. For the studied case, it is found that above a few kHz, the volume reduction of the MFT by increasing the operating frequency is not significant due to the required isolation distance and the increasing thermal stress. Therefore, there is no benefit of increasing the operating frequency above a certain level on the one hand due to the almost constant transformer volume and on another hand due to the significantly increased switching loss in the converter. Consequently, the operating frequency of the studied converter is selected to be at 4 kHz.

As an extension from the MFT optimization model, a combined model for the total efficiency optimization of the DABC is further developed. Based on the selected frequency, the optimal design of the DABC including converter operation parameters and design parameters of the MFT is obtained by using the combined optimization model. Results show that the semiconductor loss is more than 2 times higher than the transformer loss since the low loss nanocrystalline core is considered for the MFT design. The dominant part of the semiconductor loss is the conduction loss especially on the LV side of the MFT due to the high conducting current. According to the calculation, an efficiency of over 98% at the nominal power can be achieved for the final design of the DABC with the forced air-cooling. The power density of the converter can reach 3.63 kW/L, where the MFT achieves a power density of 8 kW/L and occupies around half of the total volume of the converter.

The power density and the efficiency are crucial for MFTs, on which the used core material and the geometric shape may have significant influences. To evaluate these impacts, the optimization model is used to find Pareto fronts of the MFTs considering two groups of cores:

1. Rectangular cores made by four different materials (nanocrystalline alloy, Fe-based amorphous alloy, Co-based amorphous alloy, ferrite)

2. Nanocrystalline cores with four different shapes (rectangular, square, oval, ring)

Results show that with the nanocrystalline core, the highest power density of the MFT can be achieved. For the same boxed volume, the nanocrystalline core based transformer also reaches the highest efficiency. To perform the calculation for the 2nd group of cores, adapted calculation models are implemented. It is shown that with the conventional rectangular core, the

transformer can reach the lowest boxed volume among these considered core shapes. Due to the flexibility for adapting the width and height of the window, the rectangular core is the best choice regarding the power density of the transformer. However, the difference of the achievable maximal power density of transformers in case of considered core shapes are not significant except for the ring core. Due to the limited thermal dissipation and cooling possibility of the ring core based transformer, the achievable power density is relatively low compared with transformers based on other core shapes.

Another significant part of this dissertation devotes to the investigation of the acoustic noise associated with MFTs, focusing on electromagnetic aspects. In chapter 3, origins of the acoustic noise in transformers are investigated based on a literature survey and focusing on the most relevant electromagnetic origins: the Maxwell force, the magnetostriction and the Lorentz force. These effects cause vibrations of the transformer structure and generate the acoustic noise. For each source, the cause, mechanism and the acting part on the transformer are analyzed. For tape wound cores, which are widely used for MFTs, mechanisms of the magnetostriction and the Maxwell force causing vibrations of a typical rectangular-shaped cut core are further analyzed, where the impact of the air gap is emphasized. In literatures, it is generally considered that the core vibration is the major source of the acoustic noise in transformers and the magnetostriction is the most relevant to the core vibration. However, if an air gap exists, the Maxwell force acting on the gap region is quite significant. The magnetostriction and the Maxwell force enhance with each other at these regions and induce excessive core vibrations. Furthermore, vibration and acoustic noise modeling methods for the transformer are investigated in order to find applicable methods for MFTs with emphasis on modeling the laminated structure of tape wound cores and relevant magnetic materials. It has been found that some parameters for the nanocrystalline and the amorphous alloy are not available and need to be determined by measurements, which requires special equipments. Therefore, the deriving of these parameters through analytical approximation is investigated.

In chapter 4, suitable core materials for MFTs are discussed focusing on relevant parameters with consideration of the efficiency, power density and core vibration of the transformer. It is shown that the nanocrystalline alloy is the most suitable core material for MFTs due to the low loss, relative high saturation level and near-zero magnetostriction. Then a simplified model base on the FEM for the analysis of the core vibration is implemented, where

the weak coupling between the electromagnetic and the mechanical model is considered. The model is used for some case studies to compare the aforementioned acoustic noise sources and their impact on the core vibration. Furthermore, required material parameters for the nanocrystalline alloy VITROPERM 500F and the amorphous alloy METGLAS 2605SA1, which are the most widely used core materials for MFTs, are derived based on elementary mixture rules for fiber-reinforced laminae as introduced in chapter 3. The core vibration is also compared considering both materials and different geometric shapes. Results show that the Lorentz force is comparable to the Maxwell force in case of an uncut core. The Lorentz force can be even larger than the Maxwell force if the current flowing through the winding is relatively high. The attractive force in the air gap region in case of a cut core is much more significant than the Lorentz force. This attractive force can cause more significant core vibrations compared with the vibration caused by the magnetostriction effect if a low-magnetostrictive material is considered. Furthermore, the even distribution of the magnetic field such as in the case of the ring core is advantageous for balancing the magnetic force and the magnetostriction which results in less core vibrations. Therefore, a lower acoustic noise emission can be expected for magnetic cores with such a geometric shape.

To verify the theoretical analysis, vibration and acoustic noise measurements are performed on magnetic cores made by various materials and with different geometric shapes. The test setup, sample cores and measurement results are presented in chapter 5. It is confirmed that the existence of the air gap can cause excessive core vibrations. As a result, the cut core has a much higher noise emission compared with its uncut counterpart. In this case, the acoustic noise due to the winding vibration induced by the Lorentz force is negligible compared to the core noise. The comparison among several magnetic materials shows that both the nanocrystalline alloy and the Co-based amorphous alloy feature low acoustic noise emission due to their extremely small magnetostriction. On the contrary, the noise emission of the ferrite core is moderate while the Fe-based amorphous core is extremely noisy due to the large magnetostriction. Considering the core loss, saturation level and acoustic performance, the nanocrystalline alloy is the best candidate for MFTs. By using uncut cores, extremely low acoustic noise emission can be achieved. Furthermore, customized nanocrystalline cores with oval and ring shapes are measured to compare with the standard rectangular core. The ring core shows the best acoustic performance due to the even-distributed magnetic flux and therefore magnetic forces and

magnetostrictive strains. The oval core takes the advantages of the arc shape similar as the ring core. Therefore, lower vibration and less acoustic noise emission is achieved compared with the rectangular core. Furthermore, if the vibration is weak, e.g. in case of an uncut core with low magnetostriction and/or low induction level, the winding vibration may have more significant contribution to the acoustic noise if the carried current has a high amplitude. It has been shown that the vibration and acoustic noise of the core and the winding contains higher order harmonics even under a pure AC sinusoidal voltage/current excitation. Additional harmonics in the core vibration is assumed to be caused by the nonlinear hysteresis effect and the distortion of the magnetostriction while additional harmonics in the winding vibration is considered to be induced by the nonlinear mechanical effect.

Summarizing the aforementioned results, to achieve a compact, efficient and silent design for the MFT, the nanocrystalline uncut core is the best choice. If the acoustic noise is more crucial, the ring core can be used but the power density and the efficiency of the transformer is limited. The oval core is a compromise between the acoustic noise and the size/efficiency of the transformer. By using this core shape, lower acoustic noise emission can be achieved without sacrificing too much of the power density and the efficiency compared with the design based on the rectangular core.

As a final evaluation, a prototype transformer using the nanocrystalline rectangular uncut core is built according to the design result presented in chapter 2. The transformer is operated with a SABC under similar operating conditions as in the case of a DABC. Measurement results show that a relative low acoustic noise emission of the prototype transformer is achieved with a measured sound pressure level of less than 70 dBA (including the background noise of more than 60 dBA). Since the low-magnetostrictive uncut core is used, the acoustic noise emission of the transformer due to the core vibration is very low. In this case, the major contribution to the transformer noise is from the winding vibration due to a relatively large Lorentz force caused by a high current. Accordingly, mechanical damping or potting the winding with epoxy resin can be considered to further reduce the acoustic noise emission of the transformer.

7.2 Future work

Although the research of SSTs has been on going in recent years including this work, large-scale industrial applications of the SST is still not foreseeable mainly due to the cost and reliability issues [8]. As the key component of the SST, the MFT design also faces new challenges and requires further investigations. Based on the achievements of this work, following issues regarding the acoustic noise emission and the optimal design of the MFT are proposed for future work.

Material parameters of the tape wound core based on the nanocrystalline and the amorphous alloys can be measured and magneto-elastic coupling effects, e.g. the stress dependency of the magnetostriction, can be taken into account to improve the accuracy of the model. Furthermore, the 2D model can be extended to the 3D case and the acoustic model can be added to calculate the sound pressure caused by the core vibration. Moreover, the winding can also be included and a complete model of the transformer can be implemented. The model can be used to estimate the acoustic noise level of the MFT as already been done for large power transformers presented in literatures. However, the simulation model is assumed to be more complicated to be solved for the MFT compared with the model of the LFT considering the non-sinusoidal voltage/current and a much higher frequency. Consequently, the problem needs to be solved in time domain and with a much smaller time steps. If possible, it would be interesting to develop some analytical equations to estimate the acoustic noise of the transformer and facilitate the design.

For the construction of transformers, it is more practical to use cut cores since it is more convenient to manufacture windings. Therefore, the vibration and acoustic noise issue of the MFT in case of using cut cores needs to be further investigated. Suitable measures need to be found to damp the core vibration caused by the force at the air gap region. Furthermore, a more detailed study of the winding vibration is also necessary and effective damping methods should be considered since the winding vibration could be the major contributor to the transformer noise. If it is not sufficient to reduce the vibration of the structure, other measures such as setting acoustic barriers may need to be considered in order to achieve a low noise design considering the whole SST system.

Regarding the optimization of the isolated DC-DC converter and the

MFT, the combined model used in this work can be further extended for the DABC with the FB-FB configuration. In this case, one more operating parameter needs to be included as a free parameter, i.e. the duty ratio of the voltage on the MV side as discussed in chapter 2. To obtain more accurate results, other losses such as the dielectric loss of the transformer and the loss of the DC-link capacitors need to be included in the loss calculation model. Other winding structures (e.g. the split winding) and other types of wires (e.g. copper foil, rectangular Litz-wire) could be included in the model. It would also be interesting to compare the winding vibration and the resulting acoustic noise of different windings.

Practically, it may be more suitable to consider the efficiency of the DC-DC converter at different load conditions. In this case, several operation points from light load to full load can be considered and the target of the optimization is adapted accordingly considering the overall efficiency at these operation points. Furthermore, a multi-object optimization can be implemented to include other factors as optimization objects such as the volume and the cost.

Bibliography

[1] S. Kulkarni and S. Khaparde, *Transformer Engineering - Design and Practice*. Marcel Dekker inc., 2004.

[2] L. Heinemann and G. Mauthe, "The universal power electronics based distribution transformer, an unified approach," in *Proceedings of Annual IEEE Power Electronics Specialists Conference (PESC)*, 2001, pp. 504–509.

[3] J. W. Kolar and G. Ortiz, "Solid-state-transformers: key components of future traction and smart grid systems," in *Proceedings of International Power Electronics Conference (IPEC)*, 2014.

[4] W.McMurray, "Power converter circuits having a high-frequency link," US Patent 3 517 300, June 23, 1970.

[5] J. L. Brooks, "Solid state transformer concept development," in *Naval Material Command*, Port Hueneme, CA, USA, 1980.

[6] K. Harada, F. Anan, K. Yamasaki, M. Jinno, Y. Kawata, T. Nakashima, K. Murata, and H. Sakamoto, "Intelligent transformer," in *Proceedings of Annual IEEE Power Electronics Specialists Conference (PESC)*, 1996, pp. 1337–1341.

[7] M. Kang, P. N. Enjeti, and I. J. Pitel, "Analysis and design of electronic transformers for electric power distribution system," *IEEE Transactions on Power Electronics*, vol. 14, no. 6, pp. 1133–1141, 1999.

[8] I. Villar, "Multiphysical characterization of medium-frequency power electronic transformers," Ph.D. dissertation, Éole Polytechnique Fédérale de Lausanne (EPFL), 2010.

[9] X. She, A. Q. Huang, and R. Burgos, "Review of Solid-State Transformer Technologies and Their Application in Power Distribution Systems,"

IEEE Journal of Emerging and Selected Topics in Power Electronics, vol. 1, no. 3, pp. 186–198, 2013.

[10] D. Dujic, C. Zhao, A. Mester, J. K. Steinke, M. Weiss, S. Lewdeni-Schmid, T. Chaudhuri, and P. Stefanutti, "Power Electronic Traction Transformer-Low Voltage Prototype," *IEEE Transactions on Power Electronics*, vol. 28, no. 12, pp. 5522–5534, 2013.

[11] J.-S. Lai, A. Maitra, A. Mansoor, and F. Goodman, "Multilevel intelligent universal transformer for medium voltage applications," in *Proceedings of IEEE Industry Applications Society Annual Meeting (IAS)*, 2005, pp. 1893–1899.

[12] F. Gao, Z. Li, P. Wang, F. Xu, Z. Chu, Z. Sun, and Y. Li, "Prototype of smart energy router for distribution DC grid," in *Proceedings of International Conference on Power Electronics and Drive Systems (PEDS)*, 2015.

[13] J. W. Kolar, I. Friedli, F. Krismer, and S. D. Round, "The Essence of Three-Phase AC/AC Converter Systems," in *Proceedings of Power Electronics and Motion Control Conference (EPE-PEMC)*, 2008, pp. 27–42.

[14] G. Ortiz, "High-Power DC-DC Converter Technologies for Smart Grid and Traction Applications," Ph.D. dissertation, ETH Zürich, 2014.

[15] E. R. Ronan, S. D. Sudhoff, S. F. Glover, and D. L. Galloway, "A power electronic-based distribution transformer," *IEEE Transactions on Power Delivery*, vol. 17, no. 2, pp. 537–543, 2002.

[16] H. Iman-Eini and S. Farhangi, "Analysis and Design of Power Electronic Transformer for Medium Voltage Levels," in *Proceedings of Annual IEEE Power Electronics Specialists Conference (PESC)*, 2006.

[17] T. Zhao, L. Yang, J. Wang, and A. Q. Huang, "270 kVA Solid State Transformer Based on 10 kV SiC Power Devices," in *Proceedings of IEEE Electric Ship Technologies Symposium (ESTS)*, 2007, pp. 145–149.

[18] G. Brando, A. Dannier, and A. Del Pizzo, "A simple predictive control technique of power electronic transformers with high dynamic features," in *Proceedings of IET International Conference on Power Electronics, Machines and Drives (PEMD)*, 2010.

[19] H. Fan and H. Li, "High-Frequency Transformer Isolated Bidirectional DC-DC Converter Modules With High Efficiency Over Wide

Load Range for 20 kVA Solid-State Transformer," *IEEE Transactions on Power Electronics*, vol. 26, no. 12, pp. 3599–3608, 2011.

[20] S. Bifaretti, P. Zanchetta, A. Watson, L. Tarisciotti, and J. C. Clare, "Advanced Power Electronic Conversion and Control System for Universal and Flexible Power Management," *IEEE Transactions on Smart Grid*, vol. 2, no. 2, pp. 231–243, 2011.

[21] G. Wang, S. Baek, A. Kadavelugu, F. Wang, X. She, S. Dutta, Y. Liu, T. Zhao, W. Yao, R. Gould, S. Bhattacharya, and A. Q. Huang, "Design and Hardware Implementation of Gen-1 Silicon Based Solid State Transformer," in *Proceedings of IEEE Applied Power Electronics Conference and Exposition (APEC)*, 2011.

[22] D. Grider, M. Das, A. Agarwal, J. Palmour, R. Raju, M. Schutten, S. Leslie, J. Ostop, and A. Hefner, "10 kV/120 A SiC DMOSFET Half H-Bridge Power Modules for 1 MVA Solid State Power Substation," in *Proceedings of IEEE Electric Ship Technologies Symposium (ESTS)*, 2011, pp. 131–134.

[23] G. Ortiz, M. Leibl, J. W. Kolar, and O. Apeldoorn, "Medium frequency transformers for solid-state-transformer applications - Design and experimental verification," in *Proceedings of International Conference on Power Electronics and Drive Systems (PEDS)*, 2013, pp. 1285–1290.

[24] Z. Li, P. Wang, Z. Chu, H. Zhu, Z. Sun, and Y. Li, "A three-phase 10 kVAC-750 VDC power electronic transformer for smart distribution grid," in *Proceedings of European Conference on Power Electronics and Applications (EPE)*, 2013.

[25] D. Boroyevich, I. Cvetković, D. Dong, R. Burgos, F. Wang, and F. C. Lee, "Future electronic power distribution systems - a contemplative view," in *Proceedings of International Conference on Optimization of Electrical and Electronic Equipment(OPTIM)*, 2010, pp. 1369–1380.

[26] S. Khomfoi and L. Tolbert, *Power Electronics Handbook*, 3rd ed. Elsevier, 2011, ch. Multilevel power converters, pp. 455–486.

[27] S. Inoue and H. Akagi, "A Bidirectional Isolated DC-DC Converter as a Core Circuit of the Next-Generation Medium-Voltage Power Conversion System," *IEEE Transactions on Power Electronics*, vol. 22, no. 2, pp. 535–542, 2007.

[28] R. W. De Doncker, D. M. Divan, and M. H. Kheraluwala, "A three-phase

soft-switched high-power-density DC/DC converter for high-power applications," *IEEE Transactions on Industry Applications*, vol. 27, no. 1, pp. 63–73, 1991.

[29] M. N. Kheraluwala, R. W. Gascoigne, D. M. Divan, and E. D. Baumann, "Performance characterization of a high-power dual active bridge DC-to-DC converter," *IEEE Transactions on Industry Applications*, vol. 28, no. 6, pp. 1294–1301, 1992.

[30] M. Steiner and H. Reinold, "Medium frequency topology in railway applications," in *Proceedings of European Conference on Power Electronics and Applications (EPE)*, 2007.

[31] J. E. Huber and J. W. Kolar, "Analysis and design of fixed voltage transfer ratio DC/DC converter cells for phase-modular solid-state transformers," in *Proceedings of IEEE Energy Conversion Congress and Exposition (ECCE)*, 2015.

[32] C. Meyer and R. W. De Doncker, "Design of a Three-Phase Series Resonant Converter for Offshore DC Grids," in *Proceedings of IEEE Industry Applications Annual Meeting (IAS)*, 2007, pp. 216–223.

[33] UNIFLEX project, 2013. [Online]. Available: http://www.eee.nott.ac.uk/uniflex/

[34] A. Q. Huang, M. L. Crow, G. T. Heydt, J. P. Zheng, and S. J. Dale, "The Future Renewable Electric Energy Delivery and Management (FREEDM) System: The Energy Internet," *Proceedings of the IEEE*, vol. 99, no. 1, pp. 133–148, 2011.

[35] J.-S. Lai, A. Maitra, and F. Goodman, "Performance of a Distribution Intelligent Universal Transformer under Source and Load Disturbances," in *Proceedings of IEEE Industry Applications Society Annual Meeting (IAS)*, 2006, pp. 719–725.

[36] M. R. Banaei and E. Salary, "Mitigation of current harmonics and unballances using power electronic transformer," in *Proceedings of Power Quality Conferance (PQC)*, 2010.

[37] P. Tatcho, Y. Jiang, and H. Li, "A novel line section protection for the FREEDM system based on the solid state transformer," in *Proceedings of IEEE Power and Energy Society General Meeting*, 2011, pp. 1–8.

[38] X. She, A. Q. Huang, F. Wang, and R. Burgos, "Wind Energy System

With Integrated Functions of Active Power Transfer, Reactive Power Compensation, and Voltage Conversion," *IEEE Transactions on Industrial Electronics*, vol. 60, no. 10, pp. 4512–4524, 2013.

[39] M. Vasiladiotis and A. Rufer, "A Modular Multiport Power Electronic Transformer With Integrated Split Battery Energy Storage for Versatile Ultrafast EV Charging Stations," *IEEE Transactions on Industrial Electronics*, vol. 62, no. 5, pp. 3213–3222, 2015.

[40] B. Hafez, H. S. Krishnamoorthy, P. Enjeti, S. Ahmed, and I. J. Pitel, "Medium voltage power distribution architecture with medium frequency isolation transformer for data centers," in *Proceedings of IEEE Applied Power Electronics Conference and Exposition (APEC)*, 2014, pp. 3485–3489.

[41] A. Steimel, "Power-Electronics Issues of Modern Electric Railway Systems," *Advances in Electrical and Computer Engineering*, vol. 10, no. 2, pp. 3–10, 2010.

[42] D. Dujic, F. Kieferndorf, F. Canales, and U. Drofenik, "Power electronic traction transformer technology," in *Proceedings of Annual IEEE Power Electronics Specialists Conference (PESC)*, 2012, pp. 636–642.

[43] L. Heinemann, "An actively cooled high power, high frequency transformer with high insulation capability," in *Proceedings of IEEE Applied Power Electronics Conference and Exposition (APEC)*, 2002, pp. 352–357.

[44] B. Engel, M. Victor, G. Bachmann, and A. Falk, "15 kV/16.7 Hz energy supply system with medium frequency transformer and 6.5 kV IGBTs in resonant operation," in *Proceedings of European Conference on Power Electronics and Applications (EPE)*, 2003.

[45] T. Kjellqvist, S. Norrga, and S. Östlund, "Design considerations for a medium frequency transformer in a line side power conversion system," in *Proceedings of Annual IEEE Power Electronics Specialists Conference (PESC)*, vol. 1, 2004, pp. 704–710.

[46] J. Taufiq, "Power Electronics Technologies for Railway Vehicles ," in *Proceedings of Power Conversion Conference (PCC)*, 2007, pp. 1388–1393.

[47] N. Hugo, P. Stefanutti, M. Pellerin, and A. Akdag, "Power electron-

ics traction transformer," in *Proceedings of European Conference on Power Electronics and Applications (EPE)*, 2007.

[48] T. Komrska and Z. Peroutka, "Main Traction Converter with Medium-Frequency Transformer: Control of Converters around MF Transformer," in *Proceedings of International Symposium on Power Electronics, Electrical Drives, Automation and Motion (SPEEDAM)*, 2008, pp. 1194–1198.

[49] H. Hoffmann and B. Piepenbreier, "High voltage IGBTs and medium frequency transformer in DC-DC converters for railway applications," in *Proceedings of International Symposium on Power Electronics, Electrical Drives, Automation and Motion (SPEEDAM)*, 2010, pp. 744–749.

[50] C. Zhao, J. K. Steinke, S. Lewdeni-Schmid, M. Weiss, T. Chaudhuri, M. Pellerin, and P. Stefanutti, "Design, implementation and performance of a modular power electronic transformer (PET) for railway application," in *Proceedings of European Conference on Power Electronics and Applications (EPE)*, 2011.

[51] M. Claessens, D. Dujic, F. Canales, J. K. Steinke, P. Stefanutti, and C. Vetterli, "Traction transformation - a power electronic traction transformer (PETT)," *ABB Review*, vol. 1/12, pp. 11–17, 2012.

[52] C. Zhao, D. Dujic, A. Mester, J. K. Steinke, M. Weiss, S. Lewdeni-Schmid, T. Chaudhuri, and P. Stefanutti, "Power Electronic Traction Transformer-Medium Voltage Prototype," *IEEE Transactions on Industrial Electronics*, vol. 61, no. 7, pp. 3257–3268, 2014.

[53] C. Meyer, M. Hoing, A. Peterson, and R. W. De Doncker, "Control and Design of DC Grids for Offshore Wind Farms," *IEEE Transactions on Industry Applications*, vol. 43, no. 6, pp. 1475–1482, 2007.

[54] V. Yaramasu, B. Wu, P. C. Sen, S. Kouro, and M. Narimani, "High-power wind energy conversion systems: State-of-the-art and emerging technologies," *Proceedings of the IEEE*, vol. 103, no. 5, pp. 740–788, May 2015.

[55] C. Meyer, "Key Components for Future Offshore DC Grids," Ph.D. dissertation, RWTH-Aachen University, Germany, 2007.

[56] A. Prasai, J.-S. Yim, D. Divan, A. Bendre, and S.-K. Sul, "A New Architecture for Offshore Wind Farms," *IEEE Transactions on Power Electronics*, vol. 23, no. 3, pp. 1198–1204, 2008.

[57] L. Max and T. Thiringer, "Design and Control of a DC Collection Grid for a Wind Farm," Ph.D. dissertation, Chalmers University of Technology, 2009.

[58] S. Meier, T. Kjellqvist, S. Norrga, and H.-P. Nee, "Design considerations for medium-frequency power transformers in offshore wind farms," in *Proceedings of European Conference on Power Electronics and Applications (EPE)*, 2009.

[59] J. Robinson, D. Jovcic, and G. Joos, "Analysis and Design of an Offshore Wind Farm Using a MV DC Grid," *IEEE Transactions on Power Delivery*, vol. 25, no. 4, pp. 2164–2173, 2010.

[60] F. Deng and Z. Chen, "Control of Improved Full-Bridge Three-Level DC/DC Converter for Wind Turbines in a DC Grid," *IEEE Transactions on Power Electronics*, vol. 28, no. 1, pp. 314–324, 2013.

[61] W. Chen, A. Q. Huang, C. Li, G. Wang, and W. Gu, "Analysis and Comparison of Medium Voltage High Power DC/DC Converters for Offshore Wind Energy Systems," *IEEE Transactions on Power Electronics*, vol. 28, no. 4, pp. 2014–2023, 2013.

[62] N. Holtsmark, H. J. Bahirat, M. Molinas, B. A. Mork, and H. K. Hoidalen, "An All-DC Offshore Wind Farm With Series-Connected Turbines: An Alternative to the Classical Parallel AC Model?" *IEEE Transactions on Industrial Electronics*, vol. 60, no. 6, pp. 2420–2428, 2013.

[63] E. Veilleux and P. W. Lehn, "Interconnection of Direct-Drive Wind Turbines Using a Series-Connected DC Grid," *IEEE Transactions on Sustainable Energy*, vol. 5, no. 1, pp. 139–147, 2014.

[64] R. Barrera-Cardenas and M. Molinas, "Comparative Study of Wind Turbine Power Converters Based on Medium-Frequency AC-Link for Offshore DC-Grids," *IEEE Journal of Emerging and Selected Topics in Power Electronics*, vol. 3, no. 2, pp. 525–541, 2015.

[65] M. H. Kheraluwala, D. W. Novotny, and D. M. Divan, "Coaxially wound transformers for high-power high-frequency applications," *IEEE Transactions on Power Electronics*, vol. 7, no. 1, pp. 54–62, 1992.

[66] S. Prabhakaran, C. Stephens, F. Johnson, and L. Lorio, "High frequency power transformers for future military propulsion and energy systems," in *Proceedings of Electronic Machine Technology Symposium*, 2008.

[67] K. W. Klontz, D. M. Divan, and D. W. Novotny, "An actively cooled 120 kW coaxial winding transformer for fast charging electric vehicles," *IEEE Transactions on Industry Applications*, vol. 31, no. 6, pp. 1257–1263, 1995.

[68] T. Kjellqvist, S. Norrga, S. Östlund, and K. Ilves, "Thermal evaluation of a medium frequency transformer in a line side conversion system," in *Proceedings of European Conference on Power Electronics and Applications (EPE)*, 2009.

[69] M. Pavlovsky, S. W. H. de Haan, and J. A. Ferreira, "Design for better thermal management in high-power high-frequency transformers," in *Proceedings of IEEE Industry Applications Society Annual Meeting (IAS)*, 2005, pp. 2615–2621.

[70] ——, "Reaching High Power Density in Multikilowatt DC-DC Converters With Galvanic Isolation," *IEEE Transactions on Power Electronics*, vol. 24, no. 3, pp. 603–612, 2009.

[71] H. Hoffmann and B. Piepenbreier, "Medium frequency transformer for rail application using new materials," in *Proceedings of International Electric Drives Production Conference (EDPC)*, 2011, pp. 192–197.

[72] S. S. Baek, Y. Du, G. Wang, and S. Bhattacharya, "Design considerations of high voltage and high frequency transformer for solid state transformer application," in *Proceedings of IEEE Industry Applications Society Annual Meeting (IAS)*, 2010, pp. 421–426.

[73] S. S. Baek, S. Bhattacharya, B. Cougo, and G. Ortiz, "Accurate equivalent circuit modeling of a medium-voltage and high-frequency coaxial winding DC-link transformer for solid state transformer applications," in *Proceedings of IEEE Energy Conversion Congress and Exposition (ECCE)*, 2012.

[74] I. Villar, L. Mir, I. Etxeberria-Otadui, J. Colmenero, X. Agirre, and T. Nieva, "Optimal design and experimental validation of a Medium-Frequency 400kVA power transformer for railway traction applications," in *Proceedings of IEEE Energy Conversion Congress and Exposition (ECCE)*, 2012.

[75] D. Rothmund, G. Ortiz, T. Guillod, and J. W. Kolar, "10kV SiC-based isolated DC-DC converter for medium voltage-connected Solid-State

Transformers," in *Proceedings of IEEE Applied Power Electronics Conference and Exposition (APEC)*, 2015.

[76] M. A. Bahmani, "Design and Optimization Considerations of Medium-Frequency Power Transformers in High-Power DC-DC Applications," Ph.D. dissertation, Chalmers University of Technology, 2016.

[77] [Online]. Available: http://www.sts-trafo.com

[78] G. Ortiz, J. Biela, D. Bortis, and J. W. Kolar, "1 Megawatt, 20 kHz, isolated, bidirectional 12kV to 1.2kV DC-DC converter for renewable energy applications," in *Proceedings of International Power Electronics Conference (IPEC)*, 2010, pp. 3212–3219.

[79] P. Shuai and J. Biela, "Design and optimization of medium frequency, medium voltage transformers," in *Proceedings of European Conference on Power Electronics and Applications (EPE)*, 2013, pp. 1–10.

[80] A. Belahcen, "Magnetoelasticity, magnetic forces and magnetostriction in electrical machines," Ph.D. dissertation, Helsinki University of Technology, 2004.

[81] J. Roivainen, "Unit-wave response-based modeling of electromechanical noise and vibration of electrical machines," Ph.D. dissertation, Helsinki University of technology, 2009.

[82] M. van der Giet, "Analysis of electromagnetic acoustic noise excitations: A contribution to low-noise design and to the auralization of electrical machines," Ph.D. dissertation, RWTH-Aachen University, 2011.

[83] B. Weiser, H. Pfützner, and J. Anger, "Relevance of magnetostriction and forces for the generation of audible noise of transformer cores," *IEEE Transactions on Magnetics*, vol. 36, no. 5, pp. 3759–3777, 2000.

[84] R. S. Masti, W. Desmet, and W. Heylen, "On the influence of core laminations upon power transformer noise," in *Proceedings of ISMA*, 2004, pp. 3851–3862.

[85] A. Moses, P. Anderson, T. Phophongviwat, and S. Tabrizi, "Contribution of magnetostriction to transformer noise," in *45th International Universities Power Engineering Conference (UPEC)*, 2010, pp. 1–5.

[86] O. Barre, B. Napame, M. Hecquet, and P. Brochet, "Acoustic noise emitted by passive components in magnetic devices and design of

a low-noise industrial inductor," *COMPEL: The International Journal for Computation and Mathematics in Electrical and Electronic Engineering*, vol. 27, no. 5, pp. 1053–1068, 2008.

[87] S. Schmitt, "Acoustic noise of sheeted electrical steel inductors in PWM operation – causes and mitigation," in *Proceedings of European Conference on Power Electronics and Applications (EPE)*, 2009, pp. 1–8.

[88] Y. Gao, K. Muramatsu, M. J. Hatim, and M. Nagata, "The effect of laminated structure on coupled magnetic field and mechanical analyses of iron core and its homogenization technique," *IEEE Transactions on Magnetics*, vol. 47, no. 5, pp. 1358–1361, 2011.

[89] Y. Gao, M. Nagata, K. Muramatsu, K. Fujiwara, Y. Ishihara, and S. Fukuchi, "Noise reduction of a three-phase reactor by optimization of gaps between cores considering electromagnetism and magnetostriction," *IEEE Transactions on Magnetics*, vol. 47, no. 10, pp. 2772–2775, 2011.

[90] P. Jang and G. Choi, "Acoustic noise characteristics and magnetostriction of Fe-Si powder cores," *IEEE Transactions on Magnetics*, vol. 48, no. 4, pp. 1549–1552, 2012.

[91] J. Mühlethalter, M. Schubiger, U. Badstübner, and J. W. Kolar, "Acoustic noise in inductive power components," in *Proceedings of European Conference on Power Electronics and Applications (EPE)*, 2013, pp. 1–8.

[92] J. Wang, A. Q. Huang, W. Sung, Y. Liu, and B. J. Baliga, "Smart grid technologies," *IEEE Industrial Electronic Magazine*, vol. 3, no. 2, pp. 16–23, 2009.

[93] N. Schibli, "Symmetrical multilevel converters with two quadrant DC-DC feeding," Ph.D. dissertation, Éole Polytechnique Fédérale de Lausanne (EPFL), 2000.

[94] F. Krismer, "Modeling and Optimization of Bidirectional Dual Active Bridge DC–DC Converter Topologies," Ph.D. dissertation, ETH Zürich, 2011.

[95] P. Wallmeier, "Automatisierte Optimierung von induktiven Bauelementen für Stromrichteranwendungen," Ph.D. dissertation, Universität Paderborn, 2001.

[96] J. A. Ferreira, "Improved Analytical Modeling of Conductive Losses

in Magnetic Components," *IEEE Transactions on Power Electronics*, vol. 9, no. 1, pp. 127–131, 1994.

[97] [Online]. Available: http://www.vonroll.ch/

[98] H. Singer, H. Steinbigler, and P. Weiss, "A charge simulation method for the calculation of high voltage fields," *IEEE Transactions on Power Apparatus and Systems*, vol. PAS-93, no. 5, pp. 1660–1668, 1974.

[99] [Online]. Available: http://www.huntsman.com/

[100] J. Lienhard IV and J. Lienhard V, *A heat transfer textbook*, 4th ed. Phlogiston Press, 2011.

[101] *VDI-Wärmeatlas*. Springer-Verlag, 2006.

[102] U. Drofenik, G. Laimer, and J. W. Kolar, "Theoretical Converter Power Density Limits for Forced Convection Cooling," in *Proceedings of the International PCIM Europe Conference (PCIM)*, 2005, pp. 608–619.

[103] J. Koch, "Berechnung der Kapazität von Spulen, insbesondere in Schalenkernen," *Valvo Berichte*, vol. XIV, no. 3, pp. 99–119, 1968.

[104] M. Jaritz and J. Biela, "Analytical model for the thermal resistance of windings consisting of solid or litz wire," in *Proceedings of European Conference on Power Electronics and Applications (EPE)*, 2013.

[105] [Online]. Available: www.epicpolymers.de/

[106] [Online]. Available: http://www2.dupont.com/

[107] [Online]. Available: http://www.kern-gmbh.de/

[108] [Online]. Available: http://www.vacuumschmelze.de/

[109] [Online]. Available: https://en.wikipedia.org/wiki/Acoustics

[110] L. L. Beranek and T. J. Mellow, *Acoustics: Sound Fields and Transducers*. Elsevier Inc., 2012.

[111] A. J. Ellison, C. J. Moore, and S. J. Yang, "Methods of measurement of acoustic noise radiated by an electric machine," *Proceedings of the Institution of Electrical Engineers*, vol. 116, no. 8, pp. 1419–1431, 1969.

[112] S. Yang, *Low-Noise Electrical Motors*. Oxford Science Publications, 1981.

[113] B. Goelzer, C. H. Hansen, and G. A. Sehrndt, *Occupational exposure to*

noise: evaluation, prevention and control. World Health Organization, 2001.

[114] [Online]. Available: https://www.osha.gov/dts/osta/otm/noise/health_effects/soundpropagation.html

[115] E. Du Trémolet de Lacheisserie, *Magnetostriction, Theory and Applications of Magnetoelasticity*. CRC Press, 1993.

[116] D. C. Jiles, *Introduction to Magnetism and Magnetic Materials*, 2nd ed. CRC Press, 1998.

[117] K. Delaere, "Computational and experimental analysis of electric machine vibrations caused by magnetic forces and magnetostriction," Ph.D. dissertation, K. U. Leuven, 2002.

[118] B. D. Cullity and C. D. Graham, *Introduction to Magnetic Materials*, 2nd ed. Willey, 2009.

[119] D. C. Jiles and M. K. Devine, "Recent developments in modeling of the stress derivative of magnetization in ferromagnetic materials," *Journal of Applied Physics*, vol. 76, no. 10, pp. 7015–7017, 1994.

[120] R. Hilzinger and W. Rodewald, *Magnetic Materials - Fundamentals, Products, Properties, Applications*. Publics Publishing, 2013.

[121] A. Kelley, "Measurement of spacecraft power transformer acoustic noise," *IEEE Transactions on Magnetics*, vol. 26, no. 1, pp. 281–289, 1990.

[122] [Online]. Available: https://www.comsol.com/

[123] Z. Ren, "Comparison of different force calculation methods in 3D finite element modelling," *IEEE Transactions on Magnetics*, vol. 30, no. 5, pp. 3471–3474, 1994.

[124] S. Somkun, "Magnetostriction and magnetic anisotropy in non-oriented electrical steels and stator core laminations," Ph.D. dissertation, Cardiff University, 2010.

[125] H. Altenbach, J. W. Altenbach, and W. Kissing, *Mechanics of Composite Structural Elements*. Springer-Verlag, 2004.

[126] A. Shahaj, "Mitigation of vibration in large electrical machines," Ph.D. dissertation, University of Nottingham, 2010.

[127] [Online]. Available: http://www.metglas.com/

[128] H. Czichos, *Hütte: die Grundlagen der Ingenieurwissenschaften*. Akademischer Verein Hütte, 2000.

[129] [Online]. Available: http://www.polytec.com/

[130] C. M. Harris, *Handbook of acoustical measurements and noise control*, 3rd ed. McGraw-Hill, Inc., 1991.

[131] [Online]. Available: https://www.bksv.com/

[132] *Sound power measurements*, ser. Application Note 1230. Hewlett-Packard Co., 1992.

[133] G. Müller and M. Möser, *Handbook of Engineering Acoustics*. Springer-Verlag, 2013.

[134] [Online]. Available: https://www.gras.dk/

[135] [Online]. Available: http://www.kaschke.de/home/

[136] J. H. Harlow, *Electric Power Transformer Engineering*. CRC Press, 2012.

[137] B. Garcia, J. C. Burgos, and A. M. Alonso, "Transformer tank vibration modeling as a method of detecting winding deformations-part I: theoretical foundation," *IEEE Transactions on Power Delivery*, vol. 21, no. 1, pp. 157–163, 2006.

[138] K. Hong and H. Huang, "Power transformer fault diagnosis based on vibration correlation analysis," in *Proceedings of International Mechanical Engineering Congress and Exposition (IMECE)*, 2014.

[139] S. Wada and T. Yagisawa, "On the loss and magnetostriction of electrical steel for the dc superposed flux alternation," *Journal of Magnetism and Magnetic Materials*, vol. 19, no. 1-3, pp. 39–41, 1980.

[140] M. Beltle and S. Tenbohlen, "Power transformer diagnosis based on mechanical oscillations due to AC and DC currents," *IEEE Transactions on Dielectrics and Electrical Insulation*, vol. 23, no. 3, pp. 1515–1522, 2016.

[141] N. M. L. Tan, T. Abe, and H. Akagi, "Design and performance of a bidirectional isolated DC-DC converter for a battery energy storage system," *IEEE Transactions on Power Electronics*, vol. 27, no. 3, pp.

1237–1248, 2012.

[142] S. U. Jen, C. C. Liu, H. R. Lin, and S. H. Chou, "Frequency dependence of the magnetostrictive phenomenon in Metglas 2605SA1 ribbon: A minor-loop case," *AIP Advances*, vol. 4, no. 127140, pp. 1–4, 2014.

[143] Y.-Q. Tang, J.-Q. Qiao, and Z.-H. Xu, "Numerical calculation of short circuit electromagnetic forces on the transformer winding," *IEEE Transactions on Magnetics*, vol. 26, no. 2, pp. 1039–1041, 1990.

[144] M. Ertl and S. Voss, "The role of load harmonics in audible noise of electrical transformers," *Journal of Sound and Vibration*, vol. 333, no. 8, pp. 2253–2270, 2014.

[145] C.-K. Kim, V. K. Sood, G.-S. Jang, S.-J. Lim, and S.-J. Lee, *HVDC Transmission: Power Conversion Applications in Power Systems*. John Wiley & Sons, 2009.

[146] Y. Shao, H. Guan, Y. Zhang, Z. Jin, and Z. Rao, "A vibration method for identifying the looseness of windings for large power transformers," in *Proceedings of International Conference on Signal Processing Systems (ICSPS)*, 2012.

[147] H. Ma, N. Jiang, C. Wang, and Z. Geng, "Improved power transformer winding deformation fault diagnosis method," *Applied Mechanics and Materials*, vol. 666, pp. 149–153, 2014.

[148] J. Biela and J. W. Kolar, "Cooling Concepts for High Power Density Magnetic Devices," *IEEJ Transactions on Industry Applications*, vol. 128, no. 4, pp. 500–507, 2008.